# OOCYTE MEIOTIC CELL DIVISION: SPINDLE ASSEMBLY, CHROMOSOME SEGREGATION, AND CYTOKINESIS.

by

ALEESA JOELLE SCHLIENTZ

A DISSERTATION

Presented to the Department of Biology
and the Graduate School of the University of Oregon
in partial fulfillment of the requirements
for the degree of
Doctor of Philosophy

June 2020

DISSERTATION APPROVAL PAGE

Student: Aleesa Joelle Schlientz

Title: Oocyte Meiotic Cell Division: Spindle Assembly, Chromosome Segregation, and Cytokinesis

This dissertation has been accepted and approved in partial fulfillment of the requirements for the Doctor of Philosophy degree in the Department of Biology by:

| | |
|---|---|
| Victoria Herman | Chairperson |
| Bruce Bowerman | Advisor |
| Christopher Doe | Core Member |
| Diana Libuda | Core Member |
| Bradley Nolen | Institutional Representative |

and

| | |
|---|---|
| Kate Mondloch | Interim Vice Provost and Dean of the Graduate School |

Original approval signatures are on file with the University of Oregon Graduate School.

Degree awarded June 2020

© 2020 Aleesa Joelle Schlientz

DISSERTATION ABSTRACT

Aleesa Joelle Schlientz

Doctor of Philosophy

Department of Biology

June 2020

Title: Oocyte Meiotic Cell Division: Spindle Assembly, Chromosome Segregation, and Cytokinesis

Meiosis, the specialized cell division process that results in haploid gamete formation, is characterized by a single round of genome duplication followed by two successive divisions. During meiosis, replicated homologous chromosomes must pair and recombine or cross-over to allow for efficient chromosome segregation and formation of daughter cells with the correct chromosomal content. Defects in the meiotic division process, including the failure or mis-segregation of chromosomes or failed cytokinesis, can lead to complications such as aneuploid disorders (ex. trisomy 21), miscarriages, or infertility. Female gamete precursors, called oocytes, are remarkably error-prone during the meiotic division process, with approximately 10-30% of human oocytes having an incorrect number of chromosomes. Interestingly, the process of both spindle assembly and cytokinesis are unique in oocytes and differ greatly from the mitotic and sperm meiotic processes, with oocytes forming spindles in the absence of centrosomes and the cytokinetic apparatus, the polar body contractile ring, forming distal to both spindle poles rather than between them. These aspects of the meiotic division process lead to a number of questions about the requirements for building a meiotic spindle in the absence of centrosomes, segregating chromosomes, assembling a contractile ring, and the potential

relationships between these processes. To better understand the oocyte meiotic division process, we used a combination of *Caenorhabditis elegans* genetics and spinning-disk confocal time-lapse microscopy to live-image the meiotic divisions in oocytes. We examined the requirements for the earliest stages of meiotic spindle assembly, focusing on microtubule nucleation and spindle formation dynamics, the impact of supernumerary crossovers on the process of chromosome segregation, and the relationship between oocyte meiotic spindle assembly/chromosome segregation on the assembly and dynamics of the cytokinetic contractile ring. These analyses allow for a better understanding of the functional requirements of the oocyte meiotic division process

This dissertation includes unpublished co-authored material.

CURRICULUM VITAE

NAME OF AUTHOR: Aleesa Joelle Schlientz

GRADUATE AND UNDERGRADUATE SCHOOLS ATTENDED:

University of Oregon, Eugene
University of Michigan, Ann Arbor

DEGREES AWARDED:

Doctor of Philosophy, Biology, 2020, University of Oregon
Bachelor of Science, Microbiology, 2012, University of Michigan

AREAS OF SPECIAL INTEREST:

Cell & molecular biology, genetics

PROFESSIONAL EXPERIENCE:

Graduate Employee, Department of Biology, University of Oregon 2014-2020

Laboratory Technician, Department of Molecular and Integrative Physiology, University of Michigan, 2012-2014

Laboratory Assistant, Department of Internal Medicine, University of Michigan, 2010-2012

GRANTS, AWARDS, AND HONORS:

Pete von Hippel Graduate Scholar Award, Institute of Molecular Biology, University of Oregon, 2019

Donald E. Wimber Travel Fund Award, Department of Biology, University of Oregon, 2019

Departmental Nominee for Dissertation Research Fellowship, Department of Biology, University of Oregon, 2019

Runner-up Outstanding Poster Award, Institute of Molecular Biology, University of Oregon 2016

Genetics Training Program (T32GM007413), University of Oregon, 2015-2018

UROP Summer Biomedical Life Sciences Fellowship, University of Michigan, 2011

PUBLICATIONS:

Rux, D.R., Song, J.Y., Pineault, K.M., Mandair, G.S., Swinehart, I.T., Schlientz, A.J., Garthus, K.N., Kozloff, K.M., & Wellik, D.M. (2017) Hox11 Function is Required for Region-Specific Fracture Repair. *J Bone Miner Res*, 32(8):1750-1760. doi:10.1002/jbmr.3166

Rux, D.R., Song, J.Y., Swinehart, I.T., Pineault, K.M., Schlientz, A.J., Trulik, K.G., Goldstein, S.A., Kozloff, K.M., Lucas, D., & Wellik, D.M. (2016) Regionally Restricted Hox Function in Adult Bone Marrow Multipotent Mensenchymal Stem/Stromal Cells. *Dev Cell*. 39(6):653-666 doi:10.1016/j.devcel.2016.11.008

Florida, S.E., VanDusen, K.W., Mahalingam, V.D., Schlientz, A.J., Wojtys, E.M., Wellik, D.M., & Larkin, L.M. (2016) *In vivo* structural and cellular remodeling of engineered bone-ligament-bone constructs used for anterior cruciate ligament reconstruction in sheep. *Connect Tissue Res.* 57(6)526-538 doi:10.1080/03008207.2016.1187141

Swinehart, I.T., Schlientz, A.J., Quintanilla, C.A., Mortlock, D.P., & Wellik, D.M. (2013) Hox11 genes are required for regional patterning and integration of muscle, tendon and bone. *Development*. 140(22):4574-82 doi:10.1242/dev.096693

ACKNOWLEDGMENTS

I wish to express sincere appreciation to Dr. Bruce Bowerman; whose support and mentorship was essential for the works presented here and for helping me to grow as a scientist and as a person. Additionally, special thanks are due to my dissertation advisory committee – Dr. Tory Herman, Dr. Chris Doe, Dr. Diana Libuda, and Dr. Brad Nolen – for their feedback and support over the years. I would also like to express my deepest gratitude to current and former Bowerman lab members – Chien-Hui Chuang, Austin Harvey, Molly Jud, Jie Yang, and Kenji Sugioka – for sharing their insight and expertise, and for all the fun over the years. The University of Oregon and Institute of Molecular Biology (IMB) communities were invaluable to this work, particularly Dr. Larry Scatena, who provided crucial optical expertise and maintenance, and the IMB office staff. I also thank my various collaborators, without whom much of this work would not have been possible. This work was supported in part by funding from the National Institutes of Health (T32GM007413, R01GM049869, and R35GM131749), with *C. elegans* strains generously provided by various members of the worm community, and from the Caenorhabditis Genetics Center, which is funded by NIH Office of Research Infrastructure Programs (P40 OD010440).

I am thankful to my parents, Matthew and Mary Schlientz, and to my brothers, Trevor and Tyler Schlientz, for their support and for believing in me even during the times I did not believe in myself. I do not know that I would have pursued doctoral studies without the guidance and continual support of Dr. Deneen Wellik, and for that I am perpetually grateful. Similarly, I do not know that I would have completed my doctoral studies without the support of many friends, and for that I am also forever

appreciative. Special mentions go to Emily Sutton and Maria Bañuelos for their support and camaraderie over the years, and to the trivia and movie night crews for the much-needed breaks in seemingly endless data analysis and writing. I thank Bronn and Cara Schlientz for helping to bolster my fortitude, and for providing me with companionship over the long years. Finally, I would like to thank Luke Edwards for bringing so many amazing people into my life and for being a source of solace and mirth over the years. You have been a light in my life at times when all else seemed dark, and for that I am eternally grateful.

This dissertation is dedicated to my parents, my brothers,
and to the many friends who helped me along the way.

Thank you for your love and support.

TABLE OF CONTENTS


Chapter Page

I. INTRODUCTION ..... 1

Introduction to Oocyte Meiosis ..... 2

Oocyte Meiotic Spindle Assembly and Chromosome Segregation ..... 3

Polar Body Cytokinesis ..... 7

Bridge ..... 8

II. MICROTUBULE ASSEMBLY AND POLE COALESCENCE: EARLY STEPS IN *C. ELEGANS* OOCYTE MEIOSIS I SPINDLE ASSEMBLY ..... 10

Introduction ..... 10

Results ..... 14

Wild-type Oocyte Meiosis I Spindle Assembly ..... 14

The Nuclear Lamina is Required for Assembly of the Peripheral Microtubule Cage Structure ..... 16

RAN-1 Promotes Microtubule Assembly and Normal Oocyte Nuclear Size ..... 18

TBG-1 is Required for Proper Oocyte Nuclear Positioning and Promotes both Microtubule Levels and Normal Spindle Assembly Dynamics ..... 21

KLP-15 and -16 are Required for Cage Stability and Promote Pole Coalescence ..... 24

ZYG-9 Restricts Microtubule Bundles to the Periphery During Cage Assembly and Promotes Pole Coalescence and Stability ..... 27

Discussion ..... 30

Microtubule Nucleation and *C. elegans* Oocyte Meiotic Spindle Assembly ..... 32

The Nuclear Lamina as a Platform for Assembling the Cage-like Network of Microtubule Bundles ..... 34

Chapter Page

ZYG-9/XMAP215 and the Kinesin-14 Family Members KLP-15/16 Contribute to Proper Assembly of the Cage-like Network of Microtubule Bundles ..... 35

ZYG-9/XMAP215 and the Kinesin-14 Family Members KLP-15/16 Make Distinct Contributions to Pole Coalescence ..... 37

Bridge to Chapter III ..... 39

III. EXCESS CROSSOVERS IMPEDE FAITHFUL MEIOTIC CHROMOSOME SEGREGATION IN *C. ELEGANS* ..... 41

Introduction ..... 41

Results ..... 45

Fusion Chromosomes Generate Bivalents with Multiple Crossovers and Chiasmata ..... 45

Bivalents with Multiple Crossovers have Mispatterned Ring Complexes ..... 49

Fusion Chromosome Bivalents can Form Multiple Ring Complex that All Remain Functional ..... 52

Fusion Chromosome Bivalents Show Defects in Metaphase Alignment and Bivalent Organization ..... 54

Fusion Chromosome Bivalents Show Defects in Chromosome Segregation that Carry Over into Meiosis II ..... 57

Persistent Chromatin Bridges can be Recognized and Resolved by the Oocyte ..... 60

Discussion ..... 65

Crossover Limitation Promotes Accurate Chromosome Segregation ..... 66

Mechanisms Exist to Correct Errors Caused by Supernumerary Crossovers ..... 66

Licensing of Ring Complex Formation by Crossovers ..... 68

Bridge to Chapter IV ..... 69

Chapter Page

IV. *C. ELEGANS* CLASP/CLS-2 IS REQUIRED FOR POLAR BODY EXTRUSION AND NEGATIVELY REGULATES GLOBAL CORTICAL CONTRACTILITY DURING OOCYTE MEIOSIS ..... 71

Introduction ..... 71

Results ..... 77

CLS-2 is Required for Oocyte Meiotic Spindle Assembly and Polar Body Cytokinesis ..... 77

Polar Body Extrusion Defects in *cls-2* Mutants are Not Due to Absence of the Central Spindle-Associated Proteins AuroraB/AIR-2 or MgcRacGAP/CYK-4 ..... 81

CLS-2 and MEI-1, but Not Spindle Bipolarity, are Required for Polar Body Cytokinesis ..... 82

Meiotic Spindle-Associated Furrows are Abnormal in *cls-2* and *mei-1* Mutant Oocytes ..... 83

Polar Body Contractile Ring Dynamics are More Severely Defective in the Absence of CLS-2 than in *klp-18* or *mei-1* Mutant Oocytes ..... 87

CLS-2 Negatively Regulates Membrane Ingression Throughout the Oocyte Cortex During Meiosis I ..... 91

Discussion ..... 94

Using Spindle Assembly Defective Mutants to Explore Contractile Ring Dynamics During Oocyte Polar Body Extrusion ..... 95

Roles for CLS-2 and MEI-1 in Contractile Ring Assembly and Constriction ..... 98

Negative Regulation of Oocyte Global Cortical Dynamics and its Relationship to Polar Body Extrusion ..... 100

V. CONCLUSIONS AND FUTURE DIRECTIONS ..... 104

Summary ..... 104

Chapter Page

Future Direction ..... 106

APPENDICES ..... 109

A. MATERIALS AND METHODS FOR CHAPTER II ..... 109

*C. elegans* Strains ..... 109

RNAi ..... 109

CRISPR ..... 109

Generation of gfp::zyg-9 and gfp::tac-1 Transgenic Strains ..... 109

Generation of Double Deletion Strain of *klp-15* and *klp-16* ..... 110

Image Acquisition ..... 111

Image Processing and Analysis ..... 112

Statistics ..... 113

B. SUPPLEMENTAL MATERIALS FOR CHAPTER II ..... 114

C. MATERIALS AND METHODS FOR CHAPTER III ..... 131

*C. elegans* Strains, Genetics, and Culture Conditions ..... 131

RNAi Treatments ..... 131

Immunofluorescence for Late Meiotic Prophase I ..... 132

Immunofluorescence for Prometa-, Meta- and Anaphase I and II ..... 133

Fixed Imaging ..... 134

Ring Stretching Assay ..... 136

Quantification ..... 136

Ring Structure Quantification ..... 136

Linescans ..... 137

Chapter Page

Metaphase Alignment Quantification ..... 137

Chromosome Distance Measurements ..... 138

Chromatin Bridging Quantification ..... 138

Meiosis II Quantification ..... 138

Scoring Embryonic Viability ..... 139

Live Imaging ..... 139

Statistical Analysis ..... 140

D. SUPPLEMENTAL MATERIALS FOR CHAPTER III ..... 141

E. MATERIALS AND METHODS FOR CHAPTER IV ..... 144

*C. elegans* Strain Maintenance ..... 144

*cls-2* CRISPR/Cas9 Allele Generation ..... 144

Feeding RNAi Knockdown of *mei-1* and *klp-18* ..... 145

Live-cell Imaging ..... 145

Image Analysis, Quantification, and Statistical Analysis ..... 146

F. SUPPLEMENTAL MATERIALS FOR CHAPTER IV ..... 149

REFERENCES CITED ..... 168

LIST OF FIGURES

Figure Page

2.1. Wild-type oocyte meiosis I spindle assembly ..... 12

2.2. The nuclear lamina is required for the early cage-like microtubule structure during oocyte meiosis I ..... 16

2.3. RAN knockdown reduces oocyte nuclear size and microtubule levels during oocyte meiosis I ..... 19

2.4. TBG-1 knockdown alters spindle dynamics after the microtubule cage-like structure appears and reduces microtubule levels during oocyte meiosis I ..... 23

2.5. KLP-15/16 knockdown destabilizes cage-like microtubule bundles and reduces pole coalescence ..... 24

2.6. ZYG-9 knockdown causes spindle assembly defects throughout oocyte meiosis I ..... 28

2.7. Microtubule levels are increased throughout the oocyte cortex during meiosis I after ZYG-9 knockdown ..... 30

3.1. Fusion chromosomes generate bivalents with multiple crossovers and chiasmata ..... 46

3.2. Bivalents with excess crossovers have mispatterned Ring Complexes (RCs) ..... 50

3.3. Bivalents with excess COs can form multiple functional RCs ..... 53

3.4. Bivalents with mispatterned RCs align improperly on the oocyte spindle and are not subjected to proper plus-end directed forces ..... 55

3.5. Fusion chromosome segregation is frequently aberrant ..... 58

3.6. *meT7* oocytes display several classes of chromosome segregation defects ..... 60

3.7. Oocytes can correct errors from excess COs in anaphase ..... 63

4.1. Schematics of oocyte meiotic polar body extrusion, mitotic cytokinesis and oocyte meiotic spindle assembly-defective mutants ..... 73

4.2. CLS-2 is required for oocyte meiotic spindle assembly and polar body extrusion ..... 77

Figure Page

4.3. Central spindle proteins AIR-2 and CYK-4 still associate with spindle microtubules in *cls-2* mutant oocytes ..... 82

4.4. Spindle-associated membrane furrowing during meiosis I in control and mutant oocytes ..... 84

4.5. Contractile ring non-muscle myosin NMY-2 dynamics during meiosis I in control and mutant oocytes ..... 88

4.6. Contractile ring anillin ANI-1 and non-muscle myosin NMY-2 dynamics during meiosis I in control and *cls-2* mutant oocytes ..... 89

4.7. Membrane ingressions throughout the oocyte cortex during meiosis I in control and mutant oocytes ..... 92

B.1. Supplemental Figure 1 ..... 114

B.2. Supplemental Figure 2 ..... 115

B.3. Supplemental Figure 3 ..... 116

B.4. Supplemental Figure 4 ..... 117

B.5. Supplemental Figure 5 ..... 118

B.6. Supplemental Figure 6 ..... 119

B.7. Supplemental Figure 7 ..... 120

B.8. Supplemental Figure 8 ..... 121

B.9. Supplemental Figure 9 ..... 122

B.10. Supplemental Figure 10 ..... 123

B.11. Supplemental Figure 11 ..... 124

B.12. Supplemental Figure 12 ..... 125

B.13. Supplemental Figure 13 ..... 126

B.14. Supplemental Figure 14 ..... 127

Figure Page

B.15. Supplemental Figure 15 ..... 128

B.16. Supplemental Figure 16 ..... 129

D.1. Additional characterization of CPC components ..... 141

D.2. The holocentric kinetochore cups the entirety of *meT7* ..... 141

D.3. RCs show an increased frequency of delayed disassembly in meT7 oocytes, demonstrating that errors are recognized ..... 142

F.1. CLS-2 localizes to meiotic spindles and is required for their assembly ..... 150

F.2. Control oocyte spindle-associated membrane furrows ..... 151

F.3. *cls-2(or1948)* oocyte spindle-associated membrane furrows ..... 152

F.4. *cls-2(or1948)* oocyte spindle-associated membrane furrows ..... 153

F.5. *klp-18(RNAi)* oocyte spindle-associated membrane furrows ..... 154

F.6. *mei-1(RNAi)* oocyte spindle-associated membrane furrows ..... 155

F.7. Control oocyte NMY-2::GFP contractile rings ..... 156

F.8. *cls-2(or1948)* oocyte NMY-2::GFP contractile rings ..... 157

F.9. *klp-18(RNAi)* oocyte NMY-2::GFP contractile rings ..... 158

F.10. *mei-1(RNAi)* oocyte NMY-2::GFP contractile rings ..... 159

F.11. Control oocyte membrane temporal overlays ..... 160

F.12. *cls-2(or1948)* oocyte membrane temporal overlays ..... 161

F.13. *klp-18(RNAi)* and *mei-1(RNAi)* membrane temporal overlays ..... 162

F.14. Control oocyte NMY-2::GFP cortical dynamics ..... 163

F.15. Control oocyte mNG::ANI-1 cortical dynamics ..... 164

F.16. *cls-2(or1948)* oocyte NMY-2::GFP cortical dynamics ..... 165

Figure Page

F.17. *cls-2(or1948)* oocyte NMY-2::GFP cortical dynamics ..... 166

F.18. *cls-2(or1948)* oocyte mNG::ANI-1 cortical dynamics..... 167

LIST OF TABLES

Table Page

3.1. Progeny viability following *lem-3* RNAi treatment..... 60

B.1. Supplemental Table 1..... 130

D.1 Frequency of chromosome segregation phenotypes from live imaging experiments..... 143

F.1. Table of C. elegans strains used in this study..... 149

# CHAPTER I

# INTRODUCTION

The work presented in this dissertation was largely carried out in the laboratory of Dr. Bruce Bowerman in the Department of Biology at the University of Oregon. This chapter, Chapter I, provides a broad introduction to oocyte meiosis. Chapter II contains unpublished co-authored material with other Bowerman lab members, Dr. Chien-Hui Chaung and Dr. Jie Yang, looking at the earliest stages of meiotic spindle assembly and its requirements under the supervision and assistance of Dr. Bowerman. Chapter III contains unpublished co-authored material and is the culmination of a collaborative project with the laboratories of Dr. Diana Libuda (University of Oregon) and Dr. Sadie (Sarah) Wignall (Northwestern University) examining the impact of excess crossover formation on oocyte chromosome segregation, and contains work from Libuda laboratory members Marissa Glover and Dr. Cori Cahoon, Wignall laboratory member Jeremy Hollis, and was facilitated and supervised by Drs. Bowerman, Wignall, and Libuda. Chapter IV contains unpublished co-authored material examining the relationship between oocyte meiotic spindle assembly and cytokinesis that was largely undertaken by myself under the guidance and support of Dr. Bowerman. Finally, Chapter V summarizes the advances made in the work presented in Chapters II-IV, and presents potential future directions based on these advances.

*This chapter contains unpublished material written by A.J.S.

## Introduction to Oocyte Meiosis

In sexually reproducing organisms the ability to produce haploid gametes, such as sperm and egg cells, is crucial for maintaining chromosomal copy number from generation to generation. Meiosis is the specialized cell division process that produces haploid daughter cells from a diploid precursor (Ohkura, 2015). During meiosis, the genome is duplicated and then undergoes two subsequent rounds of division called meiosis I and meiosis II. Meiosis I is a reductional division in which homologous chromosomes are segregated, while meiosis II is an equational division that segregates sister chromatids. Errors in the meiotic division process can lead to adverse outcomes such as infertility, miscarriages, and aneuploid developmental disorders, such as Down syndrome (trisomy 21) or Turner syndrome (only one X chromosome in females), wherein an individual is born with too many or too few chromosomal copies (Potapova et al., 2017). These errors in the meiotic division process can happen in either meiosis I or II and occur more commonly in female gamete precursors (oocytes) than in male gamete precursors (spermatocytes) (Hassold et al., 2001; Holubcova et al., 2015; Gruhn et al., 2019). This difference in error rate between male and female gametes leads to the question then, what is it about the female meiotic division that makes it more prone to errors?

Oocyte meiosis is unique in that the microtubule-based spindle structure that forms, and is required for the segregation of chromosomes, does so in the absence of centrosomes (Gruss, 2018). In both mitotically and sperm meiotically dividing cells, centrosomes dictate the spindle structure and help to nucleate the microtubules that the spindle is largely comprised of (Prosser et al., 2017). How, then, are microtubules

nucleated in acentrosomal oocytes, and what determines the structure of the meiotic spindle? Additionally, it is known that astral microtubules, which project outward from centrosomes to reach the cell cortex, help to dictate the formation of the contractile ring apparatus that cleaves the dividing cell into two separate daughter cells during cytokinesis (Motegi et al., 2006; Green et al., 2012; Pintard et al., 2019). How is it oocytes form a contractile apparatus in the absence of centrosomes and their astral microtubule projections? These unique features of the oocyte division process may explain the difference in error rates observed between male and female gametes.

**Oocyte Meiotic Spindle Assembly and Chromosome Segregation**

How oocytes in any species assemble an acentrosomal meiotic spindle is poorly understood, but for the purposes of this work we will focus on the meiotic spindle assembly process in *Caenorhabditis elegans* (*C. elegans*) oocytes. With its powerful genetic tools and optical transparency, *C. elegans* is an ideal model system for understanding the highly dynamic process of oocyte spindle assembly (Dumont et al., 2012; Severson et al., 2016; Mullen et al., 2019). In *C. elegans*, meiosis I spindle assembly begins with the breakdown of the nuclear envelope, and the formation of a cloud of tubulin within the perforated nuclear space (Gigant et al., 2017). This cloud of tubulin subunits is then polymerized and organized along the nuclear periphery, forming a hollow cage-like structure that surrounds the oocyte chromosomes (Wolff et al., 2016). As the spindle assembly process progresses, the microtubule cage structure condenses and microtubule minus ends are focused into spindle pole foci which coalesce together, ultimately forming a barrel-shaped bipolar spindle structure comprised of a tiled-array of

microtubules and microtubule-associated proteins (Srayko et al., 2006; Connolly et al., 2015). As meiosis I progresses and chromosomes align at the center of the spindle at metaphase, the meiotic spindle shrinks and rotates to become oriented perpendicular to the oocyte cortex, and in anaphase I the chromosomes segregate with spindle microtubules now largely being in between the segregating chromosomal masses (Laband et al., 2017). After the end of meiosis I, when one chromosomal mass is ejected from the oocyte cytoplasm during cytokinesis/polar body extrusion, this process repeats in meiosis II, with the exception of nuclear envelope breakdown and microtubule cage formation (Mullen et al., 2019). Some of these spindle assembly events have only come into focus in recent years, for example the formation of the tubulin cloud, the microtubule cage, and the coalescence of spindle poles, and as such our understanding of the molecular functions required has been limited.

While limited, we do know a small handful of proteins and their molecular functions that seem to play a role in the meiotic spindle assembly processes; these include KLP-18/kinesin-12, KLP-7/kinesin-13, the kinesin-14 family members KLP-15/16, and the katanin microtubule severing complex members MEI-1 and MEI-2. Microtubule sorting and bundling seem to be essential processes for transitioning from a microtubule cage to a bipolar spindle structure, as loss of kinesin-12/KLP-18 leads to the formation of monopolar meiotic spindles that fail to segregate chromosomes, while loss of the kinesin-14 family members KLP-15/16 result in disorganized meiotic spindles with poorly bundled microtubules (Wignall et al., 2009; Connolly et al., 2014; Wolff et al., 2016; Mullen et al., 2017). Loss of the kinesin-13 family member KLP-7 results in the formation of multipolar meiotic spindles, and excess microtubules, indicating that KLP-7

is involved in promoting spindle coalescence into a bipolar structure and microtubule regulation (Connolly et al., 2015; Gigant et al., 2017). Finally, the microtubule severing complex katanin, comprised of MEI-1 and MEI-2 in *C. elegans*, is known to be required both for microtubule severing which may promote microtubule abundance as well as the assembly of meiotic spindle poles (Srayko et al., 2006; Connolly et al., 2014). A number of other proteins have been suggested to be either required or nonessential for oocyte meiotic spindle assembly, however in many cases they have not been characterized in depth to understand where they fit into the assembly process.

One major outstanding question in the *C. elegans* meiotic spindle assembly field is how do oocytes nucleate the microtubules from which to build an acentrosomal meiotic spindle? In other organisms such as flies or mice, the small GTPase Ran has been shown to be required for microtubule nucleation (Cavazza et al., 2015; Gruss, 2018). However, work in *C. elegans* has suggested that RAN-1 is not essential for meiotic spindle assembly (Askjaer et al., 2002). Similarly, the γ-tubulin ring complex is known to be important for microtubule nucleation, but it's depletion in *C. elegans* does not lead to obvious meiotic spindle assembly defects (K. McNally et al., 2006; Roostalu et al., 2017; Tovey et al., 2018). One possible explanation for how *C. elegans* oocytes can produce an abundance of microtubules from which to build a meiotic spindle, is through the severing of microtubules by the katanin complex (MEI-1 and MEI-2), such that one polymerized microtubule becomes two microtubules after a severing event (Srayko et al., 2006). This idea, however, is predicated on having an initial microtubule population from which to amplify the number of microtubules via severing, and spontaneous self-assembly of microtubules is an energetically unfavorable process (Roostalu et al., 2017). These

differences in microtubule nucleation between *C. elegans* and other species oocytes provide an interesting opportunity to understand all the ways in which cells can nucleate microtubules in the absence of centrosomes.

In addition to the questions asking how *C. elegans* oocytes nucleate microtubules and assemble meiotic spindles, it is currently unclear how these spindles segregate chromosomes during each of the meiotic divisions. Meiotic recombination and crossover formation during meiosis I prophase are known to be required for holding homologous chromosomes together and allowing them to align and segregate appropriately during meiosis I (Smith et al., 2020). Despite being essential for meiotic chromosome segregation, *C. elegans* oocytes tightly regulate crossover formation to a single crossover per chromosome (Martinez-Perez et al., 2009). This leaves the question of whether or not preventing excess crossover formation is also involved in assuring accurate chromosome segregation. In addition to the possible role for chromosome structure in assuring accurate chromosome segregation, the mechanism(s) by which *C. elegans* oocytes segregate chromosomes are currently unclear. Attachment of spindle microtubules to chromosomes is facilitated by a multilayered protein complex called the kinetochore. However, oocytes with depleted kinetochore components had surprisingly minor chromosome segregation defects, implying that *C. elegans* kinetochores are dispensable for meiotic chromosome segregation (Dumont et al., 2010). Whether the force that mediates chromosome segregation is a pulling or pushing force on the chromosomes is not well established, but it is clear that microtubule stability and bundling are important for meiotic chromosome segregation (Dumont et al., 2010; Muscat et al., 2015; K. P. McNally et al., 2016; Laband et al., 2017; Mullen et al., 2017). Determining the

requirements for and mechanism(s) of meiotic chromosome segregation, including the impact of chromosome structure on the segregation process, are important next steps in better understanding the differences between oocyte meiosis and other cell division processes.

**Polar Body Cytokinesis**

Polar body extrusion is the final step in each of the meiotic divisions, where half of the segregating chromosomes in each division is ejected into a small cell called a polar body in an extremely asymmetric division process. However, despite the essential nature of this division process, very little is known about how the contractile ring apparatus that cleaves one cell into two assembles in oocytes (Maddox et al., 2012). In mitotically dividing cells a combination of signaling, from astral microtubules that extend from the centrosomes to the cell cortex as well as from the central spindle in between the segregating chromosomes, specifies the formation of the contractile ring between the segregating chromosomes, and thus between the mitotic spindle poles (Green et al., 2012; Basant et al., 2018; Pintard et al., 2019). However, oocytes lack centrosomes and have no substantial astral-like spindle microtubules that make contact with the oocyte cortex, and the contractile ring instead forms distal to both acentrosomal spindle poles before ingressing and constricting between the segregating chromosomal masses (Maddox et al., 2012). This physically distinct cytokinetic process in oocytes leads to many questions about how the contractile ring moves relative to the meiotic spindle, and what relationship, if any, there is between meiotic spindle structure and the ability to extrude chromosomes into a polar body.

How oocytes extrude polar bodies in any species is poorly understood, and the process seems to vary mechanically between species (Maddox et al., 2012). In *C. elegans* oocytes, the current hypothesis of how oocytes extrude chromosomes into a polar body is based on the concept of hydrostatic cytoplasmic pressure, caused by the contraction of the oocyte cortex, which leads to the outpocketing of the cortex within the polar body contractile ring (Fabritius et al., 2011; Maddox et al., 2012; Flynn et al., 2017). This hydrostatic pressure not only causes the outpocketing of the cortex, but also the outward movement of the oocyte meiotic spindle relative to the contractile ring, which then constricts at the spindle midzone to extrude a polar body. This model is largely based on a few observations, first that the absence of cortical contractility, through loss of non-muscle myosin contractility, leads to the absence of polar body extrusion (Fabritius et al., 2011). Second, an increase in cortical contractility, through loss of casein kinase 1 gamma (CSNK-1), a negative regulator of rho-GTP, can lead to the extrusion of entire meiotic spindles rather than a single segregating chromosome mass (Flynn et al., 2017). However, the relationship between cortical contractility and polar body extrusion in *C. elegans* oocytes is still unclear, largely due to the fact that the same machinery required for contraction of the oocyte cortex is also required for the assembly and constriction of the polar body contractile ring (Fabritius et al., 2011; Maddox et al., 2012). Moreover, while the polar body contractile ring typically constricts midway between the segregating chromosomal masses, the process by which this constriction is determined is unclear.

**Bridge**

In the following chapters, we will discuss the current state of our knowledge regarding the oocyte meiotic division process, and present new work that seeks to address some of the previously stated questions. In Chapter II, we will look at the earliest stages of the meiotic spindle assembly process, and seek to understand how microtubules are nucleated, and how spindles are assembled to allow for accurate chromosome segregation. Chapter III examines meiotic chromosome structure, and how it impacts meiotic spindle assembly and chromosome segregation. Chapter IV explores the relationships between meiotic spindle assembly, chromosome segregation, cortical regulation, and cytokinesis, and Chapter V provides a brief summary of Chapters II-IV and presents new avenues for research that arose from our findings.

# CHAPTER II

# MICROTUBULE ASSEMBLY AND POLE COALESCENCE: EARLY STEPS IN *C. ELEGANS* OOCYTE MEIOSIS I SPINDLE ASSEMBLY

*This chapter contains previously unpublished co-authored material.

This material is a primary research article manuscript that has been prepared and submitted for publication. This project was spearheaded by Dr. Chien-Hui Chaung, who collected, processed, and analyzed much of the data presented, with assistance from myself and Dr. Jie Yang, and with the guidance and support of Dr. Bruce Bowerman. My contribution to this material includes the generation of a key resource used within the research - a mutant *C. elegans* strain that was used extensively for data collection by Dr. Jie Yang, in addition to providing assistance with interpretation and preparation of data for presentation within the manuscript, and providing comments on the manuscript as it was in preparation.

## Introduction

*C. elegans* oocyte meiotic spindles form in the absence of centrosomes and reduce the duplicated diploid genome to a haploid content through two rounds of cell division called meiosis I and II (Dumont et al., 2012; Ohkura, 2015; Severson et al., 2016; Mullen et al., 2019). While acentrosomal microtubule nucleation pathways have been shown to mediate meiotic and mitotic spindle assembly in some settings, how *C. elegans* oocytes nucleate microtubules and assemble bipolar spindles remains poorly understood. Conserved mechanisms for microtubule nucleation, including the small GTPase Ran

pathway and γ-tubulin ring complexes, are not known to be required for oocyte meiotic cell division in *C. elegans* (Askjaer et al., 2002; K. McNally et al., 2006). Moreover, the augmin complex, which mediates microtubule branching in other animals, is not conserved in *C. elegans* (Edzuka et al., 2014). While microtubule severing by the conserved AAA+ ATPase complex called katanin promotes microtubule density in *C. elegans* oocytes, presumably by generating microtubule fragments that can further elongate (Srayko et al., 2006), mechanism(s) that nucleate microtubule substrates for katanin severing remain unknown.

Recent studies have defined a sequence of four steps that assemble bipolar spindles in *C. elegans* oocytes (Gigant et al., 2017; Mullen et al., 2017) (Figure 2.1A). First, oocyte nuclear envelope breakdown (NEBD) leads to a diffuse cloud of microtubule signal entering the nucleus. Second, microtubule bundles appear peripherally, underneath the dis-assembling nuclear lamina, to form a cage-like structure that surrounds the oocyte chromosomes. Third, the microtubule cage become organized such that multiple small foci of microtubules ends form in association with the pole-marker ASPM-1. Finally, these small pole foci coalesce to form a bipolar spindle as chromosomes congress to a metaphase plate (Connolly et al., 2015).

Defining these meiotic spindle assembly steps provides a foundation for identifying molecular mechanisms that participate in this reductive cell division. While the early microtubule cage assembles in close proximity to the nuclear lamina, how these microtubules are nucleated and whether the nuclear lamina is required for their assembly are not known. RNAi-mediated knockdown of two nearly identical minus-end directed *C. elegans* kinesin-14 family members, KLP-15 and -16, destabilizes the cage-like structure

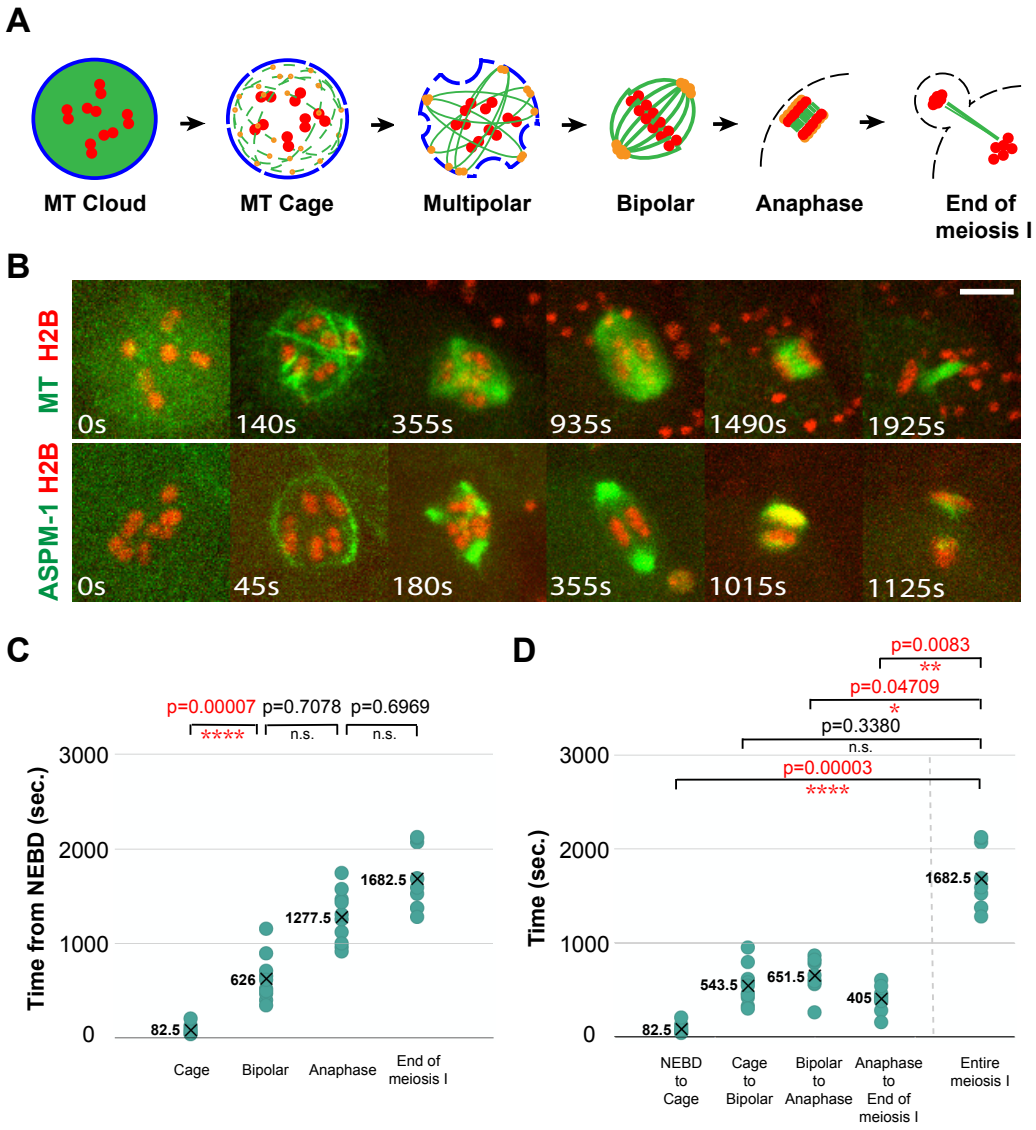


**Figure 2.1 – Wild-type oocyte meiosis I spindle assembly**

(A) Schematic of C. elegans oocyte meiosis I spindle assembly. Nuclear lamina (blue), microtubules (MT, green), chromosomes (red), spindle poles (orange), and oocyte plasma membrane (black dashed line) are shown.

(B) Time-lapse images (see Materials and Methods) of live control oocytes expressing either GFP::TBB-2 and mCherry::H2B to mark microtubules and chromosomes (upper row), or GFP::ASPM-1 and mCherry::H2B to mark spindle poles and chromosomes (lower row). Scale bars in all figures represent 5 µm.

(C) Scatter plot showing the time from nuclear envelope breakdown (NEBD) to different stages of meiosis I in control oocytes expressing GFP::TBB-2 and mCherry::H2B. For all figures, the X and the adjacent number indicate the average value for each dataset, and variance was compared using the F-test to calculate p-values.

(D) Scatter plot of the times from one stage to the next, and the entire time of meiosis I.

(Mullen et al., 2017), consistent with the demonstrated ability of kinesin-14 family members to bundle parallel microtubules (Fink et al., 2009). The small GTPase Ran has been implicated in chromosome-mediated nucleation of microtubule assembly during meiosis and mitosis in some organisms (Clarke et al., 2008), but not in *C. elegans* (Askjaer et al., 2002). RNAi knockdown of the *C. elegans* γ-tubulin TBG-1 does not prevent oocyte meiotic cell division, but TBG-1 is diffusely associated with oocyte meiotic spindles and its knockdown exacerbates the microtubule loss caused by reduced katanin function (K. McNally et al., 2006). Finally, the multiple TOG domain protein and XMAP215 family member in *C. elegans*, called ZYG-9, promotes astral microtubule stability during early embryonic mitosis and is known to be required for oocyte meiotic spindle assembly (Bellanger et al., 2003; Yang et al., 2003; Bellanger et al., 2007). XMAP215 orthologs act as microtubule polymerases in cooperation with γ-tubulin ring complexes (Gunzelmann et al., 2018; Thawani et al., 2018), and have roles in promoting both microtubule stability and instability (Kosco et al., 2001; Shirasu-Hiza et al., 2003), but the role of ZYG-9 in *C. elegans* oocytes remains poorly understood.

To improve our understanding of *C. elegans* oocyte meiosis I spindle assembly, we have used RNAi and mutations to reduce the function of several proteins implicated in this process, and live cell imaging with fluorescent protein fusions to assess their requirements. Here we report our analysis of requirements for the single nuclear lamina protein in *C. elegans* LMN-1 (Liu et al., 2000), the small GTPase RAN-1, the γ-tubulin TBG-1, the kinesin-14 family members KLP-15/16, and the XMAP215 ortholog ZYG-9. Our results indicate that the nuclear lamina is required for assembly of the cage-like array of KLP-15/16-stabilized microtubule bundles observed early in spindle formation,

although bipolar spindles still assembled after LMN-1 knockdown. Furthermore, while not by themselves required for oocyte meiotic cell division, reduction of either RAN-1 or TBG-1 decreased spindle microtubule levels and altered spindle assembly dynamics. Finally, we show that KLP-15/16 and ZYG-9 make distinct contributions both to assembly of the early microtubule cage structure and to the coalescence of pole foci to form a bipolar spindle.

## Results

### Wild-Type Oocyte Meiosis I Spindle Assembly

To observe early steps in oocyte meiosis I spindle assembly, we imaged control oocytes *in utero* using spinning disk confocal microscopy and simultaneous two-color live imaging (see Materials and Methods), first with a transgenic strain expressing within the germline a GFP fusion to β-tubulin (GFP::TBB-2) to mark microtubules and an mCherry fusion to a histone (mCherry::H2B) to mark chromosomes (Figure 2.1B and Supplemental Figure B.1 (Supplemental Figures for Chapter II can be found in Appendix B)). To assess progression through meiosis I, we designated the time at which the value for histone intensity in the nucleoplasm became equal to the value for the cytoplasm, which marks the initiation of nuclear envelope breakdown (NEBD), as t = zero and collected z-stacks encompassing the oocyte volume every 5 seconds. In all 10 control oocytes, we observed the previously described steps in spindle assembly: the rapid appearance of GFP::TBB-2 signal around chromosomes; the assembly of peripheral microtubule bundles to form a cage-like structure surrounding the chromosomes; the appearance of a multipolar spindle during prometaphase; and the coalescence of multiple

small pole foci to form a bipolar spindle by metaphase. Subsequently, during anaphase, most pole microtubules disappeared, and central spindle microtubules assembled as the segregating chromosomes moved apart. Finally, we designated the time point with the lowest level of GFP::TBB-2 signal in the spindle area, prior to meiosis II, as the end of meiosis I.

To further characterize spindle assembly, we imaged live control oocytes using a GFP fusion to the pole-marker ASPM-1 (GFP::ASPM-1) and the mCherry::H2B fusion (Figure 2.1B, Supplemental Figure B.2). As described previously (Gigant et al., 2017; Mullen et al., 2017), GFP::ASPM-1 initially localized along microtubules during cage assembly but then became restricted to multiple small pole foci that coalesced into two poles by metaphase. These GFP::ASPM-1-marked poles subsequently broadened and faded during anaphase.

While all control oocytes in the GFP::TBB-2 background underwent a similar progression in spindle morphology, the time required to complete meiosis I varied from a minimum of 1280 seconds to a maximum of 2125 seconds, a 66% increase in duration. To determine when this variability arises, we assessed the variance in timing during progression through the different stages of assembly. The most significant increase in variance occurred during the transition from the appearance of the microtubule cage structure to the establishment of spindle bipolarity (Figures 2.1C and 2.1D). The subsequent transitions, from the establishment of bipolarity to anaphase onset, and from anaphase onset to the completion of meiosis I, did not show significant further increases. Having collected data sets that established a baseline for wild-type assembly dynamics,

we next used RNAi to assess genetic requirements for the early spindle assembly steps and for timely progression through oocyte meiosis I.

## The Nuclear Lamina is Required for Assembly of the Peripheral Microtubule Cage Structure

Because the microtubule cage that assembles after the initiation of NEBD is adjacent to the nuclear lamina (Mullen et al., 2017), we first asked if the nuclear lamina is required for cage assembly. After using RNAi in the GFP::TBB-2, mCherry::H2B background to knock down the single *C. elegans* lamin LMN-1, we did not detect any peripheral microtubule bundles in 8 of 10 oocytes, and in 2 oocytes we detected only a few relatively short bundles (Figure 2.2A, Supplemental Figure B.3). Although the cage was missing or greatly reduced after LMN-1 knockdown, the overall level of microtubule signal was similar to that observed in control oocytes (Figure 2.2C), and the subsequent steps in spindle assembly appeared relatively normal, with transient multi-polar structures

**Figure 2.2 - The nuclear lamina is required for the early cage-like microtubule structure during oocyte meiosis I.**
(A-B) Time-lapse images during meiosis I of live control and *lmn-1(RNAi)* oocytes expressing either GFP::TBB-2 and mCherry::H2B (A), or GFP::ASPM-1 and mCherry::H2B (B). (C) Normalized microtubule pixel intensity in arbitrary units. The boxplot displays the datasets and the median (line) and mean (x) values for the 3 continuous time points with the highest pixel intensities for control and mutant oocytes. (D) Pole-to-pole length measured at metaphase I in control and mutant oocytes expressing GFP::ASPM-1 and mCherry::H2B. For all figures, distributions of scatter plot values were compared using the Mann-Whitney U test to calculate p-values. (E) Scatter plot showing maximum extent of chromosome segregation at the end of meiosis I for control and mutant oocytes expressing either GFP::TBB-2 and mCherry::H2B or GFP::ASPM-1 and mCherry::H2B. Numbers of oocytes that failed to segregate chromosomes at the end of meiosis I (i.e. maximum extent of chromosome segregation value = 0) were: 5 for *lmn-1(RNAi)*, 1for *tbg-1(RNAi)*, 12 for *klp-15/16(RNAi)* and 3 for *zyg-9(RNAi)* oocytes. (F) Scatter plot showing the time required to progress through meiosis I in control and mutant oocytes expressing GFP::TBB-2 and mCherry::H2B.

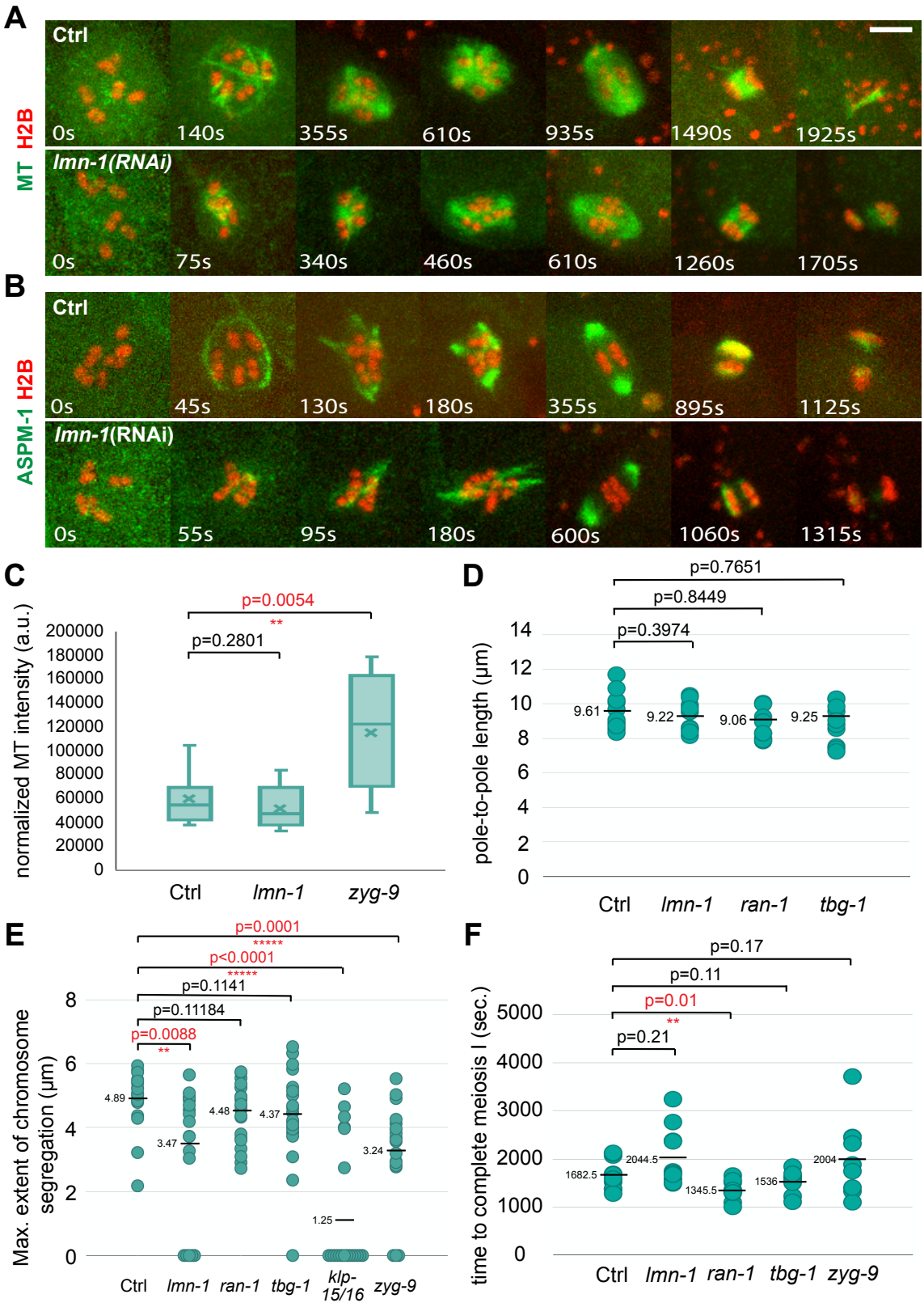


that coalesced to form bipolar spindles of normal pole-to-pole length (Figure 2.2B and

2.2D). Moreover, we still observed the disappearance of most microtubules from the poles as central spindle microtubules appeared during anaphase between the segregating chromosome masses, but the extent of chromosome segregation was reduced compared to control oocytes, and in 5 of 20 oocytes, imaged using either GFP::TBB-2 or GFP::ASPM-1, chromosome segregation completely failed (Figure 2.2E). Using the pole marker GFP::ASPM-1 (Figure 2.2B, Supplemental Figure B.4), cage-like microtubule bundles were again greatly reduced or absent, and as in control oocytes, GFP::ASPM-1 was detected along microtubules as multipolar spindles assembled. However, the GFP signal persisted along microtubules for a longer period of time before concentrating at pole foci as spindle bipolarity was established. Finally, despite these altered spindle dynamics, the time required to progress through meiosis I, although more variable, was not on average significantly different compared to control oocytes (Figure 2.2F). We conclude that the nuclear lamina is required for assembly of the microtubule cage that surrounds chromosomes early in meiosis I. While the cage structure is not required for assembly of a bipolar spindle, the dynamics of spindle assembly were altered and chromosome segregation was in some cases entirely absent after LMN-1 knockdown.

**RAN-1 Promotes Microtubule Assembly and Normal Oocyte Nuclear Size**

We next asked if known regulators of microtubule nucleation might also be required for assembly of the microtubule bundles that form the early cage structure. Previous studies of the *C. elegans* small GTPase RAN-1 and the γ-tubulin family member TBG-1 have not found them to be required for oocyte meiotic cell division (see Introduction). However, the early cage structure is not essential for bipolar spindle

assembly after LMN-1 knockdown, and whether cage assembly occurs in the absence of RAN-1 or TBG-1, and the impact of these regulators on spindle assembly dynamics, have not been addressed.

We used RNAi to knock down RAN-1 in strains expressing GFP::TBB-2 and mCherry::H2B (Figure 2.3A and Supplemental Figure B.6), GFP::ASPM-1 and mCherry::H2B (Figure 2.3B and Supplemental Figure B.7), and GFP::LMN-1 and mCherry::TBB-2 (Figures 2.3C). We observed a roughly normal sequence of spindle morphology transitions, with a microtubule and ASPM-1 cage forming soon after NEBD, followed by the appearance of multiple small pole foci that coalesced to form a bipolar spindle of normal length that segregated chromosomes to a normal extent (Figures 2.2D, 2.2E, 2.3A and 2.3B, Supplemental Figures B.6 and B.7). However, compared to control oocytes, the quantities of microtubules detected throughout meiosis I were reduced (Figure 2.3D), and the microtubule cage was smaller in diameter (Figure 2.3A and 2.3B, Supplemental Figures B.6, B.7 and B.8A). Furthermore, the time required to complete meiosis I, based on GFP::TBB-2 imaging (Figure 2.2F), was reduced from an average of

**Figure 2.3 - RAN knockdown reduces oocyte nuclear size and microtubule levels during oocyte meiosis I**

(A-C) Time-lapse images during meiosis I for live control and *ran-1(RNAi)* oocytes expressing GFP::TBB-2 and mCherry::H2B (A), GFP::ASPM-1 and mCherry::H2B (B), or GFP::LMN-1 and mCherry::TBB-2 to mark the nuclear lamina and microtubules (C). Maximum intensity z-projections (A-B), or the middle plane of the nucleus (C) are shown. (D) Normalized microtubule pixel intensity in arbitrary units measured over time with 1-minute time intervals. Time 0 = NEBD. For all figures, error bars depict one standard deviation at each time point. (E) Comparison of the length of time from one stage to the next between the control and *ran-1(RNAi)* oocytes from strains expressing either GFP::TBB-2 and mCherry::H2B or GFP::ASPM-1 and mCherry::H2B. NEBD: the time at which the value for histone intensity in the nucleoplasm became equal to the value for the cytoplasm; Metaphase: time at which chromosomes aligned on the metaphase plate; Anaphase onset: the time at which chromosomes started to separate; Maximum chromosome segregation: the time at which chromosomes separated to the maximum distance.

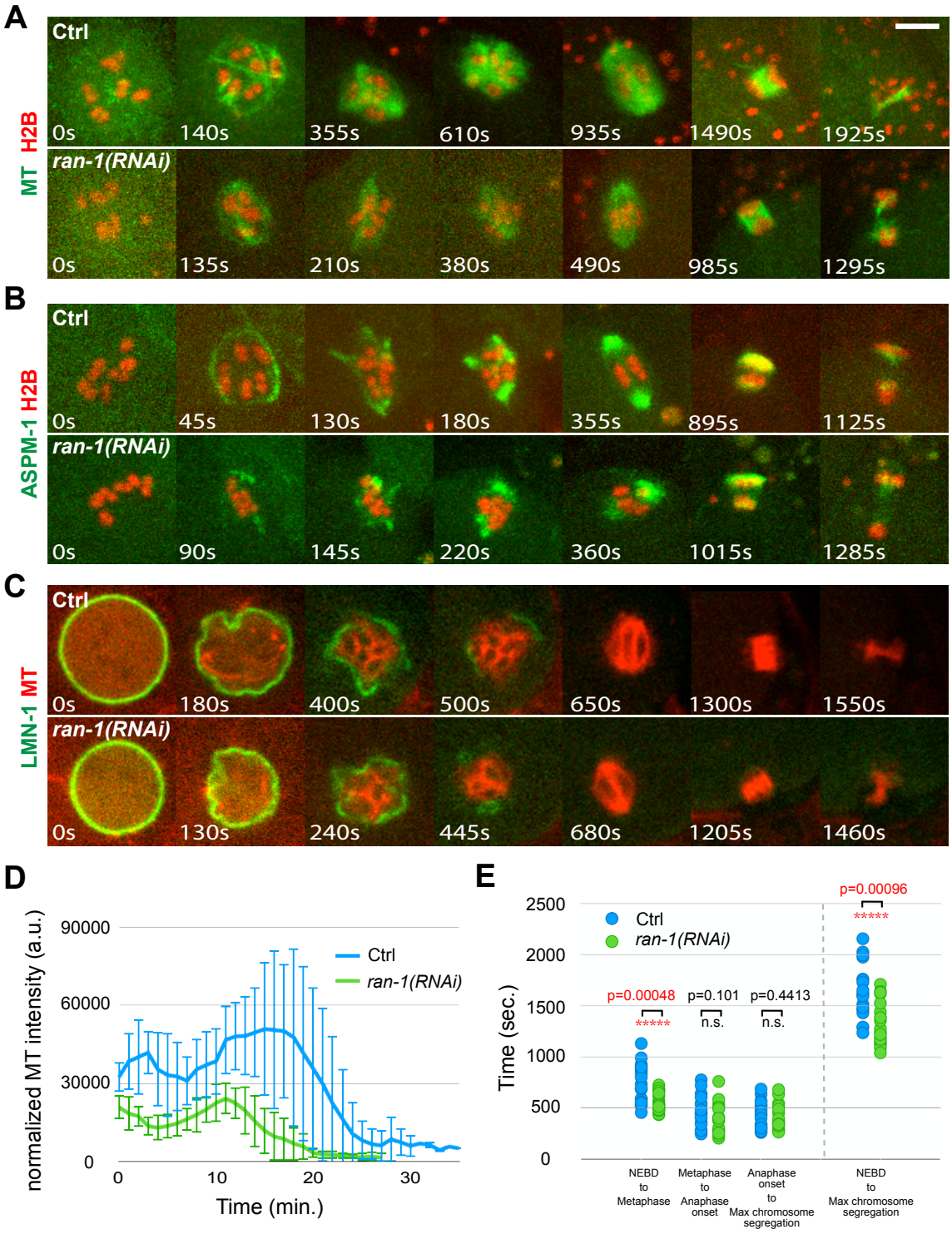


1682.5 seconds in control oocytes to an average of 1345.5 seconds after RAN-1 knockdown ($p = 0.01$). We further assessed progression through meiosis 1 based on chromosome dynamics and observed a significant decrease during the time from NEBD

to metaphase (Figure 2.3E). We also examined spindle pole dynamics with GFP::ASPM-1 and again found that the decrease in time occurred during the establishment of spindle bipolarity, between NEBD and metaphase (Supplemental Figure B.5A). To summarize, RAN-1 is at least partially required for spindle microtubule assembly during meiosis I but may not be required for a functional bipolar spindle to form. Surprisingly, reducing RAN-1 function leads to a more rapid progression through meiosis I that may result from a reduction in the time required for early pole foci to coalesce and form a bipolar spindle.

Finally, we asked if the smaller microtubule cage structure observed after RAN-1 knockdown is associated with a smaller oocyte nucleus, or if the microtubule cage forms more internally relative to the nuclear lamina in normally sized nuclei. To address this issue, we knocked down RAN-1 in a transgenic strain expressing GFP::LMN-1 and an mCherry fusion to TBB-2 (Figure 2.3C). While the timing of NEBD, based on the fragmentation and decrease of the GFP::LMN-1 signal over time appeared normal, the diameters of the oocyte nuclei were reduced to roughly the same extent as the microtubule cage structure (Figure 2.3A-2.3C and Supplemental Figures B.8A and B.8B). Similarly, the diameters of oocyte nuclei measured using Nomarski optics were reduced relative to control oocytes (Supplemental Figure B.8C and B.8D). Consistent with these findings, RAN-1 knockdown has previously been reported to result in the production of fertilized embryos with abnormally small oocyte pronuclei (Askjaer et al., 2002).

**TBG-1 is Required for Proper Oocyte Nuclear Positioning and Promotes Both Microtubule Levels and Normal Spindle Assembly Dynamics**

We next examined spindle assembly after knocking down TBG-1 in transgenic strains expressing GFP::TBB-2 and mCherry::H2B (Figure 2.4A and Supplemental Figure B.9), or GFP::ASPM-1 and mCherry::H2B (Figure 2.4B and Supplemental Figure B.10). Prior to NEBD and spindle assembly, we observed a displacement of oocyte nuclei from the cortex (Figure 2.4C), followed by a reduction in microtubule levels throughout meiosis I (Figure 2.4D). The diameter of the microtubule cage structure, though more variable, was on average not significantly different from its diameter in control oocytes (Supplemental Figure B.8A), but the subsequent dynamics of spindle assembly were distinct from those observed in both control and RAN-1 knockdown oocytes. Shortly after cage assembly, the microtubules collapsed into a small cluster around the oocyte chromosomes, rather than forming the peripheral multipolar structure observed in control oocytes. Similarly, GFP::ASPM-1 foci and the oocyte chromosomes became grouped together in a tight cluster. Subsequently, more extended microtubule structures appeared and multiple GFP::ASPM-1 foci emerged peripherally to the oocyte chromosomes and coalesced to form a bipolar spindle of normal length that segregated chromosomes to a normal though more variable extent (Figures 2.2D and 2.2E). In one case, when imaging GFP::ASPM-1, we observed a complete failure in chromosome segregation (Figure 2.2E). Finally, the time to complete meiosis I and the variance in the time required to achieve spindle bipolarity were similar to control oocytes (Figures 2.1C, 2.2F and 2.4E). In summary, as reported previously (K. McNally et al., 2006), TBG-1 was not required for bipolar spindle assembly. However, microtubule levels were reduced and the

dynamics of spindle assembly were altered and distinct from those observed after RAN-1 knockdown.

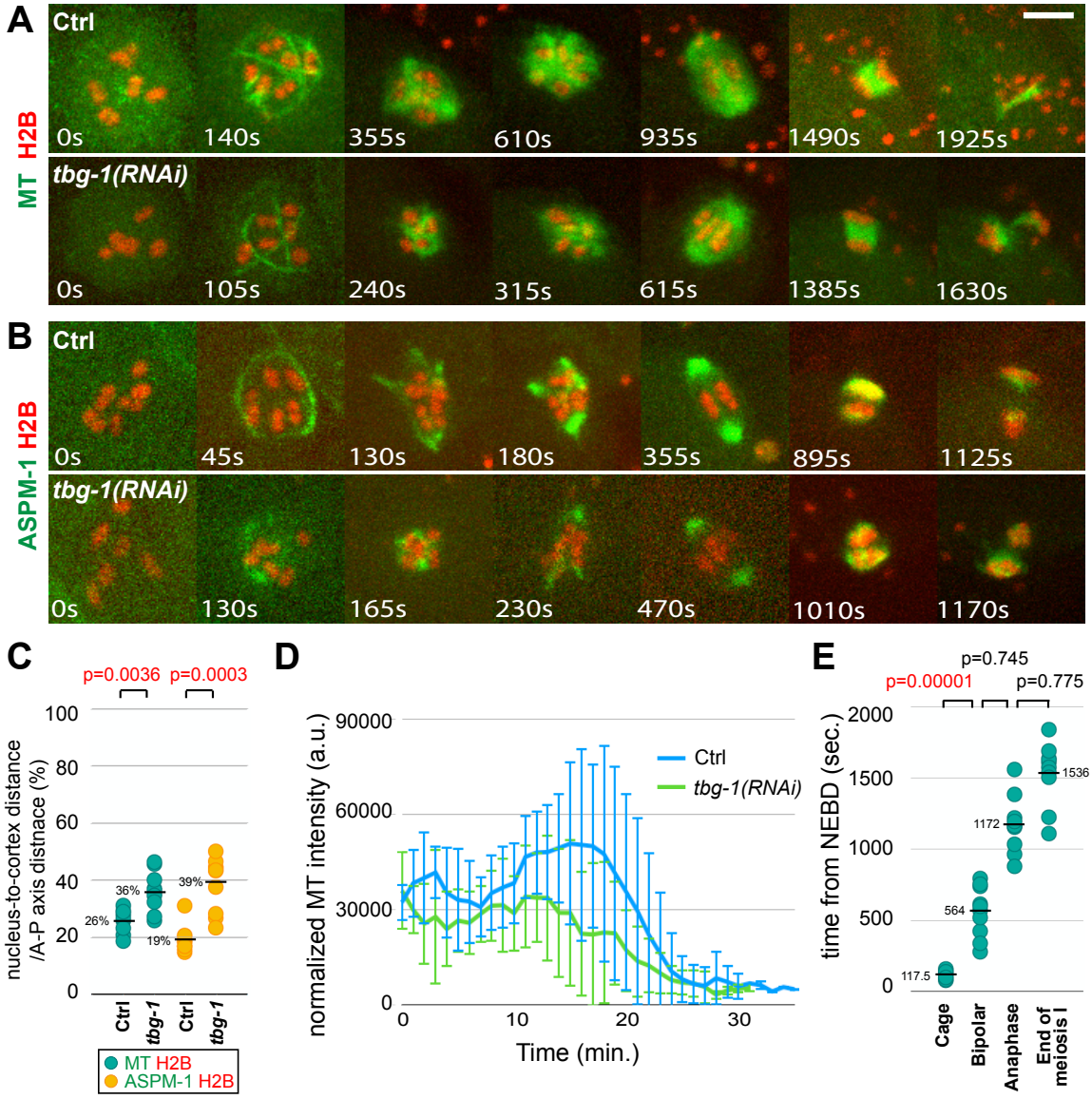


**Figure 2.4 - TBG-1 knockdown alters spindle dynamics after the microtubule cage-like structure appears and reduces microtubule levels during oocyte meiosis I**

(A-B) Time-lapse images during meiosis I of live control and *tbg-1(RNAi)* oocytes expressing either GFP::TBB-2 and mCherry::H2B (A), or GFP::ASPM-1 and mCherry::H2B (B). (C) Scatter plot showing nuclear position for control and *tbg-1(RNAi)* oocytes, measured at NEBD as the distance from the center of the nucleus to the closest edge of the oocyte on the same focal plane/the length of oocyte anterior-posterior axis. (D) Normalized microtubule pixel intensity in arbitrary units measured over time with 1-minute time intervals. Time 0 = NEBD. (E) Scatter plot showing the time from NEBD to different stages of meiosis I in *tbg-1(RNAi)* oocytes expressing

**KLP-15 and -16 are Required for Cage Stability and Promote Pole Coalescence**

The nearly identical *C. elegans* minus-end directed kinesin-14 family members KLP-15 and -16 have been shown previously to have a role in stabilizing the microtubule bundles that form the early cage structure (Mullen et al., 2017). After RNAi knockdown of KLP-15/16, the bundles were less prominent compared to control oocytes and a more diffuse spherical distribution of microtubules then surrounded the chromosomes, which underwent segregation in only about half of the depleted oocytes. As these results were obtained using RNAi, and spindle structures were assessed using immunofluorescence in fixed oocytes, we have analyzed KLP-15/16 requirements using live cell imaging with putative null alleles.

We first made a strain carrying likely null alleles for both *klp-15* and *-16*, which are on the same chromosome separated by about 3.5 map units (Figure 2.5A). Using CRISPR/Cas9, we introduced a small deletion near the 5' end of the first coding exon of *klp-16* in a strain homozygous for a previously isolated *klp-15* deletion allele, *klp-15(ok1958)*. The CRISPR-generated *klp-16* deletion resulted in a frameshift followed by multiple stop codons and likely eliminates all gene function. The resulting double mutant chromosome, *klp-15(ok1958) klp-16(or1952)*, was then balanced with a marked inversion

**Figure 2.5 - KLP-15/16 knockdown destabilizes cage-like microtubule bundles and reduces pole coalescence**
(A) Left panel: locations of *klp-15*, *aspm-1* and *klp-16* on chromosome I. Right panel: domain architectures of wild-type KLP-15/16 and the KLP-15/16 double mutant used in this study. Vertical grey lines indicate stop codons that follow the frameshift caused by the *or1952* deletion. (B) Time-lapse images during meiosis I of control and *klp-15/16(-/-)* oocytes expressing GFP::TBB-2 and mCherry::H2B. (C) Time-lapse images during meiosis 1 of control or *klp-15/16(-/-)* double mutant oocytes expressing GFP::ASPM-1and mCherry::H2B. (D) Embryonic lethality and average brood sizes for *klp-15/16(-/-)* double mutant and control strains. (E) Scatter plot showing the time required to progress through meiosis I for control and *klp-15/16(-/-)* double mutant oocytes.

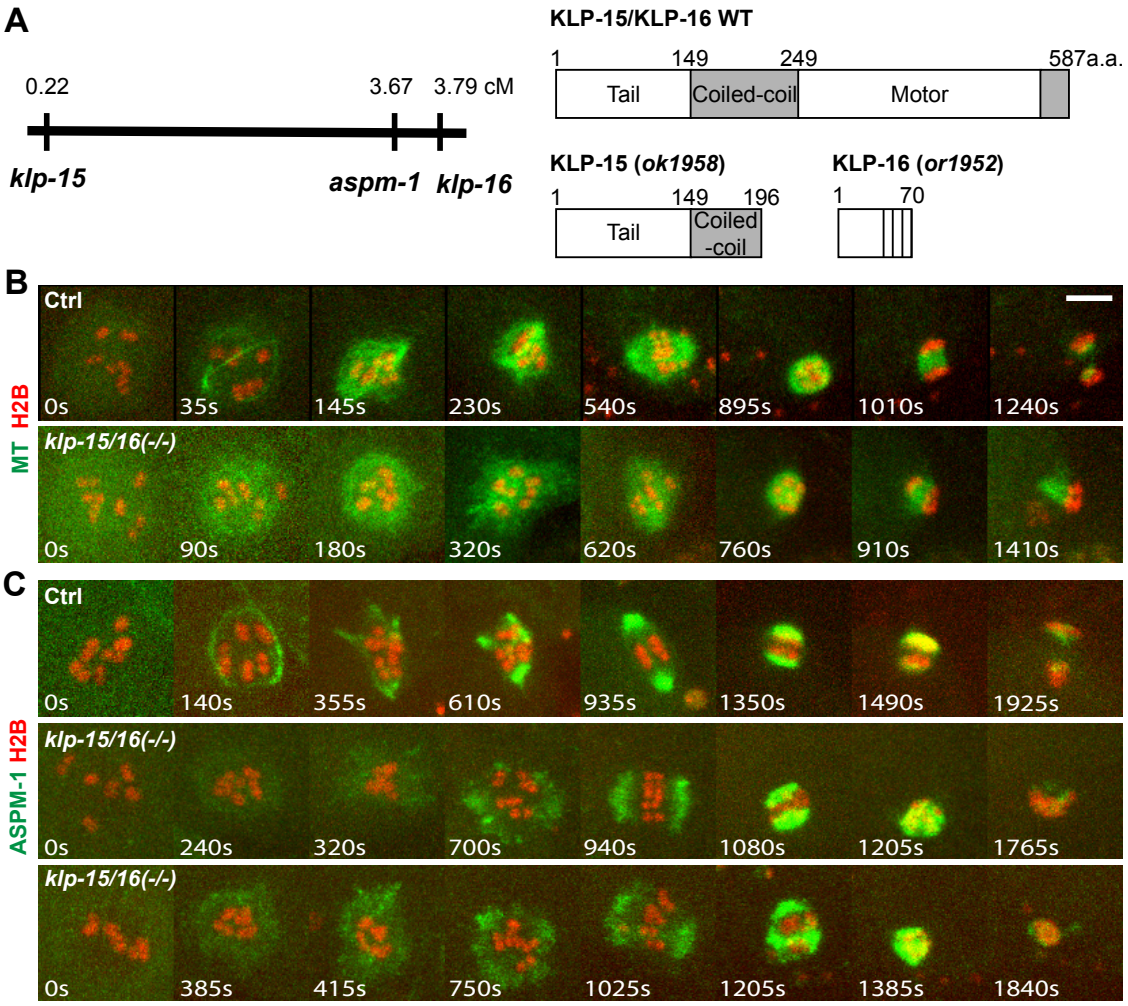


| Genotype | embryonic lethality (n=# of embryos counted) | Avg. brood size (n=# of worm broods evaluated) |
|---|---|---|
| *tmc18/+* | 0.88% (n=2606) | 261 (n=10) |
| *klp-15/16/tmc18* | 1.64% (n=2689) | 244 (n=11) |
| *klp-15/16(-/-)* | 94.69% (n=1750) | 125 (n=14) |

chromosome, *tmc18* (Dejima et al., 2018). When homozygous, these two mutations resulted in the development of fertile adults with reduced brood sizes and highly penetrant and recessive embryonic lethality (Figure 2.5D).

We next used live imaging to examine oocyte meiosis I spindle assembly in the *klp-15/16* null mutant background. We used genetic crosses to generate a *tmc18* balanced *klp-15/16* double mutant strain that expresses GFP::TBB-2 and mCherry::H2B (Figure 2.5B and Supplemental Figure B.11). Because the *aspm-1* gene resides on the same chromosome between *klp-15* and *-16* (Figure 2.5A), we obtained a CRISPR/Cas9-generated *in situ* GFP fusion to the endogenous *aspm-1* locus on the *klp-15(or1958) klp-16(or1952)* chromosome (see Materials and Methods in Appendix A), and used genetic crosses to introduce the mCherry::H2B fusion (Figure 2.5C and Supplemental Figure B.12). We observed a decreased prominence of the microtubule bundles that form the cage, as reported previously (Mullen et al., 2017), and a subsequent failure to form a bipolar spindle or segregate chromosomes in over half of the mutant oocytes (Figures 2.2E and 2.5C, Supplemental Figures B.11 and B.12). Live imaging of the *klp-15/16* double mutant with GFP::ASPM-1 also suggested that the microtubule cage was reduced in prominence. Subsequently, GFP::ASPM-1 foci were detected both peripheral to and amongst the chromosomes (Figure 2.5C, Supplemental Figure B.12). These GFP::ASPM-1 foci became more prominent over time, often forming broad poles that failed to coalesce into the more compact structures observed in control oocytes (Figure 2.1B and Supplemental Figure B.2). In some cases, broad arrays of GFP::ASPM-1 foci nearly encircled the chromosomes, and the average time to complete meiosis I was increased (Figure 2.5E). We conclude that in addition to being important for stable assembly of the microtubule cage and chromosome segregation, KLP-15/16 also are important for the coalescence of early pole foci into properly organized spindle poles.

**ZYG-9 Restricts Microtubule Bundles to the Periphery During Cage Assembly and Promotes Pole Coalescence And Stability**

The XMAP215 family member ZYG-9 is known to be required for oocyte meiotic spindle assembly (Yang et al., 2003), but the nature of this requirement remains poorly understood. To examine its role, we first assessed the dynamics of ZYG-9 localization in comparison to microtubules and ASPM-1. We used CRISPR/Cas9 to generate an *in situ* fusion of GFP to the endogenous *zyg-9* locus and genetic crosses to introduce the mCherry::H2B fusion (Figure 2.6A and Supplemental Figure B.15A). In contrast to GFP::ASPM-1, we did not detect GFP::ZYG-9 in association with the microtubule cage; rather it was initially more diffusely present near chromosomes and subsequently became enriched at multiple pole foci and also was present more diffusely throughout the spindle during pole coalescence. Upon the establishment of spindle bipolarity, GFP::ZYG-9 was enriched at the poles but in contrast to GFP::ASPM-1, GFP::ZYG-9 also was detected between the poles. ZYG-9 binds the coiled-coil TACC ortholog TAC-1, and both promote microtubule stability during early embryonic mitosis in *C. elegans* (Bellanger et al., 2003; Bellanger et al., 2007). We therefore used CRISPR/Cas9 to generate an *in situ* fusion of GFP to the endogenous *tac-1* locus and observed localization dynamics similar to GFP::ZYG-9 (Supplemental Figure B.15B). To summarize, ZYG-9 and its partner TAC-1 were both present throughout spindle assembly and both appeared more restricted in distribution than microtubules but, as assembly progressed, more broadly distributed than ASPM-1.

We next examined ZYG-9 requirements after RNAi knockdown in transgenic strains expressing GFP or mCherry fusions to TBB-2, ASPM-1 and H2B and observed multiple defects during meiosis I spindle assembly. First, when imaging spindles marked with GFP::TBB-2 or GFP::ASPM-1, microtubule bundles assembled to form a peripheral cage shortly after NEBD, but some of the microtubule bundles were not restricted to the

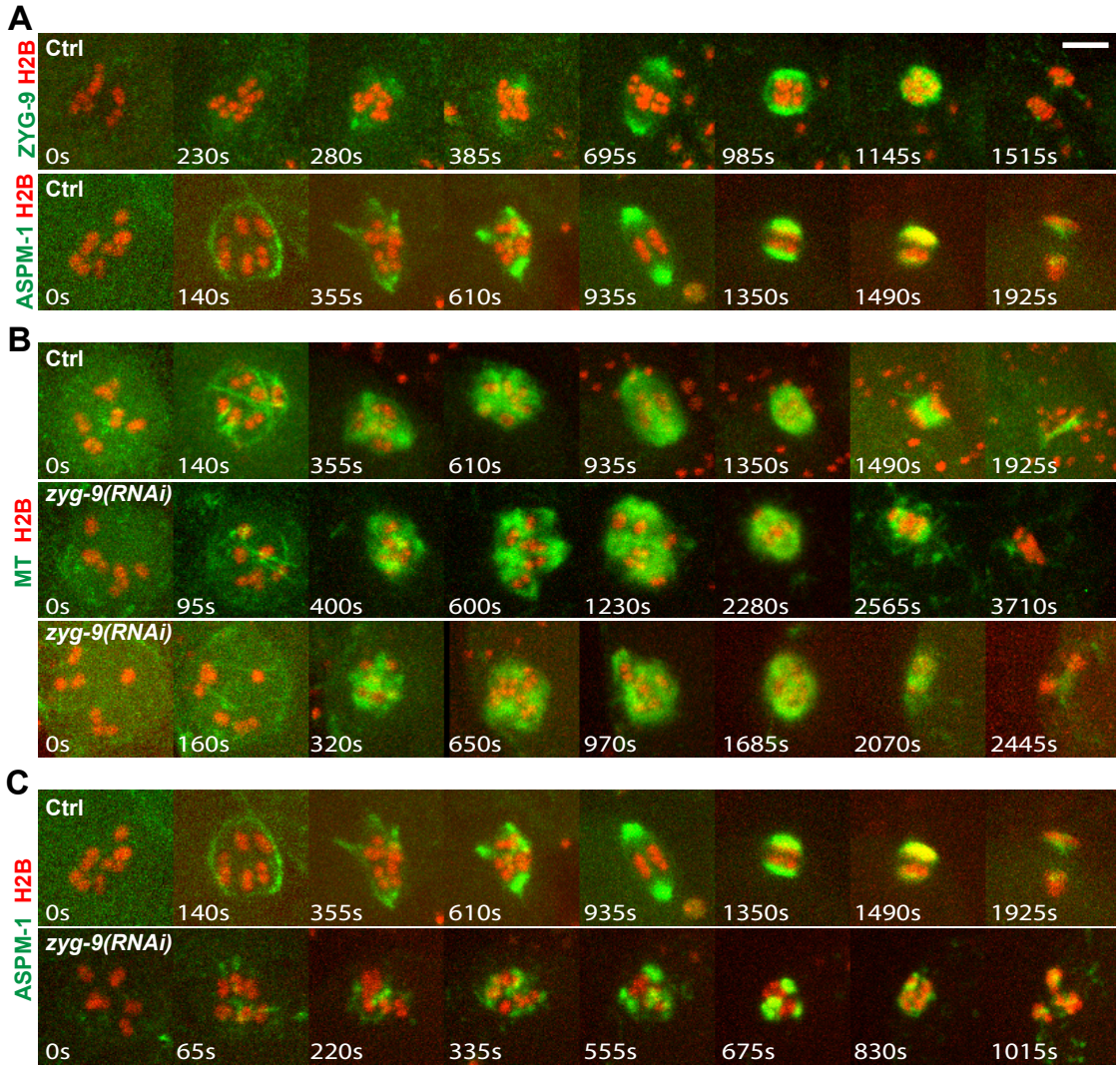


**Figure 2.6 - ZYG-9 knockdown causes spindle assembly defects throughout oocyte meiosis I.**
(A) Time-lapse images during meiosis I of live control oocytes expressing either GFP::ZYG-9 and mCherry::H2B (upper row), or GFP::ASPM-1 and mCherry::H2B (lower row). (B-C) Time-lapse images during meiosis I of live control and *zyg-9(RNAi)* oocytes expressing either GFP::TBB-2 and mCherry::H2B (B), or GFP::ASPM-1 and mCherry::H2B (C).

periphery and instead passed through the interior of the chromosome occupied space (Figure 2.6B and 2.6C, Supplemental Figures B.13 and B.14). Subsequently, foci of GFP::TBB-2 and GFP::ASPM-1 were observed not only at the periphery surrounding oocyte chromosomes, but also between some of the bivalent chromosomes. Moreover, small spindle-like structures often appeared to form around individual or small groups of bivalents, in contrast to the peripheral spindle foci that coalesced to form a bipolar spindle in control oocytes.

The abnormal dynamics of spindle assembly observed after ZYG-9 knockdown were accompanied by a significant increase in the level of oocyte spindle microtubules (Figures 2.2C and 2.6B, Supplemental Figure B.13), and a variable but significant increase in the diameter of the microtubule cage structure (Supplemental Figure B.8A). We also observed increased microtubule levels throughout the oocyte cortex during meiosis I (Figure 2.7). These increases were surprising because ZYG-9 is required for the stability of astral microtubules during early embryonic mitosis (Bellanger et al., 2003; Bellanger et al., 2007), and ZYG-9 orthologs in other species promote microtubule assembly (Akhmanova et al., 2015), although in some contexts they also promote microtubule instability (Shirasu-Hiza et al., 2003).

We also observed a striking lack of pole stability and extensive chromosome segregation defects after ZYG-9 knockdown. In control oocytes, early small pole foci stably associated with each other over time (Figure 2.1B, Supplemental Figures B.2 and B.16). In contrast, after ZYG-9 knockdown, pole foci marked by GFP::ASPM-1 fused and then often broke apart as meiosis I progressed (Figure 2.6C, Supplemental Figure

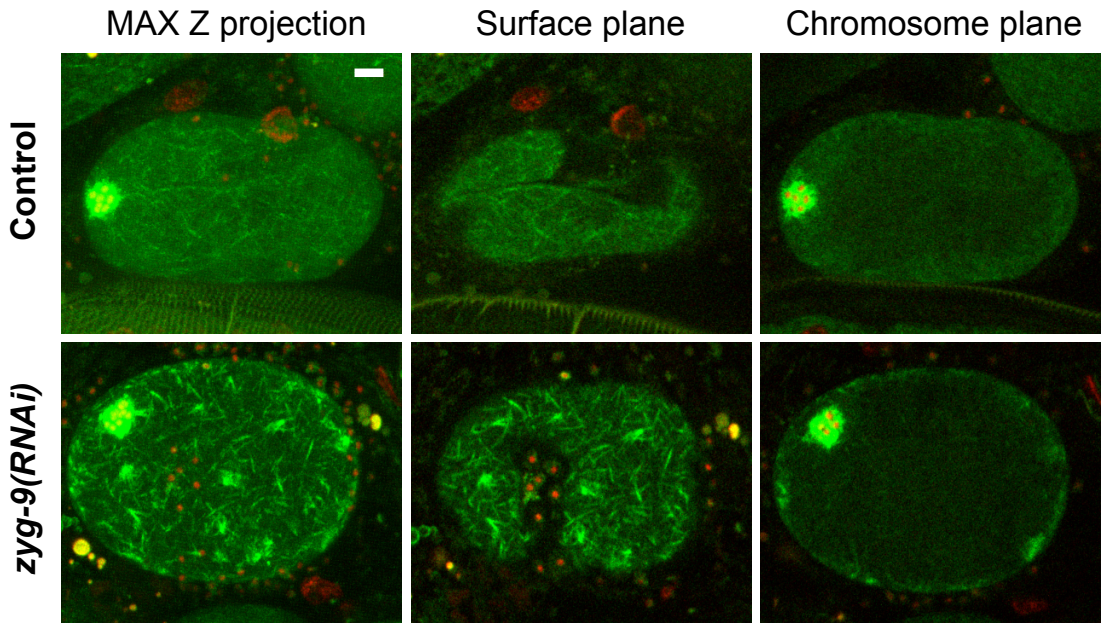


**Figure 2.7 - Microtubule levels are increased throughout the oocyte cortex during meiosis I after ZYG-9 knockdown.**
*Ex utero* spinning disk confocal images for live control (upper row) and *zyg-9(RNAi)* (lower row) oocytes expressing GFP::TBB-2 and mCherry::H2B. Pixel intensity was enhanced to in the green channel to highlight cortical microtubules. Left panels: maximum intensity z-projection image of 15 planes with 1 µm z-spacing. Middle panels: surface plane. Right panels: chromosome plane.

B.16). Consistent with a role in pole stability, chromosomes sometimes segregated into three masses during anaphase (10 of 20 oocytes), although in other cases no segregation (3 of 20 oocytes) or segregation into two masses (7 of 20 oocytes) were observed (Supplemental Figures B.5C, B.13 and B.14). Finally, we observed similar defects throughout oocyte meiosis I after knocking down the TAC-1 binding partner for ZYG-9, indicating that ZYG-9 and TAC-1 have similar if not identical requirements. In summary, ZYG-9 and TAC-1 restrict cage microtubule bundles to the periphery and promote pole coalescence and stability. Notably, they also appear to limit both spindle and cortical microtubule levels during oocyte meiosis I.

**Discussion**

We have examined the requirements for factors involved in *C. elegans* oocyte meiotic spindle assembly, with the goal of assessing their roles during a sequence of four recently described assembly steps that generate these acentrosomal and yet bipolar spindles during meiosis I. Our results show that the nuclear lamina, comprised of the single *C. elegans* nuclear lamin LMN-1, is required for assembly of the underlying cage-like microtubule structure, although this structure is not required for bipolar spindle assembly. While knockdown of either of two conserved regulators of microtubule nucleation, the small GTPase RAN-1 and TBG-1/γ-tubulin, did not prevent bipolar spindle assembly or chromosome segregation, microtubule levels after both knockdowns were reduced and spindle assembly dynamics were altered. We also identified two additional contributions to assembly of the early cage-like network of microtubule bundles. After knockdown of the XMAP215 ortholog ZYG-9, or its binding partner TAC-1, the microtubule bundles were no longer restricted to the periphery but in some cases passed through the space occupied by oocyte chromosomes. As reported previously, these microtubule bundles were reduced in prominence in mutants lacking the nearly identical minus-end directed kinesins KLP-15 and -16. Finally, both ZYG-9 and KLP-15/16 were required for early spindle pole foci to coalesce into a bipolar structure, but in distinct ways. ZYG-9 knockdown resulted in a lack of pole stability during coalescence, while pole foci failed to coalesce in *klp-15/16* mutant oocytes. Our results, considered in more detail below, document requirements for microtubule nucleation, cage assembly and pole coalescence, key steps in the assembly of acentrosomal oocyte meiosis I spindles in *C. elegans*.

**Microtubule Nucleation and *C. elegans* Oocyte Meiotic Spindle Assembly**

Although several genes are known to be required for proper organization of oocyte meiotic spindles in *C. elegans*, how microtubules are nucleated during this process has remained poorly understood (Severson et al., 2016). Two widely conserved regulators that contribute to microtubule nucleation in other contexts, γ-tubulin and the small GTPase Ran, have not been found to be required for oocyte meiotic cell division in *C. elegans* (see Introduction). However, our results indicate that both contribute to producing normal microtubule levels and spindle assembly dynamics.

RAN-1 knockdown did not appear to substantially affect any of the steps in oocyte spindle assembly: the early microtubule cage formed, small pole foci then appeared and coalesced into a bipolar spindle of normal length that segregated chromosomes to the same extent as in control oocytes. However, RAN-1 knockdown did result in the production of oocyte nuclei that were smaller in diameter, and the microtubule cage also was reduced in diameter. Moreover, microtubule levels declined to a minimum earlier than was observed in control oocytes, and the time required to progress through meiosis I was reduced.

TBG-1 knockdown also did not prevent assembly of the microtubule cage, and its diameter was similar to those in control oocytes. However, rather than proceeding to form a network of peripherally located small spindle pole foci, the cage collapsed into a condensed ball of microtubule signal surrounding the chromosomes. Subsequently, microtubules emerged from the collapsed structure, and the pole marker ASPM-1 appeared in multiple foci that coalesced to form a bipolar spindle of normal length that segregated chromosomes to the same extent as in control oocytes. In spite of these

changes in spindle assembly dynamics, we did not detect any defects in chromosome segregation by the end of meiosis I after knockdown of either RAN-1 or TBG-1, with one exception after TBG-1 knockdown, consistent with previous reports indicating the lack of an essential requirement for either of these regulators during oocyte meiosis.

While the more normal sequence of assembly events after RAN-1 knockdown and the more substantially altered assembly dynamics after TBG-1 knockdown suggest that these two regulators play distinct roles, in neither case have we been able to determine the consequences of fully eliminating gene function. For both RAN-1 and TBG-1, we analyzed oocyte meiotic defects at a time prior to which the RNAi treatments resulted in adult sterility (Appendix A), indicating that their activities were not entirely absent. More complete elimination of their functions could result in more severe and perhaps more similar defects. Indeed, defining gene requirements for oocyte meiotic spindle assembly is challenging because essential genes involved in this process are often required for fertile adults to develop. Due to earlier requirements, null alleles often result in zygotic embryonic or larval lethality, or adult sterility, precluding their use for more definitively analyzing requirements during oocyte meiosis. A recently developed alternative approach to reducing gene function at different times in development is to use CRISPR/Cas9 to tag endogenous loci with a degron motif that induces degradation of the tagged protein upon treatment with the plant hormone auxin (L. Zhang et al., 2015). While this approach does not allow one to conclusively determine null phenotypes, it can be especially useful for simultaneously reducing the functions of multiple degron-tagged proteins, as RNAi often requires different time courses for depleting different loci and is less reliable as more

genes are simultaneously targeted. Degron tagging therefore may facilitate better assessment of the potentially distinct roles of RAN-1 and TBG-1.

## The Nuclear Lamina as a Platform for Assembling the Cage-like Network of Microtubule Bundles

While we did not detect a requirement for either RAN-1 or TBG-1 in assembly of the early microtubule cage, we did find that the nuclear lamina, which directly overlies this structure, is required for its assembly. RNAi knockdown of the only *C. elegans* lamin LMN-1 nearly eliminated the peripheral microtubule bundles. Restricting the assembly of early microtubule bundles to the periphery to form a cage-like network might promote pole coalescence by having it occur only along the inner surface of the nuclear lamina, rather than throughout the volume occupied by oocyte chromosomes. Consistent with such a role, the time required to complete meiosis I in control oocytes differs due to variability in the time required for pole coalescence, and the reduced time required to complete meiosis after RAN-1 knockdown occurs during pole coalescence and correlates with a reduction in the diameter and surface area of the cage-like network.

We also detected later abnormalities as spindle assembly progressed after LMN-1 knockdown. The pole marker ASPM-1 appeared to persist along the length of microtubules for a longer period of time compared to control oocytes, before becoming enriched at the two spindle poles. Bipolar spindles of normal length ultimately assembled and the time required to complete meiosis I was more variable but not significantly increased compared to control oocytes. While alternative bipolar spindle assembly mechanisms appear to compensate for loss of the microtubule cage structure,

chromosomes were segregated to a lesser extent, and in 5 of 20 cases chromosome segregation failed. Some or all of these defects could be indirectly due to disruptions in the nuclear import of factors required for a fully functional spindle to assemble, and we did detect variable and sometimes lower levels of some kinetochore proteins after LMN-1 knockdown (data not shown). Nevertheless, our results indicate that the nuclear lamina plays an important role in *C. elegans* oocyte meiotic spindle assembly, and roles for lamins in spindle assembly have also been reported in *Xenopus* extracts and during *Drosophila* male meiosis(Tsai et al., 2006; Goodman et al., 2010; Hayashi et al., 2016).

**ZYG-9/XMAP215 and the Kinesin-14 Family Members KLP-15/16 Contribute to Proper Assembly of the Cage-like Network of Microtubule Bundles**

In addition to the nuclear lamina being required for assembly of the microtubule cage early in meiosis I spindle assembly, we also found requirements for ZYG-9 and the minus-end directed kinesins KLP-15/16 in the assembly of this structure. As reported previously based on RNAi knockdown (Mullen et al., 2017), we found that the cage microtubule bundles that formed in oocytes from worms homozygous for likely null alleles of *klp-15* and *-16* were less prominent and rapidly became undetectable, with the microtubules instead forming a diffuse cloud encompassing the oocyte chromosomes, and chromosome segregation often completely failed.

We observed a very different defect in the microtubule cage structure after depletion of ZYG-9/XMAP215, or of its binding partner TAC-1. Stable and prominent microtubule bundles formed peripherally to the oocyte chromosomes early in spindle assembly, as in control oocytes, but some of the bundles passed through the interior of

the chromosome occupied volume, rather than being restricted to the periphery. Subsequently, pole foci formed not only at the periphery but also amongst the chromosomes, and oocytes often failed to assemble bipolar spindles. In some oocytes, the spindles became tripolar and segregated chromosomes into three distinct masses, while in other cases a bipolar structure failed to emerge and chromosome segregation completely failed. We conclude that ZYG-9 and KLP-15/16 make distinct contributions to assembly of the cage-like network of microtubule bundles: KLP-15/16 are required for their stability, while ZYG-9 appears to restrict their assembly to the periphery.

In addition to the abnormal spatial organization of microtubule bundles and early spindle pole foci after ZYG-9 knockdown, we also observed increased levels both of spindle-associated microtubules and of microtubules throughout the oocyte cortex during meiosis I. This was surprising given that ZYG-9 orthologs have been reported to promote microtubule stability and act as microtubule polymerases (Akhmanova et al., 2015). Indeed, astral microtubules during early embryonic mitosis in *C. elegans zyg-9* mutants are abnormally short (Bellanger et al., 2003; Bellanger et al., 2007). Nevertheless, other studies also have reported a role for XMAP215 orthologs in promoting instability (Shirasu-Hiza et al., 2003; Brittle et al., 2005), and our analysis of ZYG-9 provides further evidence that these TOG domain proteins can promote microtubule instability. Moreover, ZYG-9 can promote both microtubule stability and microtubule instability depending on the cellular context, even when the different activities are closely spaced in time, as also appears to be true in budding yeast (Kosco et al., 2001; Shirasu-Hiza et al., 2003). Finally, our results indicate that ZYG-9 acts in concert with its conserved binding

partner, TAC-1, not only to promote microtubule stability during early embryonic mitosis, but also to promote microtubule instability during oocyte meiosis I.

A role for ZYG-9 in promoting microtubule instability may account for the spatial organization of the microtubule bundles that surround the oocyte chromosomes early in meiosis I spindle assembly. GFP::ZYG-9 and GFP::TAC-1 initially were distributed diffusely throughout the space occupied by chromosomes and were not detected in association with the peripheral microtubule bundles. Thus ZYG-9 and TAC-1 might prevent microtubule assembly in the volume occupied by chromosomes, restricting cage formation to the periphery.

**ZYG-9/XMAP215 and the Kinesin-14 Family Members KLP-15/16 Make Distinct Contributions to Pole Coalescence**

In addition to being required for proper assembly of the microtubule cage, ZYG-9 and KLP-15/16 also appear to make distinct contributions to pole coalescence. In control oocytes, multiple small GFP::ASPM-1 pole foci moved toward each other and fused upon coming into contact, only rarely undergoing fission into distinct foci after merging. How these foci move toward each other remains unknown, but a similar process of coalescence has been observed in mouse oocytes (Schuh et al., 2007). After ZYG-9 knockdown, we observed frequent examples of pole instability, in which pole foci would merge but then split apart. This process continued for an extended period of time with spindles frequently failing to become bipolar and often segregating chromosomes into three masses instead of two, or entirely failing to segregate chromosomes. By contrast, in *klp-15/16* mutant oocytes, pole foci became more prominent over time but were less

dynamic. Although these foci often formed bipolar structures, the poles were much broader, and in some cases they nearly encircled the chromosomes without ever forming distinct poles. In addition, chromosome segregation often failed entirely. We conclude that while KLP-15/16 promote pole coalescence, ZYG-9 promotes pole stability, with both playing important roles in establishing a bipolar spindle.

Our results do not provide direct mechanistic insight into how either ZYG-9 or KLP-15/16 promote pole stability and coalescence, but the known functions of these conserved proteins may be relevant. Mutations in the *Drosophila* ortholog of KLP-15/16, Ncd, also result in disorganized oocyte meiotic spindles, with unfocused poles in some cases (Matthies et al., 1996; Skold et al., 2005), and Ncd also promotes pole assembly in acentrosomal *Drosophila* S2 cells (Goshima et al., 2005; Ito et al., 2015), suggesting that these minus-end directed kinesins may have conserved roles in pole assembly. Like KLP-15/16, Ncd is localized throughout oocyte meiosis I spindles (Hatsumi et al., 1992; Mullen et al., 2017), and the ability of kinesin-14 family members to cross-link parallel microtubules might contribute to pole coalescence (Fink et al., 2009).

With respect to the pole instability caused by loss of ZYG-9 or TAC-1, both also promote microtubule instability during oocyte meiosis I, raising the possibility that excessive microtubule growth might disrupt pole coalescence. In *Drosophila*, the ZYG-9 and TAC-1 orthologs Minispindles and D-TACC also are enriched at oocyte meiotic spindle poles, and loss of their function often results in tripolar spindles (Cullen et al., 2001), although the dynamics of pole stability have not been reported. Moreover, *Drosophila* Ncd is required for Minispindles to localize to oocyte meiotic spindle poles,

and thus this minus-end directed kinesin-14 family member has been proposed to transport Minispindles to oocyte spindle poles and thereby promote pole assembly.

Finally, ZYG-9 can promote mitotic spindle assembly *in vitro* when incorporated into a centrosomal matrix that undergoes phase transitions (Woodruff et al., 2017), and the mouse XMAP215 and TACC orthologs chTOG and TACC3 have been reported to undergo phase transitions during mouse oocyte meiotic spindle assembly (So et al., 2019). Given the broad distribution of ZYG-9 and its binding partner TAC-1 during *C. elegans* oocyte meiotic spindle assembly, this protein complex may undergo phase transitions that influence microtubule and spindle pole stability. Future studies that assess in more detail the dynamics of ZYG-9/TAC-1 during oocyte meiosis I, and how ZYG-9/TAC-1 and KLP-15/16 interact, should further advance our understanding of how these regulators contribute to the assembly of bipolar but acentrosomal oocyte meiotic spindles.

**Bridge to Chapter III**

Oocyte meiosis, in any species, is a poorly understood process. While Chapter II has thus far considered questions regarding microtubule nucleation and the earliest stages of oocyte meiotic spindle assembly, relatively little is understood regarding the relationship between chromosome structure, spindle assembly, and subsequent chromosome segregation. Previous work has suggested that in *C. elegans* oocytes, microtubule attachments to kinetochores can influence acentrosomal spindle pole coalescence and lead to defects in meiotic chromosome segregation (Connolly et al., 2015). Because *C. elegans* kinetochores are holocentric and coat the length of the chromosome, this suggests that chromosome structure itself could play a role in spindle

assembly or subsequent chromosome segregation. Chapter III explores this relationship by examining the impact of altered chromosome structure, through supernumerary crossover formation between homologous chromosomes, on the ability of oocytes to accurately align and segregate chromosomes on the meiotic spindle.

# CHAPTER III

# EXCESS CROSSOVERS IMPEDE FAITHFUL MEIOTIC CHROMOSOME SEGREGATION IN *C. ELEGANS*

*This chapter contains previously unpublished co-authored material.

This material is a primary research article manuscript that has been prepared and submitted for publication. This work was part of a collaborative effort between Dr. Diana Libuda and her laboratory members Marissa Glover and Dr. Cori Cahoon, Dr. Sadie Wignall and her laboratory member Jeremy Hollis, and Dr. Bruce Bowerman and me. Presented data were collected and analyzed by Marissa Glover, Jeremy Hollis, Cori Cahoon, and myself, under the guidance and supervision of Drs. Bowerman, Wignall, and Libuda. My contribution to this material includes collecting, processing, interpreting, and preparing spinning-disk time-lapse microscopy data for presentation within the manuscript in two substantial figures as well as their accompanying legends. I also contributed towards the initial draft of the manuscript and provided comments on the manuscript as it was in preparation.

## Introduction

Meiosis is a specialized, reductional form of cell division necessary for the production of haploid sperm or egg cells. One hallmark of meiosis is the requirement of genetic exchange through recombination. Meiotic recombination is initiated by the formation of double strand DNA breaks (DSBs), which are repaired to form crossover (CO) and noncrossover events (Gray et al., 2016). Germ cells in most organisms require a

CO between homologous chromosomes to physically link each pair of homologs, enabling their proper segregation during the meiosis I division. Despite the formation of many programmed DSBs, most organisms are limited in the number of COs formed, and formation of a CO tends to inhibit formation of other COs nearby on the same chromosome pair, a conserved phenomenon known as CO interference (Sturtevant, 1913; Muller, 1916). COs that are subject to interference are considered interfering COs (or Class I COs). Additionally, some organisms have a subset of COs that are not subject to interference (called "non-interfering", or "Class II" COs), but these non-interfering COs represent only 5-35% of all meiotic COs in *A. thaliana, M. musculus*, and *S. cerevisiae* (Gray et al., 2016). While CO interference is a well conserved phenomenon among most eukaryotes, the molecular consequences that result from the occurrence of multiple interfering COs are not clear. In addition, it is also unclear how these consequences may have contributed to the conservation of CO interference.

The model organism *Caenorhabditis elegans* is a particularly powerful system to study CO regulation because it exhibits remarkably strict CO control; under wild-type conditions, only one DSB per chromosome is repaired as a CO and all COs are interfering COs (Martinez-Perez et al., 2009). Several studies have demonstrated that even in the presence of an extreme excess of DSBs (10-fold greater than wild-type levels), only a single interfering CO, marked by the pro-crossover factor COSA-1, is made per pair of homologous chromosomes (Yokoo et al., 2012; Libuda et al., 2013). Additionally, it has been shown that CO interference can operate over distances longer than the length of a normal chromosome axis (Hillers et al., 2003; Libuda et al., 2013); in the case of end-to-end fusions of chromosomes (that still accurately segregate in *C.*

*elegans*), many meioses still only have one CO per fusion chromosome pair (Hillers et al., 2003; Libuda et al., 2013).

These COs form physical connections between the homologs, known as a chiasmata. Since in *C. elegans* each chromosome pair typically has one CO that occurs off-center along the chromosome length, the chromosomes reorganize around this single chiasma to form cruciform bivalents with long and short arms (Nabeshima et al., 2005; Martinez-Perez et al., 2008). These bivalents then align on the spindle, and in anaphase I, cohesion is lost along the short arm axis, enabling segregation of homologous chromosomes (Kaitna et al., 2002; Rogers et al., 2002). Aurora B kinase (AIR-2) and other members of the conserved chromosomal passenger complex (CPC) are targeted to this short arm region in prophase to protect sister chromatid cohesion in that region until anaphase I is triggered (Martinez-Perez et al., 2008). Moreover, the CPC also directs the formation of a larger meiotic protein complex that forms upon nuclear envelope breakdown (Wignall et al., 2009; Dumont et al., 2010); at this stage, the CPC reorganizes from a linear distribution along the short arm axis to a ring encircling this region, and targets a number of other conserved proteins to form a structure known as the Ring Complex (RC). In addition to the CPC, the RC contains other conserved components, such as the kinase BUB-1 (Dumont et al., 2010) and the microtubule de-stabilizing kinesin MCAK$^{KLP-7}$ (Connolly et al., 2015; Han et al., 2015). Furthermore, SUMO and SUMO pathway enzymes localize to the RC and are required for RC assembly and stability (Pelisch et al., 2017; Davis-Roca et al., 2018). Chromosomes that lack RCs have congression and segregation errors (Muscat et al., 2015), and depletion of RC components causes a variety of meiotic defects (Schumacher et al., 1998; Romano et al.,

2003; Wignall et al., 2009; Dumont et al., 2010; Connolly et al., 2015; Laband et al., 2017; Pelisch et al., 2017; Pelisch et al., 2019) highlighting the importance of this complex.

One function of the RC is to promote chromosome congression (Wignall et al., 2009; Pelisch et al., 2017). In *C. elegans* oocyte spindles, microtubule bundles run laterally along the sides of bivalents instead of forming canonical end-on kinetochore attachments. A component of the RC, the kinesin-4 family member KLP-19, has been proposed to walk along these laterally-associated bundles towards microtubule plus ends located in the center of the spindle, thus providing chromosomes with plus-end directed forces that mediate metaphase alignment (Wignall et al., 2009). Then, at anaphase onset, the enzyme SEP-1$^{separase}$ is targeted to the midbivalent region to cleave cohesin and allow homologous chromosomes to segregate to opposite spindle poles (Siomos et al., 2001; Muscat et al., 2015). At this stage, the RCs are removed from chromosomes and remain in the center of the spindle, where they disassemble (Dumont et al., 2010; Muscat et al., 2015; Davis-Roca et al., 2017; Mullen et al., 2017; Davis-Roca et al., 2018). Oocytes extrude one set of homologs into a polar body, and then Meiosis II (MII) proceeds. The MII chromosomes assemble RCs encircling the sister chromatid interface and repeat the segregation process to form a matured haploid egg.

Although extensive research has focused on CO formation and RC function independently, it is still unclear how early meiotic processes affect chromosome structure and function in meiotic divisions. Moreover, why chromosomes in many organisms are so tightly restricted to 1-2 COs per homolog pair has not been addressed. Here we utilize a *C. elegans* strain containing a chromosome that exhibits increased crossover numbers

under specific conditions to assess the effects of supernumerary crossovers on meiosis. We find that the RC is mispatterned in the presence of multiple COs, leading to defects in chromosome congression, and that chromosomes with multiple chiasmata exhibit extensive chromatin bridging in anaphase. Thus, excess crossovers can severely impact chromosome patterning and segregation, highlighting the importance of limiting the number of recombination events between homologous chromosomes for the proper execution of meiosis. Further, our studies uncovered multiple mechanisms by which oocytes are able to correct these errors, demonstrating that species have evolved ways to combat the deleterious defects caused by excess crossing over.

## Results

### Fusion Chromosomes Generate Bivalents with Multiple Crossovers and Chiasmata

To understand the effects of multiple COs on proper chromosome segregation and gamete formation, we sought to exploit the advantages of the *C. elegans* model system to consistently generate multiple COs along a single chromosome during meiosis. Since normal *C. elegans* chromosomes typically experience only one CO per meiosis (Hillers et al., 2003; Libuda et al., 2013), we utilized a strain containing the three-chromosome fusion *meT7 (*end-on-end fusions of chromosomes *III, X*, and *IV*; Figure 3.1A*).* While wild-type strains contain six individual chromosomes, strains containing the *meT7* fusion chromosome have four individual chromosomes total (*meT7 III; X; IV* fusion chromosome, and chromosomes *I, II*, and *V;* Figure 3.1B, Left). Similar to wild type strains, *meT7*-containing strains grown under standard conditions have relatively normal progeny viability, indicating *meT7* segregation errors leading to aneuploidy are rare

(Hillers et al., 2003). Since *meT7* is three times the length of a normal chromosome, previous studies using genetic assays found the occasional occurrence of multiple COs along this fusion chromosome and that this chromosome is easily identifiable in meiotic nuclei due to its size (Hillers et al., 2003; Martinez-Perez et al., 2008).

To determine the exact number of Class I interfering COs occurring along the length of *meT7* within a population of nuclei, we assessed the number of COSA-1 foci, a cytological marker of Class I interfering COs during late pachytene (Yokoo et al., 2012), along *meT7* chromosomes in single nuclei of strains grown in standard conditions. In wild-type strains containing unfused chromosomes, the six individual chromosomes in each nucleus obtain a single CO per chromosome resulting in 6 COSA-1 foci per nucleus, with <0.4% of nuclei obtaining more than 6 foci (Yokoo et al., 2012; Libuda et al., 2013) (Figure 3.1B and Materials and Methods, which can be found in Appendix C). In contrast, strains grown at 20°C with the *meT7* fusion chromosome obtain 4-6 COSA-1

**Figure 3.1 – Fusion chromosomes generate bivalents with multiple crossovers and chiasmata**
(A) Schematic indicating the orientation of the *meT7* fusion chromosome, which fuses the *X* chromosome and chromosomes *III* and *IV*. (B) Left, schematic depicting the chromosomes in a wild-type strain (top) and the *meT7* (*X;III;IV*) fusion chromosome strain (bottom). Right, immunofluorescence images of GFP::COSA-1 in late pachytene nuclei from wild-type and *meT7* fusion chromosome strains grown at 20°C and 25°C. GFP::COSA-1 is shown in green, synaptonemal complex protein SYP-1 is shown in red, and DNA is shown in blue. Arrowheads indicate nuclei with >2 crossovers along the *meT7* fusion chromosome. Scale bars = 5µm. (C) Top, quantification of percentage of *meT7* nuclei with indicated number of GFP::COSA-1 foci on *meT7* in late pachytene at 20°C and 25°C. Number of late pachytene nuclei scored for COSA-1 foci: 20°C, n=290; 25°C n=287. Bottom, representative immunofluorescence images of single nuclei with *meT7* chromosomes with the indicated number of COSA-1 foci. White line indicates traced chromosome axis of each chromosome in a single nucleus. Yellow outline highlights the *meT7* fusion chromosome within the nucleus. (D) Three-dimensionally rendered immunofluorescence images of individual *meT7* diakinesis bivalents. Dashed lines (white) indicate traced HTP-3 axes (green), with crossing of axes indicating chiasmata. Scale bars = 1µm.

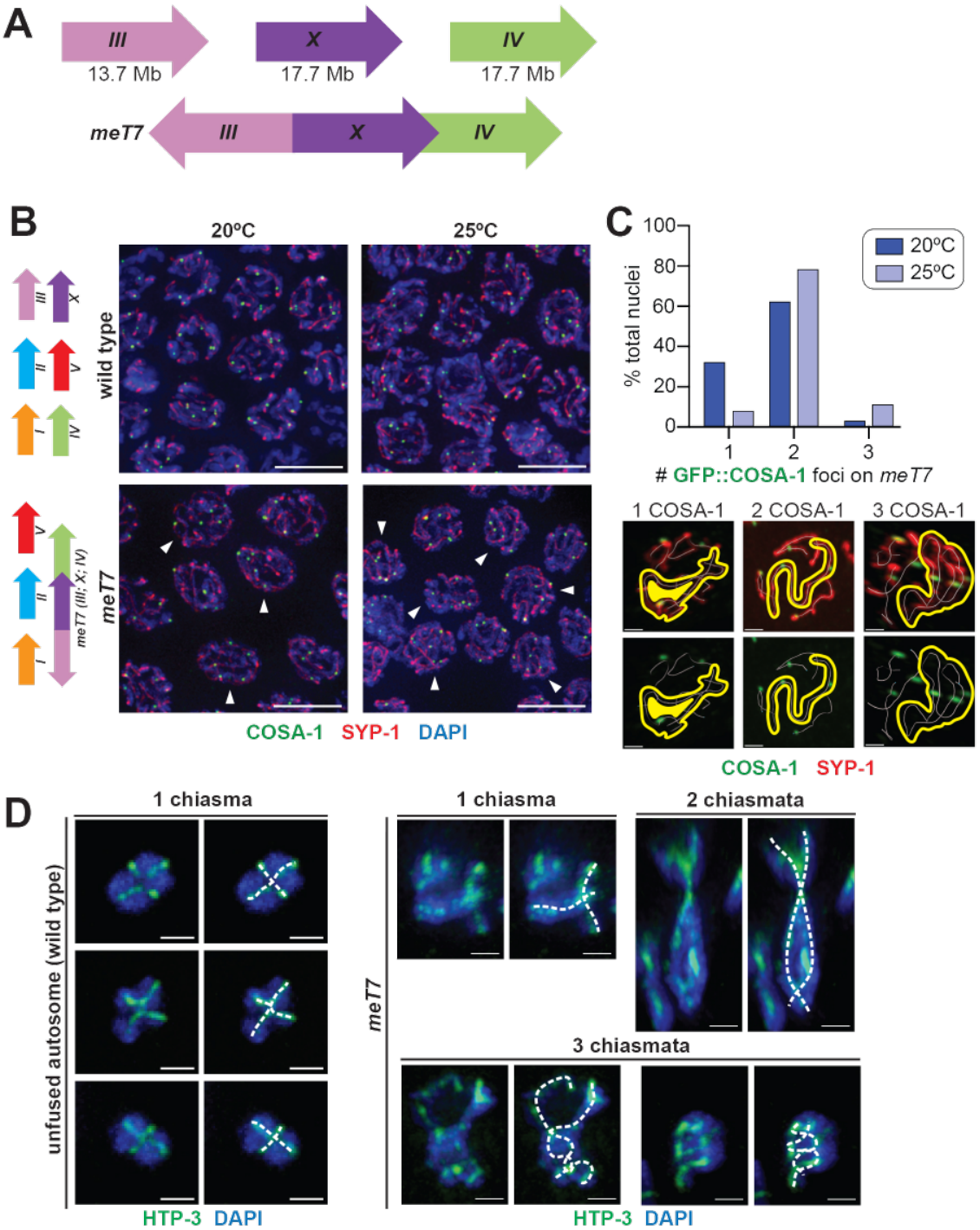


foci per late pachytene nucleus (Figure 3.1B), with 77% of *meT7* chromosomes exhibiting ≥2 COSA-1 foci (Figure 3.1C). To further increase the number of COs occurring along *meT7*, we grew strains containing the *meT7* fusion chromosome at 25°C, a temperature that was previously found to increase the number of COs along the length

of the two-chromosome fusion *mnT12* (Libuda et al., 2013). In contrast to 20°C, we found that *meT7* strains grown at 25°C had an increase in COSA-1 foci, with >90% of *meT7* chromosomes with 2 or more COSA-1 foci (Figures 3.1B and 3.1C). This enrichment of COSA-1 foci indicates the occurrence of multiple COs along the length of the *meT7* fusion chromosome, as previously reported (Hillers et al., 2003).

To determine whether these increased COSA-1 foci along *meT7* fusion chromosomes represent COs that become chiasmata, we assessed chiasma number and bivalent structure at diakinesis along fusion chromosome pairs. Using HTP-3 immunofluorescence to trace chromosome axes (Figure 3.1D), we found that 13/21 diakinesis nuclei with *meT7* bivalents at 20°C had more than one chiasma, consistent with 60-80% of the *meT7* chromosome pair having more than one COSA-1 focus at the late pachytene stage (Figure 3.1C). In *meT7* strains grown at 25°C, we found that 19/21 (90.5%) *meT7* fusion chromosomes had more than one chiasma, consistent with 90% of *meT7* chromosome pairs having 2 or more COSA-1 marked crossovers (Figure 3.1C). In accordance with previous analysis performed at 20°C (Martinez-Perez et al., 2008), we found that in the formation of long and short arms in the cruciform bivalent structure (Figure 3.1D). Previous studies have found that some meiotic chromosome structures reorganize around these CO sites starting at the late pachytene-diplotene transition, resulting in cytologically distinguishable long and short bivalent arms. In comparison to single chiasma *meT7* and non-fusion cruciform bivalent structures, these multi-chiasma *meT7* bivalent structures exhibit more than two short arms. Together, this corresponding increase in both COSA-1 foci and chiasmata indicates that the temperature-associated extra COSA-1 foci observed at pachytene in *meT7* chromosomes represent *bona fide*

cytologically-differentiated meiotic CO events that can result in atypical bivalent structures.

**Bivalents with Multiple Crossovers have Mispatterned Ring Complexes**

Given that we can increase CO numbers along an easily identifiable chromosome under a specific condition, we set out to investigate how extra chiasmata might affect other aspects of bivalent organization by assessing the Ring Complex (RC), a structure comprised of a set of critical meiotic proteins. AIR-2 and other CPC components localize along the short arms of each cruciform bivalent during diakinesis, and upon nuclear envelope breakdown, the CPC reorganizes into a ring encircling the short arm axis of the bivalent, and forms the RC by recruiting other components (Wignall et al., 2009; Dumont et al., 2010; Pelisch et al., 2017). To determine if this structure properly forms on bivalents with multiple short arm regions (resulting from excess COs) (Figure 3.1D), we compared the organization of the CPC and other RC components on wild-type and *meT7* prometaphase bivalents.

The three wild-type bivalents in the *meT7* strain formed single whole rings of AIR-2, as expected. However, while AIR-2 localized to *meT7* fusion bivalents, it was sometimes improperly shaped: 72% of *meT7* bivalents had single rings at 15°C, but other *meT7* bivalents formed either slightly (19%) or severely (10%) mispatterned structures (Figure 3.2A, 3.2B; see Materials and Methods in Appendix C for details on quantification). BIR-1$^{Survivin}$, another CPC component, colocalized with AIR-2 on all ring structure types (Figure D.1), suggesting that the pattern of AIR-2 localization reflects assembly of the entire CPC. Similar to the increase in COs and chiasmata at 25°C along

*meT7* (77% *meT7* with >2 COs at 20°C versus 90% *meT7* with >2 COs at 25°C; Figure 3.1D), these CPC patterning defects on the *meT7* bivalent increased in number and severity at 25°C (increasing to 30% and 34%, for slight and severe mispatterning, respectively, Figure 3.2A), suggesting that increased CO numbers increase the likelihood of CPC mispatterning.

We next assessed the localization of RC components that are dependent on the CPC for targeting, and found that both SUMO (Figure 3.2B) and KLP-19 (Figure 3.2C) co-localize with AIR-2 on *meT7* bivalents. Therefore, although the CPC is mispatterned, it can still target other RC components to the bivalents. Linescans across SUMO-stained bivalents showed that, in contrast to the single tight ring peak and bilobed bivalent structure characteristic of wild-type bivalents, *meT7* bivalents have much more variation in both chromosome and RC shape (Figure 3.2D). Importantly, although RCs also form in Meiosis II around the interface between sister-chromatids, the RC patterning defects mainly occurred on Meiosis I *meT7* bivalents (45% of all MI *meT7* bivalents), while only 12% of MII chromosomes formed abnormal rings ($p<0.0001$, chi-square test; Figure

**Figure 3.2 - Bivalents with excess crossovers have mispatterned Ring Complexes (RCs)**
(A) AIR-2 localization in wild type (N2) or *meT7* oocytes. Single-chromosome zooms show that AIR-2 (red) localizes in a whole ring shape encircling normal bivalents in both strains, while its localization is either whole ring-like or mispatterned on *meT7* fusion bivalents. Note that the zoomed images throughout this figure are partial projections, chosen to highlight individual chromosomes. Quantification shows that *meT7* mispatterning increases with increased temperatures (N=75, all categories). (B) SUMO (green) co-localizes with AIR-2 (red) in all ring structure types on both wild type (N2) and *meT7* fusion bivalents. (C) KLP-19 (kinesin 4) (red), localizes to both "whole ring" and "mispatterned" *meT7* RCs. (D) Line scans across bivalents show that both the bivalent and RC have wider spread and higher variance in *meT7* fusion bivalents as compared to wild type bivalents. (N=25, all categories). (E) Quantification of ring patterning in metaphase I bivalents and metaphase II sister chromatid pairs. Metaphase I bivalents have much higher rates of mispatterning as compared to metaphase II sister chromatid pairs (N=75, all categories). All scale bars = 2.5μm.

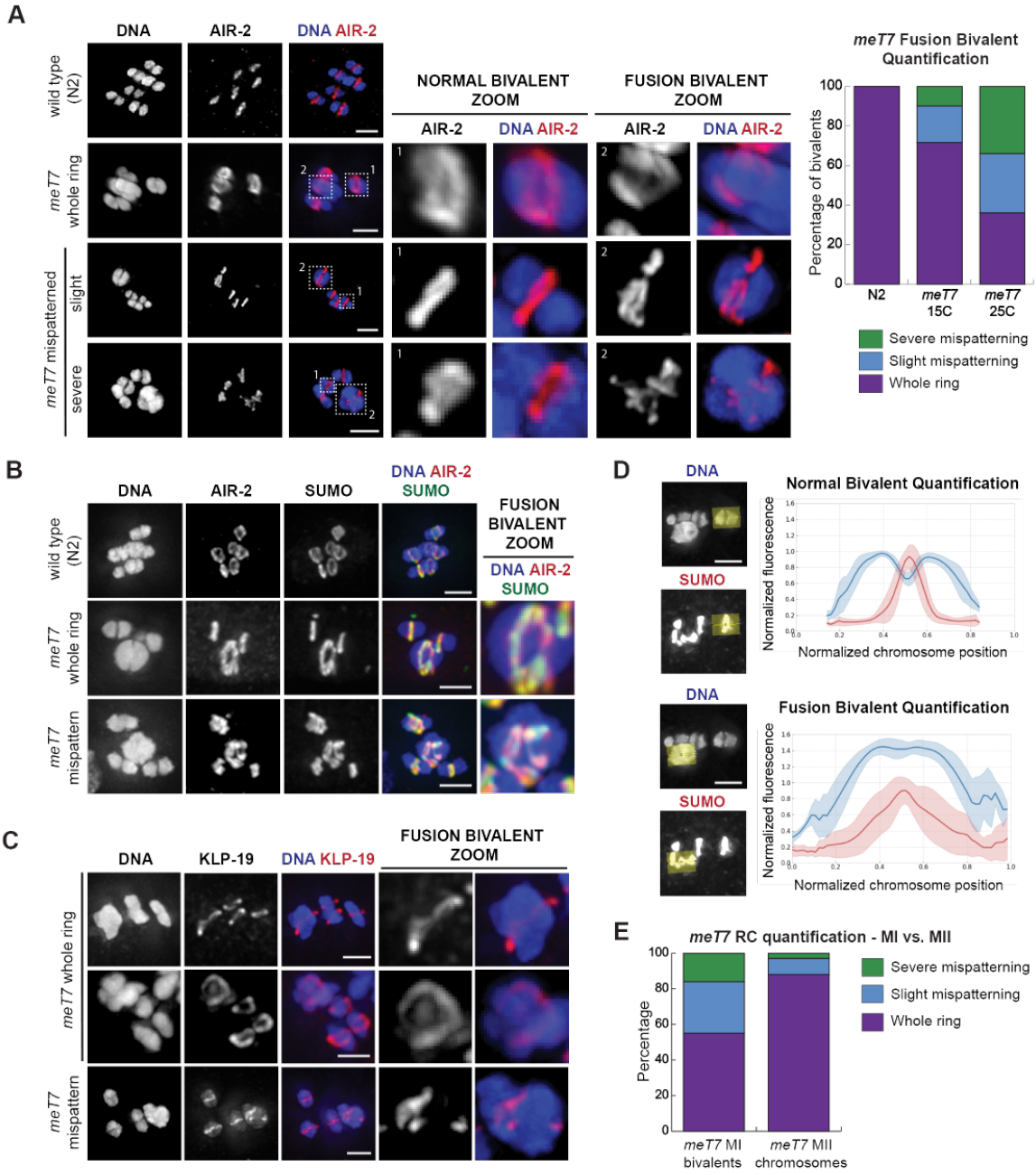


3.2E). This result is consistent with the idea that the RC defects are primarily caused by excess COs between homologous chromosomes, rather than general problems with RC formation in the *meT7* strain.

Although the RCs were mispatterned on *meT7* bivalents, kinetochore proteins appeared to load on the bivalents. Since *C. elegans* chromosomes are holocentric,

kinetochore proteins coat the bivalents in meiosis (Howe et al., 2001; Monen et al., 2005). We found that two kinetochore components, BUB-1 and SEP-1$^{Separase}$, coated the entire fused bivalent, demonstrating that the major patterning defect on fusion chromosomes was with the RCs, not the kinetochore (Figure D.2).

**Fusion Chromosome Bivalents can Form Multiple Ring Complexes that All Remain Functional**

Next, we wanted to characterize the mispatterned *meT7* RC structures. In some of our images there appeared to be multiple distinct RCs forming on a single *meT7* bivalent (e.g. Figure 3.2A, row 3; Figure 3.2B, row 3), which could reflect the ability of each chiasmata to organize its own RC. However, since many of the mispatterned RCs appeared to be complex structures, it was difficult in many cases to determine if a particular RC was comprised of multiple rings close together, or instead represented a single intertwined structure. Therefore, to distinguish between these possibilities, we performed an "RC stretching assay." This assay exploits our previous finding that under extended metaphase arrest, RCs begin to stretch away from the chromosomes towards microtubule plus ends, reflecting the fact that they contain a plus-end-directed activity that usually provides chromosomes with plus-end-directed forces (Muscat et al., 2015). For the purposes of the current study, we reasoned that this behavior might spatially separate distinct rings from one another, enabling us to distinguish and quantify the total number of rings formed on each *meT7* fusion bivalent. Additionally, we performed this "RC stretching assay" on monopolar spindles, in which the microtubule minus ends are organized at a central pole and the plus ends radiate outward forming an aster. This

additional feature enabled us to determine if the *meT7* ring structures were functional (*i.e.* whether they were able to stretch towards the outside of the aster, thus exerting plus-end forces). Consistent with previous work (Muscat et al., 2015), we found that in this RC stretching assay, rings on normal bivalents typically stretch off as one entity in a single direction towards microtubule plus ends (31/38), with 7/38 of the observed bivalents having two stretches (Figure 3.3, rows 1 and 2). In contrast, on many *meT7* bivalents, it was clear that there was more than one RC, often with two (27/38) or rarely three (2/38) separate entities stretching off of the bivalent (Figure 3.3, rows 5 and 6). Notably, the

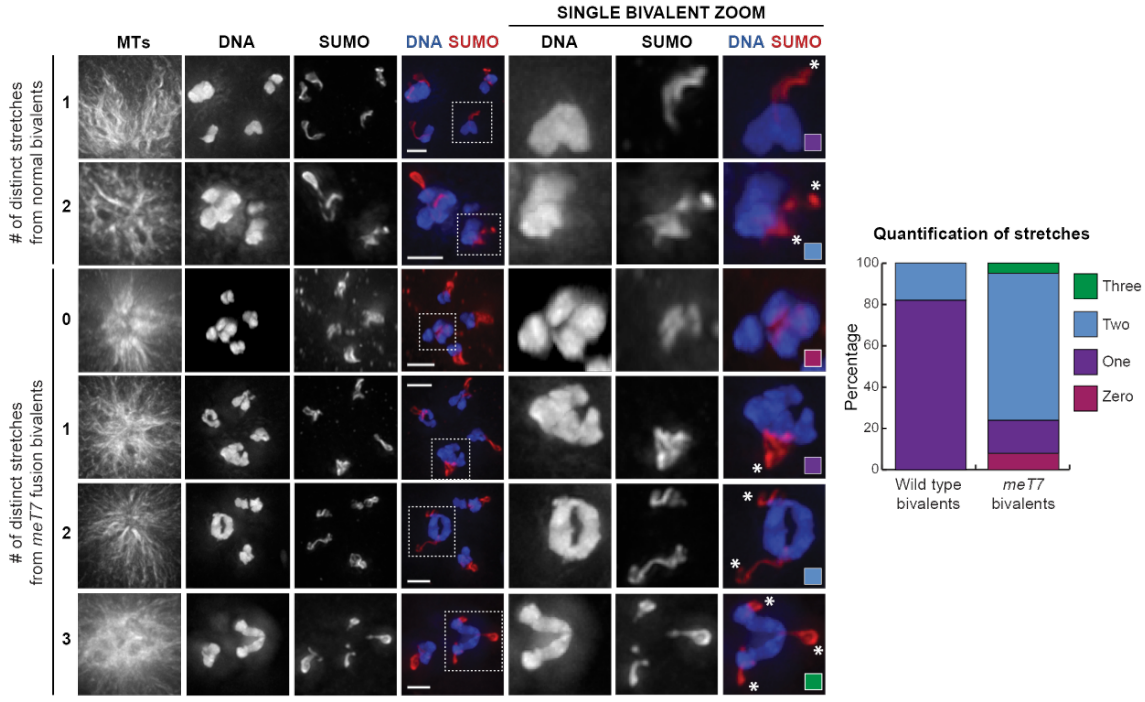


**Figure 3.3 – Bivalents with excess COs can form multiple functional RCs**
Examples and quantification of stretching RCs (visualized by SUMO staining, red) from bivalents (blue) (N=38, all conditions). In this assay, monopolar spindles were generated by depleting the force-generating motor KLP-18 (Wignall et al., 2009; Wolff et al., 2016). Zooms are partial projections, chosen to highlight individual chromosomes. RCs on monopolar spindles under prolonged metaphase arrest tend to stretch in a plus end-directed manner, towards the outside of the microtubule aster. RCs on normal bivalents tend to stretch as mostly one unit in a single direction, while RCs on *meT7* bivalents can have multiple RCs that stretch in independent directions. Asterisks denote stretching RCs. Scale bars = 2.5µm

frequency of more than one stretching RC on the *meT7* fusion chromosome (76% at 15°C) is close to the frequency of more than one CO along *meT7* (77% at 20°C; Figure 3.1C). This result suggests that multiple distinct RC structures can form at different chiasmata on the same bivalent.

Interestingly, when multiple RCs are present, they all stretch towards microtubule plus ends but end up oriented along different microtubule bundles, suggesting that the RCs are all functional and acting independently of one another; in the context of a bipolar spindle where microtubule bundles are not all in the same orientation, this could result in a single chromosome being pulled in opposite directions. Furthermore, unlike on normal bivalents, 3/38 rings on *meT7* bivalents were not stretching in any direction despite normal bivalents in the same spindle having stretching rings. Together, these results suggest that the mispatterned RCs on *meT7* may not be able to provide chromosomes with normal plus-end-directed forces.

**Fusion Chromosome Bivalents Show Defects in Metaphase Alignment and Bivalent Organization**

To investigate the possibility that *meT7* bivalents are experiencing abnormal forces, we asked whether mispatterning of the RCs in the *meT7* bivalents had functional consequences on the alignment of those bivalents on bipolar spindles. We therefore evaluated spindles where the three normal bivalents had aligned at the metaphase plate and scored the position of the *meT7* fusion bivalent. We found that while *meT7* bivalents with single whole rings aligned with the other bivalents in 92% (46/50) of these spindles,

only 62% (31/50) with mispatterned rings successfully aligned (Figure 3.4A), suggesting that defects in RC organization affect the fidelity of chromosome congression.

Building on this finding, we assessed the position of chromosomes on monopolar spindles as a read-out of plus-end directed forces (Figure 3.4B); in this context, bivalents that are able to generate normal plus-end forces migrate away from the center of the aster (Wignall et al., 2009). Unlike the RC stretching assay with monopolar spindles (Figure 3.3), this experiment does not involve an extended metaphase arrest so the RCs retain their original morphology (Figure 3.4). This analysis revealed that *meT7* bivalents with mispatterned rings do not tend to migrate as far away from the pole as the three wild-type bivalents (Figure 3.4C). Moreover, in two extreme cases (out of 12), the fusion bivalents remained stuck at the center of the monopole (Figure 3.4B, bottom row). Importantly, this defect appeared to be caused by the chromosome patterning defects and not by the large size of the fusion bivalent, since *meT7* bivalents with single rings exhibited normal chromosome movement (Figure 3.4B, 3.4C). Together, these findings suggest that the mispatterned RCs on *meT7* bivalents are not able to provide these bivalents with normal

**Figure 3.4 – Bivalents with mispatterned RCs align improperly on the oocyte spindle and are not subjected to proper plus-end directed forces**
(A) Alignment of the fusion chromosome was assessed on Metaphase I spindles; images show DNA (blue), microtubules (green) and SUMO to mark the RCs (red), and the quantification is to the right of the images. 92% of *meT7* bivalents with a whole ring aligned with the three normal bivalents, compared to 62% of *meT7* bivalents with mispatterned rings (N = 50, all conditions). Scale bars = 2.5µm. (B,C) Examples and quantification of plus-end directed movement of fused chromosome bivalents. Monnopolar spindles were generated by depleting KLP-18, and the center of the aster was determined by staining with the spindle pole marker ASPM-1 and determining the center of the ASPM-1 signal. The distance between each of the three normal bivalents and the center of the monopolar spindle was measured using Imaris, and the distance the fused chromosome bivalent traveled was compared to the average of the three normal bivalents' distance. meT7 bivalents with whole rings (N = 16) tended to move as far as normal bivalents on the monopole, while bivalents with mispatterned rings (N = 12) showed much more variation in their distance from the monopole. Scale bars = 5µm.

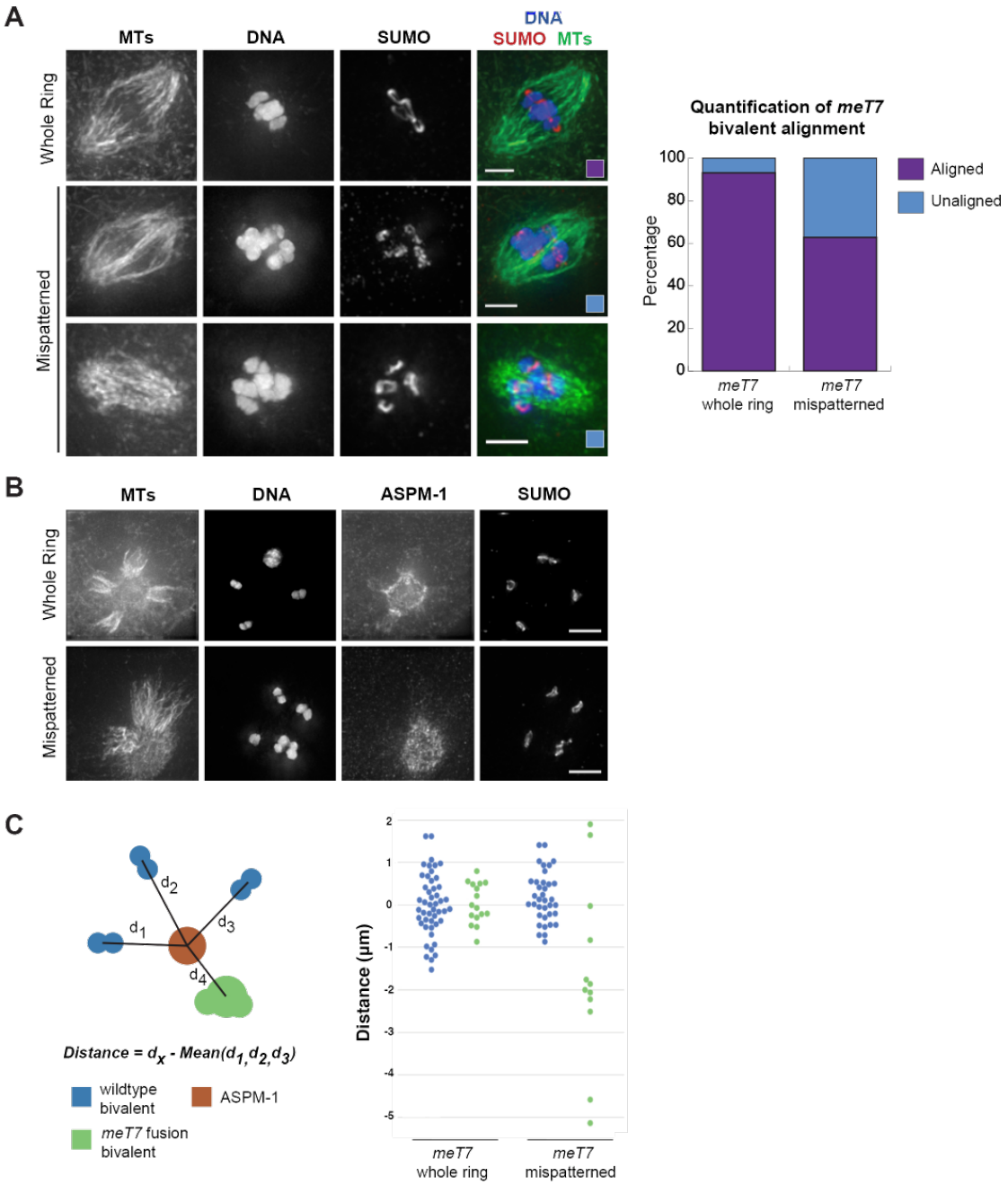


plus-end forces, potentially impacting their ability to achieve proper metaphase alignment. Since *meT7* bivalents often have multiple RCs that can function independent of each other (Figure 3.3), we postulate that these RCs could provide bivalents with forces in opposing directions thereby reducing the efficiency of chromosome movement.

**Fusion Chromosome Bivalents Show Defects in Chromosome Segregation that Carry Over into Meiosis II**

Given the defects in the structure and alignment of *meT7* bivalents, we next wanted to determine if having excess COs impacts chromosome segregation during meiosis I and II. First, we imaged anaphase I to assess the ability of homologous chromosomes to segregate. Notably, we found that in early anaphase I, the *meT7* fusion bivalent was often stuck in the middle of the spindle, lagging behind the three segregating wild-type bivalents. However, the frequency of this delayed segregation did not appear to be affected by temperature, as *meT7* bivalents showed comparable segregation delays in early anaphase I spindles at both 15°C (44/75, 58.7%) and 25°C (47/75, 62.7%) (Figure 3.5A). In contrast, in late anaphase I *meT7* bivalents had chromatin bridges that increased at higher temperatures where *meT7* experiences elevated COs (17/75, 22.7% at 15°C vs. 34/75, 45.3% at 25°C; P = 0.003, chi-square test), while wild-type bivalents segregated normally at all temperatures (Figure 3.5A). These results suggest that the early anaphase I defects are not due to increases in CO numbers, and may instead be due to the large size of the fusion chromosome. Conversely, extra COs between homologous chromosomes likely cause chromatin bridges in late anaphase I. Consistent with this hypothesis, we rarely observed chromatin bridging in anaphase II when sister chromatids rather than homologous chromosomes were segregating (2/65, 3.1%; Figure 3.5C).

To determine if the anaphase I defects had lasting consequences, we examined oocytes that progressed to Meiosis II. Notably, we observed a range of severe defects at 15°C, including oocytes that had a prominent DNA bridge connecting the *meT7* chromosome to the first polar body (5/60), as well as oocytes that had completely

retained or lost the entire *meT7* bivalent, resulting in aneuploidy (7/60, Figure 3.5B). Similar to the chromosome bridging observed in MI, these defects increased at higher temperatures (at 25°C, 9/60 were tethered to PBI and 12/60 were aneuploid), suggesting that they were the result of excess COs between *meT7* chromosomes.

To understand the temporal dynamics of *meT7* segregation, we performed live imaging using a *meT7* strain expressing GFP-tubulin and mCherry-histone to mark microtubules and chromosomes, respectively. Consistent with our fixed imaging, we found that a majority of anaphase I spindles displayed extended chromatin bridges (8/14, 57%) (Figure 3.6). Five of these bridges were unresolved, leaving the first polar body tethered to the developing meiosis II spindle. Further, in one example, *meT7* was not able to segregate in anaphase I, and the fully retained bivalent segregated with a chromatin bridge in anaphase II. Altogether, this live imaging data supports the conclusion that oocytes face severe chromosome segregation defects in the presence of supernumerary crossovers.

---

**Figure 3.5 – Fusion chromosome segregation is frequently aberrant**
(A) Anaphase I chromosome segregation in wild-type (N2) and *meT7* oocytes; shown are DNA (blue), microtubules (green), and AIR-2 (red), with quantification to the right of the images. All chromosomes segregated without errors in wild type (N2) ocoytes (rows 1 and 2), but *meT7* bivalents tended to show a delay in segregation in early anaphase compared to normal bivalents at both 15°C and 25°C (row 3, "early anaphase quantification" graph). In mid-to-late anaphase, 23% of *meT7* bivalents showed extended chromatin bridging at 15°C, which increased to 45% at 25°C (rows 4 and 5, "late anaphase quantification" graph (N = 75, all conditions). (B) Metaphase II spindles in *meT7* oocytes. While all N2 metaphase II spindles were euploid at 15°C, 8% of *meT7* were aneuploid (rows 1 and 2) and 12% had DNA tethered to the first polar body (indicated with asterisks, rows 3 and 4). These numbers increased to 15% and 20%, respectively, at 25°C (N = 60, all conditions). (C) Quantification of *meT7* chromatin bridging in anaphase I vs. anaphase II. 22% of mid-to-late *meT7* anaphase I spindles at 15°C (N = 71) and 45% at 25°C (N = 58) showed anaphase chromatin bridging, while only 3% of all *meT7* anaphase II spindles (both temperatures combined) showed anaphase chromatin bridging (N = 65). All scale bars = 2.5μm.

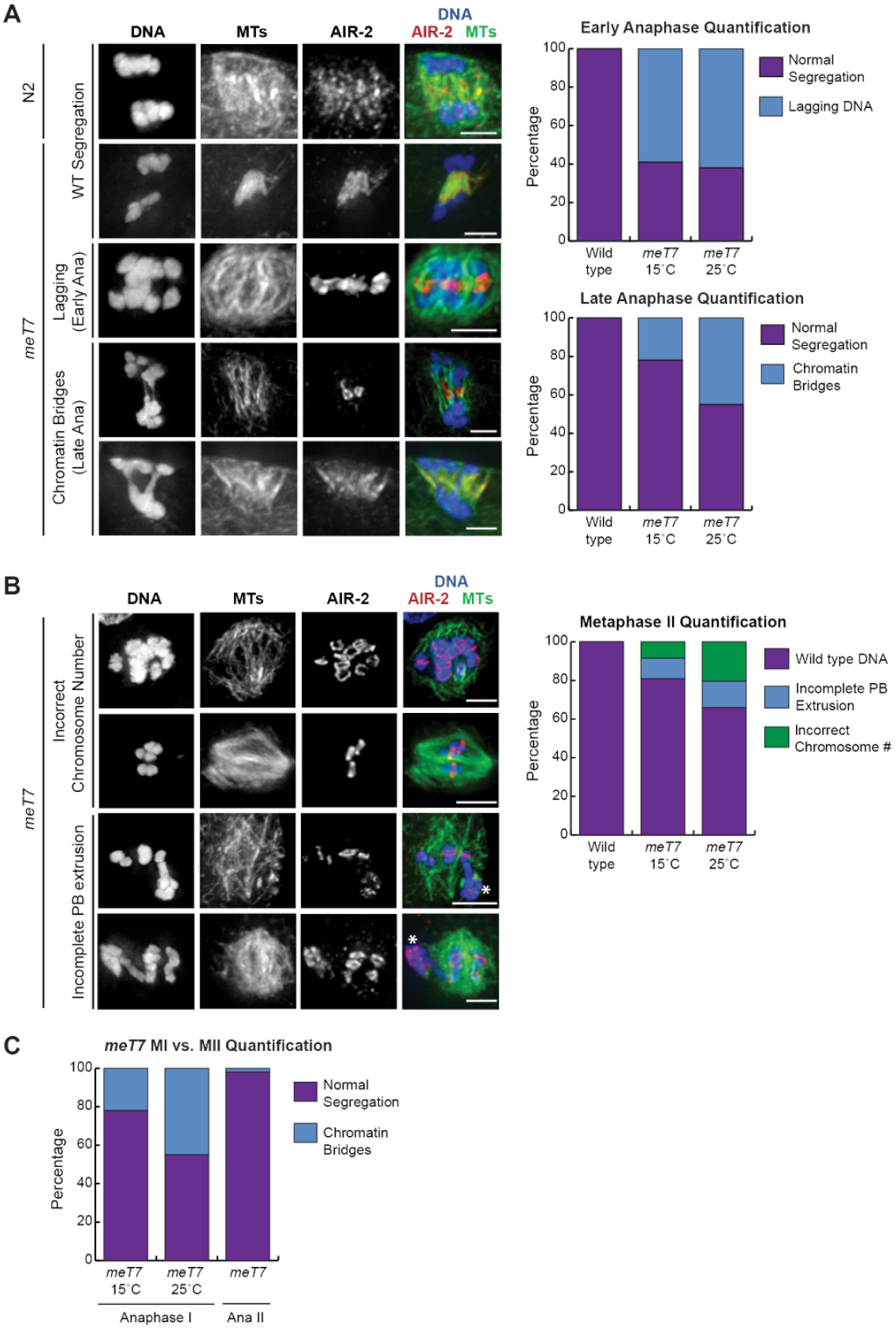
A
DNA
MTs
AIR-2
DNA
AIR-2 MTs
N2
meT7
WT Segregation
Lagging (Early Ana)
Chromatin Bridges (Late Ana)
Early Anaphase Quantification
Percentage
Normal Segregation
Lagging DNA
Wild type
meT7 15˚C
meT7 25˚C
Late Anaphase Quantification
Normal Segregation
Chromatin Bridges
B
Incorrect Chromosome Number
Incomplete PB extrusion
Metaphase II Quantification
Wild type DNA
Incomplete PB Extrusion
Incorrect Chromosome #
C
meT7 MI vs. MII Quantification
Chromatin Bridges
Anaphase I
Ana II

**Persistent Chromatin Bridges can be Recognized and Resolved by the Oocyte**

Despite the fact that we observed a variety of severe meiotic chromosome segregation defects (Figures 3.5 and 3.6), the embryonic lethality of the *meT7* strain is surprisingly low (Table 3.1). The *meT7* strain exhibits 27.6% embryonic lethality at 25ºC, indicating that most oocytes are able to generate viable progeny even in the presence of multiple COs (at 25ºC, >90% of *meT7* chromosomes have ≥2 COSA-1 foci; Figure 3.1C) and chromosome segregation defects (at 25ºC, ~50% of *meT7* anaphase I nuclei have chromatin bridges; Figures 3.5 and 3.6). Similarly, Meiosis II oocytes have fewer defects than would be expected given the frequency of errors in Meiosis I, and in our live

| Genotype | RNAi Treatment | Total number of eggs laid (# broods evaluated) | % viable progeny | % inviable embryos |
|---|---|---|---|---|
| Wild type | n/a | 2,483 (15) | 99.5 | 0.5 |
| *GFP::TBB-2 mCh::HIS-11* | n/a | 2,303 (15) | 98.4 | 1.6 |
| *meT7 (III;X;IV)* | n/a | 1,196 (15) | 72.4 | 27.6 |
| *meT7 (III;X;IV) GFP::TBB-2 mCh::HIS-11* | n/a | 1,230 (15) | 63.2 | 36.8 |
| Wild type | *lem-3* | 625 (5) | 98.6 | 1.4 |
| *GFP::TBB-2 mCh::HIS-11* | *lem-3* | 533 (5) | 98.1 | 1.9 |
| *meT7 (III;X;IV)* | *lem-3* | 1,256 (10) | 66.1 | 33.9 |
| *meT7 (III;X;IV) GFP::TBB-2 mCh::HIS-11* | *lem-3* | 582 (10) | 45.4 | 54.6 |

**Table 3.1 – Progeny viability following *lem-3* RNAi treatment.**

**Figure 3.6 – *meT7* oocytes display several classes of chromosome segregation defects.**
(A) Time-lapse spinning disk confocal montages during anaphase meiosis I (MI) and anaphase meiosis II (MII) in live wild-type and *meT7* oocytes expressing GFP::TBB-2 and mCherry::HIS-11 to mark microtubules and histones respectively. Examples of *meT7* chromosome segregation phenotypes are shown in i-vi. White arrowheads point to *meT7* fused chromosomes as they fail to segregate in anaphase I (iii), yellow arrowheads indicate anaphase I *meT7* chromatin bridges between segregating chromosomes (iv, v, vi) and blue arrowheads point to chromatin tethers between the MI polar body (MPB) and the anaphase II spindle (v, vi). White arrows indicate lagging chromosome(s) in anaphase II (ii). Time zero is the time at which chromosome segregation appears to begin. Scale bars = 5μm. (B) *meT7* chromosome segregation phenotype descriptions and observation frequency. Of the 8 *meT7* oocytes that had chromatin bridges at anaphase I, 3/8 bridges were able to resolve prior to the end of anaphase I. For the remaining 5 *meT7* oocytes that were not able to resolve their anaphase I bridges, 4/8 extruded the tether (with the associated chromatid) into the MPB at anaphase II and 1/8 exhibited persistent tethers through anaphase II.

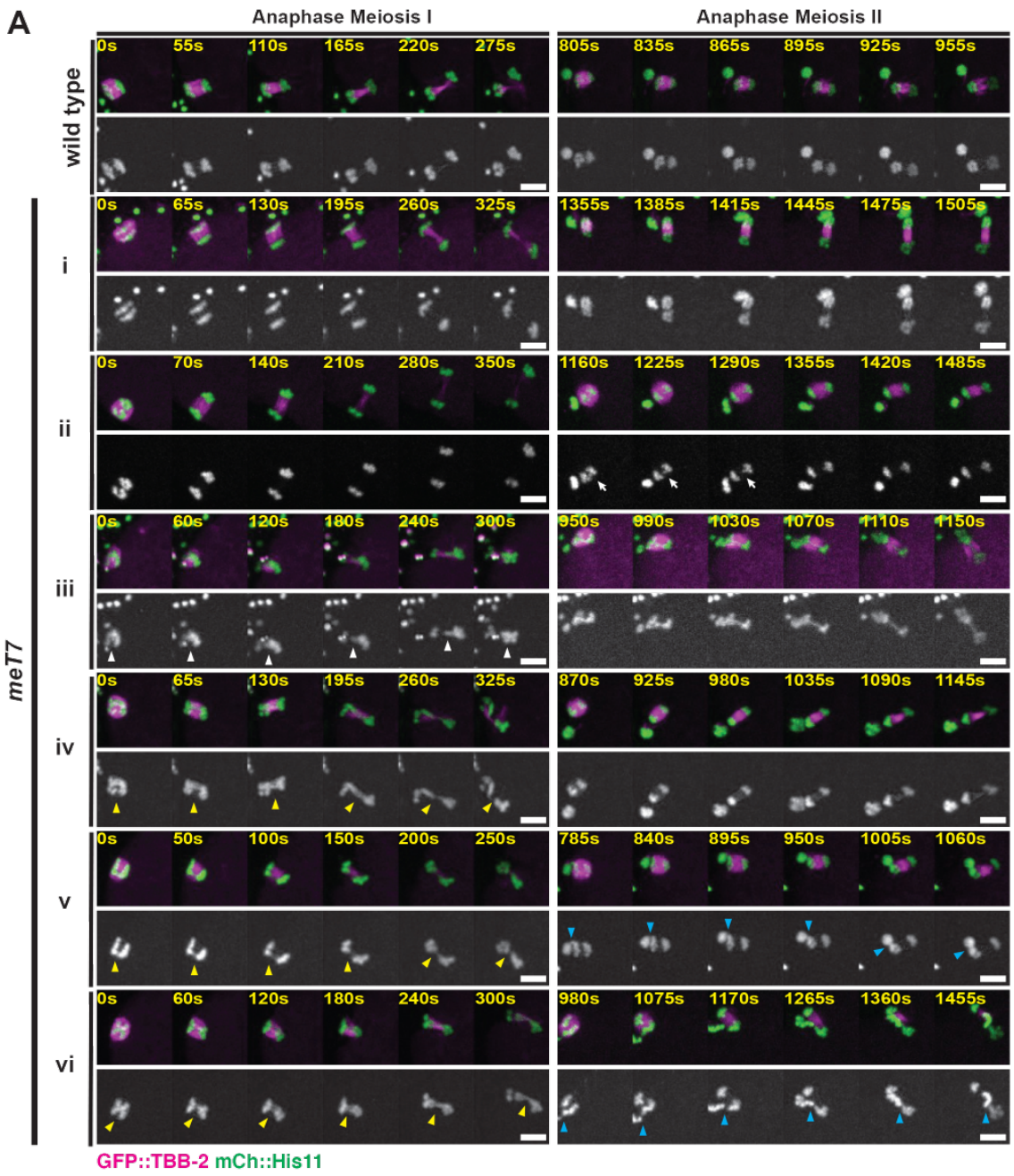


B

| | | | | MI Anaphase Bridge | | |
|---|---|---|---|---|---|---|
| *meT7* Phenotypes | i Normal Segregation (MI and MII) | ii Normal Segregation (MI), Lagging Chromosome(s) (MII) | iii *meT7* Segregation Fails (MI) | iv Bridge Resolves | v MII Spindle Tether | vi MII Spindle and MPB Tether |
| Frequency Observed | 3/14 | 2/14 | 1/14 | 3/14 | 4/14 | 1/14 |

imaging we noticed instances where anaphase I DNA bridges were resolved as the oocyte progressed to Meiosis II (Figure 3.6). Thus, oocytes appear to have mechanisms to correct and resolve chromosome segregation defects. Supporting this idea, *meT7* oocytes

appear to detect errors. We recently demonstrated that *C. elegans* oocytes recognize meiotic errors and respond by delaying AIR-2 relocalization to the spindle in mid anaphase (Davis-Roca et al., 2017). Thus, we assessed AIR-2 localization and found that *meT7* oocytes delay AIR-2 relocalization at higher rates than wildtype oocytes at both 15°C (3/31, 9.7%, in wild type vs. 7/31, 22.6% in *meT7*) and at 25°C (14/42, 33.3% in wild type vs. 12/29, 41.3% in *meT7*), further suggesting that these oocytes are responding to and attempting to resolve error (Figure D.3).

One protein that we hypothesized might contribute to error correction is LEM-3, a late-acting nuclease proposed to resolve chromatin connections in mitotic and meiotic anaphase (Hong, Sonneville, et al., 2018; Hong, Velkova, et al., 2018). Therefore, we depleted *lem-3* with RNAi in the *meT7* strain and assessed chromosome segregation. In support of our hypothesis, we found that *lem-3*-depleted *meT7* oocytes had significantly higher proportions of anaphase I bridges at both 15°C (15/52, 28.8%, in control vs. 26/52, 50.0%, in *lem-3 RNAi;* P = 0.024, chi-square test) and 25°C (25/49, 51.0%, in control vs. 27/37, 72.97%, in *lem-3 RNAi*; P = 0.039, chi-square test; Figure 3.7A). Moreover, these defects persisted into Meiosis II in higher proportions compared to oocytes without *lem-3* depletion, and MII spindles had increased instances of both aneuploidy (at 15°C, 4/48 in control vs. 4/31 in *lem-3 RNAi, P* = 0.006, chi-square test*;* at 25°C, 6/41 in control vs. 6/28 in *lem-3 RNAi,* P=0.015, chi-square test) and tethered polar bodies (at 15°C, 5/48 in control vs. 12/31 in *lem-3 RNAi;* at 25°C, 9/41 in control vs. 14/28 in *lem-3 RNAi*, Figure 3.7A). Live imaging of *lem-3* depleted *meT7* oocytes corroborated these findings, showing an increase in chromosome segregation defects, including two cases in which chromatin bridges appeared to fragment (2/13, 15%), and one failure to extrude a Meiosis

I polar body (1/13, 7%) (Figure 3.7B; Table D.1). In five cases, the *meT7* chromosome was unable to segregate in anaphase I and subsequently extruded into the first polar body (5/13, 38%) (Figure 3.7B). Together, these results suggest that LEM-3 plays a role in correcting *meT7* chromosome segregation defects during oocyte meiosis.

Furthermore, our analysis suggested another potential mechanism that could contribute to error correction in cases of chromatin bridges caused by excess COs. Specifically, we noticed that when oocytes had polar body tethers that persisted into anaphase II, the segregating sister chromatid connected to the polar body tether was often segregated to the cortical side (23/26 cases; Figure 3.5C), meaning that the tether was expelled with the second polar body, leaving the oocyte euploid. This fixed imaging result is supported by our live imaging, where we found that in 4/5 movies containing persisting tethers in anaphase II (Figure 3.6A v-vi, 3.6B v-vi), the sister chromatid

---

**Figure 3.7 – Oocytes can correct errors from excess COs in anaphase**
(A) Effects of *lem-3* RNAi on *meT7* anaphase I and metaphase II spindles; shown are DNA (blue), microtubules (green) and SUMO (red). Frequency of anaphase I bridges on *meT7* increased following *lem-3(RNAi)* at both 15°C (29% for control compared to 50% for *lem-3(RNAi)*; P = 0.024, chi-square test; N = 52 for each condition) and 25°C (51% compared to 73%, P = 0.039, chi-square test; N = 49 for control and N = 37 for *lem-3(RNAi)*). Frequency of polar body extrusion delays, scored in *meT7* metaphase II spindles, increased at both 15°C (11% to 39%; P = 0.006, chi-square test; N = 48 for control and N = 31 for *lem-3(RNAi)*) and 25°C (22% to 50%; P = 0.015, chi-square test; N = 41 for control and N = 28 for *lem-3(RNAi)*), as did aneuploidy in meiosis II at 15°C (8% to 13%) and 25°C (15% to 21%). In 23/26 *lem-3(RNAi)* oocytes in which the polar body tether persisted into anaphase II, the tethered sister chromatid appeared to be segregating to the cell cortex (three examples shown, polar body denoted with asterisks). Scale bars = 2.5µm (B) Time-lapse montages of anaphase I and II in *lem-3* depleted wild type and *meT7* oocytes expressing GFP::TBB-2 (microtubules) and mCherry::HIS-11 (histones). Yellow arrowheads indicate an anaphase I chromatin bridge. Blue arrowhead denotes a possible chromosome fragment after bridge breaking. White arrowheads point to a failure to segregate *meT7* in Meiosis I and extrusion into the first polar body. Time zero is the time at which chromosome segregation appears to begin. Scale bars = 5µm. (C) Model for effects of supernumerary crossovers in *C. elegans* meiosis.

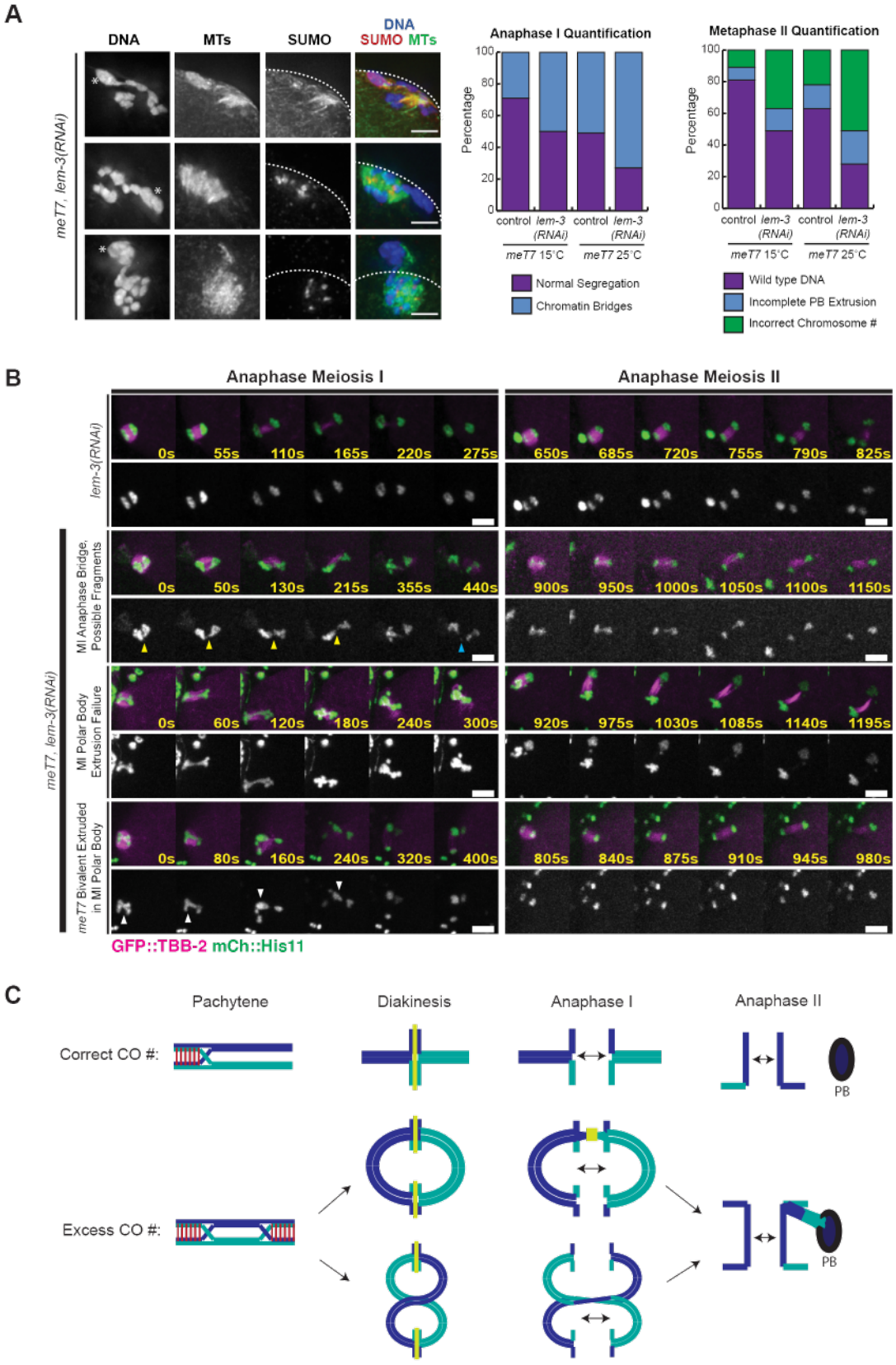


associated with the chromosome tether was extruded with the second polar body during

Meiosis II (Figure 3.6A v, 3.6B v). Currently, it is unclear whether the oocyte actively recognizes the tether or whether the DNA tether biases the direction of spindle rotation towards the cortex, thereby facilitating its own elimination. In either case, this mechanism could serve to eliminate improperly segregated chromosomes from the resulting gamete.

**Discussion**

In summary, our work provides molecular insights into how crossover limitation promotes proper chromosome congression and segregation in the oocyte. We found that increased COs cause defects in bivalent organization that impact the ability of chromosomes to achieve metaphase alignment. An increased number of COs leads to the designation of multiple short arms and subsequent formation of extra RCs (Figure 3.7C). Interestingly, when multiple RCs form along a single chromosome, they all appear to be functional. The inability to inactivate extra RCs in *C. elegans* meiosis appears to have consequences, as there are chromosome congression errors that likely arise from differential forces exerted on bivalents. This result highlights the importance of proper RC patterning, and demonstrates that the structure of this protein complex affects its function. Moreover, our studies revealed that increasing CO number has consequences for homolog segregation, as bivalents with excess crossovers have frequent chromatin bridging during the first meiotic division. These frequently observed chromosome bridges may be due in part to the formation of extra RCs along a single chromosome, which may cause chromosome alignment issues along the metaphase I plate (Figure 3.7C).

**Crossover Limitation Promote Accurate Chromosome Segregation**

Strong CO interference, where there is only ~1-3 COs per chromosome pair per meiosis, is observed in several model systems, including fruit flies, worms, and mice (Gray et al., 2016). Even in human oocytes, CO interference is strong, with 1-2 COs per homolog (Wang et al., 2017). Although CO interference was initially observed over a century ago in *Drosophila* and subsequently found to be widely conserved among many model systems, the consequences of extra interfering COs along a pair of homologous chromosomes has not been directly determined. Our study is the first, to our knowledge, in any organism to assess these consequences. Our findings in *C. elegans* suggest that CO interference helps promote proper meiotic chromosome alignment by limiting homolog pairs to one crossover per bivalent under normal circumstances (thereby preventing the difficulties that ensue when bivalents assemble multiple RCs). Moreover, CO limitation may promote accurate chromosome segregation by creating a chromosome structure that facilitates the loss of cohesion in the correct domain, thereby preventing chromosome bridging. Thus, the ability to limit crossovers is important for the faithful execution of meiosis, which may represent a driving force that has contributed to the conservation of CO interference in many organisms. In the future, it will be interesting to investigate how supernumerary COs affect meiotic chromosome segregation in other organisms.

**Mechanisms Exist to Correct Errors Caused by Supernumerary Crossovers**

Our studies also uncovered two mechanisms that counteract defects caused by excess COs. We found that depletion of the conserved nuclease LEM-3/Ankle1 increases

the frequency and persistence of anaphase bridging, consistent with its previously proposed role in processing erroneous recombination intermediates and correcting meiotic errors (Hong, Velkova, et al., 2018). In the future, it will be interesting to determine whether additional proteins assist in processing DNA tethers. In addition to its role in meiotic recombination, the BLM/HIM-6 helicase (which localizes to interfering CO sites, (Woglar et al., 2018)) has been shown in multiple systems to localize to and to help resolve ultrafine DNA bridges during both mitotic and meiotic chromosome segregation (K. L. Chan et al., 2007; McVey et al., 2007; K. L. Chan et al., 2009; Schvarzstein et al., 2014; Hong et al., 2016; Y. W. Chan et al., 2018). Similarly, the nucleases MUS-81, SLX-1 and SLX-4 have genetic interactions with both LEM-3 (Hong, Velkova, et al., 2018) and HIM-6 (Agostinho et al., 2013) and may act combinatorially to resolve DNA bridging due to excess COs. Further, topoisomerase II has been shown to remove DNA tethers from heterochromatin regions that connect achiasmate homologs in *Drosophila* (Hughes et al., 2014). Given the conservation of the nuclease LEM-3/Ankle1, these mechanisms that counteract the effects of multiple COs may be augmented in organisms that occasionally experience more than one CO along a chromosome.

Although nucleases can serve as a generalized solution to resolve erroneous DNA connections, we also discovered a second mechanism specific to oocytes. In oocytes where a DNA tether was not resolved in anaphase I, the tethered DNA was preferentially extruded from the oocyte in anaphase II, presumably resulting in a euploid egg. This mechanism is made possible by the asymmetric nature of the oocyte divisions, in which half of the genetic material is discarded into the polar body during each division. This asymmetry has been shown to allow the preferential elimination of univalent

chromosomes in *C. elegans* (Cortes et al., 2015), and here provides a second opportunity for error correction in the presence of excess COs. It is interesting to speculate on whether the oocyte spindle actively recognizes the DNA tether, or whether the tether passively biases the rotation of the spindle, positioning the tethered chromosome adjacent to the cortex, where it will be extruded into the second polar body. Currently, little is known about how spindle rotation is influenced in *C. elegans*; however, previous work has shown that the minus-end binding protein ASPM-1 is brighter on the spindle pole that rotates towards the cortex, suggesting that spindle asymmetry could play a role (Vargas et al., 2017) similar to spindle asymmetry and selfish centromeres in mouse oocytes (Akera et al., 2017). Going forward, it would be interesting to ask whether unresolved DNA connections influence spindle factors to allow for preferential spindle rotation as a form of meiotic drive.

**Licensing of Ring Complex Formation by Crossovers**

Our results further establish how the coordination and interplay between recombination and chromosome segregation are critical for the maintenance of genomic integrity through generations. We observed that the occurrence of multiple crossovers leads to the formation of multiple RCs. Moreover, we found a strong correlation between CO number and eventual RC number along a single chromosome. This result leads to the compelling hypothesis that a CO site may be a licensing event for RC formation. Through either its specific DNA conformation or the recombination machinery associated with it, a CO may designate a location along the chromosome for RC components to assemble. Previous experiments have already found that Aurora B kinase localizes to

sites of COs (Martinez-Perez et al., 2008). Further, the HIM-6/BLM helicase has been found to localize to interfering CO sites and helps maintain chiasmata until metaphase I (Schvarzstein et al., 2014; Hong et al., 2016). Future experiments exploring whether there is direct interaction between recombination machinery and RC components may establish this connection between CO sites and RC formation.

Overall, our study provides new molecular insights into how excess COs affect chromosome congression and segregation. Further, our results indicate the existence of mechanisms to assist with correcting errors associated with the formation of excess COs, thereby lending important insight into how some organisms, such as *Saccharomyces cerevisiae*, can tolerate more than two interfering COs per chromosome. Future studies investigating why certain organisms can experience higher levels of interfering COs will lend further insight into these critical mechanisms for maintaining genomic integrity through generations.

**Bridge to Chapter IV**

Thus far, Chapters II and III have discussed how oocytes nucleate microtubules and efficiently assemble meiotic spindles, and how chromosome architecture can influence chromosome segregation by meiotic spindles. However, even less well understood than those processes is the process by which oocytes undergo cytokinesis, and what the potential relationship might be between meiotic spindle assembly, chromosome segregation, and the cytokinetic process. Chapter IV delves into the relationship between oocyte meiotic spindle assembly, chromosome segregation, and polar body extrusion by

examining the polar body extrusion process across three spindle-assembly defective mutants.

# CHAPTER IV

# *C. ELEGANS* CLASP/CLS-2 IS REQUIRED FOR POLAR BODY EXTRUSION AND NEGATIVELY REGULATES GLOBAL CORTICAL CONTRACTILITY DURING OOCYTE MEIOSIS

*This chapter contains previously unpublished co-authored material.

This material is a primary research article manuscript that has been prepared for publication. My contribution to this material includes collecting, processing, interpreting, and preparing all of the data for presentation within the manuscript, writing the initial draft of the manuscript, and manuscript editing. This work was done under the guidance and supervision of Dr. Bruce Bowerman, who provided insight and expertise in addition to helping edit the manuscript and associated figures for publication submission.

## Introduction

Oocyte meiosis comprises a single round of genome replication followed by two highly asymmetric cell divisions that produce a single haploid gamete and two small polar bodies that contain discarded chromosomes (Dumont et al., 2012; Ohkura, 2015; Severson et al., 2016; Mullen et al., 2019). An acentrosomal spindle segregates homologous chromosomes during the first reductional division, called meiosis I, and half of the recombined homologs are extruded into the first polar body. The equational meiosis II division then segregates sister chromatids, with half extruded into a second polar body and half remaining in the oocyte cytoplasm. Despite being essential for

reducing oocyte ploidy, little is known about the cues that organize and influence the actomyosin contractile ring that mediates polar body extrusion.

The oocyte contractile ring initially forms distal to the membrane-proximal meiotic spindle pole, with the spindle axis oriented orthogonally to the overlying cell cortex (Maddox et al., 2012). During anaphase the contractile ring ingresses past both the membrane-proximal pole and one set of the segregating chromosomes to then constrict and ultimately separate the nascent polar body from the oocyte. These dynamics contrast substantially with mitotic cytokinesis (Figure 4.1A), during which signals from astral microtubules and the central spindle position the contractile ring midway between the two spindle poles (Green et al., 2012; Basant et al., 2018; Pintard et al., 2019). While the signals required for contractile ring assembly and constriction during mitotic cytokinesis are relatively well understood, how oocyte meiotic spindles influence contractile ring dynamics during polar body extrusion is not known.

In *Caenorhabditis elegans*, several genes are required for polar body extrusion, but how their functions are coordinated remains poorly understood. Similar to mitotic cytokinesis, polar body cytokinesis requires filamentous actin and the non-muscle myosin II heavy-chain NMY-2 and light-chains MLC-4 and MLC-5 (Swan et al., 1998; Shelton et al., 1999; Fabritius et al., 2011). The cytoskeletal scaffolding protein anillin/ANI-1 facilitates transformation of the initial actomyosin contractile ring into a midbody tube, with anillin depletion resulting in large and unstable polar bodies that often fuse with the oocyte (Dorn et al., 2010). Consistent with its role as a key activator of cortical actomyosin, the small GTPase RhoA (RHO-1) and its RhoGEF ECT-2 also are required for oocyte polar body extrusion (Schonegg et al., 2006; Fabritius et al., 2011).

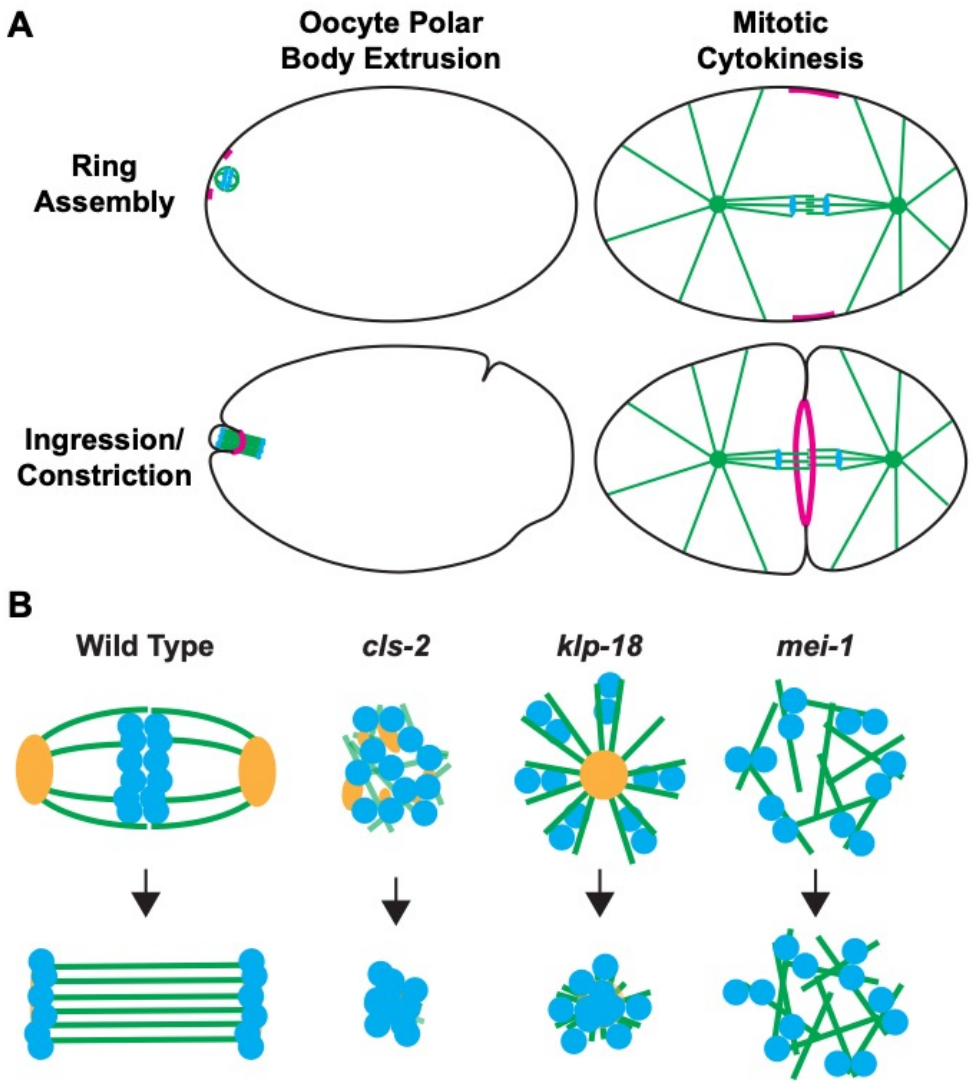


**Figure 4.1 – Schematics of oocyte meiotic polar body extrusion, mitotic cytokinesis and oocyte meiotic spindle assembly-defective mutants.**
(A) The positioning and dynamics of contractile ring assembly and ingression during oocyte polar body extrusion and mitotic cytokinesis. (B) Illustrations of oocyte meiotic spindle structure in control and mutant oocytes. Green = microtubules, blue = chromosomes, magenta = contractile rings, and orange = ASPM-1 pole marker, black = plasma membrane. See text for details.

Knockdown of the centralspindlin complex, comprised of MgcRacGAP/CYK-4 and kinesin-6/ZEN-4, results in the assembly of abnormally large contractile rings and a subsequent failure in extrusion (Fabritius et al., 2011). Finally, the chromosomal

passenger complex (CPC) member Aurora B/AIR-2 also is required (Schumacher et al., 1998).

Formation of the contractile ring distal to both meiotic spindle poles raises the question of how the ring moves relative to the spindle such that it constricts midway between segregating chromosomes. One mechanism proposed for *C. elegans* is that global contraction of actomyosin throughout the oocyte cortex produces a hydrostatic cytoplasmic force that, combined with depletion of cortical actomyosin overlying the membrane-proximal pole, leads to an out-pocketing of the membrane within the contractile ring and pushes the spindle into the protruding pocket (Fabritius et al., 2011; Flynn et al., 2017). In support of this hypothesis, increased global cortical contractility due to depletion of casein kinase 1 gamma (CSNK-1), a negative regulator of RhoA activity, often results in extrusion of the entire meiotic spindle (Flynn et al., 2017). However, assessing whether global cortical contractility is required for polar body extrusion has been challenging due to the overlap in requirements for global cortical contractility and polar body contractile ring assembly and constriction.

Despite a stereotyped spatial relationship between the oocyte meiotic spindle and contractile ring assembly and ingression, little is known about how the spindle might influence ring assembly and dynamics. Nevertheless, four observations suggest that the meiotic spindle provides important cues. First, meiotic spindles that fail to translocate to the oocyte cortex induce the formation of membrane furrows that ingress deeply towards the displaced spindle (Fabritius et al., 2011). Second, loss of the centralspindlin complex, which localizes to the central spindle during anaphase, results in the formation of rings with an abnormally large diameter (Fabritius et al., 2011). Third katanin/*mei-1* mutants,

which assemble apolar spindles, produce very large polar bodies (Mains et al., 1990; Clandinin et al., 1993) . Finally, while work in mice suggests that chromosomes themselves may provide cues for ring assembly and polar body extrusion via the small GTPase Ran (Deng et al., 2007; Deng et al., 2009), knock down of *C. elegans* RAN-1 does not prevent polar body extrusion (Askjaer et al., 2002; Chuang et al., 2020). These findings suggest that in *C. elegans* the oocyte meiotic spindle provides cues that influence contractile ring assembly and ingression.

To explore the relationship between meiotic spindle assembly and polar body extrusion, we have examined oocyte cortical actomyosin dynamics in three spindle assembly defective mutants that each lack the function of a conserved protein: CLASP/CLS-2, kinesin-12/KLP-18, or katanin/MEI-1 (Figure 4.1B). CLASP family proteins promote microtubule stability through their association with microtubules and their tubulin heterodimer-binding TOG (Tumor Over-expressed Gene) domains, decreasing the frequency of microtubule catastrophe and promoting rescue of de-polymerizing microtubules (Al-Bassam et al., 2010; Patel et al., 2012; Byrnes et al., 2017; Aher et al., 2018). Moreover, human CLASPs have been shown to influence not only microtubule stability and dynamics, but also to interact with actin filaments and potentially crosslink filamentous actin and microtubules (Tsvetkov et al., 2007). CLS-2 is one of three *C. elegans* CLASPs and is required for mitotic central spindle stability as well as oocyte meiotic spindle assembly and chromosome segregation (Dumont et al., 2010; Espiritu et al., 2012; Maton et al., 2015; Pelisch et al., 2019). Vertebrate kinesin-12/KLP-18 family members promote mitotic spindle bipolarity by contributing to forces that push apart anti-parallel microtubules (Tanenbaum et al., 2009; Vanneste et al., 2009;

Sturgill et al., 2013). Consistent with such a function, *C. elegans* oocytes lacking the kinesin-12 family member KLP-18 form monopolar meiotic spindles that draw chromosomes towards a single spindle pole and thus fail in chromosome segregation (Wignall et al., 2009; Connolly et al., 2014; Wolff et al., 2016). The widely conserved microtubule severing complex katanin is encoded by two *C. elegans* genes, *mei-1* and *mei-2* (Clark-Maguire et al., 1994; Srayko et al., 2000). Loss of either subunit results in the formation of apolar meiotic spindles that fail to congress or segregate chromosomes (Connolly et al., 2014; K. McNally et al., 2014; Joly et al., 2016).

Here we report our use of fluorescent protein fusions and live cell imaging to characterize polar body extrusion during meiosis I in mutants lacking the function of CLS-2, KLP-18 or MEI-1. Previous studies indicate that both CLS-2 and MEI-1 are involved in polar body extrusion, with oocytes lacking CLS-2 frequently failing to extrude polar bodies (Dumont et al., 2010; Laband et al., 2017; Pelisch et al., 2019), and oocytes lacking MEI-1 forming very large polar bodies (Mains et al., 1990; Clandinin et al., 1993; Han et al., 2009; Gomes et al., 2013). Furthermore, *klp-18* mutants sometimes lack an oocyte pronucleus, suggesting that all oocyte chromosomes can be extruded (Connolly et al., 2014). However, the process of polar body extrusion has not been directly examined in any of these mutants. Our live imaging of contractile ring assembly and ingression in these mutant backgrounds shows that bipolar spindle assembly and chromosome segregation are not required for oocyte contractile ring assembly and polar body extrusion. However, CLS-2 is required for proper contractile ring assembly or stability and also acts as a negative regulator of global cortical membrane ingressions,

while MEI-1 may be required late in polar body extrusion for contractile ring constriction.

## Results

### CLS-2 is Required for Oocyte Meiotic Spindle Assembly and Polar Body Extrusion

To investigate the role of CLS-2, we first examined the localization of a CLS-2::GFP fusion in live oocytes (Figure 4.2A, Supplemental Figure F.1 (Supplemental Figures for Chapter IV can be found in Appendix F)). Consistent with previous reports, CLS-2::GFP initially localized to meiosis I spindle microtubules and kinetochore cups, and to small patches dispersed throughout the oocyte cortex (Dumont et al., 2010; Laband et al., 2017; Pelisch et al., 2019). Around the time of anaphase onset, the cortical CLS-2::GFP patches disappeared and CLS-2::GFP localized to the central spindle between the segregating chromosomes (Dumont et al., 2010; Laband et al., 2017; Pelisch

**Figure 4.2 – CLS-2 is required for oocyte meiotic spindle assembly and polar body extrusion**
(A) Control oocytes expressing CLS-2::GFP and mCherry:H2B during meiosis I; dashed boxes indicate the zoomed-in regions shown in top row. (B) Protein domain map for wild type CLS-2 (Maton et al., 2015), and location of first premature stop codon due to frameshift in *cls-2(or1948)*. (C) Table of embryonic viability in wild type (N2) and *cls-2* CRISPR-generated loss of function alleles. (D) *C*ontrol and mutant oocytes expressing GFP::Tubulin and mCherry::H2B during meiosis I; t = 0 seconds (0s) corresponds to the end of meiosis I and beginning of meiosis II (see Materials and methods). (E) Comparison of integrated spindle microtubule pixel intensity over time between control (n = 17) and *cls-2* mutant oocytes (n = 9 @ -340s, n = 10 @ -330 to -300s, n = 11 @ -290 to -160s, and n = 12 @ -150 to 0s), with the average intensity indicated and one standard deviation indicated. Here and in subsequent figure panels, T = 0s corresponds to the end of meiosis I and beginning of meiosis II, unless indicated otherwise (see Materials and methods). (F) Control and mutant oocytes expressing GFP::ASPM-1 and mCherry::H2B during meiosis I. (G) Percent of control and mutant oocytes that extrude a polar body during meiosis I, as determined by mCherry or GFP-fused histone signal remaining stably ejected from the oocyte cytoplasm for the duration of imaging (see Materials and methods).

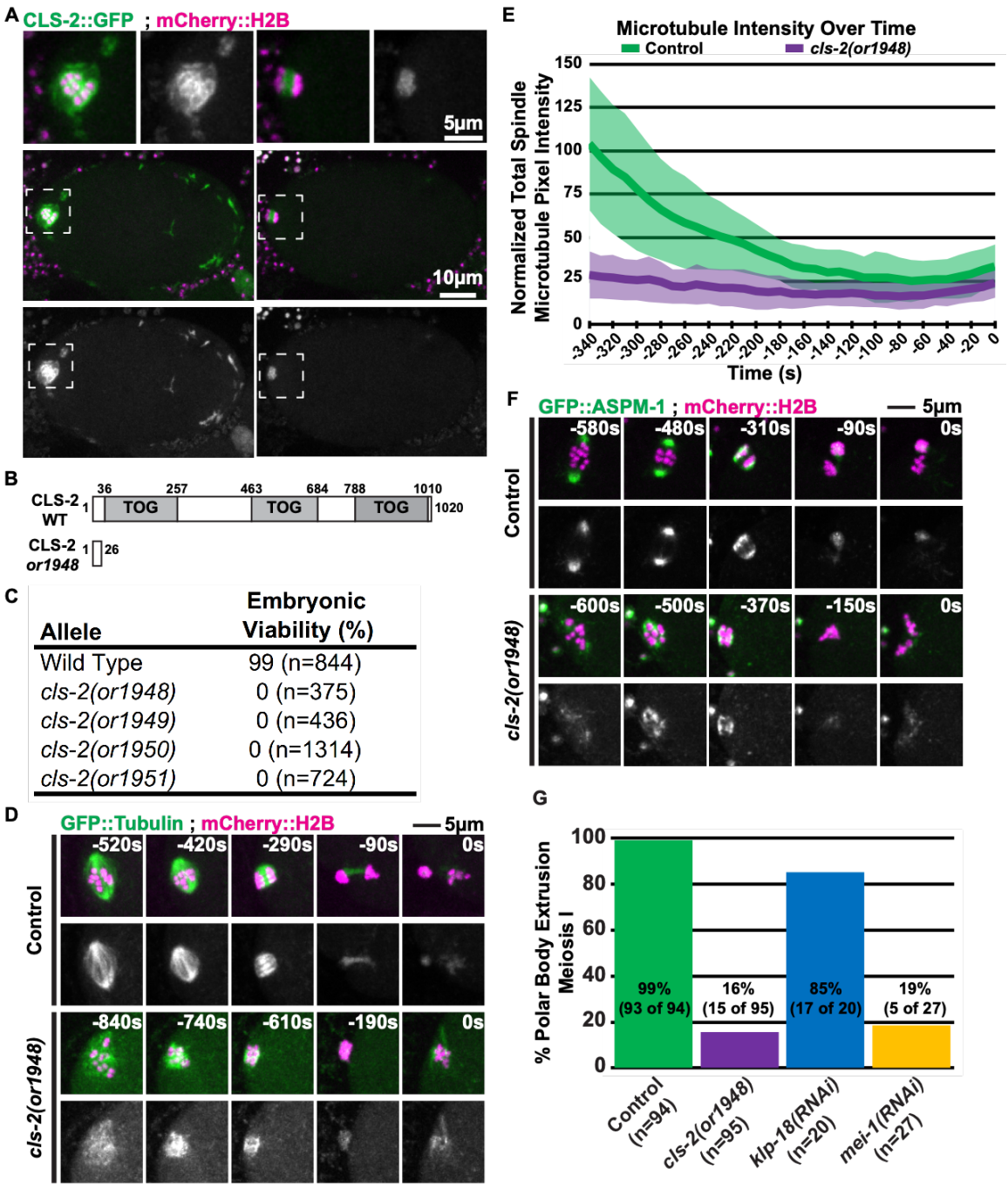


et al., 2019). These results suggest that CLS-2 might have roles not only at the oocyte meiotic spindle but also throughout the oocyte cortex.

Previous studies of CLS-2 requirements have used RNA interference (RNAi) or auxin-induced degradation of degron-tagged CLS-2 to reduce its function and have

emphasized its central spindle function. To more definitively assess its roles during oocyte meiosis, we used CRISPR/Cas9 to generate putative null alleles. Each of the four alleles we isolated contains small insertions or deletions that result in frame shifts and premature stop codons before the first TOG domain, likely making them null (Figure 4.2B, Supplemental Figure D.1). All are recessive, and homozygous mutant hermaphrodites exhibit fully penetrant embryonic lethality (Figure 4.2C). To investigate CLS-2 requirements, we have used the *cls-2(or1948)* allele, and hereafter we refer to oocytes from homozygous *cls-2(or1948)* hermaphrodites as *cls-2* mutants.

We first used *ex utero* live cell imaging with transgenic strains that express GFP fused to a β-tubulin (GFP::TBB-2) and mCherry fused to a histone H2B (mCherry::H2B) to examine microtubule and chromosome dynamics during meiosis I in control and *cls-2* mutant oocytes (Figure 4.2D; see Materials and methods in Appendix E). Control oocytes formed barrel shaped bipolar spindles that shortened and rotated to become perpendicular to the oocyte cortex prior to anaphase and polar body extrusion (n=19). Consistent with previous reports (Dumont et al., 2010; Laband et al., 2017; Pelisch et al., 2019), the meiosis I spindles in *cls-2* mutants were disorganized and lacked any obvious bipolarity, with chromosomes moving into a small cluster before failing to segregate (n=13). Furthermore, microtubule levels appeared to be reduced, and quantification of the integrated spindle microtubule intensity over time showed a substantial reduction in microtubule levels throughout meiosis I compared to control oocytes (Figure 4.2E), consistent with the established roles of CLASP family members in promoting microtubule stability (see Introduction). To assess when defects in meiosis I spindle assembly first appear in *cls-2* oocytes, we used *in utero* live cell imaging and observed

the early assembly of a normal cage-like microtubule structure that surrounded the oocyte chromosomes, followed by a rapid collapse of this microtubule structure to form an abnormally small cluster associated with the oocyte chromosomes (Supplemental Figure F.1) (n=5). To further examine spindle assembly in *cls-2* mutants, we also imaged meiosis I in oocytes from transgenic strains expressing an endogenous fusion of GFP to the pole marker ASPM-1 and mCherry::H2B (Figure 4.2F). As described previously (Connolly et al., 2015), multiple small GFP::ASPM-1 foci coalesced to form a bipolar spindle in control oocytes (n=14). In *cls-2* mutants, the GFP::ASPM-1 foci failed to coalesce to form two spindle poles but rather moved over time to form a single tight cluster of multiple small foci, and chromosomes again moved into a small cluster and failed to segregate (n=11). We conclude that CLS-2 plays an important role in promoting microtubule stability throughout meiosis I and is required early in bipolar spindle assembly and for chromosome segregation.

In addition to the extensive meiotic spindle defects, we also observed that *cls-2* mutants frequently failed to extrude a polar body at the end of meiosis I, consistent with previous reports (Dumont et al., 2010; Pelisch et al., 2019). Control oocytes regularly extruded a polar body at the end of meiosis I, as scored using transgenic strains expressing either GFP::H2B or mCherry::H2B and observing whether oocyte chromosomes remained extruded for the duration of live imaging (93 of 94 oocytes; Figure 4.2G). In contrast, polar body extrusion failed in about 84% of the *cls-2* mutant oocytes (80 of 95, Figure 2G). This finding suggests that CLS-2 might play a direct role in polar body extrusion, or that the spindle defects observed in *cls-2* mutants might indirectly disrupt extrusion.

**Polar Body Extrusion Defects in *cls-2* Mutants are Not Due to Absence of the Central Spindle-Associated Proteins AuroraB/AIR-2 or MgcRacGAP/CYK-4**

Because *cls-2* mutant oocytes fail to assemble a central spindle or segregate chromosomes and CLS-2::GFP localizes to the central spindle, and because the central spindle-associated protein AuroraB/AIR-2 and the centralspindlin component MgcRacGAP/CYK-4 are required for polar body extrusion (Schumacher et al., 1998; Dumont et al., 2010; Fabritius et al., 2011; Davis-Roca et al., 2017), we first considered whether the polar body extrusion defects might be due to a failure to localize central spindle proteins to the disorganized spindle microtubules in *cls-2* oocytes. To address this possibility, we used transgenic strains expressing GFP fusions to either AIR-2 or CYK-4 and examined their localization in control and *cls-2* mutant oocytes. As reported previously, both proteins localized to the central spindle during anaphase in control oocytes (Figures 4.3A and 4.3B) (n=12 GFP::AIR-2 and n=12 CYK-4::GFP). In *cls-2* mutants, despite the lack of spindle organization, both AIR-2 and CYK-4 localized to the spindle region (Figures 4.3A and 4.3B) (n=15 GFP::AIR-2 and n=11 CYK-4::GFP). While we cannot rule out the possibility that improper localization of AIR-2 and CYK-4 to the defective spindle might be responsible for the failure to extrude polar bodies in *cls-2* mutants, this failure cannot be explained by a simple loss of these central spindle-associated proteins from the mutant spindle microtubules.

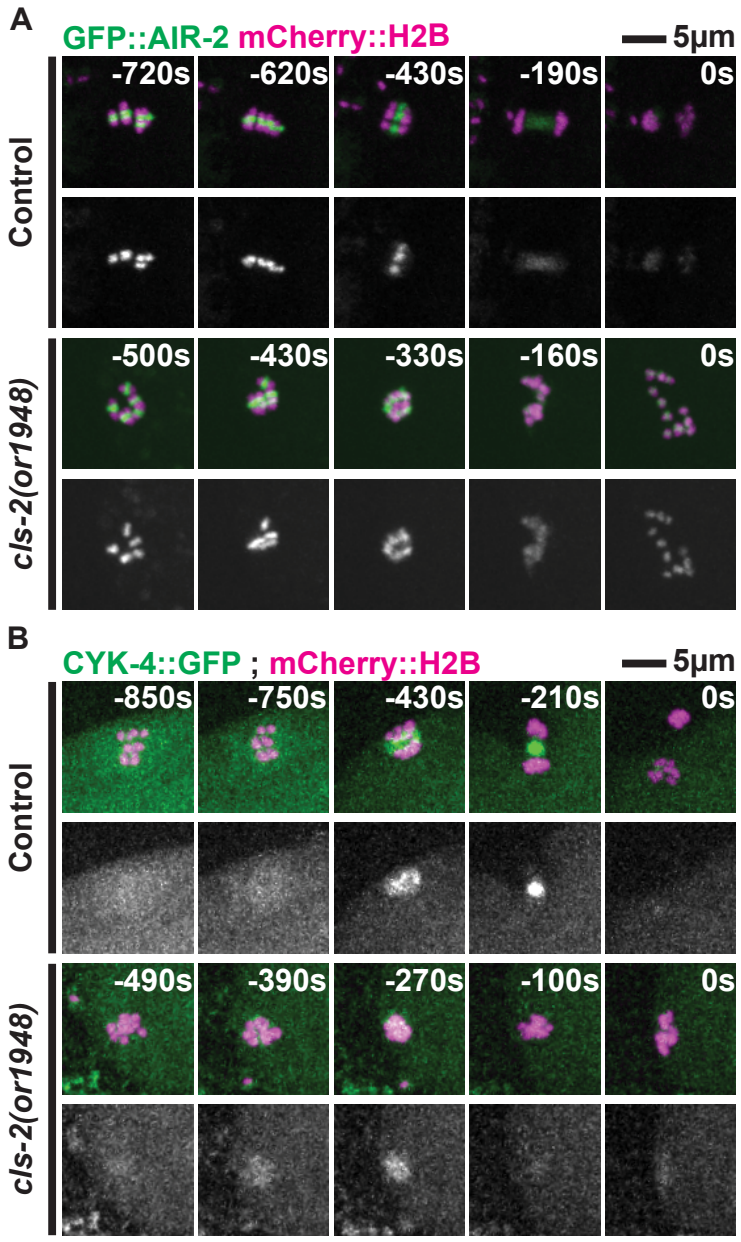


**Figure 4.3 – Central spindle proteins AIR-2 and CYK-4 still associate with spindle microtubules in *cls-2* mutant oocytes.**
Control and *cls-2* mutant oocytes expressing GFP::AIR-2 and mCherry::H2B (A) or GFP::CYK-4 and mCherry::H2B (B) during meiosis I.

## CLS-2 and MEI-1, but Not Spindle Bipolarity, are Required for Polar Body Extrusion

Because the relationship between spindle structure and polar body extrusion is unclear, we next took a comparative approach and also examined meiosis I polar body

extrusion after using RNAi to knock down either kinesin-12/KLP-18 or katanin/MEI-1. As illustrated schematically in Figure 4.1B, *klp-18* mutants assemble monopolar spindles while *mei-1* spindles are apolar, and both fail to segregate chromosomes (see Introduction). We first simply assessed whether polar body extrusion was successful, again using live imaging with transgenic strains expressing either GFP::H2B or mCherry::H2B fusions and scoring whether chromosomes were retained in polar bodies for the duration of imaging (Figure 4.2G). In *klp-18* mutants, chromosomes were successfully retained in a polar body in 15 of 20 oocytes. In contrast, after MEI-1 knockdown, chromosomes were extruded and retained in a polar body in only 5 of 27 oocytes. The absence of meiosis I polar body extrusion in *mei-1* mutant oocytes was surprising because *mei-1* mutants were originally described as typically having abnormally large polar bodies (Mains et al., 1990; Clandinin et al., 1993), but how often polar body extrusion succeeds or fails has not been reported. Our data indicate that meiosis I polar body extrusion usually fails and suggest that the abnormally large polar bodies observed in *mei-1* mutants result from defects in meiosis II (see Discussion).

Based on the frequent success of polar body extrusion in *klp-18* mutants, we conclude that spindle bipolarity and chromosome segregation are not required for polar body extrusion. Thus, the failed extrusions in *cls-2* and *mei-1* mutants are not simply due to an absence of spindle bipolarity or a failure to segregate chromosomes.

**Meiotic Spindle-Associated Furrows are Abnormal in *cls-2* and *mei-1* Mutant Oocytes**

To better understand the polar body extrusion defects in oocytes lacking CLS-2 or MEI-1, we next examined the spindle-associated membrane furrows that mediate polar body extrusion in transgenic strains expressing mCherry fused to a plasma membrane marker (mCherry::PH) and GFP::H2B (Figures 4.4A and 4.4B, Supplemental Figure F.2). In 9 of 16 control oocytes, we observed early membrane furrows that ingressed until they pinched together to encapsulate and extrude chromosomes into the first polar body. In 6 of 16 control oocytes we observed early membrane furrows that were not as clearly resolved in our imaging data but eventually led to polar body extrusion, and in one oocyte furrows were not obvious but a polar body was nevertheless extruded.

In contrast, we observed extensive spindle-associated membrane furrowing defects in *cls-2* mutants (Figures 4.4C-E, Supplemental Figures F.3 and F.4). In 7 of 19 oocytes we observed two furrows in cross-section that retracted before pinching together, one oocyte that formed two furrows that pinched together but failed late in polar body extrusion, and one oocyte that formed two furrows and successfully extruded a polar body (Supplemental Figure F.3). One of 19 oocytes appeared to form three spindle-associated furrows in cross-section and extruded a polar body (Supplemental Figure F.3). In 7 of 19 oocytes we observed only a single visible spindle-associated furrow in cross-

**Figure 4.4 – Spindle-associated membrane furrowing during meiosis I in control and mutant oocytes**

Images show projections of five focal planes encompassing the chromosomes during meiosis I in oocytes expressing an mCherry fusion to a PH domain to mark the plasma membrane using sum projections and GFP::H2B using maximum projections. Representative examples of control (A, B), *cls-2* mutant (C-E), *klp-18(RNAi)* (F, G) and *mei-1(RNAi)* (H, I) oocytes. Polar body extrusion failed in C-E and H, and was successful in all others. T = 0s corresponds to the timepoint immediately before cortical furrowing begins. See text for details.

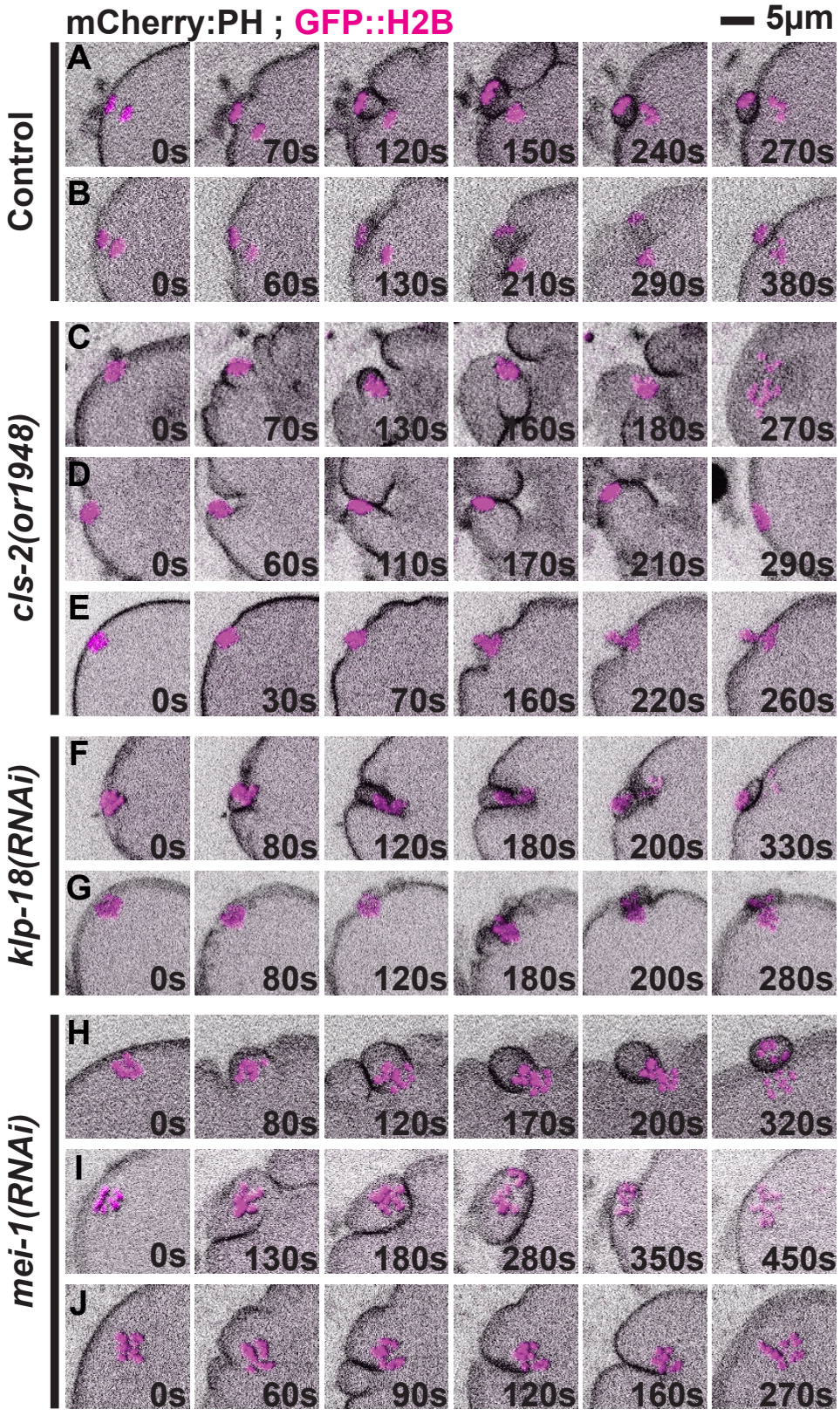


section that ingressed either to one side of, or directly toward the oocyte chromosomes

(Figure 4.4D, Supplemental Figure F.4), suggesting that the contractile ring collapsed into a more linear ingressing structure rather than maintaining a ring-like shape. Finally, in one oocyte the membrane dynamics were indistinct, but chromosomes were extruded into a polar body (Figure 4.4E), and in one oocyte there was no obvious spindle-associated furrowing and polar body extrusion failed (Supplemental Figure F.4).

In oocytes depleted of *klp-18*, we observed furrows that more nearly resembled those in control oocytes (Figures 4.4F and G, Supplemental Figure F.5). In 4 of 10 oocytes, we observed two furrows in cross-section that ingressed more deeply and then pinched together (Figure 4.4F), and only 1 of these 4 failed in polar body extrusion. In 6 of 10 oocytes, we observed shallow furrows adjacent to the oocyte chromosomes (Figure 4.4G), and only 1 of these 6 failed to extrude a polar body.

After MEI-1 knockdown, we observed furrows that initially resembled those in control oocytes but were more widely spaced and often failed late during constriction (Figures 4.4H-J, Supplemental Figure F.6). In 2 of 11 oocytes, we observed two furrows in cross-section that ingressed and pinched together to extrude a polar body (Figure 4.4H). In 3 of 11 oocytes two furrows ingressed and pinched together but then regressed and released chromosomes back into the oocyte cytoplasm (Figure 4.4I). In 5 of 11 oocytes two furrows ingressed but retracted before pinching together and failed in polar body extrusion (Figure 4.4J), and finally in 1 of 11 oocytes we observed only a single spindle-associated furrow in cross-section that failed to extrude a polar body.

To summarize, in *klp-18* mutant oocytes we observed spindle-associated furrows that usually encapsulated chromosomes and extruded polar bodies, although the oocyte chromosomes were often in close proximity to the membrane with furrows that were

shallow and difficult to detect. In *cls-2* and *mei-1* mutants, meiosis 1 polar body extrusion frequently failed but we observed distinct defects. While membrane furrowing initially appeared normal but eventually failed in most *mei-1* mutant oocytes, *cls-2* oocytes often appeared abnormal early in furrow ingression and exhibited more severe defects as extrusion attempts progressed.

**Polar Body Contractile Ring Dynamics are More Severely Defective in the Absence of CLS-2 than in *klp-18* or *mei-1* Mutant Oocytes**

We next examined assembly and ingression of the contractile ring during oocyte meiosis I, using live cell imaging with transgenic strains expressing both a GFP fusion to the non-muscle myosin II NMY-2 and mCherry::H2B. In 11 of 11 control oocytes, NMY-2::GFP foci initially assembled into discontinuous but discernible rings over the membrane proximal pole, after spindle rotation and before extensive chromosome segregation, and then became more continuous and prominent as they ingressed and constricted between the segregating chromosomes to extrude polar bodies (Figure 4.5A, Supplemental Figure F.7).

In *cls-2* mutant oocytes, the assembly and stability of NYM-2::GFP contractile ring structures were severely defective (Figure 4.5B, Supplemental Figure F.8). In 7 of 11 oocytes, fragmented or partial contractile rings assembled and 6 of these oocytes failed to extrude a polar body, while 3 of 11 oocytes formed abnormal assemblies of NMY2::GFP that were more linear and not ring-like, although 2 of these extruded a polar body.

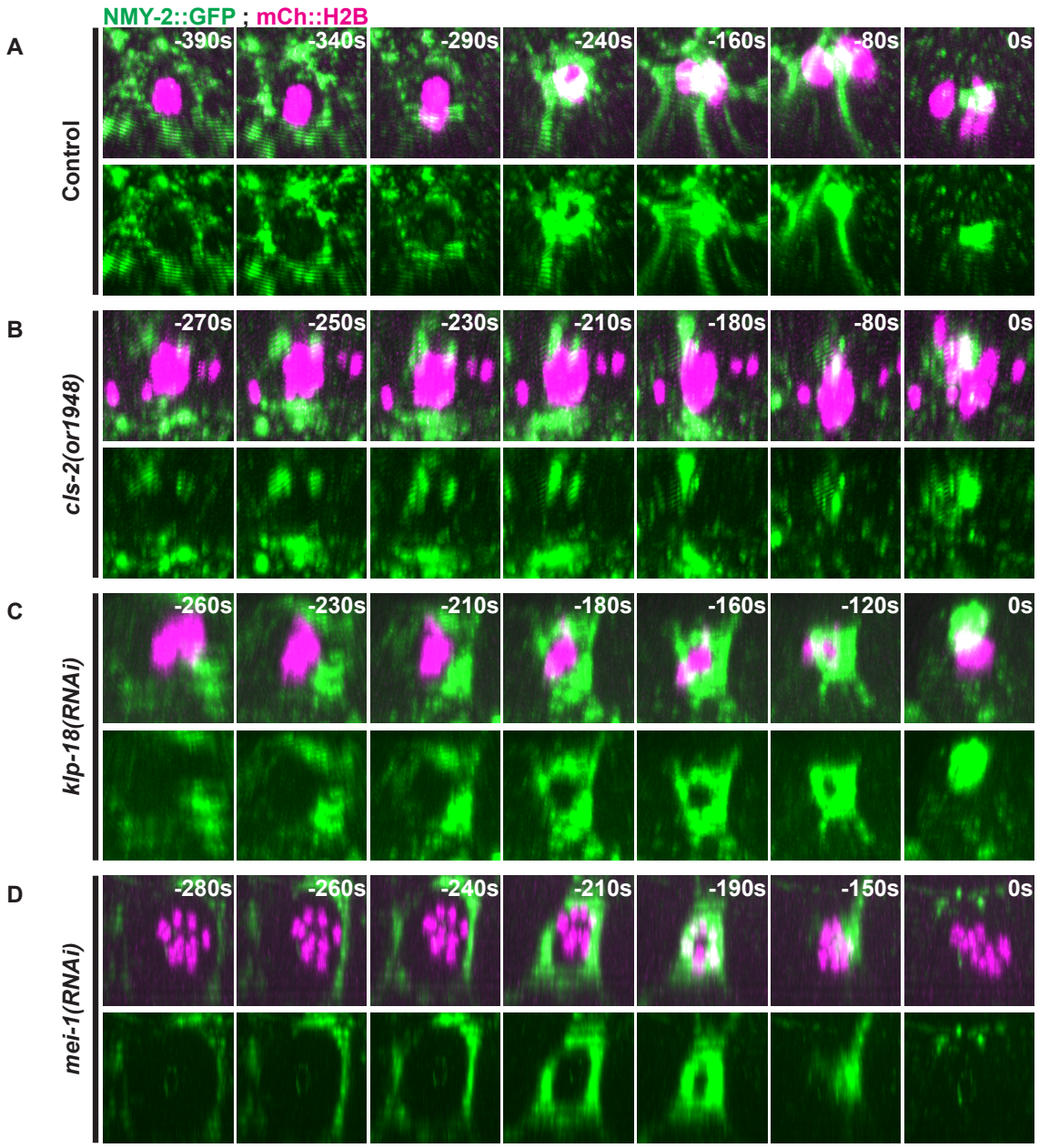


**Figure 4.5 – Contractile ring non-muscle myosin NMY-2 dynamics during meiosis I in control and mutant oocytes.**
Three-dimensionally projected and rotated images of control (A), *cls-2* mutant (B), *klp-18(RNAi)* (C), and *mei-1(RNAi)* (D) oocytes expressing NMY-2::GFP and mCherry::H2B. Z-stacks were rotated as to look down on contractile ring assembly and dynamics over time.

Finally, 1 of 11 oocytes formed a relatively normal looking contractile ring that extruded a polar body. The fragmented or partial contractile rings observed in *cls-2* mutants often collapsed into single bright foci or bands during constriction.

Contractile ring assembly and dynamics appeared much more normal in *klp-18* mutant oocytes (Figure 4.5C, Supplemental Figure F.9). In 10 of 10 oocytes after KLP-18 knockdown, NMY-2::GFP foci assembled into rings that ingressed and constricted with dynamics similar to those observed in control oocytes, and in 9 of the 10 oocytes chromosomes were stably extruded into polar bodies.

In MEI-1 knockdown oocytes, ring assembly and ingression were much more normal compared *to cls-2* mutants, but we nevertheless observed a range of later defects and eventual failures to extrude polar bodies (Figure 4.5D, Supplemental Figure F.10). In 11 of 13 oocytes, the NMY-2::GFP rings that initially formed were larger in diameter compared to control oocytes, and in 3 of these 11 oocytes the rings constricted and successfully extruded a polar body. In another 5 of these 11 oocytes, the rings constricted extensively but ultimately regressed and failed at polar body extrusion, while in 3 the rings ingressed and only constricted partially before regressing and failing to extrude polar bodies. Finally, in 2 of 13 oocytes, ring assembly and ingression were more defective and polar body extrusion failed.

To further characterize the polar body extrusion defects in *cls-2* mutants, we also examined ring assembly and dynamics in transgenic strains expressing mNeonGreen fused to the anillin ANI-1 (mNG::ANI-1), which is dispensable for assembly of the actomyosin contractile ring but required for its conversion from a ring to a tube during

---

**Figure 4.6 – Contractile ring anillin ANI-1 and non-muscle myosin NMY-2 dynamics during meiosis I in control and *cls-2* mutant oocytes.**
Three-dimensionally projected and rotated images of control and *cls-2* mutant oocytes expressing mNeonGreen::ANI-1 and mCherry::H2B (A) or NMY-2::mKate2, mNeonGreen::ANI-1, and mCherry::H2B, with overlays shown in top row for each set. Z-stacks were rotated so as to look down on contractile ring assembly and dynamics over time.

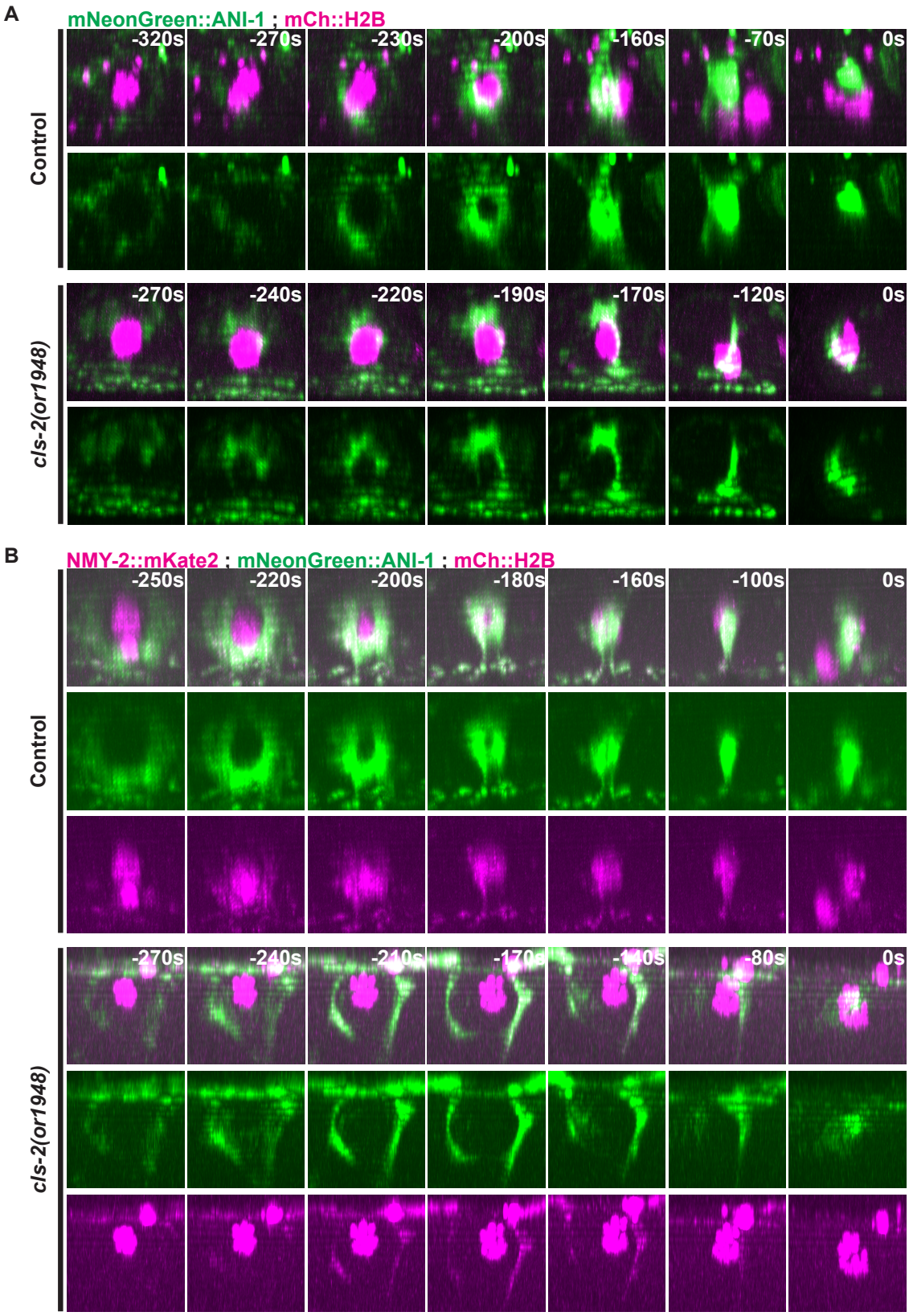


constriction (Dorn et al., 2010; Piekny et al., 2010), and mCherry::H2B (Figure 4.6A). In

10 of 10 control oocytes, mNG::ANI-1 assembled into contractile rings that ingressed and constricted between segregating chromosomes to extrude a polar body, while in 10 of 10 *cls-2* oocytes a fragmented contractile ring structure formed and failed to extrude a polar body. We also used two-color live imaging to examine NMY-2::mKate2 and mNG::ANI-1 simultaneously, and observed that these two contractile ring components were co-localized in both control and *cls*-2 mutant oocytes (Figure 4.6B) (n=11 control, n=13 *cls-2(or1948)*). We conclude that CLS-2 is required for proper ring assembly and ingression dynamics of not only NMY-2 but also ANI-1.

**CLS-2 Negatively Regulates Membrane Ingression Throughout the Oocyte Cortex During Meiosis I**

Global contraction of the oocyte actomyosin cortex has been proposed to promote polar body extrusion by generating a hydrostatic cytoplasmic force that (i) produces an out-pocketing of the actomyosin depleted membrane inside the meiotic contractile ring, and (ii) pushes the spindle partially into the extruded membrane pocket (see Introduction). To explore the relationship between spindle structure, global cortical contractility and polar body extrusion, we next examined membrane ingressions throughout the oocyte cortex during meiosis I in control and mutant oocytes, using transgenic strains expressing mCherry::PH and GFP::H2B fusions. To document these membrane ingressions, we used temporal overlays of a single central z-plane to portray simultaneously the membrane position at all time points throughout the period of global cortical furrowing. In control oocytes, we observed the spindle-associated furrows and a

small number of additional furrows along the oocyte cortex (Figure 4.7A, Supplemental Figure F.11) (n=16).

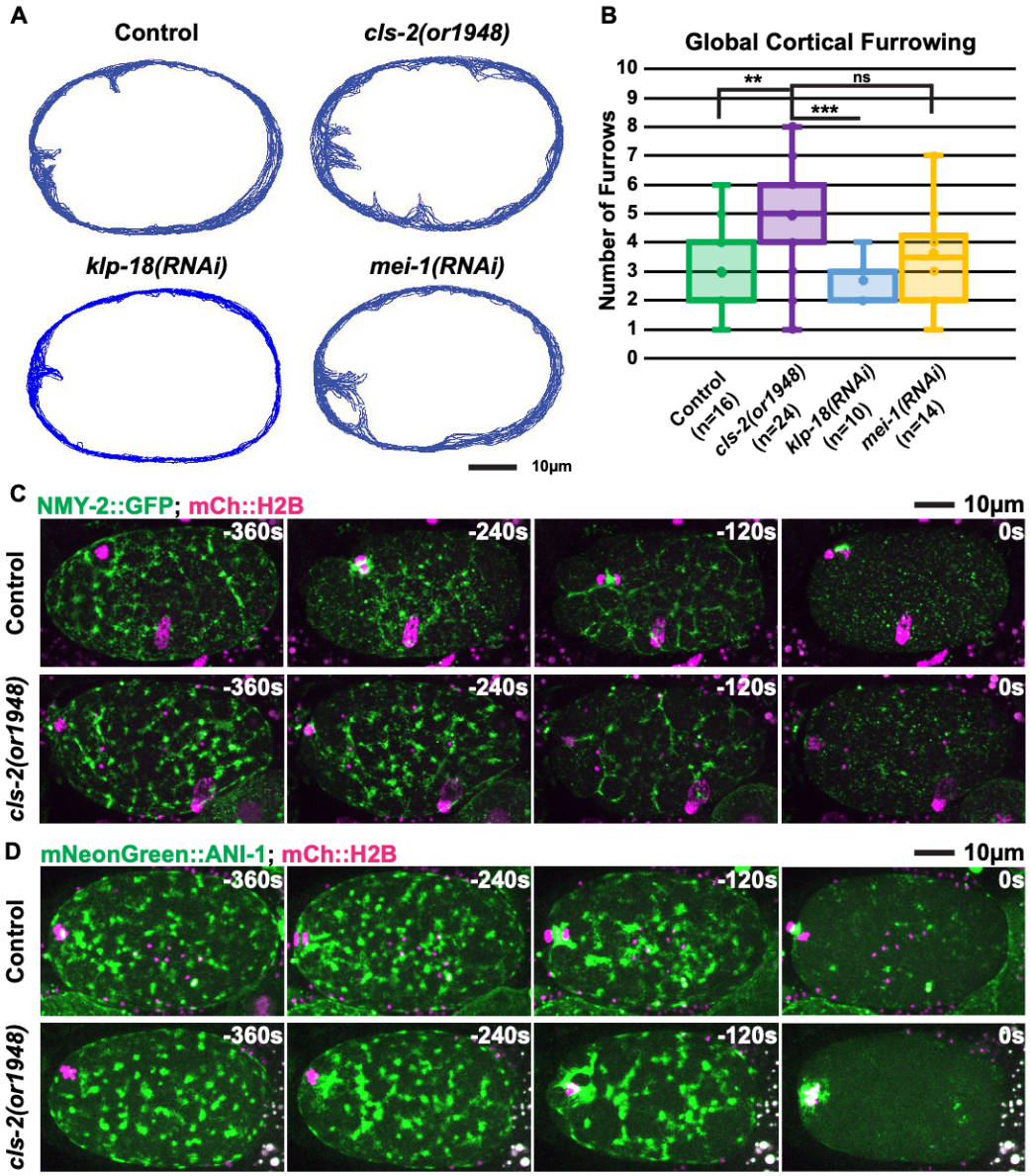


**Figure 4.7 – Membrane ingressions throughout the oocyte cortex during meiosis I in control and mutant oocytes**

(A) Membrane temporal overlays for control, *cls-2* mutant, *klp-18(RNAi)*, and *mei-1(RNAi)* oocytes representing the membrane positions of a single focal plane during the period of meiosis I global cortical furrowing for a single oocyte of each genotype. (B) Quantification of the number of global cortical furrows in control and mutant oocytes (see Materials and methods). t-Test results: Control vs *cls-2(or1948)* p = 0.0014 (**), *cls-2(or1948)* vs *klp-18(RNAi)* p = 3.14E-5 (***), *cls-2(or1948)* vs *mei-1(RNAi)* p = 0.054 (ns). (C and D) *C*ontrol and *cls-2* mutant oocytes expressing (C) NMY-2::GFP and mCherry::H2B or (D) mNeonGreen::ANI-1 and mCherry::H2B.

In contrast, *cls-2* mutant oocytes exhibited more extensive cortical furrowing compared to control oocytes (n=24), while oocytes depleted of either KLP-18 or MEI-1 more nearly resembled control oocytes (Figure 4.7A, Supplemental Figures F.12 and F.13) (n=10 *klp-18(RNAi)* and n=14 *mei-1(RNAi)*). Quantification of global cortical furrowing showed that *cls-2* oocytes had significantly more furrows compared to control and *klp-18* oocytes (Figure 4.7B). We conclude that CLS-2 negatively regulates global cortical furrowing, and we suspect that the CLS-2::GFP patches detected throughout the oocyte cortex are responsible for this regulation (Figure 4.2A, Supplemental Figure F.1; see Discussion).

We next examined the dynamics of the cortical actomyosin cytoskeleton, which mediates the furrowing that occurs throughout the oocyte cortex during polar body extrusion. In control oocytes, NMY-2 and ANI-1 localized to dynamic patches throughout the oocyte cortex during meiosis I contractile ring assembly and ingression, and then dissipated late in anaphase when global cortical furrowing ends (Figures 4.7C and 4.7D, Supplemental Figures F.14 and F.15) (n=11 NMY-2::GFP, n=10 mNG::ANI-1). To determine if the increased global cortical furrowing in *cls-2* oocytes is caused by an increase in NMY-2 or ANI-1 patch size or duration, we examined the dynamics of NMY-2::GFP and mNG::ANI-1 and observed dynamics similar to those in control oocytes (Figures 4.7C and 4.7D, Supplemental Figures F.16-F.18) (n=11 NMY-2::GFP, n=10 mNG::ANI-1), and we did not detect any statistically significant difference in the area occupied by the cortical NMY-2::GFP patches throughout the period of global cortical furrowing and polar body extrusion. These data suggest that the excess global cortical furrowing observed in *cls-2* oocytes is not due to altered NMY-2 or ANI-1 patch

dynamics. While the increased global cortical furrowing in CSNK-1 knockdown oocytes is associated with altered NMY-2 and ANI-1 cortical patch dynamics and with extrusion of the entire meiosis I spindle into polar bodies (Flynn et al., 2017), the increased global cortical furrowing in *cls-2* mutants does not correlate with altered cortical patch dynamics and is instead associated with polar body extrusion failure. Thus, the relationship between global cortical furrowing and polar body extrusion is complex and requires further investigation (see Discussion).

**Discussion**

Remarkably little is known about the relationship between spindle structure and contractile ring assembly and constriction during oocyte meiotic cell division. To gain insight into the cues that influence contractile ring dynamics during polar body extrusion, we have examined contractile ring assembly and constriction in three different *C. elegans* spindle assembly-defective mutants. Our results indicate that the *C. elegans* CLASP family member CLS-2 is required not only for assembly of a bipolar meiosis I spindle and for chromosome segregation, but also for an early stage in oocyte meiosis I contractile ring assembly or stability. This requirement for CLS-2 is not due simply to a failure in assembling bipolar spindles or to a lack of chromosome segregation, because *klp-18/kinesin-12* mutant oocytes formed monopolar spindles and failed to segregate chromosomes but did assemble stable contractile rings that usually extruded chromosomes into a polar body. We have further shown that *mei-1/katanin* mutant oocytes, which assemble apolar and disorganized oocyte meiosis I spindles, also usually failed to extrude polar bodies. However, while CLS-2 was required early for contractile

ring assembly or stability, MEI-1 appears to be required to limit the initial diameter of the contractile ring and for later steps in ring constriction. Finally, we also observed increased global cortical furrowing during meiosis I in *cls-2* mutant oocytes but not in *klp-18* or *mei-1* mutants, raising the possibility that proper regulation of cortical membrane ingressions throughout the oocyte may be required for contractile ring assembly or stability during polar body cytokinesis. Our results highlight the value of exploring the relationship between mutant oocyte meiotic spindle structures and polar body contractile ring dynamics.

**Using Spindle Assembly Defective Mutants to Explore Contractile Ring Dynamics During Oocyte Polar Body Extrusion**

While the requirements for several factors that control oocyte meiotic spindle assembly in *C. elegans* have been described (Dumont et al., 2012; Severson et al., 2016; Mullen et al., 2019), the impact of the resulting spindle assembly defects on polar body extrusion has remained largely unexplored. Indeed, anecdotal observations have suggested that polar body extrusion can occur even in mutants with severe oocyte spindle assembly defects. For example, reducing the function of the microtubule severing complex katanin, comprised of MEI-1 and -2 in *C. elegans*, results in severely defective apolar spindles that have greatly reduced levels of microtubules and fail to organize or segregate chromosomes and yet often produce abnormally large polar bodies. However, the dynamics of contractile ring assembly, ingression and constriction in *mei-1/katanin* mutants has not been directly examined. Similarly, mutant oocytes lacking the kinesin-12 family member KLP-18 assemble monopolar spindles that fail to segregate chromosomes

but often produce zygotes that completely lack an egg pronucleus, indicating that all of the oocyte chromosomes are sometimes extruded into polar bodies, but again the process of polar body extrusion in *klp-18* mutants has not been directly examined. In mouse oocytes, DNA-coated beads have been shown to promote the assembly of a polar body-like cortical protrusion, which requires the small GTPase Ran that mediates chromatin signaling and, if allowed to assemble a bead-associated spindle structure, can lead to successful extrusion (Deng et al., 2007; Deng et al., 2009). However, knockdown of the *C. elegans* Ran family member RAN-1 does not prevent chromosome segregation or polar body extrusion (Askjaer et al., 2002; Chuang et al., 2020), suggesting that chromatin cues do not mediate contractile ring assembly. Moreover, meiotic spindles that fail to translocate to the oocyte cortex induce the formation of membrane furrows that ingress deeply toward the spindle (Fabritius et al., 2011), and *C. elegans* mutant oocytes lacking central spindle proteins have been shown to produce abnormally large contractile rings that often fail to extrude chromosomes into a polar body (Fabritius et al., 2011), suggesting that the oocyte meiotic spindle does influence ring assembly and function.

Given the critical roles of astral and central spindle microtubules in promoting the assembly of a contractile ring during mitosis (Green et al., 2012; Basant et al., 2018; Pintard et al., 2019), the distinct dynamics and geometry of oocyte meiotic contractile rings compared to mitotic contractile rings (Figure 4.1A), and the indications that oocyte meiotic spindles influence contractile ring dynamics in *C. elegans,* we have characterized polar body extrusion in *C. elegans* mutants that are severely defective in oocyte spindle assembly. We were first motivated to do so based on our observation that *cls-2* oocytes frequently failed to extrude chromosomes, in contrast to anecdotal and indirect

observations that other *C. elegans* mutants with severe oocyte meiotic spindle assembly defects can extrude chromosomes into polar bodies.

Because *cls-2* mutant oocytes failed to assemble bipolar spindles or segregate chromosomes, we also examined polar body extrusion in *klp-18/kinesin-12* mutant oocytes that assemble monopolar spindles and also fail to segregate chromosomes (Wignall et al., 2009; Connolly et al., 2014; Wolff et al., 2016). In contrast to *cls-2* mutants, in which contractile ring assembly or stability and membrane ingression were severely defective, contractile ring assembly and ingression appeared much more normal in *klp-18* mutant oocytes and chromosomes were usually extruded into a polar body. We conclude that the defects in *cls-2* mutant oocytes are not due a failure to assemble a bipolar spindle or to segregate chromosomes, but rather reflect a more specific requirement for CLASP/CLS-2.

A specific requirement for CLS-2 is further supported by our analysis of oocyte meiotic contractile ring assembly and dynamics in *katanin/mei-1* oocytes, which assemble spindles that lack any polarity and completely fail to organize the dispersed oocyte chromosomes throughout meiosis I (Connolly et al., 2014; K. McNally et al., 2014; Joly et al., 2016). Furthermore, similar to *cls-2* oocytes, microtubule levels are substantially reduced in *mei-1* mutant oocytes (Srayko et al., 2006). Nevertheless, stable contractile rings usually formed in *mei-1* mutant oocytes, although the rings appeared somewhat larger in diameter than in control oocytes, and we frequently observed extensive furrow ingressions that often enclosed the oocyte chromosomes but usually failed to complete constriction and regressed late in cytokinesis. We conclude that contractile rings can assemble and remain stable until late in polar body extrusion, even

when oocyte meiotic spindle assembly is at least as severely defective as in *cls-2* mutant oocytes.

**Roles for CLS-2 and MEI-1 in Contractile Ring Assembly and Constriction**

While our analysis indicates that CLS-2 is required early for the assembly or stability of the oocyte meiosis I contractile ring, we do not know if the defects reflect a direct or indirect requirement, or how CLS-2 functions at a molecular level to promote polar body extrusion. Consistent with studies showing that CLASP family members associate with microtubules and promote microtubule stability (Al-Bassam et al., 2010; Patel et al., 2012; Byrnes et al., 2017; Aher et al., 2018), *cls-2* mutant oocytes have reduced levels of spindle microtubules throughout meiosis I. Moreover, *cls-2* mutant oocytes fail to assemble bipolar spindles or segregate chromosomes, with ASPM-1 pole foci and chromosomes instead converging into a small amorphous cluster. While the contractile ring assembly defects we observed could be an indirect consequence of aberrant spindle assembly and structure, the more normal contractile ring dynamics observed in both *klp-18* and *mei-1* mutant oocytes suggest that CLS-2 has a more specific role in mediating ring assembly or stability. Notably, human CLASP proteins have been shown to associate with actin filaments and may cross-link microtubules and filamentous actin (Tsvetkov et al., 2007). Furthermore, mutations in the *Drosophila* CLS-2 ortholog Orbit/Mast cause spermatocyte cytokinesis defects that appear to result from a loss of central spindle microtubules that normally promote assembly of the contractile ring (Inoue et al., 2004). Thus, it is possible that the contractile ring assembly or stability

defects in *cls-2* mutants are due to a loss of microtubule and microfilament interactions that require CLS-2.

Consistent with a role for CLS-2 in bridging spindle microtubules and cortical actin filaments, we observed CLS-2::GFP throughout the oocyte spindles at the time when contractile ring assembly begins. However, at the time that ring assembly begins, very few spindle microtubules have been observed in close proximity to the cell cortex (Crowder et al., 2015). Biochemical studies of CLS-2 and its potential interactions with microtubules and actin filaments, along with higher resolution imaging of CLS-2, spindle microtubules and cortical microfilaments in oocytes may improve our understanding of how CLS-2 promotes the proper assembly and stability of the contractile ring during polar body extrusion.

Contractile ring dynamics during meiosis I were more normal after *mei-1* RNAi knockdown, but the furrows nevertheless often regressed and polar body extrusion usually failed. Previous studies have shown that partial loss of function mutations in *mei-1* result in abnormally large second polar bodies that are produced after meiosis II, as a result of decreased microtubule severing that is required for complete disassembly of the oocyte meiosis II spindle (Han et al., 2009; Gomes et al., 2013). Our results provide the first systematic examination of polar body extrusion during meiosis I after depletion of katanin/MEI-1, and it is possible that the late failures in polar body cytokinesis that we observed also reflect a requirement for microtubule severing. Alternatively, similar defects are observed in oocytes lacking the centralspindlin components CYK-4 and ZEN-4 (Schumacher et al., 1998; Dumont et al., 2010; Fabritius et al., 2011; Davis-Roca et al., 2017), and it is possible that central spindle proteins are mis-regulated after MEI-1

knockdown. Further investigation of MEI-1 and its interactions with central spindle proteins may improve our understanding of this late requirement for MEI-1 during polar body extrusion.

**Negative Regulation of Oocyte Global Cortical Dynamics and its Relationship to Polar Body Extrusion**

In addition to the defects in contractile ring dynamics during polar body extrusion in *cls-2* mutant oocytes, we also observed increased membrane ingressions throughout the oocyte cortex. Furthermore, we detected CLS-2::GFP in small patches throughout the cortex in control oocytes. These patches were present early in meiosis I but dissipated before anaphase chromosome segregation, prior to initiation of the membrane ingressions that occur during anaphase in wild-type oocytes. While the excessive global furrowing in *cls-2* mutants may result from loss of the cortical CLS-2 patches, if so then CLS-2 may act prior to the initiation of global cortical furrowing to down-regulate the ingressions. Alternatively, low levels of cortical CLS-2 that were not detected with our imaging methods might contribute to this negative regulation of membrane furrowing throughout the oocyte cortex.

The molecular mechanism by which cortical CLS-2 patches might down-regulate global membrane ingression during oocyte meiosis I is not clear. Our observations that NMY-2 and ANI-1 dynamics were not altered in *cls*-2 oocytes suggests that the increased membrane ingression is not be due to an increase in cortical actomyosin contractility but perhaps is an indirect consequence of defects in the stiffness of the oocyte cortex. The observations that CLASP orthologs can interact with both cortical microtubules and actin

filaments may be consistent with such a role for CLS-2 (Tsvetkov et al., 2007). Moreover, oocyte polar body extrusion has been described as a bleb-like process, with local weakening of the actomyosin cytoskeleton inside the contractile ring promoting an out-pocketing of the membrane to form a polar body (Fabritius et al., 2011; Maddox et al., 2012). Studies of bleb formation in other cellular contexts have shown that microtubule destabilization can result in bleb formation (Hagmann et al., 1999; Tinevez et al., 2009; Sugiyama et al., 2015). Thus, it is possible that loss of CLS-2 promotes membrane ingressions throughout the cortex due to destabilization of cortical microtubules and a corresponding decrease in cortical stiffness, although we have not yet detected statistically significant differences in the levels of cortical microtubules in *cls-2* oocytes (data not shown). Alternatively, mammalian CLASPs mediate linkage between microtubule plus ends and the cell cortex (Mimori-Kiyosue et al., 2005; Lansbergen et al., 2006), and such interactions might also influence cortical stiffness in *C. elegans* oocytes. Other factors, including the kinesin-13 family member KLP-7 and the TOG domain protein and XMAP215 ortholog ZYG-9, have been shown to down-regulate cortical microtubule levels during oocyte meiotic cell division in *C. elegans* (Gigant et al., 2017; Chuang et al., 2020). Further investigation both of microtubule and actomyosin dynamics, using higher resolution light microscopy methods, and studies of how microfilament and microtubule regulators interact to influence oocyte cortical dynamics, may improve our understanding of how global cortical contractility and membrane dynamics influence contractile ring dynamics during polar body extrusion.

Comparing the consequences of reducing the functions of the casein kinase CNSK-1 and CLS-2 indicates that the relationship between global cortical dynamics and

polar body extrusion is complex. CSNK-1 also limits membrane ingressions throughout the oocyte cortex during meiosis I but appears to do so through negative regulation of actomyosin dynamics, and CSNK-1 knockdown often results in extrusion of the entire meiotic spindle and all of the oocyte chromosomes into the first polar body (Flynn et al., 2017). This outcome has led to a model in which global cortical contraction generates a hydrostatic cytoplasmic force that promotes an out-pocketing of the plasma membrane as the spindle is pushed through the contractile ring and into the forming polar body. While such a mechanism may operate, it also is clear that the contractile ring and associated plasma membrane ingress substantially prior to constricting roughly midway along the axis of the spindle during polar body extrusion. These dynamics suggest that the spindle and the contractile ring interact to promote furrow ingression and constriction. Moreover, the increased global membrane ingressions in *cls-2* oocytes do not appear to result from increased actomyosin contractility and are accompanied by defects in ring assembly or stability and a frequent failure to extrude a polar body. Thus, it appears that negative regulation of global cortical membrane ingression during oocyte meiotic cell division can both promote and prevent the extrusion of chromosomes into polar bodies. These different outcomes presumably reflect differences in how CSNK-1 and CLS-2 influence the cortical cytoskeleton and its dynamics. One possible explanation for these different outcomes is that a loss of cortical stiffness in *cls-2* oocytes might allow for increased membrane ingression throughout the oocyte cortex, while at the same time disrupting contractile ring assembly and/or preventing any increase in the hydrostatic cytoplasmic force that has been proposed to push the meiotic spindle partly into the budding polar body (Flynn et al., 2017). Further investigation of cortical cytoskeleton dynamics, and the

interactions of factors that regulate these dynamics during polar body extrusion, should improve our understanding of this poorly understood but fundamentally important biological process.

# CHAPTER V

# CONCLUSIONS AND FUTURE DIRECTIONS

*This chapter contains unpublished material written by A.J.S.

## Summary

Chapter I introduced oocyte meiosis, explaining how it differs from both mitosis and sperm meiosis in regard to both the spindle assembly and cytokinetic processes. A brief overview was given regarding what is currently known about *C. elegans* oocyte meiotic spindle assembly, chromosome segregation, and polar body cytokinesis. This chapter also presented numerous remaining questions relating to oocyte meiosis, including how oocytes nucleate microtubules, how chromosome structure influences chromosome segregation, and how oocyte meiotic spindle assembly and chromosome segregation relates to polar body contractile ring assembly and dynamics.

Chapter II shed new light on the process by which oocytes nucleate microtubules and assemble spindles in the absence of centrosomes, and the influence of these processes on chromosome segregation. This work indicates that the nuclear lamina is required for the assembly of the microtubule cage structure during meiosis I. Additionally, this work showed that while not essential for oocyte meiotic spindle assembly, γ-tubulin/TBG-1 and the small GTPase RAN-1 both influence oocyte microtubule abundance and spindle assembly dynamics. This finding suggests that these two mechanisms for microtubule nucleation could work in parallel to one another during oocyte meiosis. The microtubule polymerase ZYG-9/XMAP215 is required for limiting the microtubule cage structure to

the nuclear periphery during the earliest stages of spindle assembly, as well as for the coalescence and stability of the meiotic spindle poles. Consistent with previous reports based on RNAi, the kinesin-14 family members KLP-15 and KLP-16 were shown to be required for microtubule bundling, and the coalescence of early spindle pole foci. In total these results add a great deal to our understanding of the processes and molecular players required for *C. elegans* oocytes to assemble meiotic spindles and bring us closer to answering questions related to how oocytes nucleate microtubules and organize them into a functional spindle structure.

Chapter III examined the relationship between chromosome structure itself, through the use of novel *C. elegans* mutants that have supernumerary crossover formation, on chromosome segregation and, to a lesser extent, meiotic spindle assembly. This work suggests that limitation of crossover formation in *C. elegans* oocytes helps to promote chromosome alignment and segregation. Chromosomes with excess crossovers frequently formed chromatin bridges between the segregating chromosomal masses, and our data show that the nuclease *lem-3* can assist in resolving these chromatin bridges.

Chapter IV delved into the final stages of the meiotic division process, and investigated at the relationship between meiotic spindle assembly, chromosome segregation, and polar body extrusion through detailed examination of the polar body extrusion process in known spindle assembly defective mutants - CLS-2/CLASP, KLP-18/kinesin-12, and MEI-1/katanin. This work showed that oocyte meiotic spindle bipolarity and chromosome segregation are not required for polar body extrusion, but the spindle assembly proteins MEI-1 and CLS-2 are, albeit in different fashions. MEI-1 is required for late polar body contractile ring constriction and scission, while CLS-2 is

required for the early assembly or stability of polar body contractile rings, as well as for negative regulation of membrane ingression throughout the oocyte cortex. The excess membrane ingression observed in *cls-2* mutants suggests that regulation of cortical contractility or membrane ingression may be required for the assembly or stability of polar body contractile rings. Our results also highlighted the value of exploring the relationship between oocyte meiotic spindle structure and cytokinetic contractile ring dynamics. While the findings presented in Chapters II-IV have provided new answers and insights into the oocyte meiotic division process, they have also left new and interesting questions to be explored.

**Future Directions**

Two very broad questions that remain are how exactly microtubule nucleation occurs, and how are microtubules regulated throughout the meiotic division process? Findings presented in Chapter II suggest that microtubule nucleation in *C. elegans* oocytes does not happen through a single microtubule nucleation pathway (ex. either via γ-tubulin or chromosome-derived RanGTP-based nucleation), and that the nucleation and regulation of microtubules in the absence of centrosomes is a complex process. Additionally, findings in both Chapter II and Chapter IV suggest that this regulation of microtubules, not only in the meiotic spindle but also along the oocyte cortex, may influence not only the spindle assembly and chromosome segregation process, but also the ability for oocytes to undergo polar body extrusion as well. Is it possible then that microtubules are differentially regulated in the meiotic spindle and at the oocyte cortex? Do microtubules at the oocyte cortex play a functional role in regulating membrane

ingression or cortical contractility, as suggested in Chapter IV, or do they serve some other purpose?

In addition to understanding the role of microtubules and their regulation during the oocyte meiotic division process, there is also the question of whether or how the meiotic spindle or the chromosomes signal to the oocyte cortex to regulate process of polar body extrusion. Work presented in Chapter II and elsewhere suggests that chromosome based RanGTP signaling in *C. elegans*, unlike other model systems, is not required for cortical differentiation and polar body extrusion (Askjaer et al., 2002; Deng et al., 2007). While meiotic spindle bipolarity and chromosome segregation do not seem to be required for polar body extrusion (Chapter IV), it is unclear what meiotic spindle-derived signaling may be required to dictate the assembly and constriction dynamics of the polar body contractile ring. Understanding this signaling, and how it might interact with the contraction of the oocyte cortex, will be an important future step in understanding the relationship between meiotic spindles and polar body cytokinesis. Another intriguing area for future analysis is also whether the dynamics of polar body contractile rings are altered in the presence of chromosome segregation defects, like those discussed in Chapter III, to act as a possible correction mechanism to prevent oocyte and future embryo aneuploidy.

In addition to raising many new questions regarding the process of oocyte meiotic division, the work presented here also raises new questions about the required components themselves. How are the many genes and proteins described here, and in other work looking at the meiotic division process, regulated? How are they coordinated with each other to allow for faithful chromosome segregation and cytokinesis, and the

production of viable gametes? An important future extension of this work will be to begin characterizing the meiosis II division process, as the work presented in Chapters II-IV largely focuses on meiosis I, and we currently do not have an understanding of if or how these processes may be differentially regulated. While we have significantly expanded our insight into the meiotic division process, we have also generated a multitude of new and exciting questions for exploration in the future.

# APPENDIX

# APPENDIX A: MATERIALS AND METHODS FOR CHAPTER II

## *C. elegans* Strains

*C. elegans* strains used in this study are listed in Supplemental table 1. All strains were maintained at 20ºC on standard nematode growth medium plates seeded with *E. coli* strain OP50.

## RNAi

All RNAi experiments were carried out by feeding *E. coli* strain HT115(DE3) induced to express double-stranded RNA corresponding to each gene as previously described (Timmons et al., 1998; Kamath et al., 2001). The bacteria clones were picked from an RNAi library (Kamath et al., 2003). Synchronized larvae were washed with M9 three times and then plated on the induced plates and grown at 20ºC until imaging. The feeding time varies from gene to gene in order to achieve maximum gene reduction without causing sterilization. For *tac-1*, worms were fed for 96 to 100 hours; for *tbg-1* and *zyg-9*, 48 to 52 hours; for *lmn-1*, 24 to 28 hours and for *ran-1*, 16 to 20 hours.

## CRISPR

Generation of *gfp::zyg-9* and *gfp::tac-1* Transgenic Strains

The appropriate sgRNA and PAM sites for *zyg-9* were selected by using the website http://crispr.mit.edu/. The repair oligo for *gfp::zyg-9* was obtained by asymmetric PCR using primers containing flanking bases at both the 5' and 3' ends of the PAM site to

amplify the GFP-coding region from pCFJ150-GFP(dpiRNA)::CDK-1 (D. Zhang et al., 2018); Addgene plasmid#107938). The injection mixture of *gfp::zyg-9* repair oligo, co-CRISPR marker *dpy-10* repair oligo(Arribere et al., 2014, IDT), *dpy-10* crRNA (GCTACCATAGGCACCACGAG, IDT), trRNA (IDT) and Cas9-NLS nucleases (IDT) were injected into wild-type N2 young adults. The F1 progeny of the injected animals were selected for the roller phenotype and screened for GFP expression. The non-roller/dumpy F2 progeny of the F1 animals with correct GFP expression were identified and then further outcrossed with N2.

The transgenic strain of *gfp::tac-1* was made by the same approach as described above but with *gfp::tac-1* repair oligo and *tac-1* crRNA (CAACACAACCTTCACCAAAG, IDT).

Generation of Double Deletion Strain of *klp-15* and *klp-16*

The *klp-15(ok1958) klp-16(or1952)* double mutant strain was generated by the same approach as described above, with a few modifications. The injection mix was injected into *klp-15(ok1958)* single mutants, with *klp-16* crRNA(TACTATCGGAGCACCGCCGA, IDT) and no repair template was provided. Injected hermaphrodites were kept at 15$^{o}$C, and their broods were screened for *dpy-10* roller or dumpy co-conversion worms. Broods produced by hermaphrodites with the *dpy-10* co-conversion marker were screened for potential *klp-15/16* double mutant phenotypes (embryonic lethality), and lines identified as possibly carrying mutations to both *klp-15* and *klp-16* were balanced and Sanger sequenced after PCR amplification to identify the CRISPR/Cas9 induced mutation. The *in situ* fusion of GFP to the endogenous *aspm-1*

locus in the *klp-15(ok1958) klp-16(or1952)* background was made by SunyBiotech using CRISPR/Cas-9 with the allele designation *GFP::aspm-1(syb1260)*.

**Image Acquisition**

*In utero* filming of oocytes was accomplished by mounting young adult worms with single row of embryos on a 5% agarose pad, with 1.5µl each of M9 buffer and 0.1µm polystyrene microspheres (Polysciences Inc.) on a microscope slide covered with a coverslip. *Ex utero* filming of oocytes for data in Supplemental Figure 16A was done by cutting open young adult worms in 3µl of egg buffer (118mM NaCl, 48mM KCl, 2mM $CaCl_2$, 2mM $MgCl_2$, and 25mM HEPES, PH 7.3) on a coverslip before mounting onto a 2% agarose pad on a microscope slide; all other data is from *in utero* imaging. Nomarski images were acquired on AxioSkop compound microscope (Zeiss) equipped with CCD camera using ImageJ software (National Institutes of Health). Fluorescence imaging was performed using a Leica DMi8 microscope outfitted with a spinning disk confocal unit – CSU-W1 (Yokogawa) with Borealis (Andor), dual iXon Ultra 897 (Andor) cameras, and a 100x HCX PL APO 1.4-0.70NA oil objective lens (Leica). Metamorph (Molecular Devices) imaging software was used for controlling image acquisition. For *in utero* movies of oocytes from GFP::LMN-1, mCherry::H2B and GFP::TAC-1, mCherry::H2B strains, the 488nm and 561nm channels were imaged simultaneously every 10 seconds with 1µm Z-spacing; every 5 seconds for oocytes from all other transgenic strains expressing fluorescent markers. 14 focal planes/z-stack were collected for all *klp-15/16* mutant oocytes and the control oocytes expressing GFP::TBB-2, mCherry::H2B in Figure 6; 21 focal planes/z-stack were collected for all other oocytes. Time lapse images in

figures depict maximum projections for all fluorescent proteins except for GFP::LMN-1, which were single focal planes of maximum oocyte diameters. Time lapse supplemental movies show maximum projections for all z-stack focal planes unless otherwise indicated.

**Image Processing and Analysis**

General imaging process—including merging red/green channels, cropping, stabilizing and z-projected images—was performed with ImageJ software (National Institutes of Health). Three-dimensional projection and rotation movies were made by using imaris software (Bitplane).

Normalized microtubule pixel intensity quantification was carried out by ImageJ software. The spindle area was determined by generating auto-threshold (set on Otsu) in a cropped area in the microtubule channel around the spindle in the projected z stack (Max intensity) treated with gaussian blur (sigma set at 2) at time points throughout meiosis I. The regions of interest (ROIs) were selected accordingly and saved in ROI manager. Measurements of microtubule intensity were taken by applying the saved ROIs to the projected z stack (sum slices) in the microtubule channel at the corresponding time points. Both the area of the ROIs and the mean gray value (MeanGV) were automatically calculated. In addition, an area excluding the spindle was selected and the MeanGV was calculated for the cytoplasm. Measurements of chromosome intensity were taken by selecting the oocyte chromosome area in the histone channel in the projected z stack (Max intensity) at the corresponding time points and the maximum gray value (MaxGV) were calculated. Additionally, an area excluding the oocyte and the sperm chromosomes

was selected and the MaxGV was calculated for the cytoplasm. All of the measurements were placed into the following formula: (MeanGV (spindle)-MeanGV (cytoplasm))/(MaxGV (chromosomes)-MaxGV (cytoplasm)) × area(spindle) = normalized microtubule pixel intensity.

**Statistics**

p-values comparing distributions for all scatter plots were calculated using the Mann-Whitney U test. p-values comparing variance for all scatter plots were calculated using the F-test.

# APPENDIX B: SUPPLEMENTAL MATERIALS FOR CHAPTER II

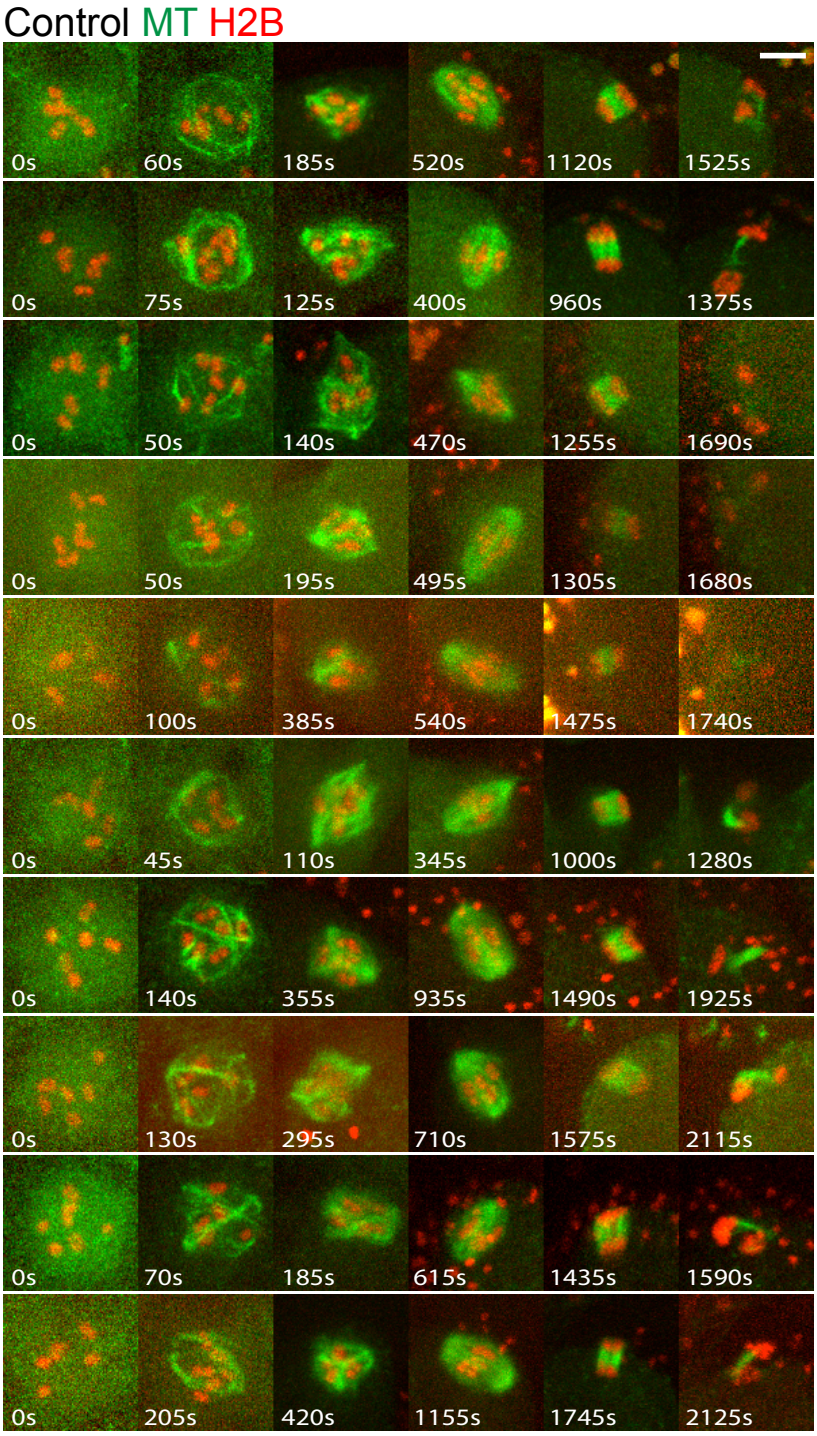


**Figure B.1 - Supplemental Figure 1**
Time-lapse images during meiosis I for 10 live control oocytes expressing GFP::TBB-2 and mCherry::H2B.

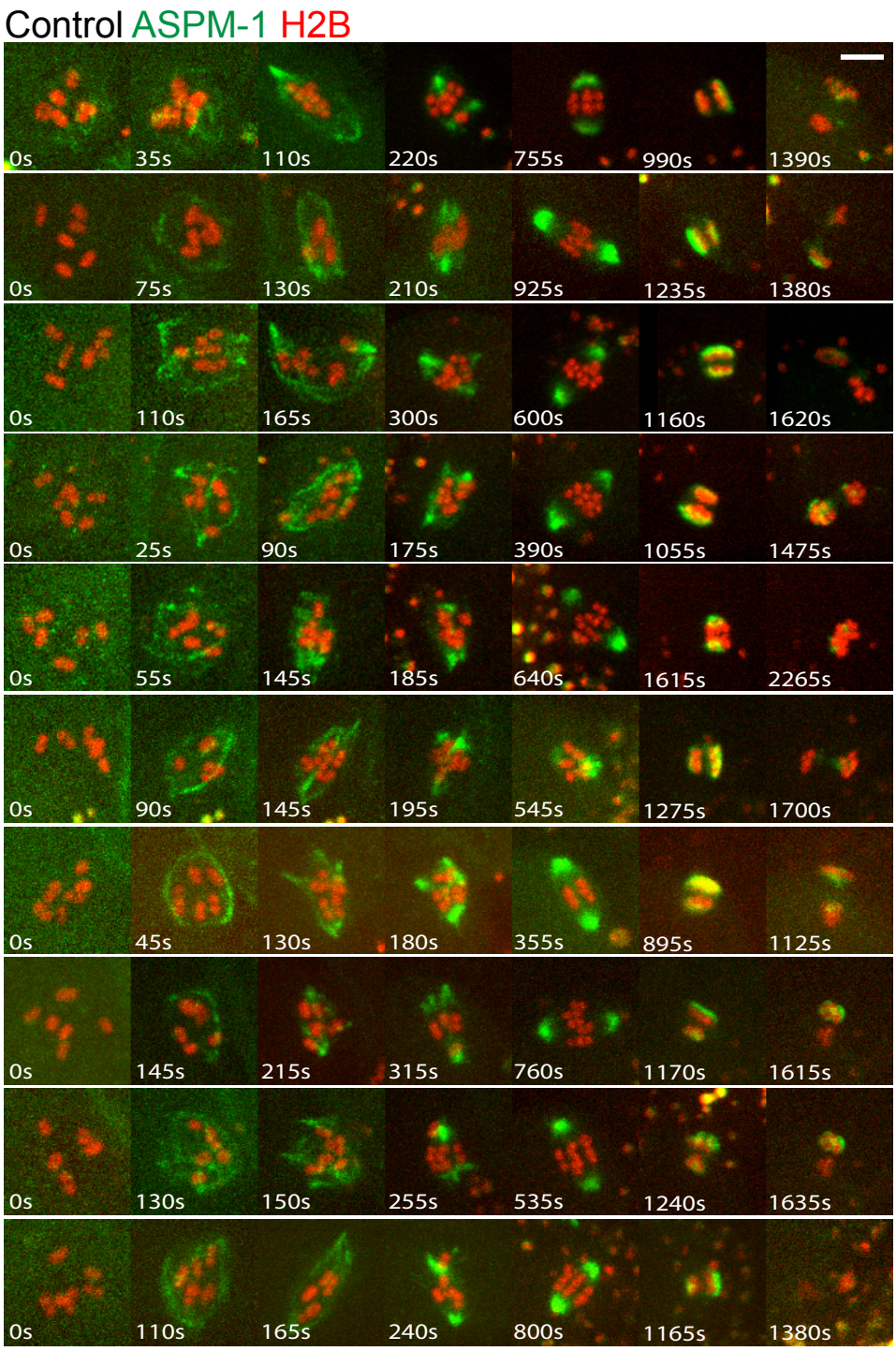


**Figure B.2 - Supplemental Figure 2**
Time-lapse images during meiosis I for 10 live control oocytes expressing GFP::ASPM-1 and mCherry::H2B.

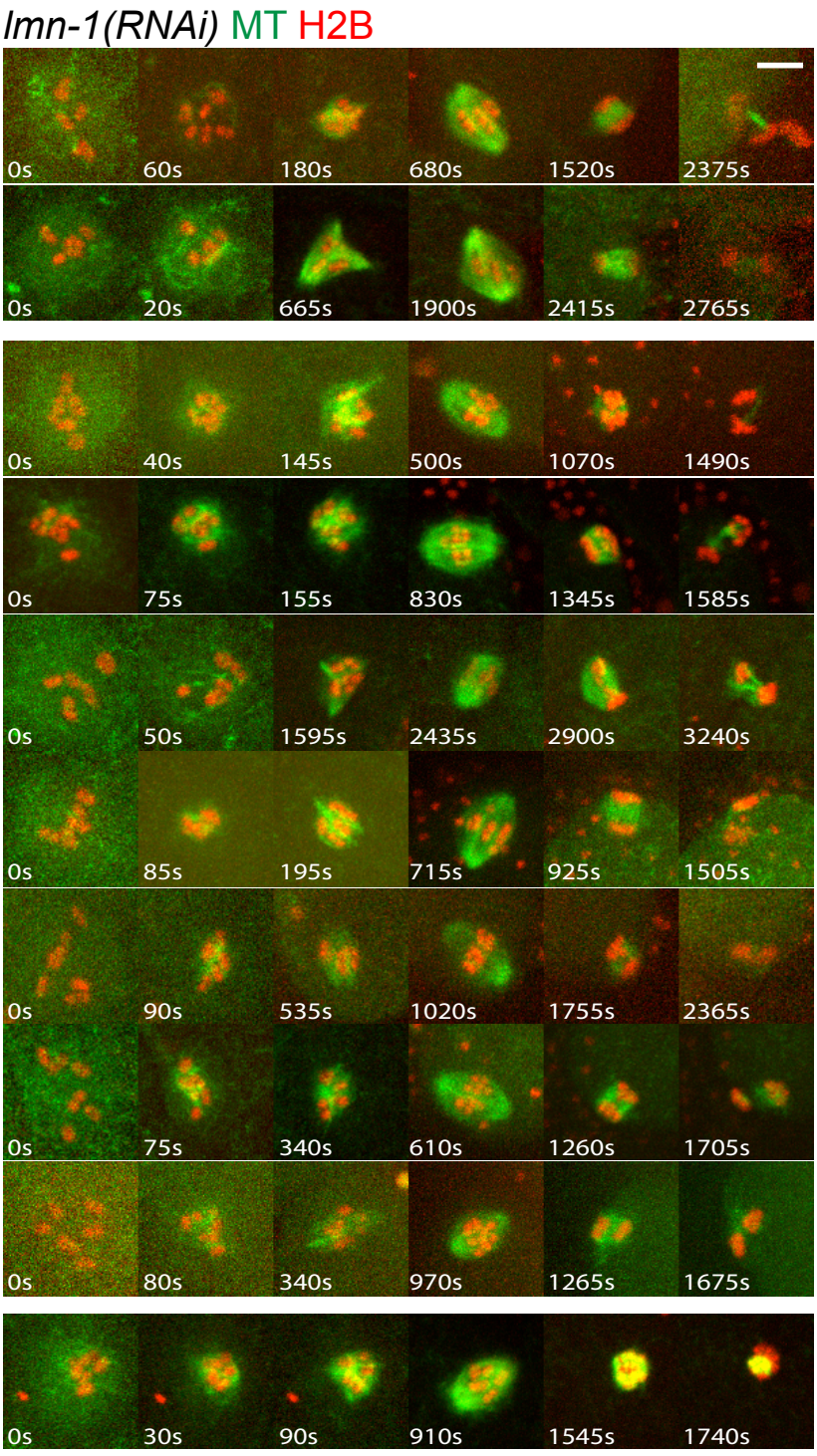


**Figure B.3 - Supplemental Figure 3**
Time-lapse images during meiosis I for 10 live *lmn-1(RNAi)* oocytes expressing GFP::TBB-2 and mCherry::H2B. Rows 1 & 2: oocytes with cage structure; Rows 3-9 oocytes without cage structure; Row 10: oocyte without cage and no chromosome segregation. In all figures, cage structures and chromosome segregation were assessed using Imaris software to rotate 3D images

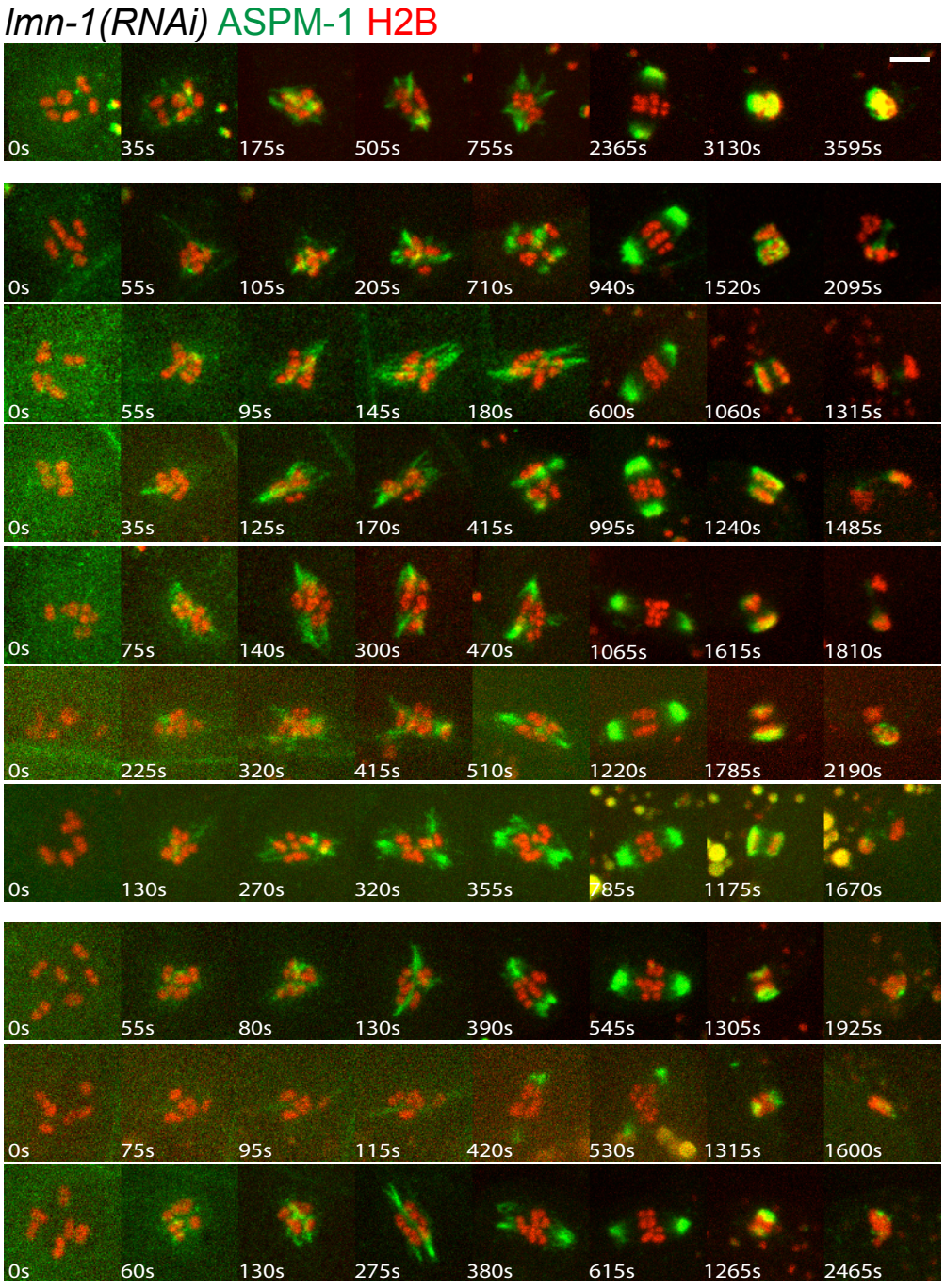


**Figure B.4 - Supplemental Figure 4**
Time-lapse images during meiosis I for 10 live *lmn-1(RNAi)* oocytes expressing GFP::ASPM-1 and mCherry::H2B. Row 1 oocyte with cage structure and no chromosome segregation; rows 2-7 oocytes without cage structure; row 8-10 oocytes without cage and no chromosome segregation.

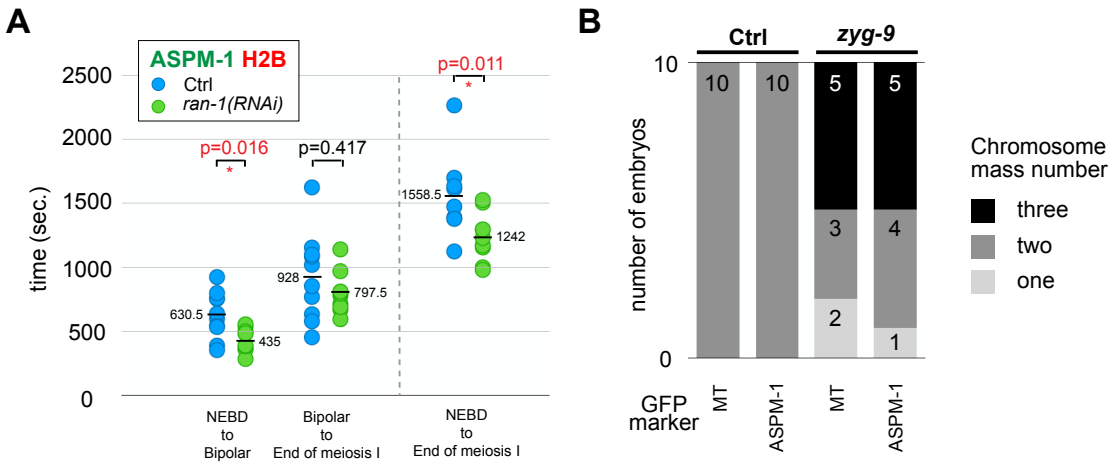


**Figure B.5 - Supplemental Figure 5**
(A) Scatter plot showing comparisons of the time from NEBD to spindle bipolarity establishment (Bipolar), from spindle bipolarity establishment to the end of meiosis I, and entire time to progress through meiosis I between control and *ran-1(RNAi)* oocytes expressing GFP::ASPM-1 and mCherry::H2B.
(B) The number of segregating chromosome masses detected in control and *zyg-9(RNAi)* oocytes at the end of meiosis I for strains expressing either GFP::TBB-2 and mCherry::H2B, or GFP::ASPM-1 and mCherry::H2B. Numbers within the bars indicate the number of embryos in each category.

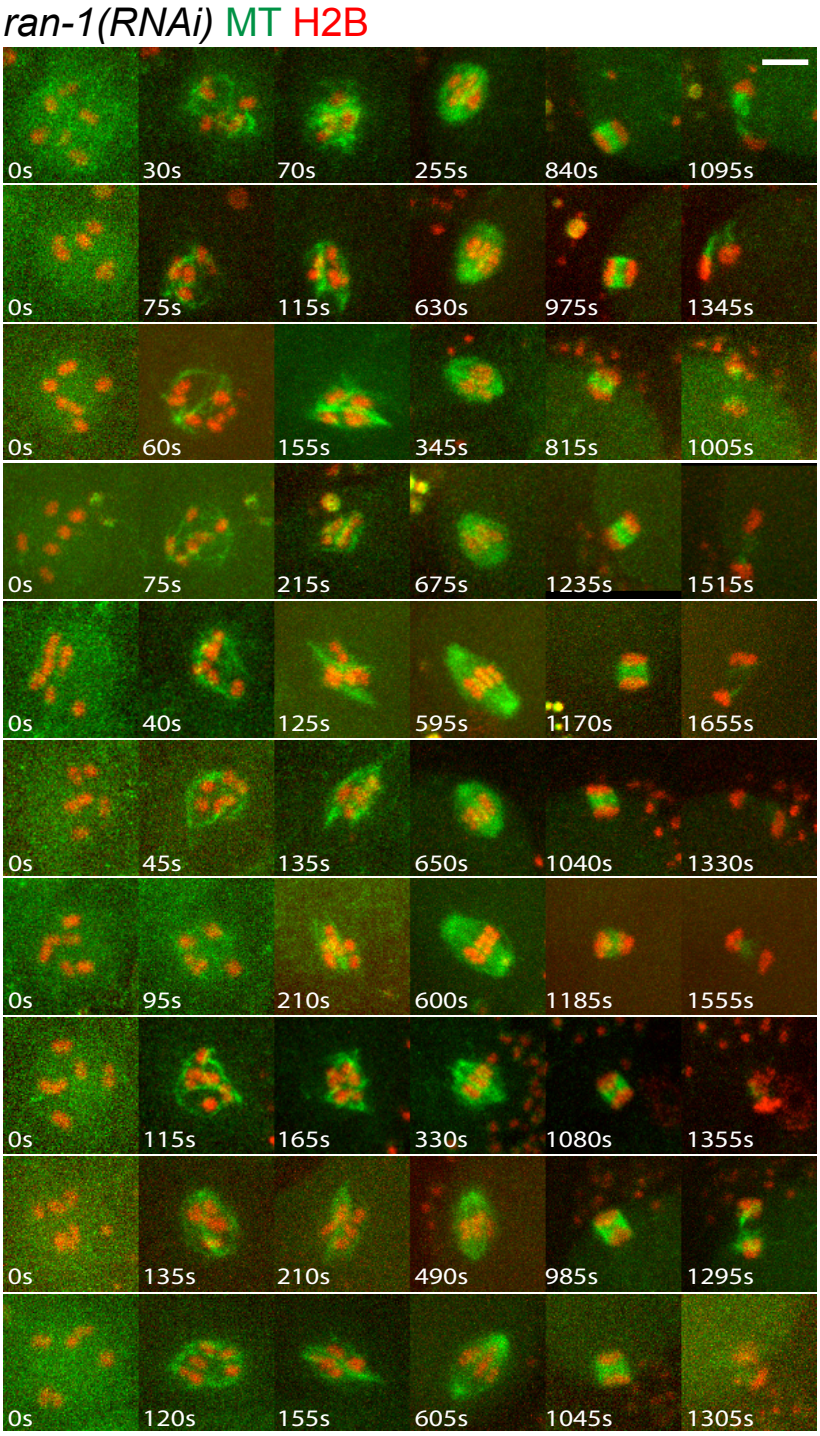


**Figure B.6 - Supplemental Figure 6**
Time-lapse images during meiosis I for 10 live *ran-1(RNAi)* oocytes expressing GFP::TBB-2 and mCherry::H2B.

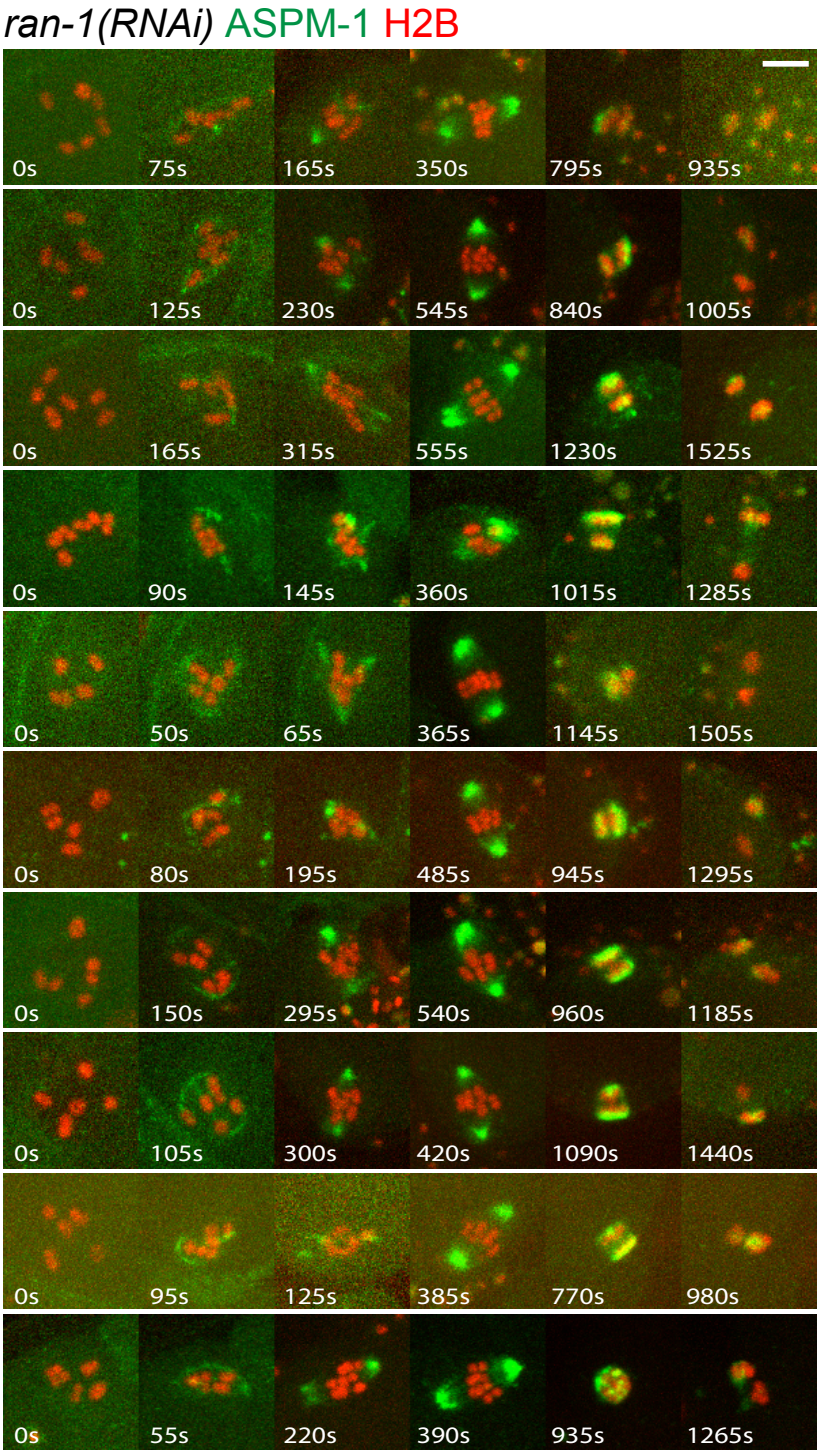


**Figure B.7 - Supplemental Figure 7**
Time-lapse images during meiosis I for 10 live *ran-1(RNAi)* oocytes expressing GFP::ASPM-1 and mCherry::H2B.

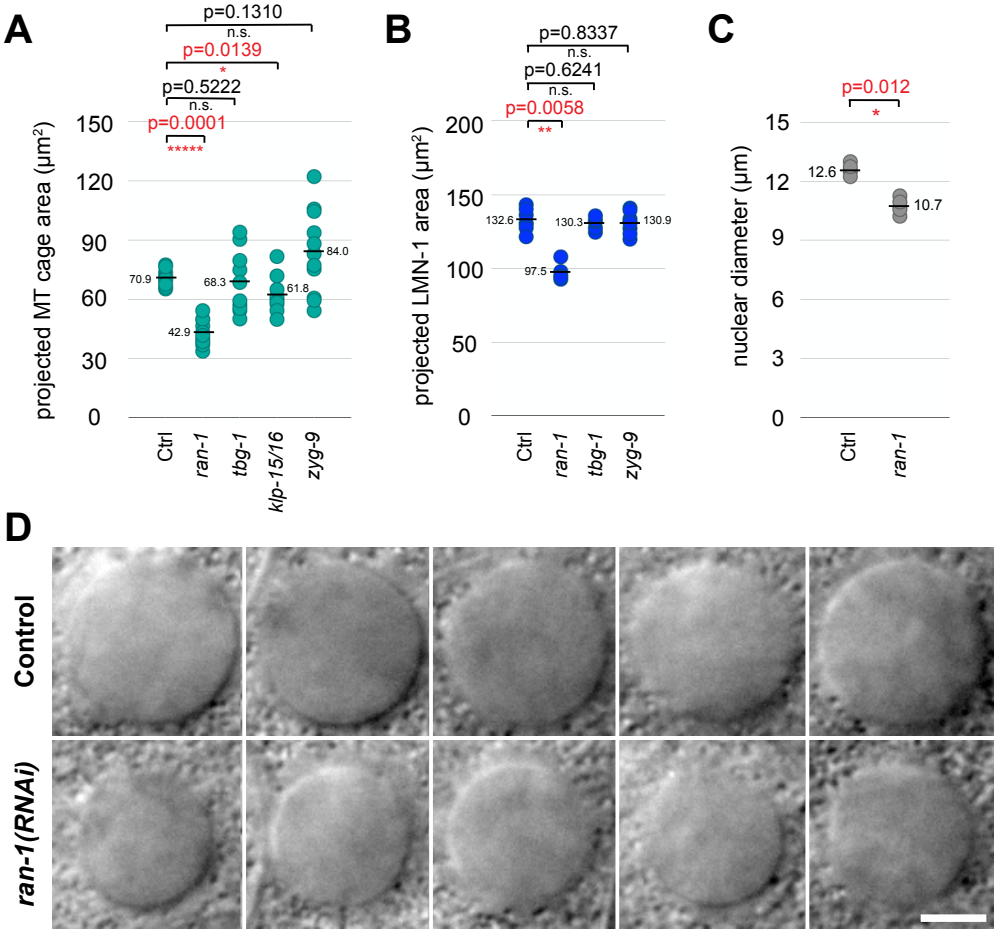


**Figure B.8 - Supplemental Figure 8**
(A) Scatter plot showing projected areas of the microtubule cage-like structure meiosis I in control and mutant oocytes expressing GFP::TBB-2 and mCherry::H2B.
(B) Scatter plot showing projected nuclear lamina area measured at the cage stage of meiosis I for control and mutant oocytes expressing GFP::LMN-1 and mCherry:: TBB-2.
(C) Scatter plot showing nuclear diameter of control and *ran-1(RNAi)* oocytes measured using Nomarski images (8D).
(D) Nomarski images of control and *ran-1(RNAi)* oocyte nuclei 2 seconds before nuclear envelope break down.

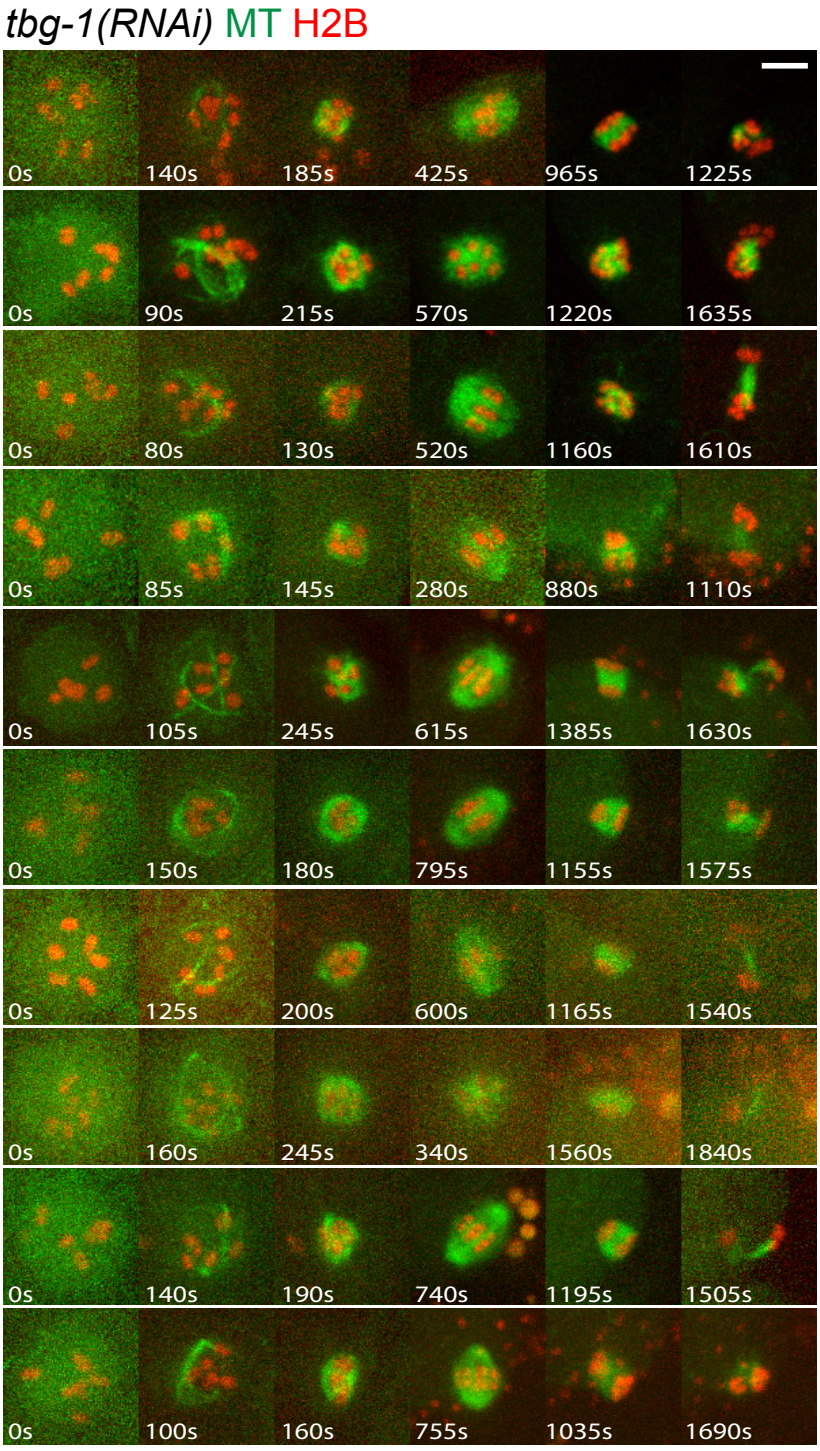


**Figure B.9 - Supplemental Figure 9**
Time-lapse images during meiosis I for 10 live *tbg-1(RNAi)* oocytes expressing GFP::TBB-2 and mCherry::H2B.

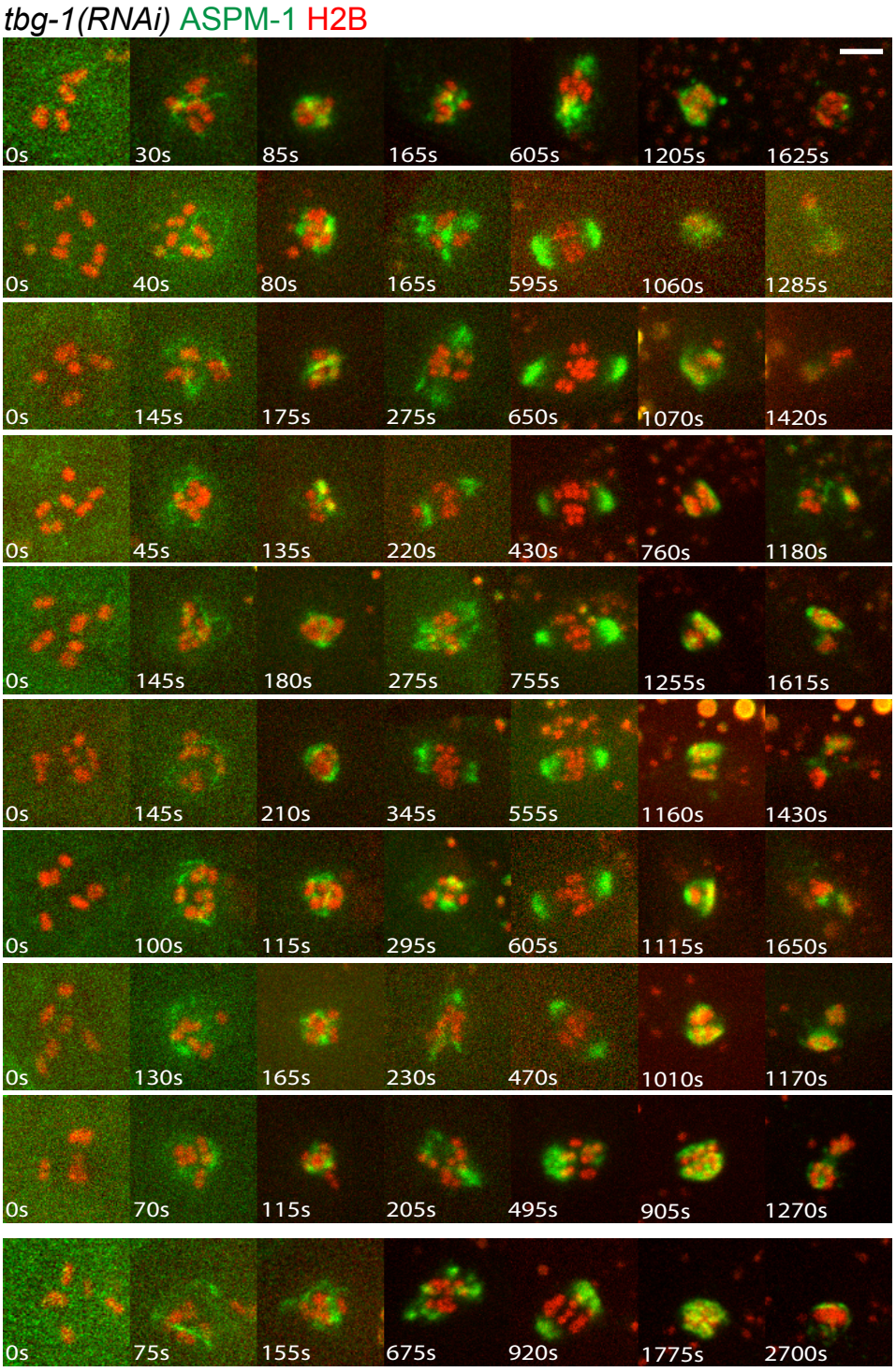


**Figure B.10 - Supplemental Figure 10**
Time-lapse images during meiosis I for 10 live tbg-1(RNAi) oocytes expressing GFP::ASPM-1 and mCherry::H2B. Rows 1-9 oocytes with chromosome segregation; row 10 oocyte without chromosome segregation.

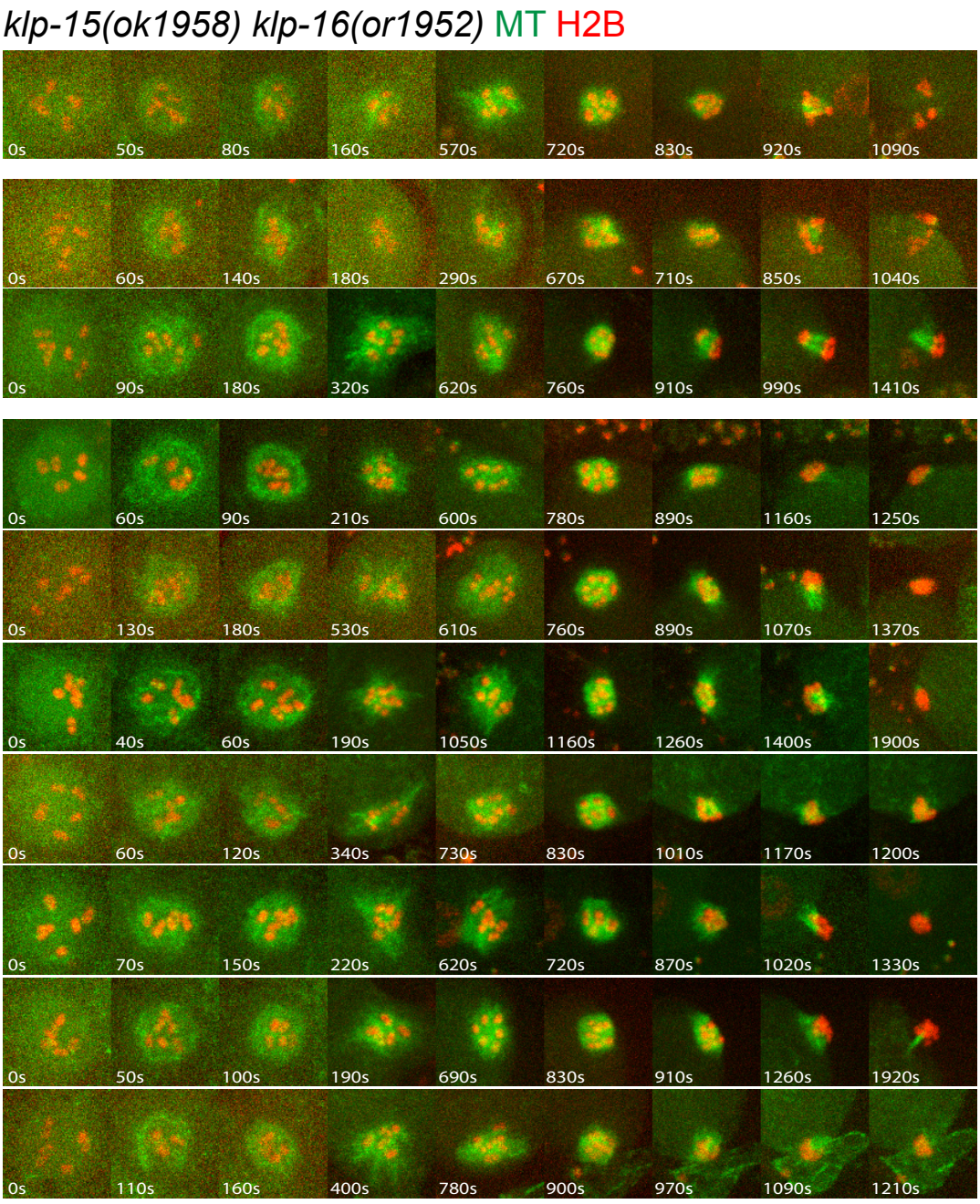


**Figure B.11 - Supplemental Figure 11**
Time-lapse images during meiosis I for 10 live *klp-15/16(-/-)* double mutant oocytes expressing GFP::TBB-2 and mCherry::H2BB. Row 1 oocyte with chromosomes segregated into three masses; rows 2 & 3 oocytes with chromosomes segregated into two masses; rows 4-10 oocytes with no chromosome segregation.

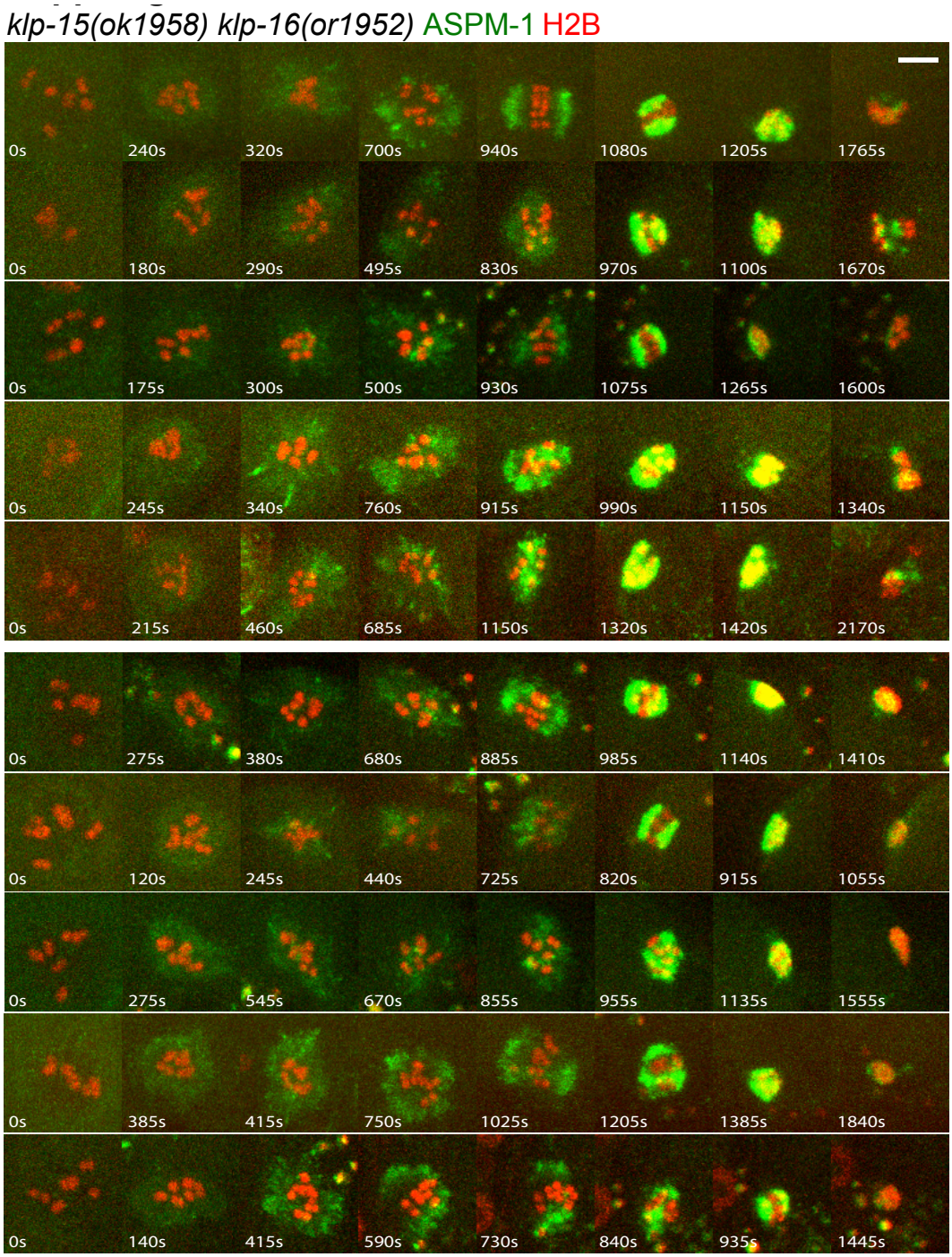


**Figure B.12 - Supplemental Figure 12**
Time-lapse images during meiosis I for 10 live *klp-15/16(-/-)* double mutant oocytes expressing GFP::ASPM-1 and mCherry::H2B. Rows 1-5 oocytes with chromosomes segregated into two masses; rows 6-10 oocytes with no chromosome segregation.

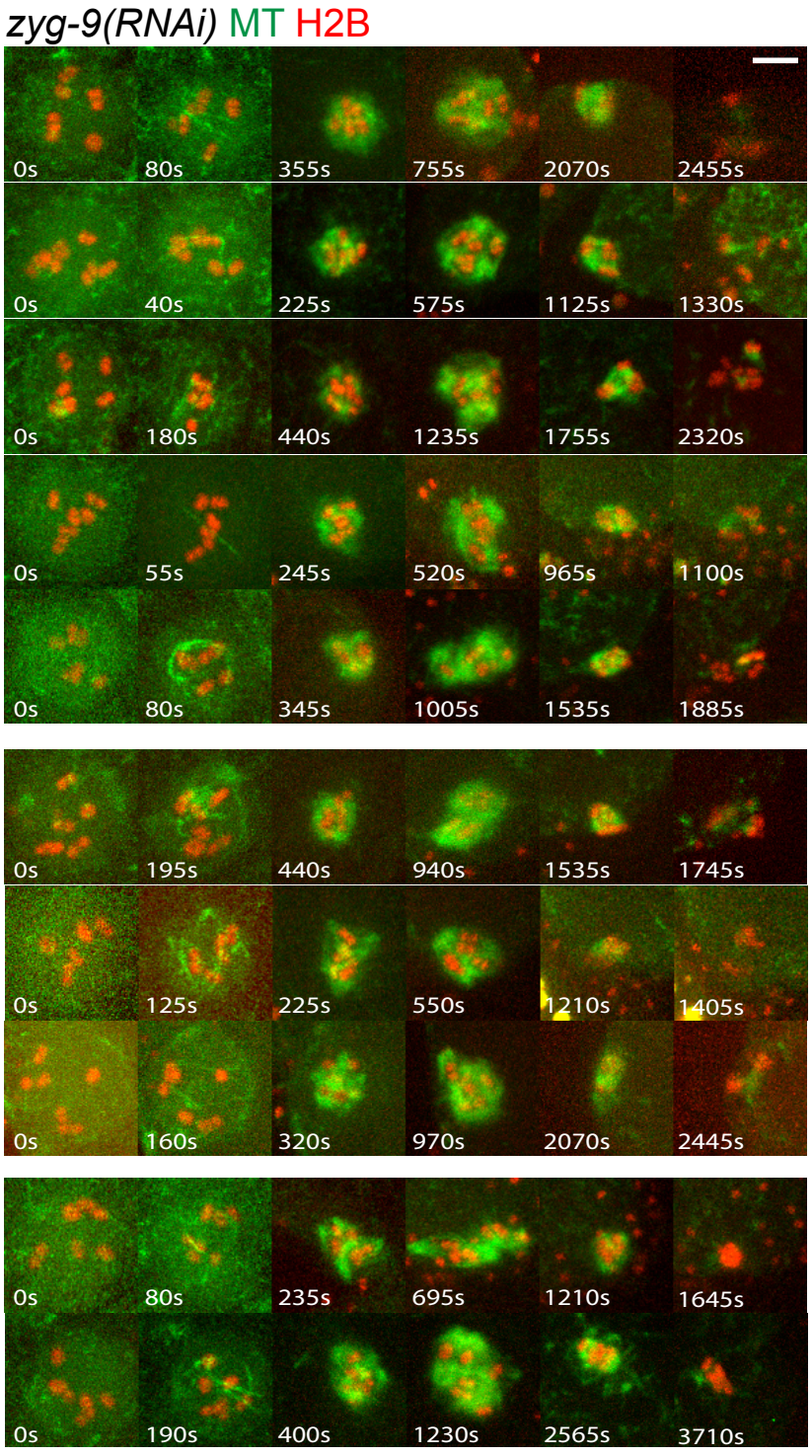


**Figure B.13 - Supplemental Figure 13**
Time-lapse images during meiosis I for 10 live *zyg-9(RNAi)* oocytes expressing GFP::TBB-2 and mCherry::H2B. Rows 1-5 oocytes with chromosomes segregated into three masses; rows 6-9 oocytes with chromosomes segregated into two masses; row 10 no chromosome segregation.

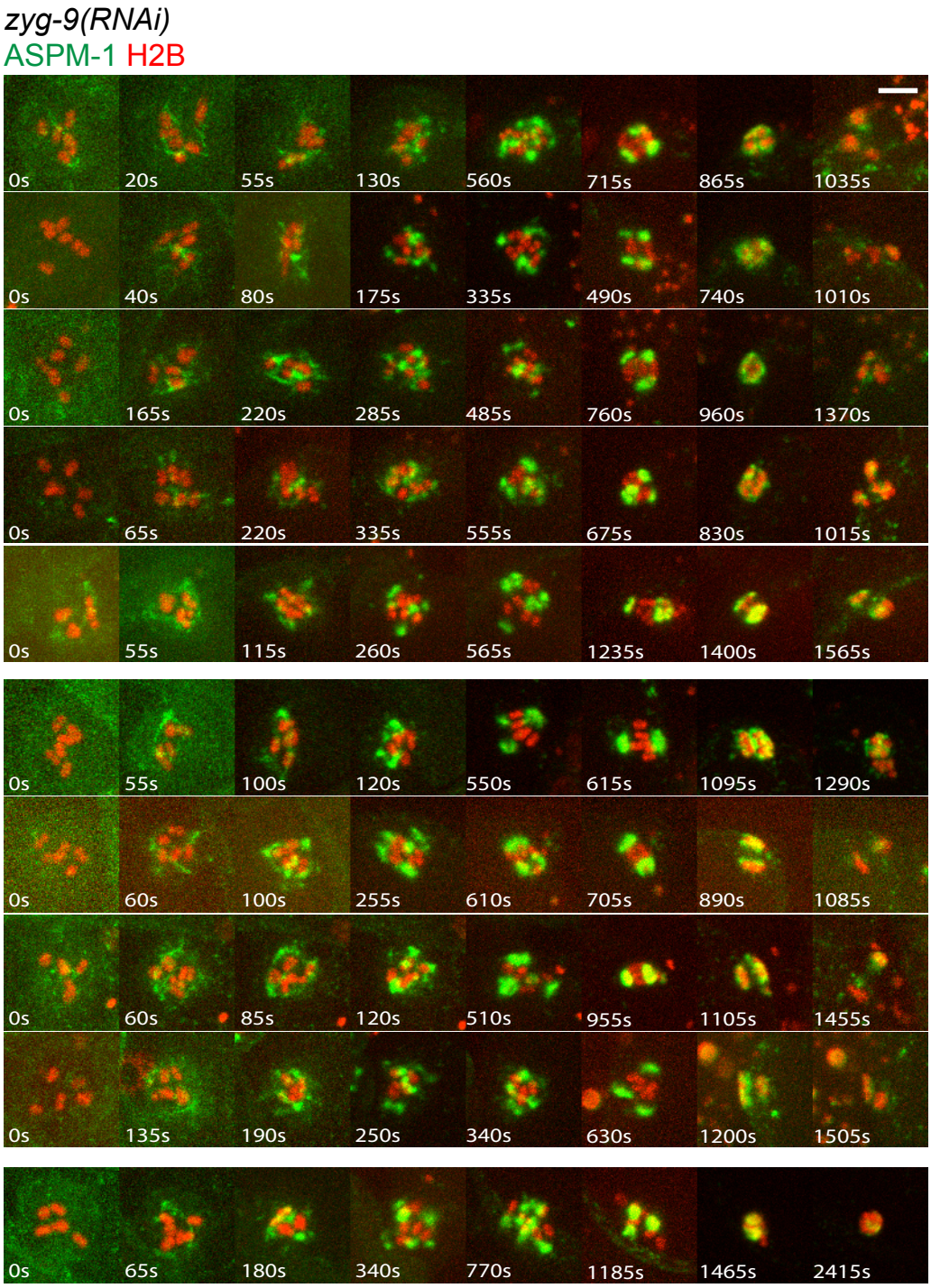


**Figure B.14 - Supplemental Figure 14**
Time-lapse images during meiosis I for 10 live *zyg-9(RNAi)* oocytes expressing GFP::ASPM-1 and mCherry::H2B. Rows 1-5 oocytes with chromosomes segregated into 3 masses; rows 6-9 oocytes with chromosome segregated into two masses; row 10 no chromosome segregation.

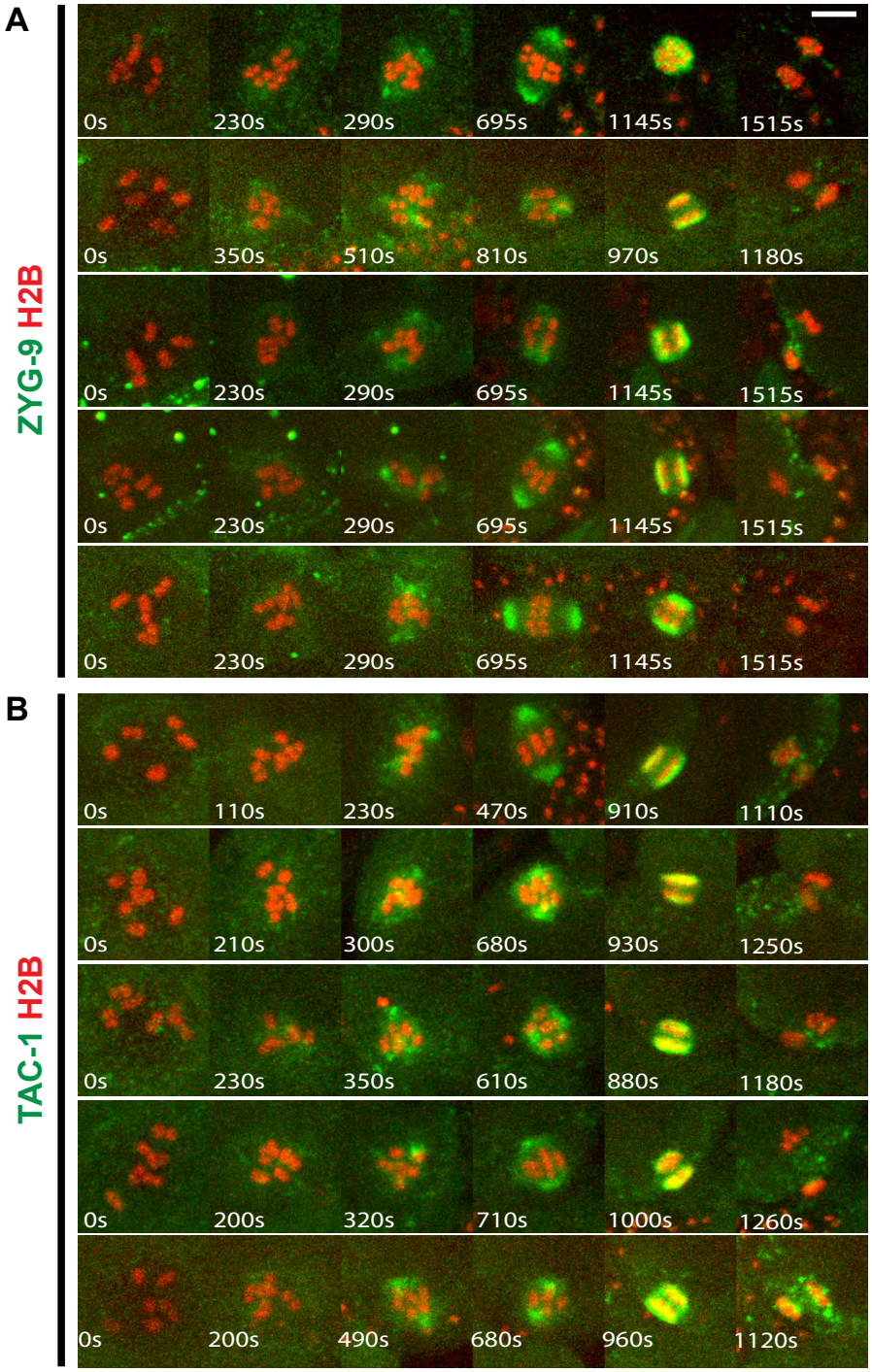


**Figure B.15 - Supplemental Figure 15**
Time-lapse images during meiosis I for live control oocytes expressing either GFP::ZYG-9 and mCherry::H2B (A), or GFP::TAC-1 and mCherry::H2B (B).

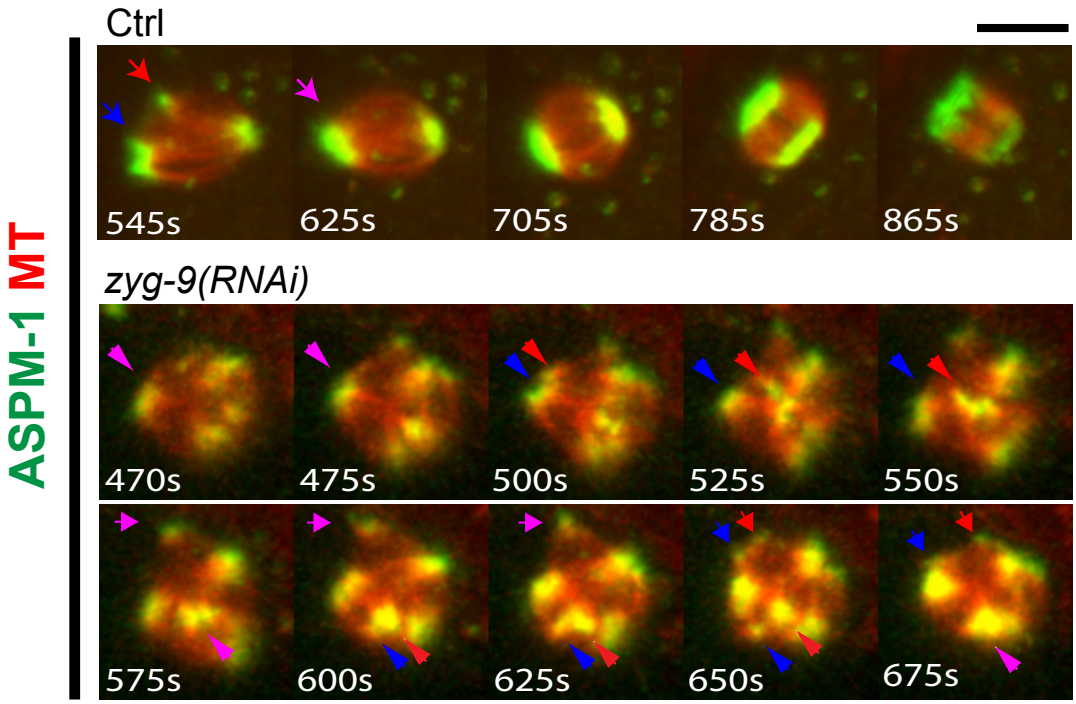


**Figure B.16 - Supplemental Figure 16**
Time-lapse images during meiosis I for live control and *zyg-9(RNAi)* oocytes expressing GFP::ASPM-1 and mCherry::TBB-2. Times after NEBD are indicated. Pink arrowheads indicate spindle poles that split into two foci that are then marked by red and blue arrowheads.

| Strain name | Genotype |
|---|---|
| N2 | (ancestral) |
| EU2876 | *aspm-1(or1935[gfp::aspm-1]) I; itIs37[pie-1p::mCherry::H2B::pie-1 3'UTR + unc-119(+)] IV* |
| EU2942 | *ruIs57[pie-1p::gfp::tubulin + unc-119(+)]; itIs37[pie-1p::mCherry::H2B::pie-1 3'UTR + unc-119(+)] IV* |
| EU3006 | *aspm-1(or1935[gfp::aspm-1]) I; tbb-2(tj29[mCherry::tbb-2]) III* |
| EU3091 | *ijmSi49[pJD479; Pmex-5::gfp::lmn-1::3'tbb-2] I; tbb-2(tj29[mCherry::tbb-2]) III* |
| EU3115 | *klp-15(ok1958) klp-16(or1952)/ tmC18[dpy-5(tmIs1236)] I; itIs37[pie-1p::mCherry::H2B::pie-1 3'UTR + unc-119(+)] IV; ruIs57[pie-1p::gfp::tubulin + unc-119(+)]* |
| EU3121 | *tac-1(or1955[gfp::tac-1]) II; itIs37[pie-1p::mCherry::H2B::pie-1 3'UTR + unc-119(+)] IV (may contain unc-119(ed3) III)* |
| EU3169 | *zyg-9(or1956[gfp::zyg-9]) II; itIs37[pie-1p::mCherry::H2B, unc-119(+)]IV (may contain unc-119(ed3) III)* |
| RB1593 | *klp-15(ok1958)* |
| EU3201 | *klp-15(ok1958) aspm-1(syb1260[gfp::aspm-1]) klp-16(or1952) /tmC18[dpy-5(tmIs1236)] I; itIs37[pie-1p::mCherry::H2B::pie-1 3'UTR + unc-119(+)] IV* |

**Table B.1 - Supplemental Table 1**

# APPENDIX C: MATERIALS AND METHODS FOR CHAPTER III

## *C. elegans* Strains, Genetics, and Culture Conditions

All strains are from the Bristol N2 background and were maintained at 15°C or 20°C and crossed at 20°C under standard conditions. Temperatures used for specific experiments are indicated below. For all experiments with meiotic mutants, homozygous mutant worms were derived from balanced heterozygous parents by selecting progeny lacking a dominant marker (Unc and/or GFP) associated with the balancer. For experiments marked 25°C, L4 worms were shifted to 25°C 24-48 hours prior to dissection.

The following strains were used in this study:

N2: Bristol wild-type strain.

AV311: *dpy-18(e364) unc-3(E151) meT7*(*III; X; IV*). (Hillers and Villeneuve 2003)

AV630: *meIs8[unc-119(+) Ppie-1::gfp::cosa-1] II.* (Yokoo et al. 2012)

OD868: *ItSi220*[pOD1249/pSW077; *Pmex-5::GFP-tbb-2-operon-linker-mCherry-his-11; cb-unc119(+)*]*I* (Wang et al. 2015)

DLW11: *meIs8[unc-119(+) Ppie-1::gfp::cosa-1] II*; *dpy-18(e364) unc-3(e151) meT7* (*III;X;IV*). (This study)

DLW30: *ItSi220 I*; *dpy-18(e364) unc-3(E151) meT7*(*III; X; IV*) (This study)

## RNAi Treatments

RNAi by feeding was performed as previously described (Muscat et al. 2015). Worms were synchronized at the L1 phase by bleaching adults and allowing resultant

eggs to hatch on unseeded NGM plates at 20°C for 20-24 hrs. Synchronized L1s were then washed off of the unseeded NGM plates with M9 and placed on NGM+1mM IPTG+100μg ampicillin plates that were poured within 30 days of use and freshly seeded one day before use with clones picked from the Ahringer Lab RNAi feeding library (Kamath and Ahringer 2003) or the empty L4440 vector (referred to as "control RNAi" in figures and text). The RNAi plates with L1s were then placed at 15°C and grown to adulthood. For RNAi experiments performed at 25°C, L4 worms were shifted to 25°C for 40-48 hours prior to dissection.

**Immunofluorescence for Late Meiotic Prophase I**

Immunofluorescence was performed as in ((Libuda et al., 2013). Gonads from adult worms at 18-24 hours post-L4 stage were dissected in 1x egg buffer with 0.1% Tween on VWR Superfrost Plus slides, fixed for 5 min in 1% paraformaldehyde, flash frozen with liquid nitrogen, and then fixed for 1 minute in 100% methanol at -20°C. Slides were washed 3 x 5 min in 1x PBST and blocked for one hour in 0.7% BSA in 1x PBST. Primary antibody dilutions were made in 1x PBST and added to slides. Slides were covered with a parafilm coverslip and incubated in a humid chamber overnight (14-18 hrs). Slides were washed 3 x 10 min in 1x PBST. Secondary antibody dilutions were made at 1:200 in 1x PBST using Invitrogen goat or donkey AlexaFluor labeled antibodies and added to slides. Slides were covered with a parafilm coverslip and placed in a humid chamber in the dark for 2 hrs. Slides were washed 3 x 10 min in 1x PBST in the dark. All washes and incubations were performed at room temperature, unless otherwise noted. 2 μg/ml DAPI was added to slides and slides were subsequently incubated in the dark with

a parafilm coverslip in a humid chamber. Slides were washed once for 5 min in 1x PBST prior to mounting with Vectashield and a 20 x 40 mm coverslip with a 170 ± 5 μm thickness. Slides were sealed with nail polish immediately following mounting and then stored at 4°C prior to imaging. All slides were imaged (as described below) within two weeks of preparation. The following primary antibody dilutions were used: rabbit anti-GFP (1:1000) (Yokoo et al., 2012); chicken anti-GFP (1:1000) (Abcam 13970); guinea pig anti-SYP-1 (1:200) (MacQueen et al., 2002); rabbit anti-HIM-3 (1:200) (Zetka et al. 1999) and, chicken anti-HTP-3 (1:500) (MacQueen et al., 2005).

**Immunofluorescence for Prometa-, Meta- and Anaphase I and II**

Immunofluorescence was performed as in (Oogema et al. 2001). Briefly, adult worms were picked into a drop of M9 media on poly-l-lysine coated slides (Fisher scientific), cut in half to release oocytes, covered with a coverslip and frozen for 7 minutes in liquid nitrogen. The coverslip was quickly cracked off, and slides were fixed in -20°C methanol for 35 minutes. Samples were then rehydrated in PBS and blocked in AbDil (PBS with 4% BSA, 0.1% Triton X-100, 0.02% Sodium Azide) for one hour at room temperature, and then washed with PBST (PBS + 0.1% Triton X-100). Primary antibodies were diluted in AbDil, applied to samples and incubated overnight at 4°C. Samples were washed with PBST, and secondary antibodies were diluted in AbDil, applied to samples, and incubated for 2 hours at room temperature. Slides were washed and incubated with Hoechst 33342 (Invitrogen) at 1:1000 in PBST for 10 minutes at room temperature. Slides were washed a final time and mounted in 0.5% p-

phenylenediamine in 90% glycerol, 20mM Tris, pH 8.8, sealed with nail polish, and stored at 4°C prior to imaging.

The following antibodies were used: rat anti-AIR-2 (1:500, Davis-Roca et al. 2017), rabbit anti-SEP-1 (1:200, gift from Andy Golden), rabbit anti-BIR-1 (1:800, this study), mouse anti-SUMO (1:500, gift from Federico Pelisch), rabbit anti-BUB-1 (1:1000, Davis-Roca et al. 2018), rabbit anti-ASPM-1 (1:5000, gift from Arshad Desai), Mouse anti-α-tubulin-FITC (1:500, DM1α, Sigma) and rabbit anti-KLP-19 (1:2500, this study). KLP-19 and BIR-1 polyclonal antibodies were generated by Covance using recombinant GST-BIR-1 (Full length protein) and GST-KLP-19 (amino acids 371-1084) as antigens (purification performed as in Davis-Roca et al. 2018). Antibody sera was then affinity purified and used at indicated concentrations. Alexa-fluor conjugated secondary antibodies were used at 1:500.

**Fixed Imaging**

For Figure 1, IF slides were imaged at 512 x 512 pixel dimensions on an Applied Precision DeltaVision microscope using a 60x objective with 1.5x optivar. Images were acquired as Z-stacks at 0.2 μm intervals and deconvolved with Applied Precision softWoRx deconvolution software. For quantification of GFP::COSA-1 foci, nuclei that were in the last 4-5 rows of late pachytene and were completely contained within the image stack were analyzed. Foci were quantified manually from deconvolved three-dimensional stacks. *meT7* chromosomes in pachytene nuclei were identified based on size. Regardless of temperature (20°C or 25°C), all three wild-type/non-fused chromosomes in the nuclei of the *meT7* strains contained only one GFP::COSA-1 focus

per chromosome (n=30), which is consistent with all chromosomes in wild-type strains and the wild-type/unfused chromosomes in *mnT12 (X;IV)* fusion chromosome strain (this study, Libuda et al. 2013, Yokoo et al. 2012). Given the consistency of COSA-1 counts for the 3 wild-type/non-fused chromosome in the *meT7* strains, the number of COSA-1 foci per *meT7* was calculated by subtracting 3 from the total number of COSA-1 foci per nucleus. For visualization and quantitation of chiasmata (Figures 1D), individual *meT7* bivalents from diakinesis nuclei in -2, -3, or -4 oocytes were identified based on size, cropped, and rotated in three-dimensions using Imaris (Bitplane/Oxford Instruments) three-dimensional rendering software. Scoring of chiasmata was based primarily on HTP-3 (chromosome axis) or HIM-3 (chromosome axis) and DAPI staining, as GFP::COSA-1 dissociates from chromosomes during progression through the diakinesis stage. For Figure 1B-C, images shown are projections through three-dimensional data stacks encompassing whole nuclei, generated with a maximum-intensity algorithm with the softWoRx (Applied Precision) software. For Figure 1D, the images of *meT7* bivalents shown are snapshots of a Imaris three-dimensional rendering of individual diakinesis bivalents with maximum intensity rendering for HTP-3. The images of wild type unfused autosome bivalents in Figure 1D are projections through three-dimensional data stacks encompassing the whole bivalent, generated with a maximum intensity algorithm with the softWoRx (Applied Precision) software.

For Figures 2, 3, 4, 5, and 7a, IF slides were imaged at 256 x 256 pixel dimensions on an Applied Precision DeltaVision microscope using a 100x oil objective (NA = 1.4), housed in the Northwestern Univeresity Biological Imaging Facility supported by the Northwestern University Office for Research. Images were acquired as

Z-stacks at 0.2 μm intervals and deconvolved (ratio method, 15 cycles) with Applied Precision softWoRx deconvolution software. Images are maximum projections of entire spindles unless otherwise noted in the figure legends. Meiosis stages were determined by eye based on protein localization, chromosome-to-chromosome distance, chromosome size and polar body presence. *meT7* chromosomes were identified based on size.

**Ring Stretching Assay**

Ring stretching on monopolar spindles in Figure 3 was performed as in (Muscat et al. 2015). Worms were grown on RNAi plates with a 1:1 mixture of *emb-30* and *klp-18* RNAi feeding clones from the Ahringer library to induce an arrest in metaphase on a monopolar spindle. RC components tend to stretch away from bivalents in extended metaphase arrest; spindles in extended arrest were determined by eye based on significant ring stretching of the three normal bivalents. The number of stretching rings on either *meT7* or a control normal bivalent was counted using Imaris.

**Quantification**

Ring Structure Quantification

To assess ring structure, RCs on *meT7* bivalents were rotated in Imaris. Rings were scored by eye and considered mispatterned if they had more than one plane, consisted of more than one individual unit, or had more than one major loop. For Figure 2A, Rings were considered “slightly mispatterned” if they consisted of two distinct units on a single plane or appeared as two connected loops on a single plane. Rings with more

than two units, multiple loops at different angles or planes on the bivalent, or rings with many fragments were considered “severely mispatterned.”

Linescans

For Figure 2, linescans were performed in ImageJ. Fluorescence intensity linescans of normal or fused chromosomes were performed along the pole-pole axis, as determined by tubulin intensity, at 40 x 30 pixels (L x W) (n = 25). Only clearly bipolar spindles were used for analysis, and all images had the same exposure conditions. Both chromosome length and fluorescence intensity were normalized to a maximum of 1, and the average (solid line) and standard error of the mean (SEM, shaded), of both DNA and SUMO were plotted using the ggplot2 package in Jupyter Notebook.

Metaphase Alignment Quantification

For Figure 4A, *meT7* worms were arrested in metaphase using *emb-30* RNAi. The metaphase plate was determined by rotating the image in 3D using Imaris until a single plane could be determined by eye based on SUMO-stained RCs on chromosomes I, II and V. The average total width of SUMO intensity of chromosomes I, II and V was measured using Imaris per spindle at the determined metaphase plate. The *meT7* fusion chromosome was considered “unaligned” if greater than 50% of its SUMO intensity fell outside of 2 standard deviations of the average width of chromosomes I, II and V from the determined metaphase plate.

Chromosome Distance Measurements

For Figure 4B, chromosome-to-pole distances were measured using Imaris. The center of the monopole was determined by using the "Surfaces" tool to determine the volume of the ASPM-1 region and to assign the center of this volume. Then, the distance between this point and the center of each chromosome was measured. Per spindle, the average of the distances to chromosomes I, II and V was subtracted from each individual distance to chromosomes I, II, or V (green points on the diagram/graph in Figure 3C) or to the fused chromosome (blue points). For Figure S3, "mid-to-late anaphase" was defined as having a chromosome-to-chromosome segregation distance of 2.5μM as measured by Imaris using the "surfaces" tool (Davis-Roca et al. 2017).

Chromatin Bridging Quantification

DNA was denoted as bridged if in anaphase the width of the bridge was less than the width at either end of the segregating chromosomes. Otherwise, a single *meT7* chromosome mass in anaphase was marked as showing delayed segregation, and two distinct segregating *meT7* masses with no connecting DNA were considered wild type.

Meiosis II Quantification

By eye, ploidy was determined based on chromosome counts on MII spindles (i.e. oocytes were considered aneuploid if the number of Hoechst-stained bodies was not equal to 4). Incomplete polar body extrusion was defined by a clear continual strand of DNA connecting a polar body to a chromatid pair within a forming or formed MII

spindle. Polar bodies were determined to be DNA masses in close proximity to, yet remaining outside of, forming MII spindles.

**Scoring Embryonic Viability**

Viability counts (percent hatching) were determined by singling out 5-15 L4s onto individual plates and growing them at 25°C until broods were produced. Mothers were transferred to new plates each day and allowed to produce broods until they no longer laid fertilized embryos. After mothers were moved, embryos and larvae were counted, and then returned to 25°C and allowed to develop for 18-24 hours (wild type) or 40-48 hours (*meT7*) before counting unhatched embryos. *meT7* embryos were given more time to develop, as the strain develops more slowly than wild type.

**Live Imaging**

Live imaging of oocyte meiotic chromosome segregation in wild type and *meT7* fluorescent fusion lines was accomplished by cutting open adult worms with a single row or less of embryos in 4µl of egg buffer (118mM NaCl, 48mM KCl, 2mM $CaCl_2$, 2mM $MgCl_2$, and 0.025 mM HEPES, filter sterilized before HEPES addition) on a coverslip and gently mounting onto a 2% agarose pad on a microscope slide. Worms were synchronized by hypochlorite hatch-off, and plated worms were upshifted at 25°C overnight before imaging. Oocytes were imaged using a spinning disk confocal unit, CSU-W with Borealis (Andor), and dual iXon Ultra 897 (Andor) cameras mounted on an inverted Leica DMi8 microscope, with a 100x HCX PL APO 1.4NA oil objective lens (Leica). The imaging system was controlled via Metamorph (Molecular Devices)

software. Oocytes were imaged every 5 seconds with 1μm Z-spacing (16μm total Z-stack) and the 488nm and 561nm channels were imaged simultaneously. After recording, movies were maximum projected, cropped, and color channels were adjusted independently for brightness and contrast in ImageJ (National Institutes of Health).

**Statistical Analysis**

All reported p-values are based on Pearson's chi-square statistical tests comparing stated frequency distributions. A P-value less than 0.05 was considered statistically significant.

# APPENDIX D: SUPPLEMENTAL MATERIALS FOR CHAPTER III

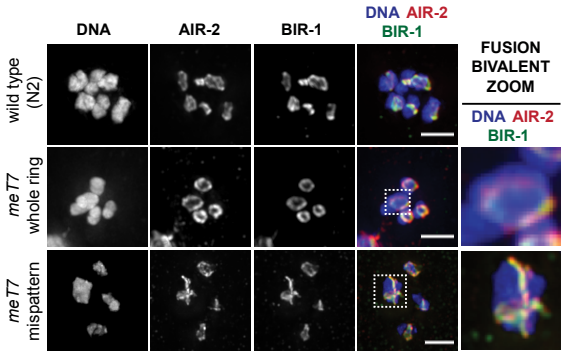


**Figure D.1 – Additional characterization of CPC components (related to Figure 3.2)**
BIR-1 (green) and AIR-2 (red) colocalize on all ring structure types on *meT7*. Scale bars = 2.5µm

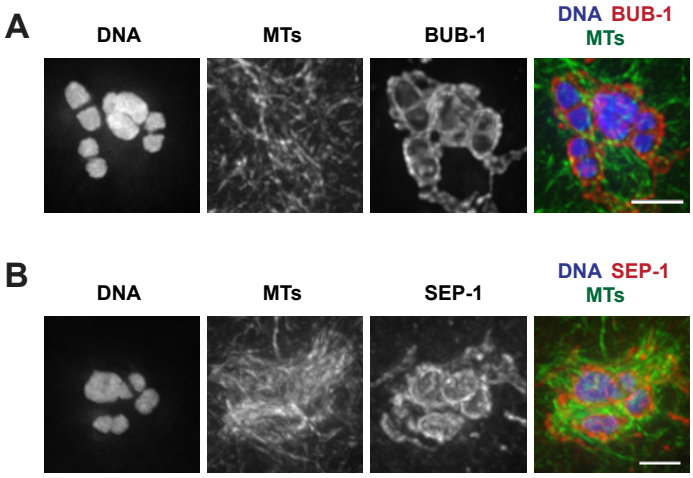


**Figure D.2 – The holocentric kinetochore cups the entirety of *meT7***
(A) Localization of kinase BUB-1 (red) on prometaphase I chromosomes (blue); microtubules shown in green. Since C. elegans chromosomes are holocentric, kinetochore proteins cup the ends of normal bivalents, in addition to forming filaments within the spindle. In meT7 fusion bivalents, the kinetochore cups the entirety of the bivalent. (B) Localization of SEP-1 (as another marker of the kinetochore, red) on prometaphase I chromosomes (blue), demonstrating the same organization as BUB-1. All scale bars = 2.5µm.

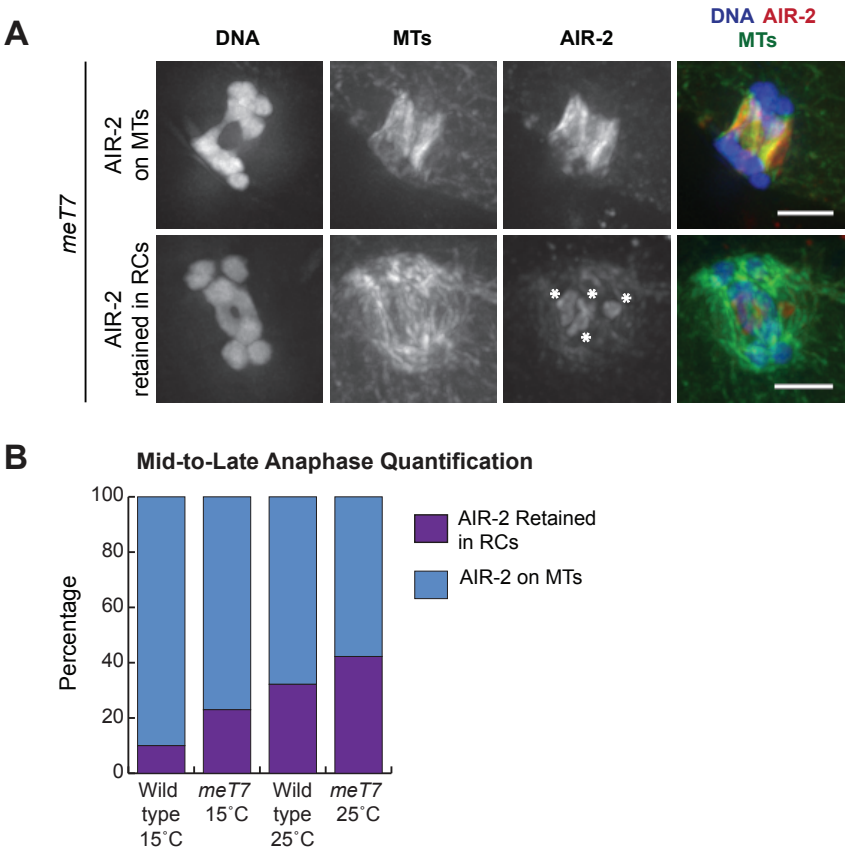


**Figure D.3 – RCs show an increased frequency of delayed disassembly in *meT7* oocytes, demonstrating that errors are recognized**
(A) In late anaphase, AIR-2 (red) either relocalizes to the spindle (top row) or stays RC-associated in meT7 (bottom row; RCs indicated with asterisks), indicative of an RC disassembly delay. Scale bars = 2.5µm. (B) Quantification of Air-2 localization in late anaphase. At 15°C, 10% of N2 spindles showed a delay in ring disassembly, whereas 23% of meT7 spindles showed the same behavior (N=31, both conditions). The frequency of RC delayed disassembly increased at 25°C to 33% in wild type (N=42) and 41% in *meT7* spindles (N=29).

| | Condition | | | |
|---|---|---|---|---|
| **Phenotype** | **Wild Type** | **Wild Type *lem-3(RNAi)*** | ***meT7* (III;X;IV)** | ***meT7* (III;X;IV) *lem-3(RNAi)*** |
| **Normal Segregation (MI and MII)** | 15/15 | 8/8 | 3/14 | 3/13 |
| **Normal Segregation MI, MII maybe lagging chromosome** | - | - | 2/14 | - |
| ***meT7* Bivalent Remains in Cytoplasm (MI)** | - | - | 1/14 | - |
| **MI Anaphase Bridge - Resolves** | - | - | 3/14 | - |
| **MI Anaphase Bridge – MII Spindle Tether** | - | - | 5/14 | 2/13 |
| **MI Anaphase Bridge – Possible Fragments** | - | - | - | 2/13 |
| **MI Fails Polar Body Extrusion** | - | - | - | 1/13 |
| ***meT7* Bivalent Extruded into Polar Body (MI)** | - | - | - | 5/13 |

**Table D.1 – Frequency of chromosome segregation phenotypes from live imaging experiments**

# APPENDIX E: MATERIALS AND METHODS FOR CHAPTER IV

## *C. elegans* Strain Maintenance

All *C. elegans* strains used in this study (Supplemental Table 1, found in Appendix F), were maintained at 20ºC as described previously (Brenner, 1974).

## *cls-2* CRISPR/Cas9 Allele Generation

Mutations in *cls-2* were generated by injecting young adult N2 hermaphrodites with the following mixture (Paix et al., 2015): 25µM *cls-2* crRNA (ATCAGCCGATCGACTCCGGG), 5µM *dpy-10* crRNA (GCTACCATAGGCACCAC GAG), 30µM trRNA, 2.1µg/µl Cas9-NLS, and 2.5µM *dpy-10* single-strand DNA (ssDNA, CACTTGAACTTCAATACGGCAAGATGAGAATGACTGGAAACCGTA CCGCATGCGGTGCCTATGGTAGCGGAGCTTCACATGGCTTCAGACCAACAGC CTAT). No homologous repair template was used for *cls-2,* and *cls-2* DNA breaks were allowed to repair randomly. Before injection, the trRNA and crRNAs were mixed and incubated at 95ºC for 5 minutes, before cooling at room temperature for 5 minutes. After cooling, Cas9-NLS (QB3-Berkeley MacroLab) was added to the annealed trRNA and crRNAs and allowed to incubate for another 5 minutes at room temperature before the *dpy-10* ssDNA repair template was added. After injection, hermaphrodites were singled out and their broods were screened for *dpy-10* roller or dumpy co-conversion worms, which were allowed to produce broods. Those broods were then evaluated for potential *cls-2* phenotypes (embryonic lethality), and lines identified as potentially carrying

mutations to *cls-2* were balanced. PCR amplified fragments were Sanger sequenced to identify the CRISPR/Cas9-induced mutations.

**Feeding RNAi Knockdown of *mei-1* and *klp-18***

RNAi knockdown of *mei-1* and *klp-18* was achieved by plating hypochlorite synchronized L1 larvae onto *E. coli* (HT115) lawns induced to express dsRNA corresponding to *mei-1* or *klp-18 (Kamath et al., 2001)*. Plated worms were either maintained at 20ºC until adults were imaged (*mei-1*) or maintained at 20ºC and upshifted to 26ºC 16 hours prior to imaging (*klp-18*) to ensure robust knockdown, as determined by the formation of monopolar meiotic spindles in both meiosis I and II. The *mei-1* RNAi vector was from the Ahringer RNAi library (Fraser et al., 2000). The *klp-18* RNAi vector was made by amplifying a portion of the *klp-18* coding sequence from isolated N2 genomic DNA (using primers 5'ACCGGCAGATCTGATATCATCGATGAATTCT CCAACTTTCAAATGCCACA-3' and 5'-ACGGTATCGATAAGCTTGATATCGAA TTCCTTCGATATGGAAGAAAGC GG-3'), which was inserted into the L4440 vector backbone using the NEBuilder HiFi DNA assembly cloning kit (NEB).

**Live-cell Imaging**

All imaging was carried out using a Leica DMi8 microscope outfitted with a spinning disk confocal unit – CSU-W1 (Yokogawa) with Borealis (Andor), dual iXon Ultra 897 (Andor) cameras, and a 100x HCX PL APO 1.4-0.70NA oil objective lens (Leica). Metamorph (Molecular Devices) imaging software was used for controlling image acquisition. The 488nm and 561nm channels were imaged simultaneously every

10 seconds with 1μm Z-spacing (either 16μm or 21μm total Z-stacks depending on the fluorescent markers used, with the same stack size used for all movies utilizing the same fluorescent markers).

*In utero* live imaging of oocytes was accomplished by mounting adult worms with a single row or less of embryos in 1.5μl of M9 mixed with 1.5μl of 0.1μm polystyrene Microspheres (Polysciences Inc.) on a 6% agarose pad with a coverslip gently laid over top. *Ex utero* imaging of oocytes was carried out by cutting open adult worms with a single row or less of embryos in 4μl of egg buffer (118mM NaCl, 48mM KCl, 2mM $CaCl_2$, 2mM $MgCl_2$, and 0.025 mM of HEPES, filter sterilized before HEPES addition) on a coverslip before mounting onto a 2% agarose pad on a microscope slide.

**Image Analysis, Quantification, and Statistical Analysis**

General image analysis and quantification of microtubules and global cortical furrowing was carried out using FIJI software (Schindelin et al., 2012). Three-dimensional projection and rotation of movies used to look at polar body contractile rings was carried out using Imaris software (Bitplane). Meiosis I polar body extrusion success was evaluated based on whether oocytes extruded any chromosomes marked by GFP or mCherry histone 2B (H2B) into a polar body that remained extruded for the period of imaging, either until meiosis I had obviously ended and meiosis II spindle assembly began, or until pronuclei began to decondense in the one-cell stage embryo after meiosis II. The end of meiosis I and beginning of meiosis II was considered to be the time at which the chromosomes left in the oocyte cytoplasm began to visibly separate from each other. Projections for spindle-associated furrow examination were made by manually

isolating the 5 most spindle-associated z-planes for each time point during the period of global cortical furrowing and then sum projecting the mCherry::PH membrane signal. Membrane temporal overlays were created by overlaying the outlined membrane regions of interest for the period of furrowing (detailed below) to create a single image.

Total spindle microtubule pixel intensity was determined using the following formula: (Mean Grey Value (spindle)/Mean Grey Value (cytoplasm)) × spindle area = total spindle microtubule pixel intensity. The mean grey values for both the meiotic spindle and cytoplasm were determined by drawing a region of interest around either the meiotic spindle or a portion of oocyte cytoplasm devoid of adjacent sperm in maximum projected Z-stacks and measuring the mean grey value of the selected region in ImageJ. Spindle area was determined by measuring the area of the region of interest encompassing the meiotic spindle.

Quantification of global cortical furrowing was accomplished by drawing regions of interest over the oocyte membrane signal (mCherry::PH) for a single central z-slice for the entire period of global cortical furrowing. Regions of interest were then converted to a high contrast stack of membrane positions over time, which were then analyzed using the ADAPT plugin (Barry et al., 2015) for ImageJ in order to determine curvature values across the oocyte membrane. A furrow was defined as being at least two consecutive membrane points with negative mean curvature values and a standard deviation of mean curvature at least two standard deviations above the average standard deviation of mean curvature value for the entire oocyte membrane. Membrane points fitting the criteria of a furrow (above) that were separated by a single membrane point not fitting the criteria were considered as part of the same furrow for the purposes of counting. For statistical

analysis of global cortical furrowing (Figure 4.7), one-way ANOVA was used to determine if there was any difference in the mean furrowing between genotypes, F-Tests to compare the variances, and two-tailed Student's t-Tests between genotypes to compare the means directly (assuming either equal or unequal variances depending on the F-Test results). Statistical analysis and graphs were completed using Excel (Microsoft).

# APPENDIX F: SUPPLEMENTAL MATERIALS FOR CHAPTER IV

| Strain # | Genotype |
|---|---|
| N2 | *Wild type* |
| EU3020 | *cls-2(or1948) /qC1[qIs26] III* |
| EU3021 | *cls-2(or1949) /qC1[qIs26] III* |
| EU3022 | *cls-2(or1950) /qC1[qIs26] III* |
| EU3023 | *cls-2(or1951) /qC1[qIs26] III* |
| EU3030 | *ijmSi3 [pJD342/pJD330; Chrl_5'mex-5_cls-2reenc::GFP_3'tbb-2; cb-unc-119(+)] I; unc-119(ed3) III?; itIs37[pie-1p::mCherry::H2B::pie-1 3'UTR + unc-119(+)] IV* |
| EU2942 | *ruIs57[pie-1p::GFP::tubulin + unc-119(+)]; itIs37[pie-1p::mCherry::H2B::pie-1 3'UTR + unc-119(+)] IV* |
| EU3025 | *cls-2(or1948) /qC1[qIs26] III ; ruIs57[pie-1p::GFP::tubulin + unc-119(+)]; itIs37[pie-1p::mCherry::H2B::pie-1 3'UTR + unc-119(+)] IV* |
| EU2876 | *or1935[GFP::aspm-1] I; itIs37[pie-1p::mCherry::H2B::pie-1 3'UTR + unc-119(+)] IV* |
| EU3031 | *or1935[GFP::aspm-1] I ; cls-2(or1948)/qC1[qIs26] III ; itIs37[pie-1p::mCherry::H2B::pie-1 3'UTR + unc-119(+)] IV* |
| OD224 | *unc-119(ed3) III; ltIs37 [pAA64; pie-1/mCHERRY::his-58; unc-119(+)] ltIs14 [pASM05; pie-1/GFP-TEV-STag::air-2; unc-119(+)]IV* |
| EU3108 | *cls-2(or1948) /qC1[qIs26] III; ltIs37 [pAA64; pie-1/mCHERRY::his-58; unc-119(+)] ltIs14 [pASM05; pie-1/GFP-TEV-STag::air-2; unc-119(+)]IV* |
| EU3061 | *mgSi43 [cyk-4p::cyk-4::GFP::pie-1 3'UTR + Cbr-unc-119(+)] II ; itIs37[pie-1p::mCherry::H2B::pie-1 3'UTR + unc-119(+)] IV* |
| EU3067 | *cls-2(or1948) /qC1[qIs26] III ; mgSi43 [cyk-4p::cyk-4::GFP::pie-1 3'UTR + Cbr-unc-119(+)] II ; itIs37[pie-1p::mCherry::H2B::pie-1 3'UTR + unc-119(+)] IV* |
| EU3122 | *ruIs32[unc-119(+) pie-1::GFP::H2B] (may contain unc-119 (eds) III; ltIs44V[pie-1p-mCherry::PH(PLC1delta1) + unc-119(+)]* |
| EU3105 | *cls-2(or1948) /qC1[qIs26] ruIs32[unc-119(+) pie-1::GFP::H2B] (may contain unc-119 (eds) III; ltIs44V[pie-1p-mCherry::PH(PLC1delta1) + unc-119(+)]* |
| EU3080 | *nmy-2(cp13[nmy-2::gfp + LoxP]) I; itIs37[pie-1p::mCherry::H2B::pie-1 3'UTR + unc-119(+)] IV* |
| EU3079 | *nmy-2(cp13[nmy-2::gfp + LoxP]) I; cls-2(or1948) /qC1[qIs26] III; itIs37[pie-1p::mCherry::H2B::pie-1 3'UTR + unc-119(+)] IV* |
| EU3146 | *ani-1(mon7[mNeonGreen^3xFlag::ani-1]) III; itIs37[pie-1p::mCherry::H2B::pie-1 3'UTR + unc-119(+)] IV* |
| EU3153 | *cls-2(or1948) /qC1[qIs26] ani-1(mon7[mNeonGreen^3xFlag::ani-1]) III; itIs37[pie-1p::mCherry::H2B::pie-1 3'UTR + unc-119(+)] IV* |
| EU3166 | *nmy-2(cp52[nmy-2::mkate2 + LoxP unc-119(+) LoxP]) I; ani-1(mon7[mNeonGreen^3xFlag::ani-1]) III; itIs37[pie-1p::mCherry::H2B::pie-1 3'UTR + unc-119(+)] IV* |
| EU3172 | *nmy-2(cp52[nmy-2::mkate2 + LoxP unc-119(+) LoxP]) I; cls-2(or1948)/qC1[qIs26] ani-1(mon7[mNeonGreen^3xFlag::ani-1]) III; itIs37[pie-1p::mCherry::H2B::pie-1 3'UTR + unc-119(+)] IV* |

**Table F.1 - Table of *C. elegans* strains used in this study**

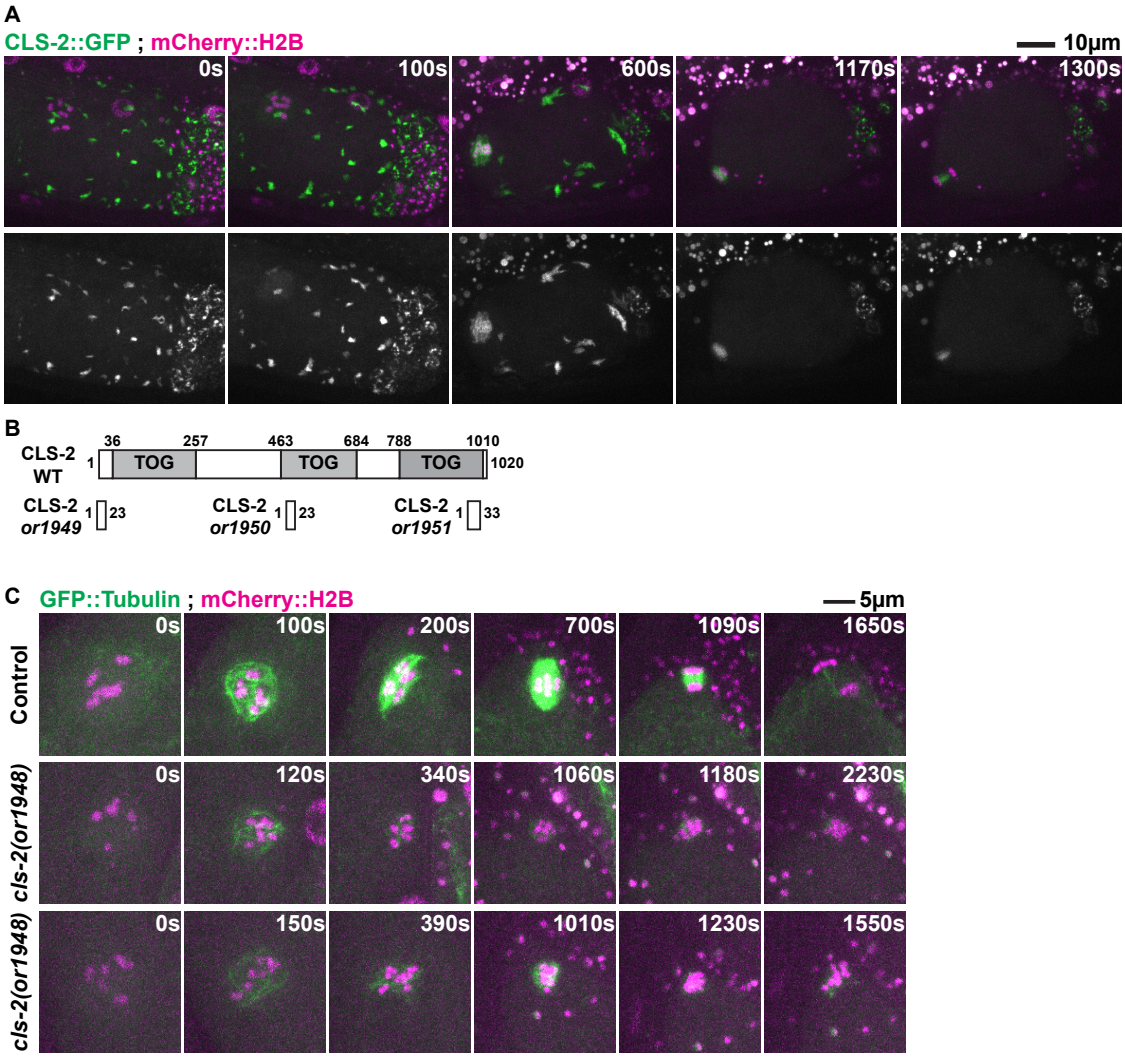


**Figure F.1 – CLS-2 localizes to meiotic spindles and is required for their assembly**

(A) *In utero* time-lapse spinning disk confocal images of CLS-2::GFP and mCherry::H2B.

(B) Protein domain maps of wild type CLS-2 and CRISPR-generated *cls-2* alleles *or1949*, *or1950*, and *or1951*. Each mutation results in multiple early stop codons before the first TOG domain, with the first stop codon indicated.

(C) *In utero* time-lapse spinning disk confocal images of control and *cls-2* mutant oocytes with GFP::TBB-2 and mCherry::H2B. t = 0 seconds corresponds to nuclear envelope breakdown.

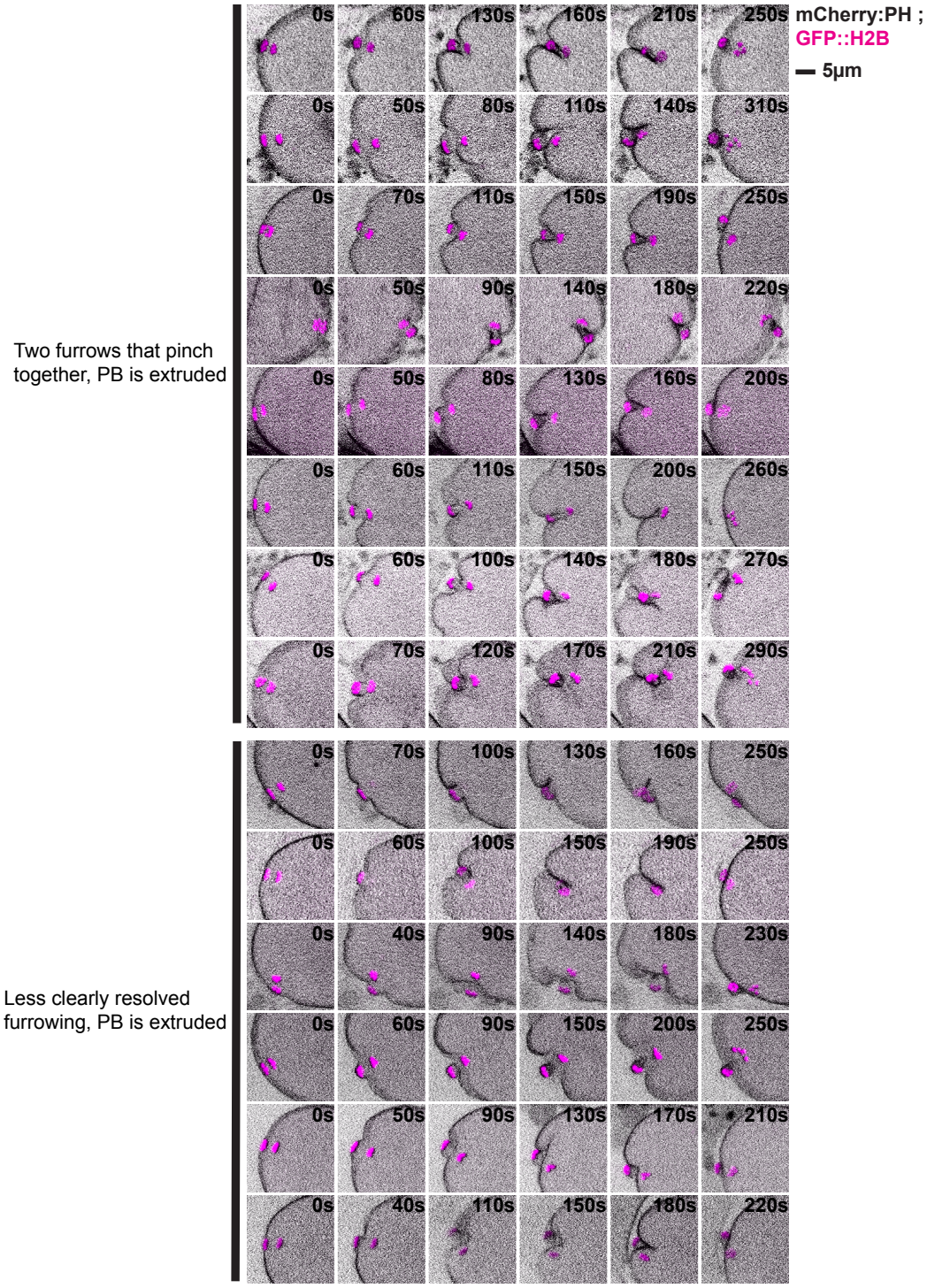


**Figure F.2 – Control oocyte spindle-associated membrane furrows**
Time-lapse spinning disk confocal images of control oocytes expressing mCherry::PH and GFP::H2B; t = 0 seconds here and in subsequent figure 4.4 related supplements (supplemental figures 4.3-4.6) corresponds to the time point immediately before global cortical furrowing begins, unless otherwise stated.

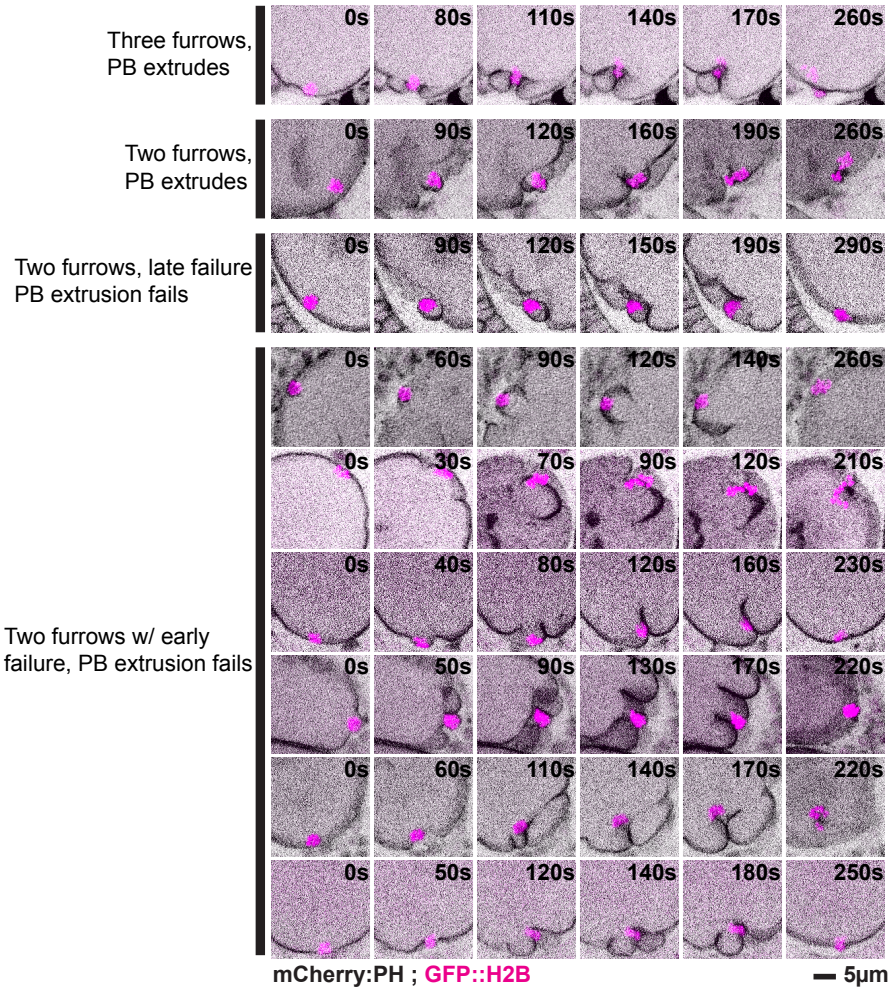


**Figure F.3 – *cls-2(or1948)* oocyte spindle-associated membrane furrows**
Time-lapse spinning disk confocal images of *cls-2* mutant oocytes expressing mCherry::PH and GFP::H2B.

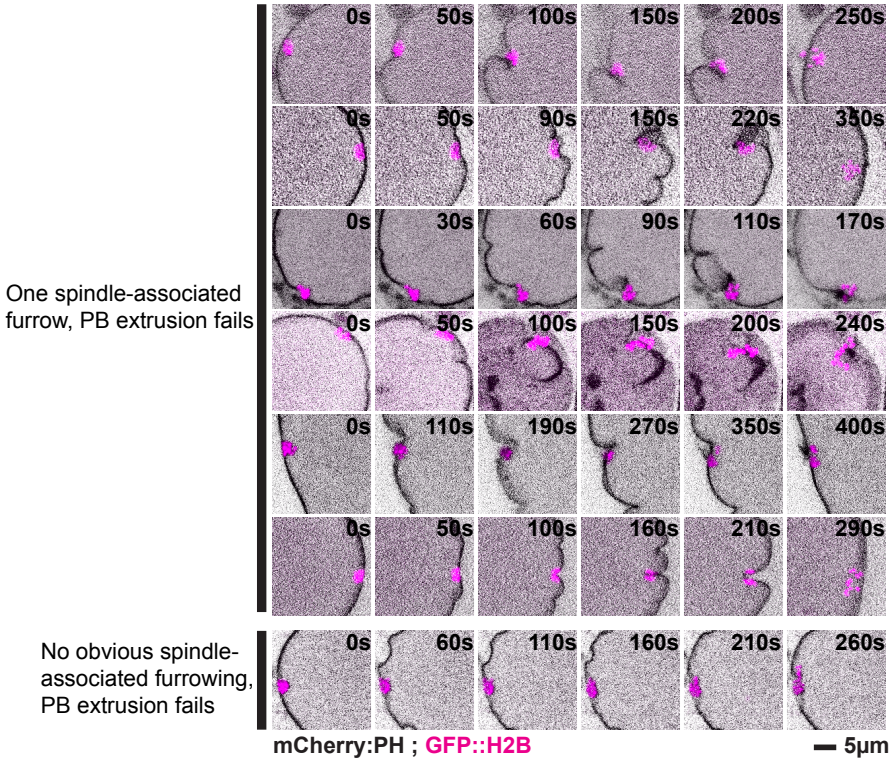


**Figure F.4 – *cls-2(or1948)* oocyte spindle-associated membrane furrows**
Time-lapse spinning disk images of *cls-2* mutant oocytes expressing mCherry::PH and GFP::H2B.

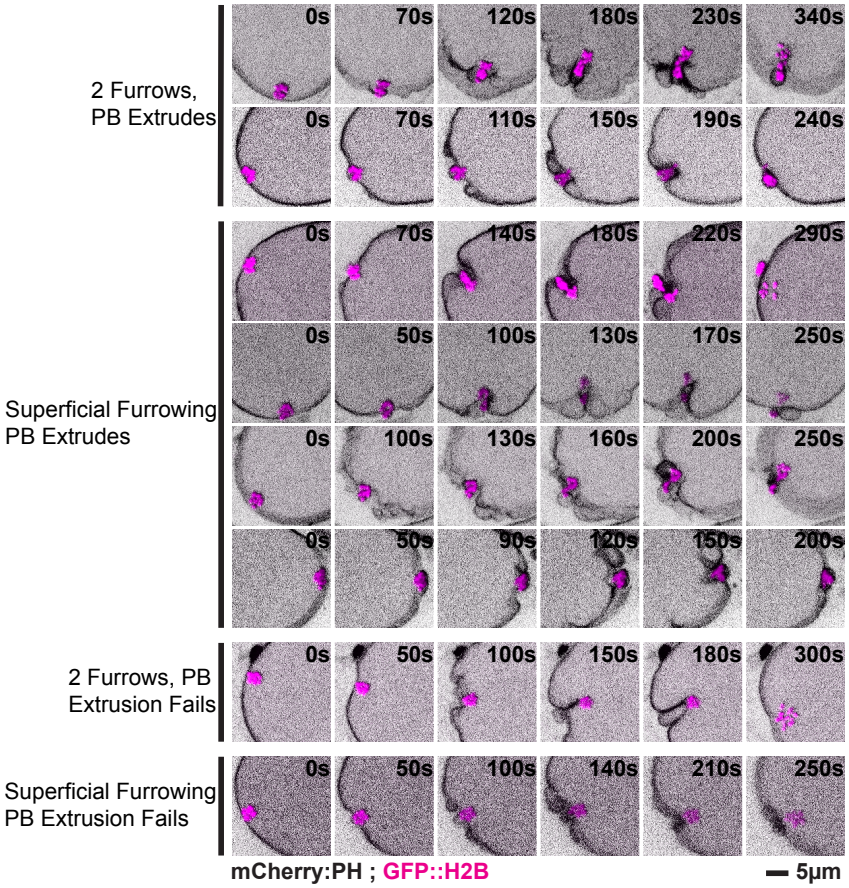


**Figure F.5 – *klp-18(RNAi)* oocyte spindle-associated membrane furrows**
Time-lapse spinning disk confocal images of *klp-18(RNAi)* oocytes expressing mCherry::PH and GFP::H2B.

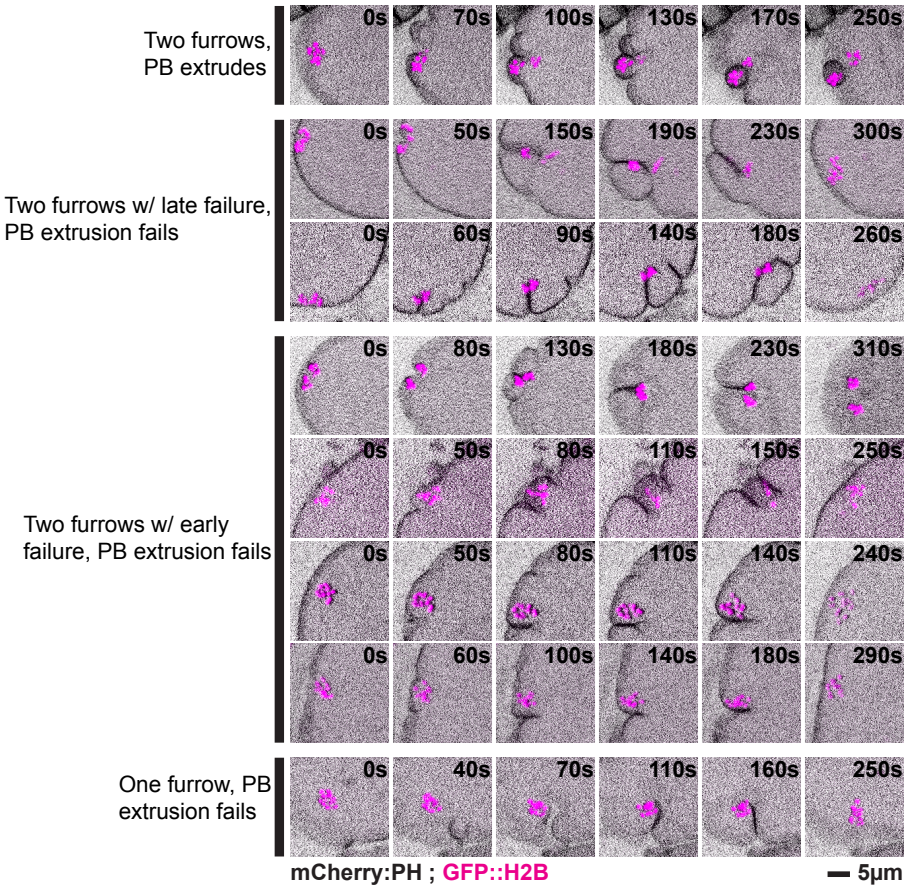


**Figure F.6 – *mei-1(RNAi)* oocyte spindle-associated membrane furrows**
Time-lapse spinning disk confocal images of *mei-1(RNAi)* oocytes expressing mCherry::PH and GFP::H2B.

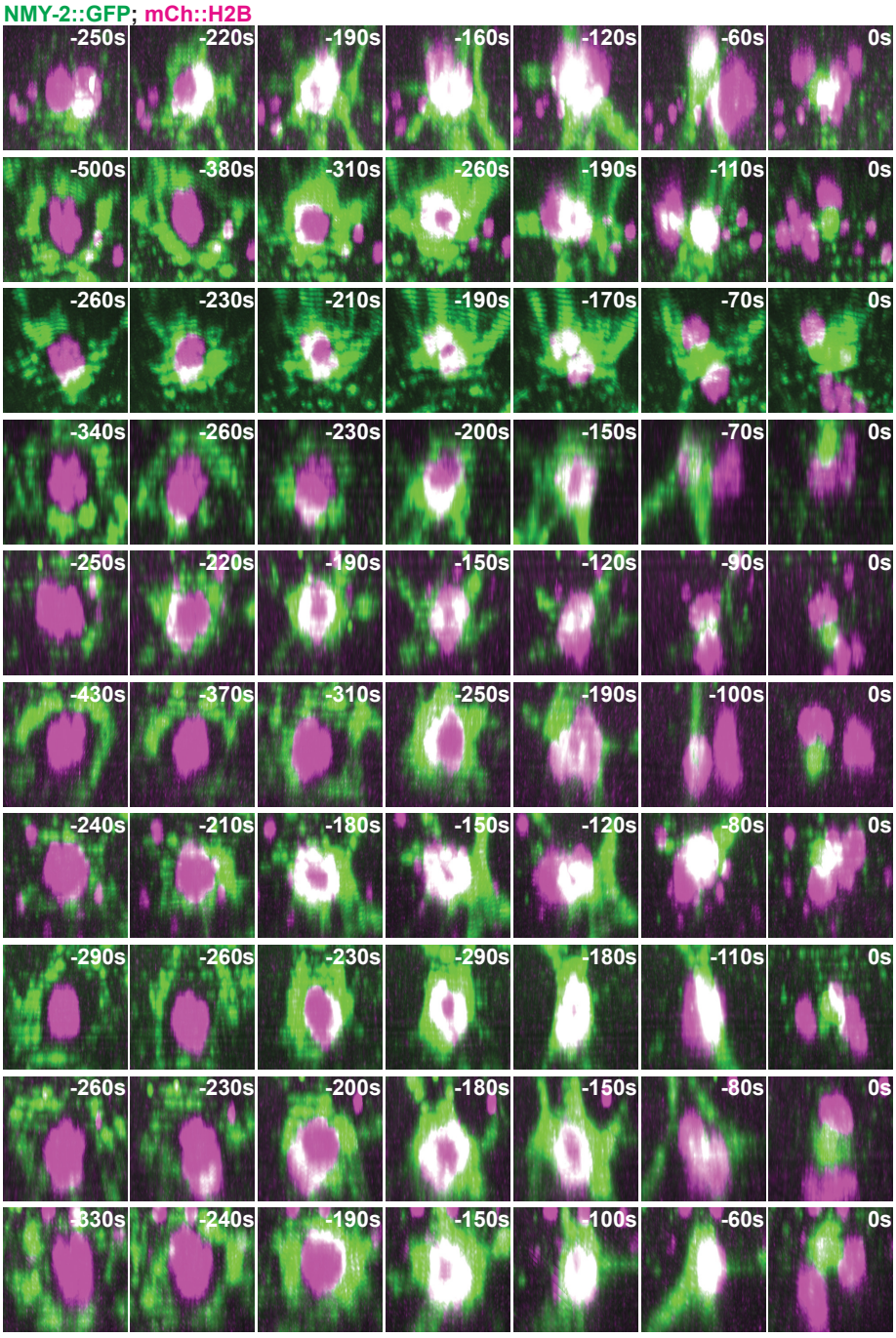


**Figure F.7 – Control oocyte NMY-2::GFP contractile rings**
Three-dimensionally projected and rotated spinning disk confocal time-lapse images of control oocytes expressing NMY-2::GFP and mCherry::H2BB; t = 0 seconds in this and subsequent figure 4.5 related supplements (supplemental figures 4.8-4.10)

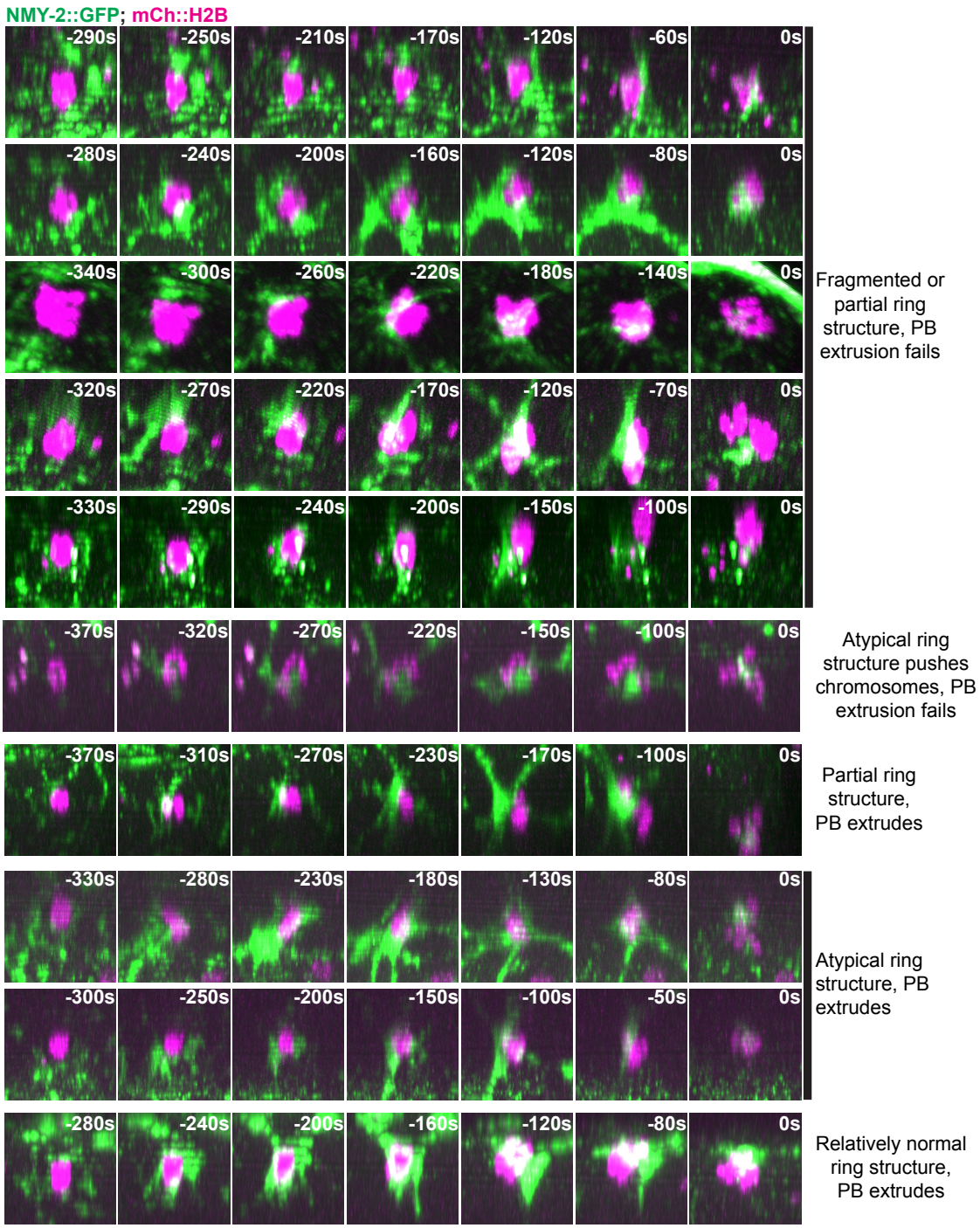


**Figure F.8 – *cls-2(or1948)* oocyte NMY-2::GFP contractile rings**
Three-dimensionally projected and rotated spinning disk confocal time-lapse images of *cls-2* mutant oocytes expressing NMY-2::GFP and mCherry::H2B.

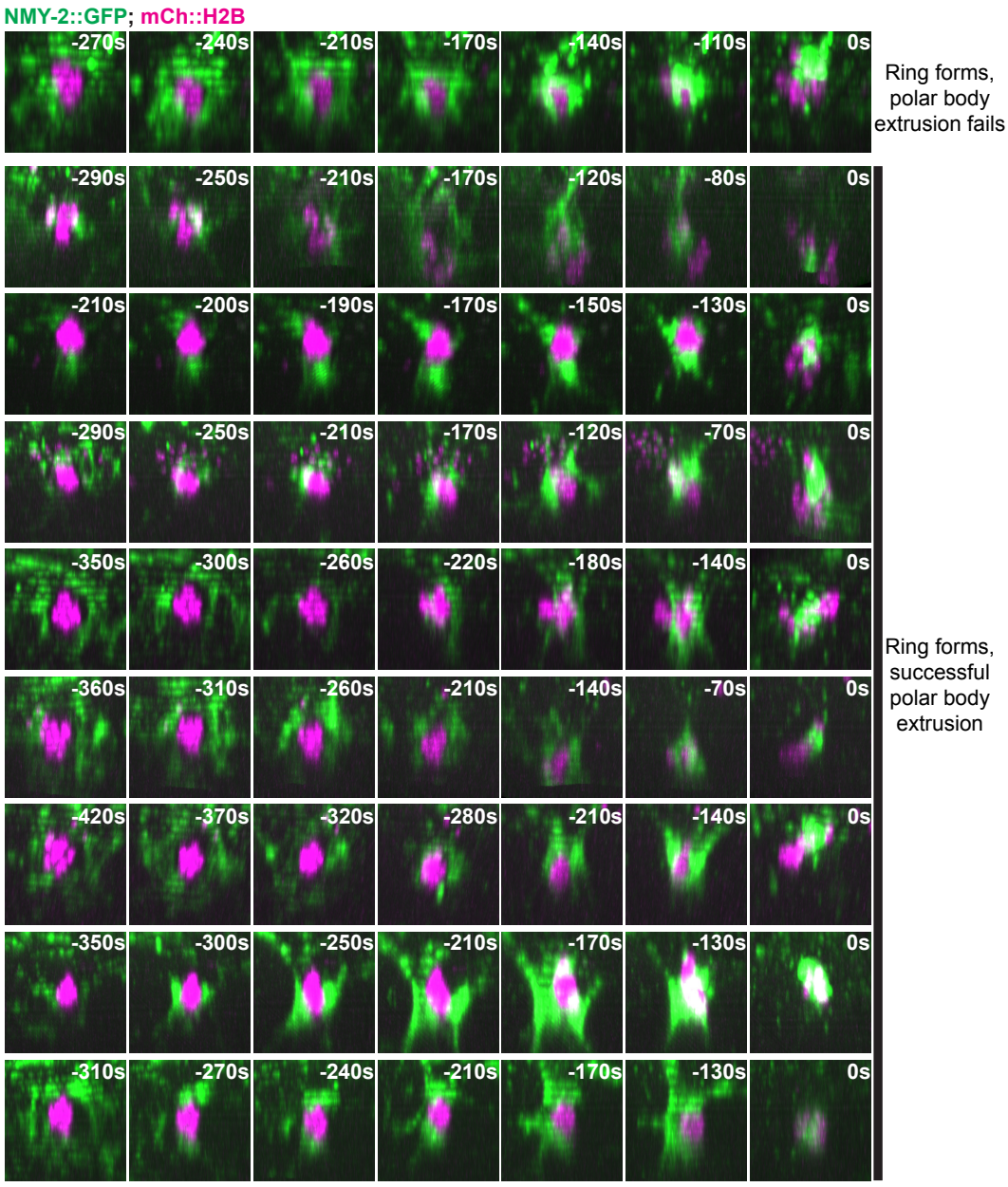


**Figure F.9 – *klp-18(RNAi)* oocyte NMY-2::GFP contractile rings**
Three-dimensionally projected and rotated spinning disk confocal time-lapse images of *klp-18(RNAi)* oocytes expressing NMY-2::GFP and mCherry::H2B.

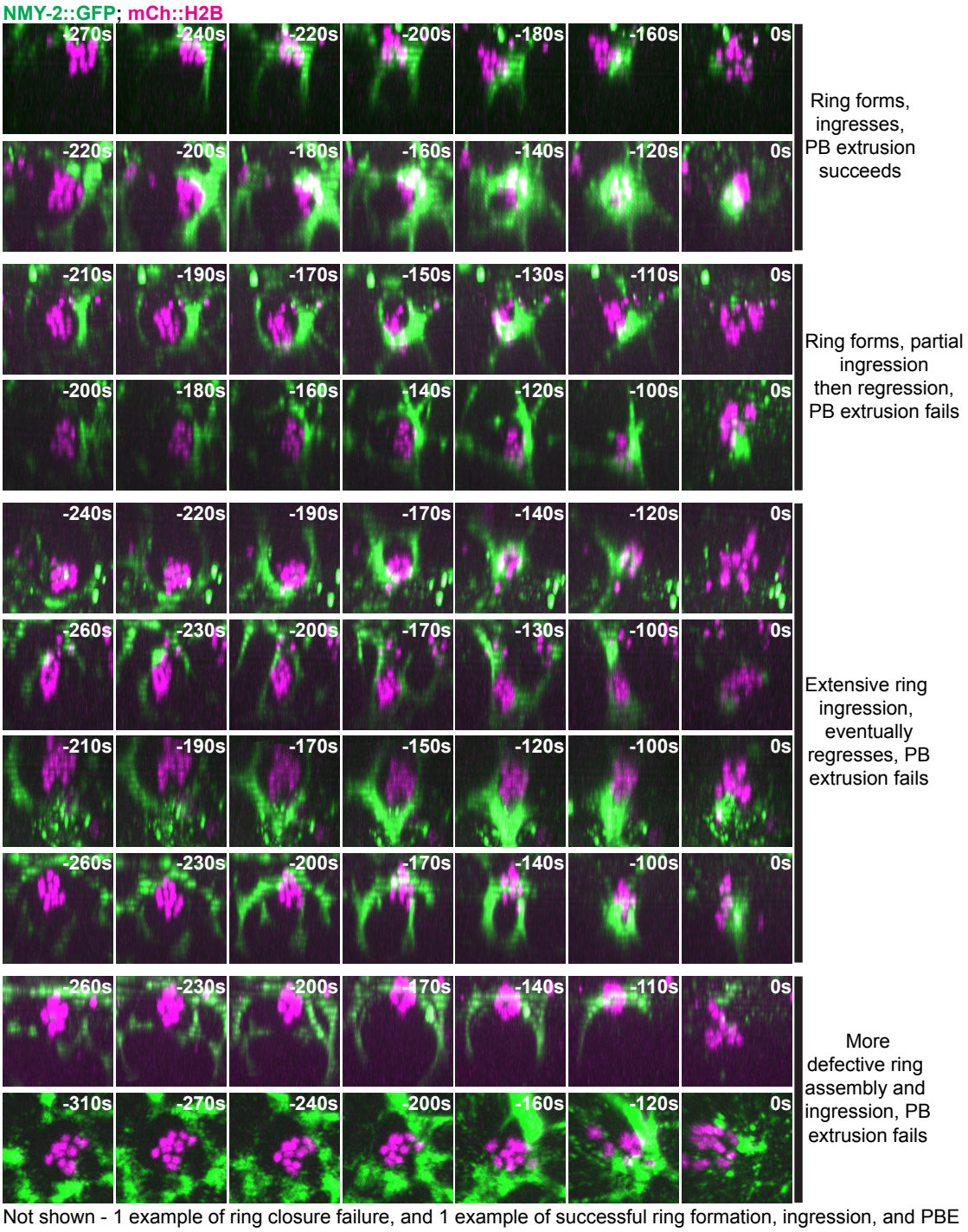


**Figure F.10 – *mei-1(RNAi)* oocyte NMY-2::GFP contractile rings**
Three-dimensionally projected and rotated spinning disk confocal time-lapse images of *mei-1(RNAi)* oocytes expressing NMY-2::GFP and mCherry::H2B.

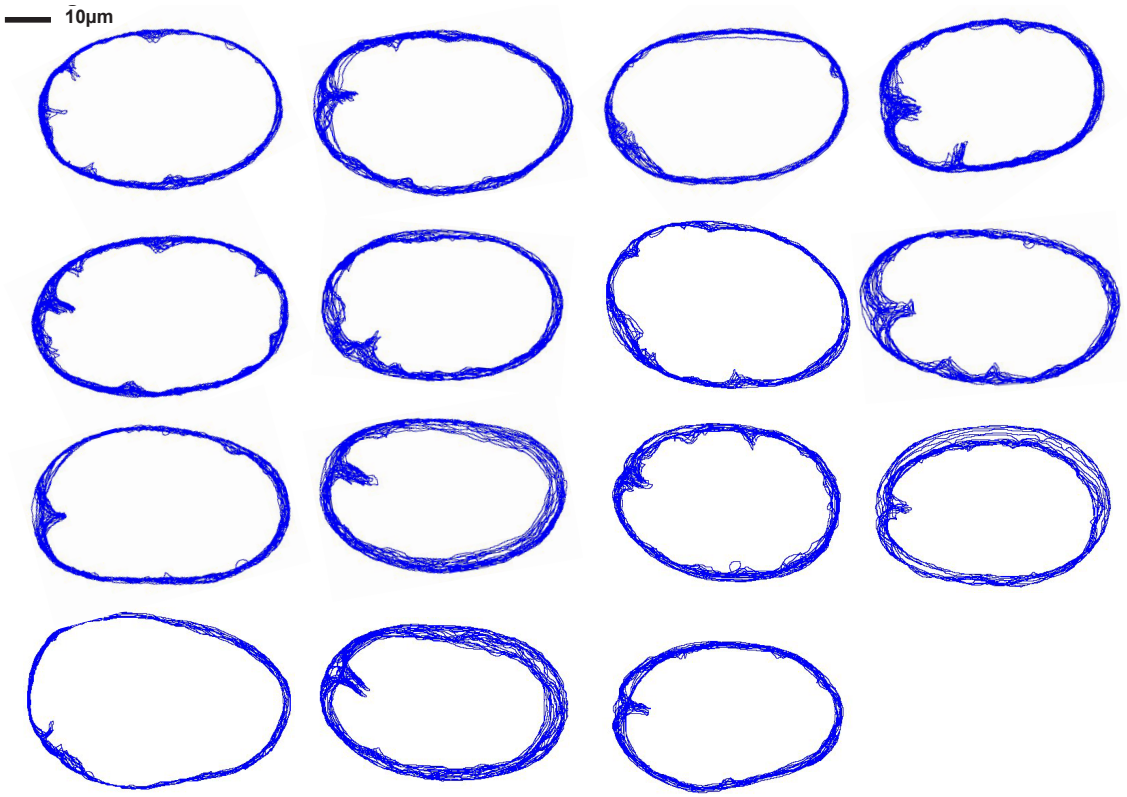


**Figure F.11 – Control oocyte membrane temporal overlays**
Control oocyte membrane temporal overlays depicting membrane positions over time at a single focal plane throughout meiosis I.

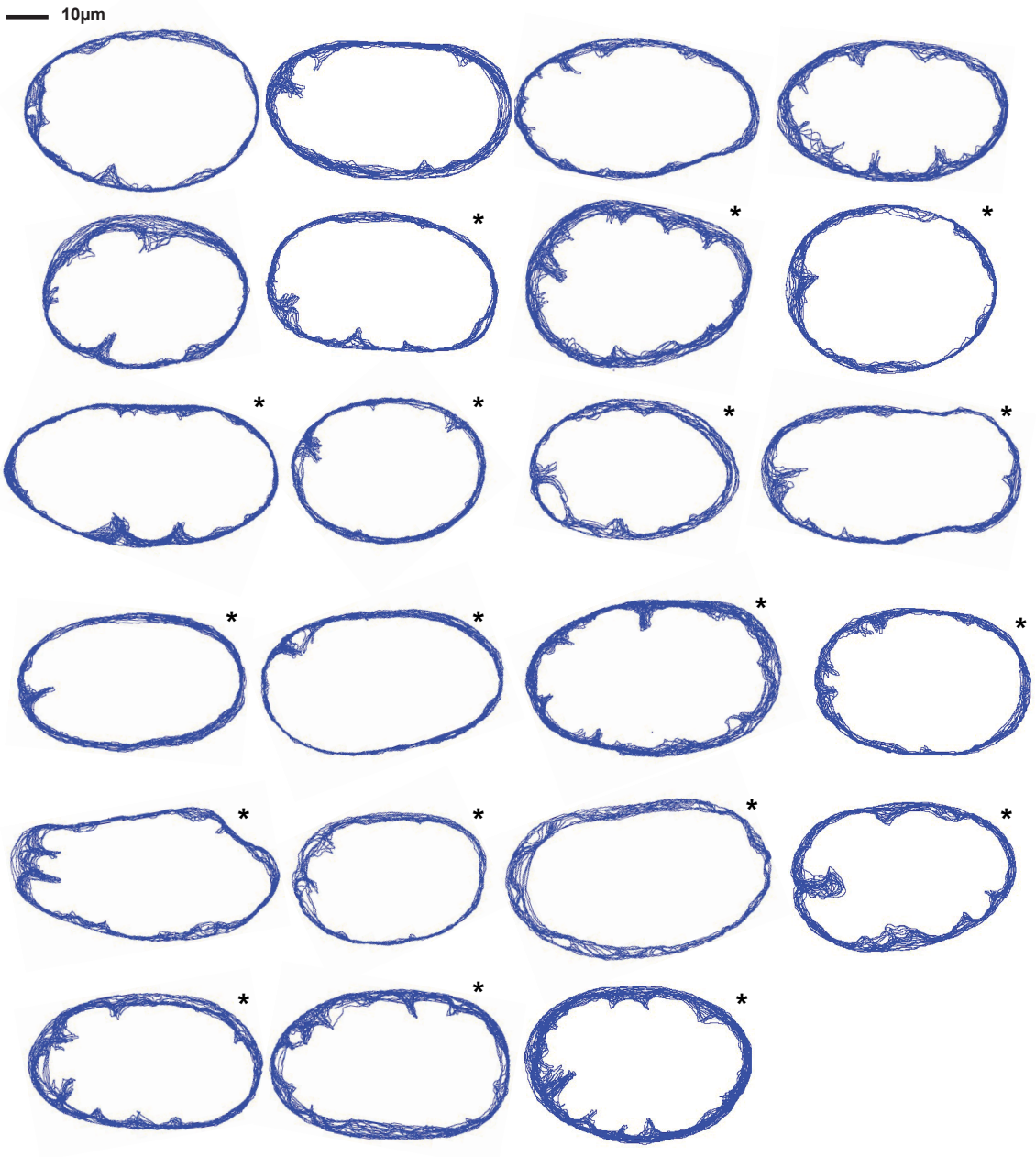


**Figure F.12 – *cls-2(or1948)* oocyte membrane temporal overlays**
*cls-2* mutant oocyte membrane temporal overlays depicting membrane positions over time at a single focal plane throughout meiosis I. Asterisks indicate oocytes in which polar body extrusion failed.

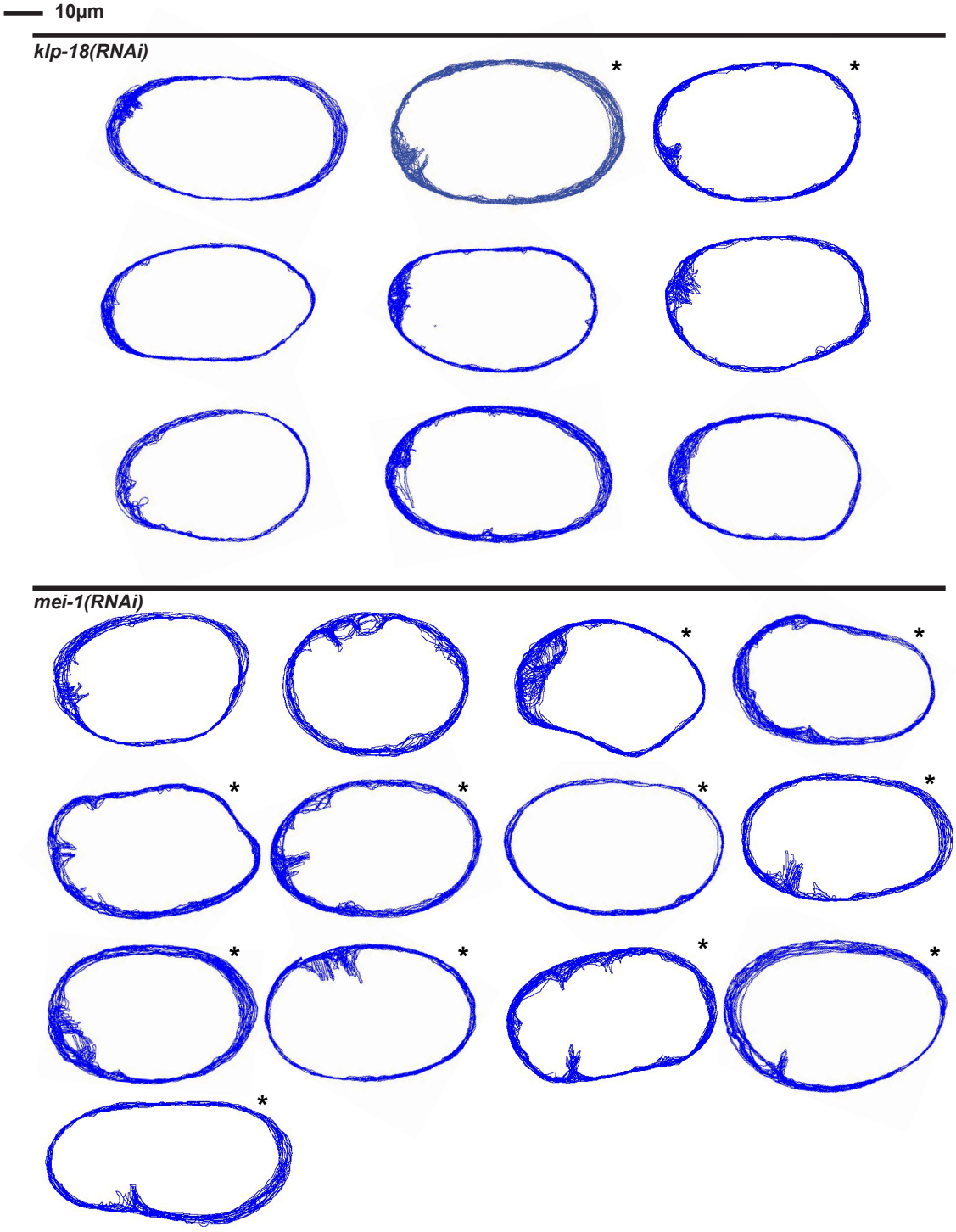


**Figure F.13 – *klp-18(RNAi)* and *mei-1(RNAi)* membrane temporal overlays**
*klp-18(RNAi)* and *mei-1(RNAi)* oocyte membrane temporal overlays depicting membrane positions over time at a single focal plane throughout meiosis I. Asterisks indicate oocytes in which polar body extrusion failed.

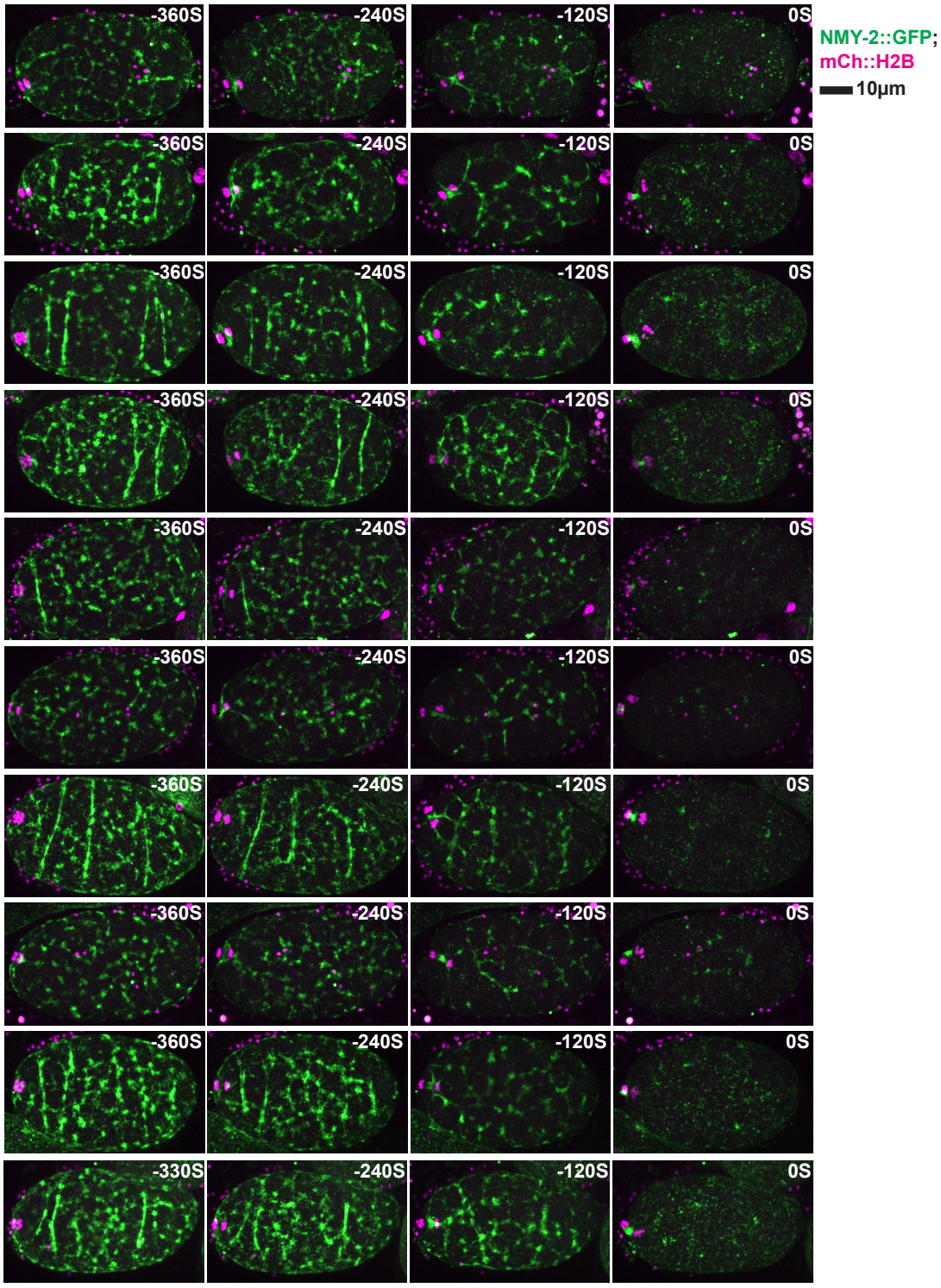


**Figure F.14 – Control oocyte NMY-2::GFP cortical dynamics**
Time-lapse spinning disk confocal images of control oocytes expressing NMY-2::GFP and mCherry::H2B; t = 0 seconds corresponds to the end of meiosis I and beginning of meiosis II in this and subsequent figure 4.7 supplements (supplemental figures 4.15-4.18)

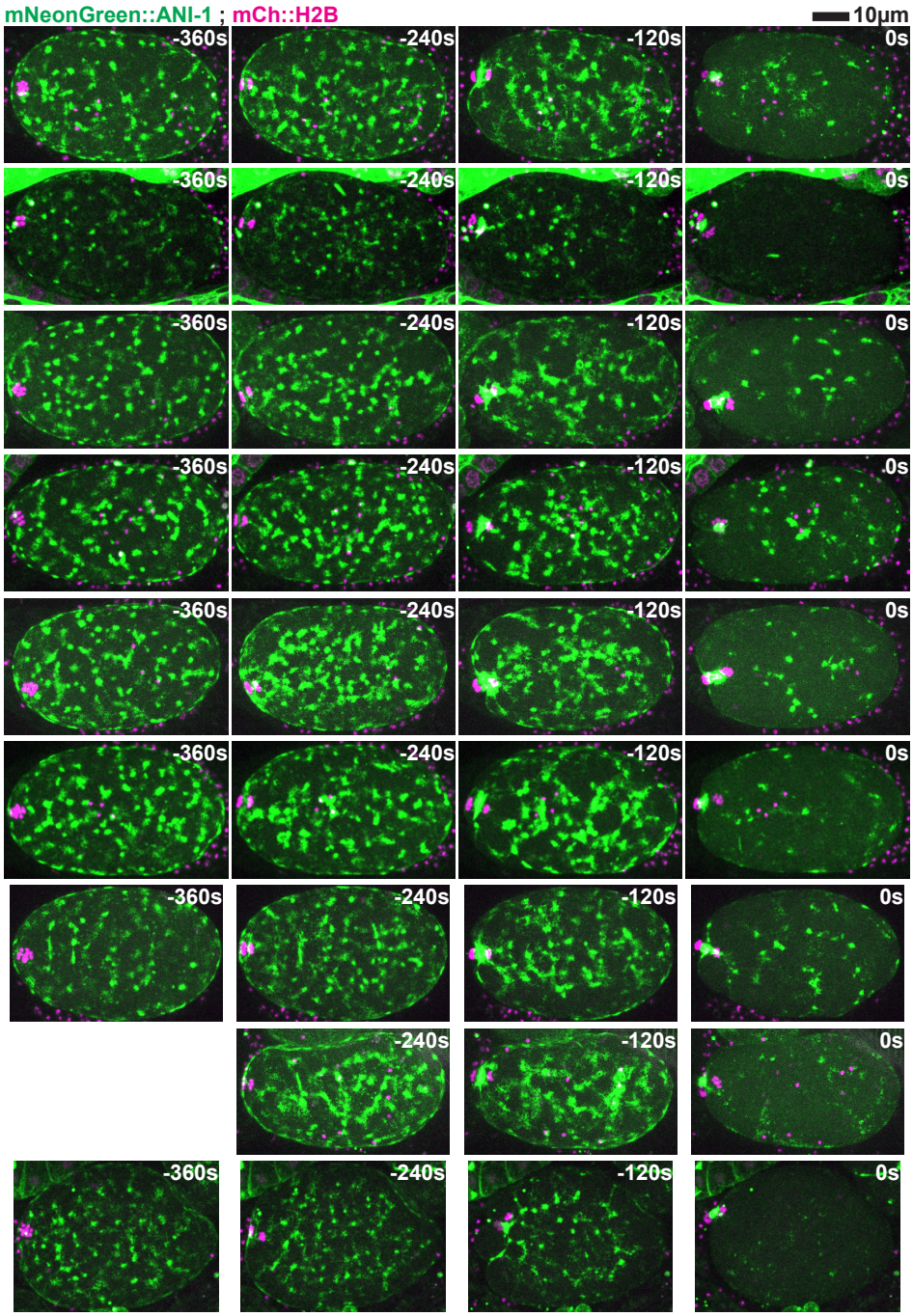


**Figure F.15 – Control oocyte mNG::ANI-1 cortical dynamics**
Time-lapse spinning disk confocal images of control oocytes expressing mNeonGreen::ANI-1 and mCherry::H2B.

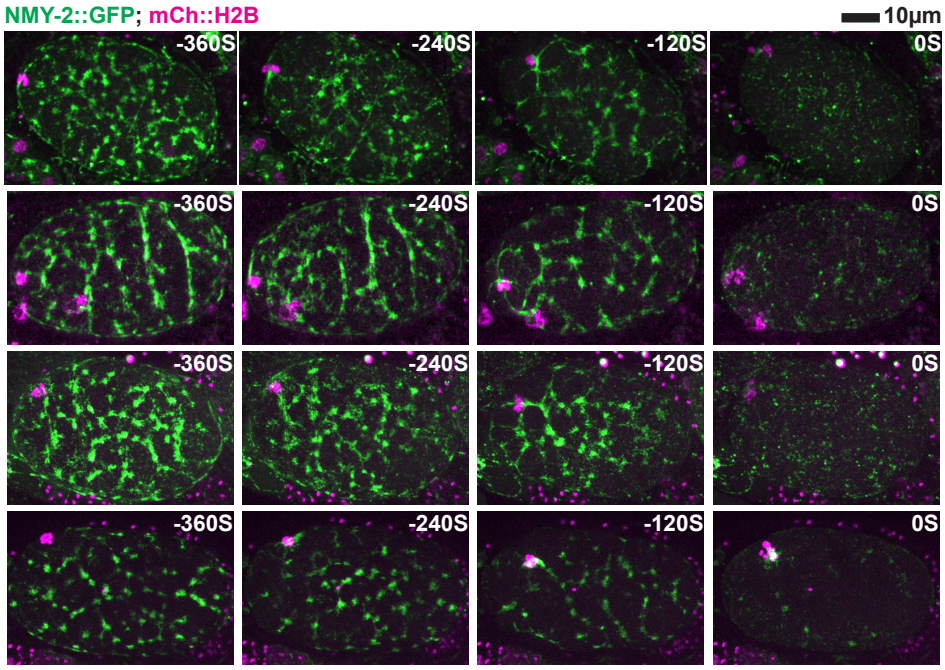


**Figure F.16 – *cls-2(or1948)* oocyte NMY-2::GFP cortical dynamics**
Time-lapse spinning disk confocal images of *cls-2* mutant oocytes expressing NMY-2::GFP and mCherry::H2B. All oocytes shown succeed in polar body extrusion.

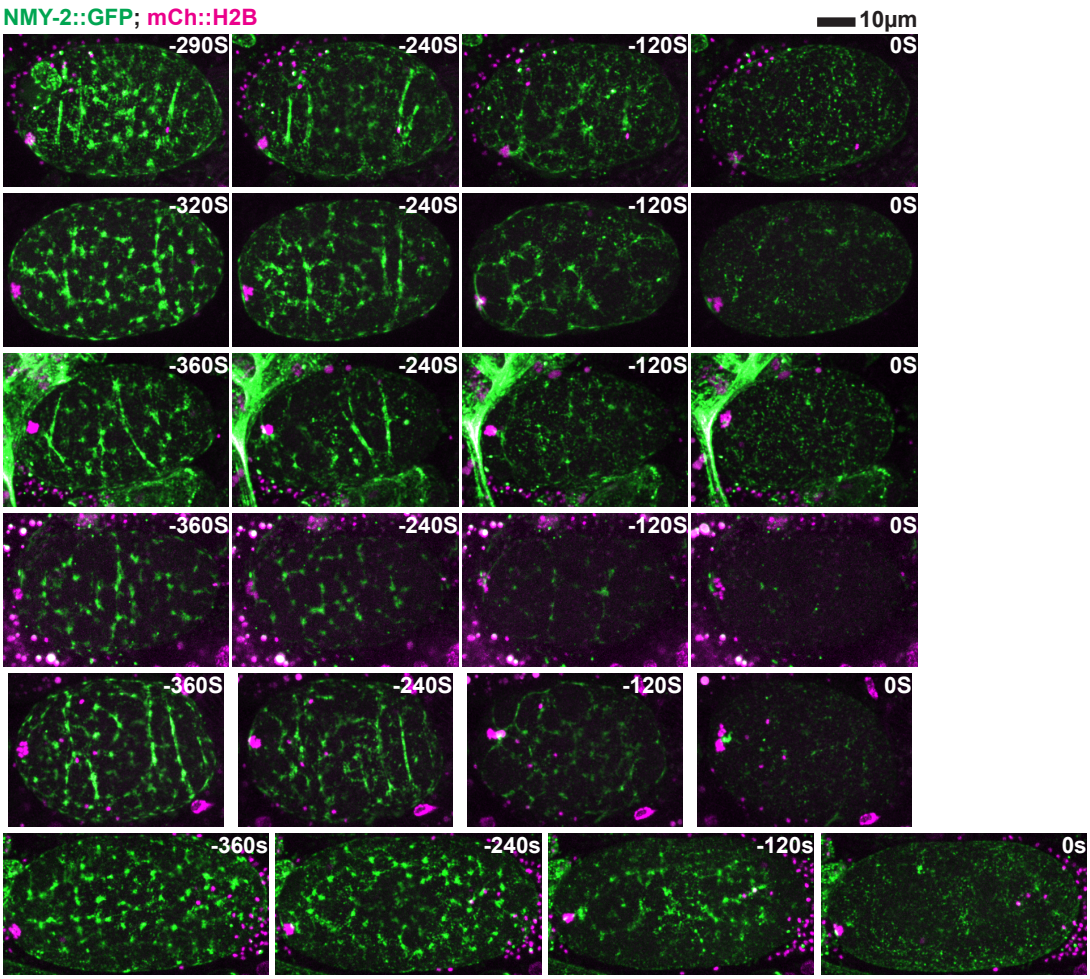


**Figure F.17 – *cls-2(or1948)* oocyte NMY-2::GFP cortical dynamics**
Time-lapse spinning disk confocal images of *cls-2* mutant oocytes expressing NMY-2::GFP and mCherry::H2B. All oocytes shown failed in polar body extrusion.

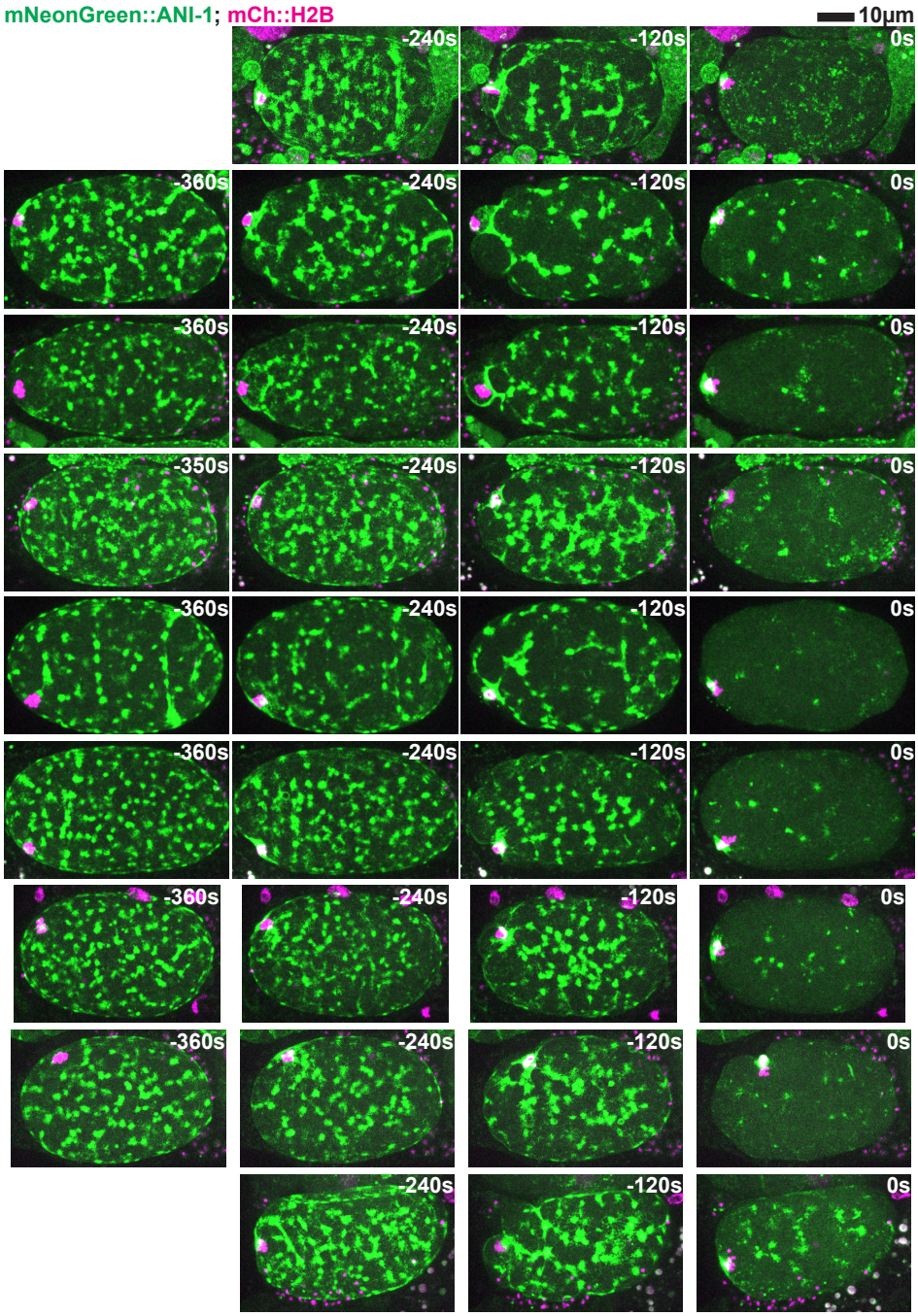


**Figure F.18 – *cls-2(or1948)* oocyte mNG::ANI-1 cortical dynamics**
Time-lapse spinning disk confocal images of *cls-2* mutant oocytes expressing mNeonGreen::ANI-1 and mCherry::H2B. All oocytes shown failed in polar body extrusion.

# REFERENCES CITED


Agostinho, A., Meier, B., Sonneville, R., Jagut, M., Woglar, A., Blow, J., Jantsch, V., & Gartner, A. (2013). Combinatorial regulation of meiotic holliday junction resolution in C. elegans by HIM-6 (BLM) helicase, SLX-4, and the SLX-1, MUS-81 and XPF-1 nucleases. *PLoS Genet, 9*(7), e1003591. doi:10.1371/journal.pgen.1003591

Aher, A., Kok, M., Sharma, A., Rai, A., Olieric, N., Rodriguez-Garcia, R., Katrukha, E. A., Weinert, T., Olieric, V., Kapitein, L. C., Steinmetz, M. O., Dogterom, M., & Akhmanova, A. (2018). CLASP Suppresses Microtubule Catastrophes through a Single TOG Domain. *Dev Cell, 46*(1), 40-58 e48. doi:10.1016/j.devcel.2018.05.032

Akera, T., Chmatal, L., Trimm, E., Yang, K., Aonbangkhen, C., Chenoweth, D. M., Janke, C., Schultz, R. M., & Lampson, M. A. (2017). Spindle asymmetry drives non-Mendelian chromosome segregation. *Science, 358*(6363), 668-672. doi:10.1126/science.aan0092

Akhmanova, A., & Steinmetz, M. O. (2015). Control of microtubule organization and dynamics: two ends in the limelight. *Nat Rev Mol Cell Biol, 16*(12), 711-726. doi:10.1038/nrm4084

Al-Bassam, J., Kim, H., Brouhard, G., van Oijen, A., Harrison, S. C., & Chang, F. (2010). CLASP promotes microtubule rescue by recruiting tubulin dimers to the microtubule. *Dev Cell, 19*(2), 245-258. doi:10.1016/j.devcel.2010.07.016

Askjaer, P., Galy, V., Hannak, E., & Mattaj, I. W. (2002). Ran GTPase cycle and importins alpha and beta are essential for spindle formation and nuclear envelope assembly in living Caenorhabditis elegans embryos. *Mol Biol Cell, 13*(12), 4355-4370. doi:10.1091/mbc.E02-06-0346

Barry, D. J., Durkin, C. H., Abella, J. V., & Way, M. (2015). Open source software for quantification of cell migration, protrusions, and fluorescence intensities. *J Cell Biol, 209*(1), 163-180. doi:10.1083/jcb.201501081

Basant, A., & Glotzer, M. (2018). Spatiotemporal Regulation of RhoA during Cytokinesis. *Curr Biol, 28*(9), R570-R580. doi:10.1016/j.cub.2018.03.045

Bellanger, J. M., Carter, J. C., Phillips, J. B., Canard, C., Bowerman, B., & Gonczy, P. (2007). ZYG-9, TAC-1 and ZYG-8 together ensure correct microtubule function throughout the cell cycle of C. elegans embryos. *J Cell Sci, 120*(Pt 16), 2963-2973. doi: 10.1242/jcs.004812

Bellanger, J. M., & Gonczy, P. (2003). TAC-1 and ZYG-9 form a complex that promotes microtubule assembly in C. elegans embryos. *Curr Biol, 13*(17), 1488-1498.

Brenner, S. (1974). The genetics of Caenorhabditis elegans. *Genetics, 77*(1), 71-94.

Brittle, A. L., & Ohkura, H. (2005). Mini spindles, the XMAP215 homologue, suppresses pausing of interphase microtubules in Drosophila. *Embo J, 24*(7), 1387-1396. doi:10.1038/sj.emboj.7600629

Byrnes, A. E., & Slep, K. C. (2017). TOG-tubulin binding specificity promotes microtubule dynamics and mitotic spindle formation. *J Cell Biol, 216*(6), 1641-1657. doi:10.1083/jcb.201610090

Cavazza, T., & Vernos, I. (2015). The RanGTP Pathway: From Nucleo-Cytoplasmic Transport to Spindle Assembly and Beyond. *Front Cell Dev Biol, 3*, 82. doi:10.3389/fcell.2015.00082

Chan, K. L., North, P. S., & Hickson, I. D. (2007). BLM is required for faithful chromosome segregation and its localization defines a class of ultrafine anaphase bridges. *EMBO J, 26*(14), 3397-3409. doi:10.1038/sj.emboj.7601777

Chan, K. L., Palmai-Pallag, T., Ying, S., & Hickson, I. D. (2009). Replication stress induces sister-chromatid bridging at fragile site loci in mitosis. *Nat Cell Biol, 11*(6), 753-760. doi:10.1038/ncb1882

Chan, Y. W., Fugger, K., & West, S. C. (2018). Unresolved recombination intermediates lead to ultra-fine anaphase bridges, chromosome breaks and aberrations. *Nat Cell Biol, 20*(1), 92-103. doi:10.1038/s41556-017-0011-1

Chuang, C.-H., Schlientz, A. J., Yang, J., & Bowerman, B. (2020). Microtubule Assembly and Pole Coalescence: Early Steps in *C. elegans* Oocyte Meiosis I Spindle Assembly. *BioRxiv*. doi:10.1101/2020.02.03.933051

Clandinin, T. R., & Mains, P. E. (1993). Genetic studies of mei-1 gene activity during the transition from meiosis to mitosis in Caenorhabditis elegans. *Genetics, 134*(1), 199-210.

Clark-Maguire, S., & Mains, P. E. (1994). mei-1, a gene required for meiotic spindle formation in Caenorhabditis elegans, is a member of a family of ATPases. *Genetics, 136*(2), 533-546.

Clarke, P. R., & Zhang, C. (2008). Spatial and temporal coordination of mitosis by Ran GTPase. *Nat Rev Mol Cell Biol, 9*(6), 464-477. doi:10.1038/nrm2410

Connolly, A. A., Osterberg, V., Christensen, S., Price, M., Lu, C., Chicas-Cruz, K., Lockery, S., Mains, P. E., & Bowerman, B. (2014). Caenorhabditis elegans oocyte meiotic spindle pole assembly requires microtubule severing and the calponin homology domain protein ASPM-1. *Mol Biol Cell, 25*(8), 1298-1311. doi:10.1091/mbc.E13-11-0687

Connolly, A. A., Sugioka, K., Chuang, C. H., Lowry, J. B., & Bowerman, B. (2015). KLP-7 acts through the Ndc80 complex to limit pole number in C. elegans oocyte meiotic spindle assembly. *J Cell Biol, 210*(6), 917-932. doi:10.1083/jcb.201412010

Cortes, D. B., McNally, K. L., Mains, P. E., & McNally, F. J. (2015). The asymmetry of female meiosis reduces the frequency of inheritance of unpaired chromosomes. *Elife, 4*, e06056. doi:10.7554/eLife.06056

Crowder, M. E., Flynn, J. R., McNally, K. P., Cortes, D. B., Price, K. L., Kuehnert, P. A., Panzica, M. T., Andaya, A., Leary, J. A., & McNally, F. J. (2015). Dynactin-dependent cortical dynein and spherical spindle shape correlate temporally with meiotic spindle rotation in Caenorhabditis elegans. *Mol Biol Cell, 26*(17), 3030-3046. doi:10.1091/mbc.E15-05-0290

Cullen, C. F., & Ohkura, H. (2001). Msps protein is localized to acentrosomal poles to ensure bipolarity of Drosophila meiotic spindles. *Nat Cell Biol, 3*(7), 637-642. doi:10.1038/35083025

Davis-Roca, A. C., Divekar, N. S., Ng, R. K., & Wignall, S. M. (2018). Dynamic SUMO remodeling drives a series of critical events during the meiotic divisions in Caenorhabditis elegans. *PLoS Genet, 14*(9), e1007626. doi:10.1371/journal.pgen.1007626

Davis-Roca, A. C., Muscat, C. C., & Wignall, S. M. (2017). Caenorhabditis elegans oocytes detect meiotic errors in the absence of canonical end-on kinetochore attachments. *J Cell Biol, 216*(5), 1243-1253. doi:10.1083/jcb.201608042

Dejima, K., Hori, S., Iwata, S., Suehiro, Y., Yoshina, S., Motohashi, T., & Mitani, S. (2018). An Aneuploidy-Free and Structurally Defined Balancer Chromosome Toolkit for Caenorhabditis elegans. *Cell Rep, 22*(1), 232-241. doi:10.1016/j.celrep.2017.12.024

Deng, M., & Li, R. (2009). Sperm chromatin-induced ectopic polar body extrusion in mouse eggs after ICSI and delayed egg activation. *PLoS One, 4*(9), e7171. doi:10.1371/journal.pone.0007171

Deng, M., Suraneni, P., Schultz, R. M., & Li, R. (2007). The Ran GTPase mediates chromatin signaling to control cortical polarity during polar body extrusion in mouse oocytes. *Dev Cell, 12*(2), 301-308. doi:10.1016/j.devcel.2006.11.008

Dorn, J. F., Zhang, L., Paradis, V., Edoh-Bedi, D., Jusu, S., Maddox, P. S., & Maddox, A. S. (2010). Actomyosin tube formation in polar body cytokinesis requires Anillin in C. elegans. *Curr Biol, 20*(22), 2046-2051. doi:10.1016/j.cub.2010.10.030

Dumont, J., & Desai, A. (2012). Acentrosomal spindle assembly and chromosome segregation during oocyte meiosis. *Trends Cell Biol, 22*(5), 241-249. doi:10.1016/j.tcb.2012.02.007

Dumont, J., Oegema, K., & Desai, A. (2010). A kinetochore-independent mechanism drives anaphase chromosome separation during acentrosomal meiosis. *Nat Cell Biol, 12*(9), 894-901. doi:10.1038/ncb2093

Edzuka, T., Yamada, L., Kanamaru, K., Sawada, H., & Goshima, G. (2014). Identification of the augmin complex in the filamentous fungus Aspergillus nidulans. *PLoS ONE, 9*(7), e101471. doi:10.1371/journal.pone.0101471

Espiritu, E. B., Krueger, L. E., Ye, A., & Rose, L. S. (2012). CLASPs function redundantly to regulate astral microtubules in the C. elegans embryo. *Dev Biol, 368*(2), 242-254. doi:10.1016/j.ydbio.2012.05.016

Fabritius, A. S., Flynn, J. R., & McNally, F. J. (2011). Initial diameter of the polar body contractile ring is minimized by the centralspindlin complex. *Dev Biol, 359*(1), 137-148. doi:10.1016/j.ydbio.2011.08.013

Fink, G., Hajdo, L., Skowronek, K. J., Reuther, C., Kasprzak, A. A., & Diez, S. (2009). The mitotic kinesin-14 Ncd drives directional microtubule-microtubule sliding. *Nat Cell Biol, 11*(6), 717-723. doi:10.1038/ncb1877

Flynn, J. R., & McNally, F. J. (2017). A casein kinase 1 prevents expulsion of the oocyte meiotic spindle into a polar body by regulating cortical contractility. *Mol Biol Cell, 28*(18), 2410-2419. doi:10.1091/mbc.E17-01-0056

Fraser, A. G., Kamath, R. S., Zipperlen, P., Martinez-Campos, M., Sohrmann, M., & Ahringer, J. (2000). Functional genomic analysis of C. elegans chromosome I by systematic RNA interference. *Nature, 408*(6810), 325-330. doi:10.1038/35042517

Gigant, E., Stefanutti, M., Laband, K., Gluszek-Kustusz, A., Edwards, F., Lacroix, B., Maton, G., Canman, J. C., Welburn, J. P. I., & Dumont, J. (2017). Inhibition of ectopic microtubule assembly by the kinesin-13 KLP-7 prevents chromosome segregation and cytokinesis defects in oocytes. *Development, 144*(9), 1674-1686. doi:10.1242/dev.147504

Gomes, J. E., Tavernier, N., Richaudeau, B., Formstecher, E., Boulin, T., Mains, P. E., Dumont, J., & Pintard, L. (2013). Microtubule severing by the katanin complex is activated by PPFR-1-dependent MEI-1 dephosphorylation. *J Cell Biol, 202*(3), 431-439. doi:10.1083/jcb.201304174

Goodman, B., Channels, W., Qiu, M., Iglesias, P., Yang, G., & Zheng, Y. (2010). Lamin B counteracts the kinesin Eg5 to restrain spindle pole separation during spindle assembly. *J Biol Chem, 285*(45), 35238-35244. doi:10.1074/jbc.M110.140749

Goshima, G., Nedelec, F., & Vale, R. D. (2005). Mechanisms for focusing mitotic spindle poles by minus end-directed motor proteins. *J Cell Biol, 171*(2), 229-240. doi:10.1083/jcb.200505107

Gray, S., & Cohen, P. E. (2016). Control of Meiotic Crossovers: From Double-Strand Break Formation to Designation. *Annu Rev Genet, 50*, 175-210. doi:10.1146/annurev-genet-120215-035111

Green, R. A., Paluch, E., & Oegema, K. (2012). Cytokinesis in animal cells. *Annu Rev Cell Dev Biol, 28*, 29-58. doi:10.1146/annurev-cellbio-101011-155718

Gruhn, J. R., Zielinska, A. P., Shukla, V., Blanshard, R., Capalbo, A., Cimadomo, D., Nikiforov, D., Chan, A. C., Newnham, L. J., Vogel, I., Scarica, C., Krapchev, M., Taylor, D., Kristensen, S. G., Cheng, J., Ernst, E., Bjorn, A. B., Colmorn, L. B., Blayney, M., Elder, K., Liss, J., Hartshorne, G., Grondahl, M. L., Rienzi, L., Ubaldi, F., McCoy, R., Lukaszuk, K., Andersen, C. Y., Schuh, M., & Hoffmann, E. R. (2019). Chromosome errors in human eggs shape natural fertility over reproductive life span. *Science, 365*(6460), 1466-1469. doi:10.1126/science.aav7321

Gruss, O. J. (2018). Animal Female Meiosis: The Challenges of Eliminating Centrosomes. *Cells, 7*(7). doi:10.3390/cells7070073

Gunzelmann, J., Ruthnick, D., Lin, T. C., Zhang, W., Neuner, A., Jakle, U., & Schiebel, E. (2018). The microtubule polymerase Stu2 promotes oligomerization of the gamma-TuSC for cytoplasmic microtubule nucleation. *Elife, 7*. doi:10.7554/eLife.39932

Hagmann, J., Burger, M. M., & Dagan, D. (1999). Regulation of plasma membrane blebbing by the cytoskeleton. *J Cell Biochem, 73*(4), 488-499.

Han, X., Adames, K., Sykes, E. M., & Srayko, M. (2015). The KLP-7 Residue S546 Is a Putative Aurora Kinase Site Required for Microtubule Regulation at the Centrosome in C. elegans. *PLoS One, 10*(7), e0132593. doi:10.1371/journal.pone.0132593

Han, X., Gomes, J. E., Birmingham, C. L., Pintard, L., Sugimoto, A., & Mains, P. E. (2009). The role of protein phosphatase 4 in regulating microtubule severing in the Caenorhabditis elegans embryo. *Genetics, 181*(3), 933-943. doi:10.1534/genetics.108.096016

Hassold, T., & Hunt, P. (2001). To err (meiotically) is human: the genesis of human aneuploidy. *Nat Rev Genet, 2*(4), 280-291. doi:10.1038/35066065

Hatsumi, M., & Endow, S. A. (1992). The Drosophila ncd microtubule motor protein is spindle-associated in meiotic and mitotic cells. *J Cell Sci, 103 ( Pt 4)*, 1013-1020.

Hayashi, D., Tanabe, K., Katsube, H., & Inoue, Y. H. (2016). B-type nuclear lamin and the nuclear pore complex Nup107-160 influences maintenance of the spindle envelope required for cytokinesis in Drosophila male meiosis. *Biol Open, 5*(8), 1011-1021. doi:10.1242/bio.017566

Hillers, K. J., & Villeneuve, A. M. (2003). Chromosome-wide control of meiotic crossing over in C. elegans. *Curr Biol, 13*(18), 1641-1647. doi:10.1016/j.cub.2003.08.026

Holubcova, Z., Blayney, M., Elder, K., & Schuh, M. (2015). Human oocytes. Error-prone chromosome-mediated spindle assembly favors chromosome segregation defects in human oocytes. *Science, 348*(6239), 1143-1147. doi:10.1126/science.aaa9529

Hong, Y., Sonneville, R., Agostinho, A., Meier, B., Wang, B., Blow, J. J., & Gartner, A. (2016). The SMC-5/6 Complex and the HIM-6 (BLM) Helicase Synergistically Promote Meiotic Recombination Intermediate Processing and Chromosome Maturation during Caenorhabditis elegans Meiosis. *PLoS Genet, 12*(3), e1005872. doi:10.1371/journal.pgen.1005872

Hong, Y., Sonneville, R., Wang, B., Scheidt, V., Meier, B., Woglar, A., Demetriou, S., Labib, K., Jantsch, V., & Gartner, A. (2018). LEM-3 is a midbody-tethered DNA nuclease that resolves chromatin bridges during late mitosis. *Nat Commun, 9*(1), 728. doi:10.1038/s41467-018-03135-w

Hong, Y., Velkova, M., Silva, N., Jagut, M., Scheidt, V., Labib, K., Jantsch, V., & Gartner, A. (2018). The conserved LEM-3/Ankle1 nuclease is involved in the combinatorial regulation of meiotic recombination repair and chromosome segregation in Caenorhabditis elegans. *PLoS Genet, 14*(6), e1007453. doi:10.1371/journal.pgen.1007453

Howe, M., McDonald, K. L., Albertson, D. G., & Meyer, B. J. (2001). HIM-10 is required for kinetochore structure and function on Caenorhabditis elegans holocentric chromosomes. *J Cell Biol, 153*(6), 1227-1238. doi:10.1083/jcb.153.6.1227

Hughes, S. E., & Hawley, R. S. (2014). Topoisomerase II is required for the proper separation of heterochromatic regions during Drosophila melanogaster female meiosis. *PLoS Genet, 10*(10), e1004650. doi:10.1371/journal.pgen.1004650

Inoue, Y. H., Savoian, M. S., Suzuki, T., Mathe, E., Yamamoto, M. T., & Glover, D. M. (2004). Mutations in orbit/mast reveal that the central spindle is comprised of two microtubule populations, those that initiate cleavage and those that propagate furrow ingression. *J Cell Biol, 166*(1), 49-60. doi:10.1083/jcb.200402052

Ito, A., & Goshima, G. (2015). Microcephaly protein Asp focuses the minus ends of spindle microtubules at the pole and within the spindle. *J Cell Biol, 211*(5), 999-1009. doi:10.1083/jcb.201507001

Joly, N., Martino, L., Gigant, E., Dumont, J., & Pintard, L. (2016). Microtubule-severing activity of the AAA+ ATPase Katanin is essential for female meiotic spindle assembly. *Development, 143*(19), 3604-3614. doi:10.1242/dev.140830

Kaitna, S., Pasierbek, P., Jantsch, M., Loidl, J., & Glotzer, M. (2002). The Aurora B Kinase AIR-2 Regulates Kinetochores during Mitosis and Is Required for Separation of Homologous Chromosomes during Meiosis. *Current Biology, 12*(10), 798-812. doi:10.1016/s0960-9822(02)00820-5

Kamath, R. S., Fraser, A. G., Dong, Y., Poulin, G., Durbin, R., Gotta, M., Kanapin, A., Le Bot, N., Moreno, S., Sohrmann, M., Welchman, D. P., Zipperlen, P., & Ahringer, J. (2003). Systematic functional analysis of the Caenorhabditis elegans genome using RNAi. *Nature, 421*(6920), 231-237.

Kamath, R. S., Martinez-Campos, M., Zipperlen, P., Fraser, A. G., & Ahringer, J. (2001). Effectiveness of specific RNA-mediated interference through ingested double-stranded RNA in Caenorhabditis elegans. *Genome Biol, 2*(1), RESEARCH0002. doi:10.1186/gb-2000-2-1-research0002

Kosco, K. A., Pearson, C. G., Maddox, P. S., Wang, P. J., Adams, I. R., Salmon, E. D., Bloom, K., & Huffaker, T. C. (2001). Control of microtubule dynamics by Stu2p is essential for spindle orientation and metaphase chromosome alignment in yeast. *Mol Biol Cell, 12*(9), 2870-2880. doi:10.1091/mbc.12.9.2870

Laband, K., Le Borgne, R., Edwards, F., Stefanutti, M., Canman, J. C., Verbavatz, J. M., & Dumont, J. (2017). Chromosome segregation occurs by microtubule pushing in oocytes. *Nat Commun, 8*(1), 1499. doi:10.1038/s41467-017-01539-8

Lansbergen, G., Grigoriev, I., Mimori-Kiyosue, Y., Ohtsuka, T., Higa, S., Kitajima, I., Demmers, J., Galjart, N., Houtsmuller, A. B., Grosveld, F., & Akhmanova, A. (2006). CLASPs attach microtubule plus ends to the cell cortex through a complex with LL5beta. *Dev Cell, 11*(1), 21-32. doi:10.1016/j.devcel.2006.05.012

Libuda, D. E., Uzawa, S., Meyer, B. J., & Villeneuve, A. M. (2013). Meiotic chromosome structures constrain and respond to designation of crossover sites. *Nature, 502*(7473), 703-706. doi:10.1038/nature12577

Liu, J., Rolef Ben-Shahar, T., Riemer, D., Treinin, M., Spann, P., Weber, K., Fire, A., & Gruenbaum, Y. (2000). Essential roles for Caenorhabditis elegans lamin gene in nuclear organization, cell cycle progression, and spatial organization of nuclear pore complexes. *Mol Biol Cell, 11*(11), 3937-3947. doi:10.1091/mbc.11.11.3937

MacQueen, A. J., Colaiacovo, M. P., McDonald, K., & Villeneuve, A. M. (2002). Synapsis-dependent and -independent mechanisms stabilize homolog pairing during meiotic prophase in C. elegans. *Genes Dev, 16*(18), 2428-2442. doi:10.1101/gad.1011602

MacQueen, A. J., Phillips, C. M., Bhalla, N., Weiser, P., Villeneuve, A. M., & Dernburg, A. F. (2005). Chromosome sites play dual roles to establish homologous synapsis during meiosis in C. elegans. *Cell, 123*(6), 1037-1050. doi:10.1016/j.cell.2005.09.034

Maddox, A. S., Azoury, J., & Dumont, J. (2012). Polar body cytokinesis. *Cytoskeleton (Hoboken), 69*(11), 855-868. doi:10.1002/cm.21064

Mains, P. E., Kemphues, K. J., Sprunger, S. A., Sulston, I. A., & Wood, W. B. (1990). Mutations affecting the meiotic and mitotic divisions of the early Caenorhabditis elegans embryo. *Genetics, 126*(3), 593-605.

Martinez-Perez, E., & Colaiacovo, M. P. (2009). Distribution of meiotic recombination events: talking to your neighbors. *Curr Opin Genet Dev, 19*(2), 105-112. doi:10.1016/j.gde.2009.02.005

Martinez-Perez, E., Schvarzstein, M., Barroso, C., Lightfoot, J., Dernburg, A. F., & Villeneuve, A. M. (2008). Crossovers trigger a remodeling of meiotic chromosome axis composition that is linked to two-step loss of sister chromatid cohesion. *Genes Dev, 22*(20), 2886-2901. doi:10.1101/gad.1694108

Maton, G., Edwards, F., Lacroix, B., Stefanutti, M., Laband, K., Lieury, T., Kim, T., Espeut, J., Canman, J. C., & Dumont, J. (2015). Kinetochore components are required for central spindle assembly. *Nat Cell Biol, 17*(7), 953. doi:10.1038/ncb3199

Matthies, H. J., McDonald, H. B., Goldstein, L. S., & Theurkauf, W. E. (1996). Anastral meiotic spindle morphogenesis: role of the non-claret disjunctional kinesin-like protein. *The Journal of cell biology, 134*(2), 455-464.

McNally, K., Audhya, A., Oegema, K., & McNally, F. J. (2006). Katanin controls mitotic and meiotic spindle length. *J Cell Biol, 175*(6), 881-891.

McNally, K., Berg, E., Cortes, D. B., Hernandez, V., Mains, P. E., & McNally, F. J. (2014). Katanin maintains meiotic metaphase chromosome alignment and spindle structure in vivo and has multiple effects on microtubules in vitro. *Mol Biol Cell, 25*(7), 1037-1049. doi:10.1091/mbc.E13-12-0764

McNally, K. P., Panzica, M. T., Kim, T., Cortes, D. B., & McNally, F. J. (2016). A novel chromosome segregation mechanism during female meiosis. *Mol Biol Cell, 27*(16), 2576-2589. doi:10.1091/mbc.E16-05-0331

McVey, M., Andersen, S. L., Broze, Y., & Sekelsky, J. (2007). Multiple functions of Drosophila BLM helicase in maintenance of genome stability. *Genetics, 176*(4), 1979-1992. doi:10.1534/genetics.106.070052

Mimori-Kiyosue, Y., Grigoriev, I., Lansbergen, G., Sasaki, H., Matsui, C., Severin, F., Galjart, N., Grosveld, F., Vorobjev, I., Tsukita, S., & Akhmanova, A. (2005). CLASP1 and CLASP2 bind to EB1 and regulate microtubule plus-end dynamics at the cell cortex. *J Cell Biol, 168*(1), 141-153. doi:10.1083/jcb.200405094

Monen, J., Maddox, P. S., Hyndman, F., Oegema, K., & Desai, A. (2005). Differential role of CENP-A in the segregation of holocentric C. elegans chromosomes during meiosis and mitosis. *Nat Cell Biol, 7*(12), 1248-1255. doi:10.1038/ncb1331

Motegi, F., Velarde, N. V., Piano, F., & Sugimoto, A. (2006). Two phases of astral microtubule activity during cytokinesis in C. elegans embryos. *Dev Cell, 10*(4), 509-520. doi:10.1016/j.devcel.2006.03.001

Mullen, T. J., Davis-Roca, A. C., & Wignall, S. M. (2019). Spindle assembly and chromosome dynamics during oocyte meiosis. *Curr Opin Cell Biol, 60*, 53-59. doi:10.1016/j.ceb.2019.03.014

Mullen, T. J., & Wignall, S. M. (2017). Interplay between microtubule bundling and sorting factors ensures acentriolar spindle stability during C. elegans oocyte meiosis. *PLoS Genet, 13*(9), e1006986. doi:10.1371/journal.pgen.1006986

Muller, H. J. (1916). The Mechanism of Crossing-Over. *The American Naturalist, 50*(592), 193-221. doi:10.1086/279534

Muscat, C. C., Torre-Santiago, K. M., Tran, M. V., Powers, J. A., & Wignall, S. M. (2015). Kinetochore-independent chromosome segregation driven by lateral microtubule bundles. *Elife, 4*, e06462. doi:10.7554/eLife.06462

Nabeshima, K., Villeneuve, A. M., & Colaiacovo, M. P. (2005). Crossing over is coupled to late meiotic prophase bivalent differentiation through asymmetric disassembly of the SC. *J Cell Biol, 168*(5), 683-689. doi:10.1083/jcb.200410144

Ohkura, H. (2015). Meiosis: an overview of key differences from mitosis. *Cold Spring Harb Perspect Biol, 7*(5). doi:10.1101/cshperspect.a015859

Paix, A., Folkmann, A., Rasoloson, D., & Seydoux, G. (2015). High Efficiency, Homology-Directed Genome Editing in Caenorhabditis elegans Using CRISPR-Cas9 Ribonucleoprotein Complexes. *Genetics, 201*(1), 47-54. doi:10.1534/genetics.115.179382

Patel, K., Nogales, E., & Heald, R. (2012). Multiple domains of human CLASP contribute to microtubule dynamics and organization in vitro and in Xenopus egg extracts. *Cytoskeleton (Hoboken), 69*(3), 155-165. doi:10.1002/cm.21005

Pelisch, F., Bel Borja, L., Jaffray, E. G., & Hay, R. T. (2019). Sumoylation regulates protein dynamics during meiotic chromosome segregation in C. elegans oocytes. *J Cell Sci, 132*(14). doi:10.1242/jcs.232330

Pelisch, F., Tammsalu, T., Wang, B., Jaffray, E. G., Gartner, A., & Hay, R. T. (2017). A SUMO-Dependent Protein Network Regulates Chromosome Congression during Oocyte Meiosis. *Mol Cell, 65*(1), 66-77. doi:10.1016/j.molcel.2016.11.001

Piekny, A. J., & Maddox, A. S. (2010). The myriad roles of Anillin during cytokinesis. *Semin Cell Dev Biol, 21*(9), 881-891. doi:10.1016/j.semcdb.2010.08.002

Pintard, L., & Bowerman, B. (2019). Mitotic Cell Division in *Caenorhabditis elegans*. *Genetics, 211*(1), 35-73. doi:10.1534/genetics.118.301367

Potapova, T., & Gorbsky, G. J. (2017). The Consequences of Chromosome Segregation Errors in Mitosis and Meiosis. *Biology (Basel), 6*(1). doi:10.3390/biology6010012

Prosser, S. L., & Pelletier, L. (2017). Mitotic spindle assembly in animal cells: a fine balancing act. *Nat Rev Mol Cell Biol, 18*(3), 187-201. doi:10.1038/nrm.2016.162

Rogers, E., Bishop, J. D., Waddle, J. A., Schumacher, J. M., & Lin, R. (2002). The aurora kinase AIR-2 functions in the release of chromosome cohesion in Caenorhabditis elegans meiosis. *J Cell Biol, 157*(2), 219-229. doi:10.1083/jcb.200110045

Romano, A., Guse, A., Krascenicova, I., Schnabel, H., Schnabel, R., & Glotzer, M. (2003). CSC-1: a subunit of the Aurora B kinase complex that binds to the survivin-like protein BIR-1 and the incenp-like protein ICP-1. *J Cell Biol, 161*(2), 229-236. doi:10.1083/jcb.200207117

Roostalu, J., & Surrey, T. (2017). Microtubule nucleation: beyond the template. *Nat Rev Mol Cell Biol, 18*(11), 702-710. doi:10.1038/nrm.2017.75

Schindelin, J., Arganda-Carreras, I., Frise, E., Kaynig, V., Longair, M., Pietzsch, T., Preibisch, S., Rueden, C., Saalfeld, S., Schmid, B., Tinevez, J. Y., White, D. J., Hartenstein, V., Eliceiri, K., Tomancak, P., & Cardona, A. (2012). Fiji: an open-source platform for biological-image analysis. *Nat Methods, 9*(7), 676-682. doi:10.1038/nmeth.2019

Schonegg, S., & Hyman, A. A. (2006). CDC-42 and RHO-1 coordinate acto-myosin contractility and PAR protein localization during polarity establishment in C. elegans embryos. *Development, 133*(18), 3507-3516. doi:10.1242/dev.02527

Schuh, M., & Ellenberg, J. (2007). Self-organization of MTOCs replaces centrosome function during acentrosomal spindle assembly in live mouse oocytes. *Cell, 130*(3), 484-498. doi:10.1016/j.cell.2007.06.025

Schumacher, J. M., Golden, A., & Donovan, P. J. (1998). AIR-2: An Aurora/Ipl1-related protein kinase associated with chromosomes and midbody microtubules is required for polar body extrusion and cytokinesis in Caenorhabditis elegans embryos. *J Cell Biol, 143*(6), 1635-1646. doi:10.1083/jcb.143.6.1635

Schvarzstein, M., Pattabiraman, D., Libuda, D. E., Ramadugu, A., Tam, A., Martinez-Perez, E., Roelens, B., Zawadzki, K. A., Yokoo, R., Rosu, S., Severson, A. F., Meyer, B. J., Nabeshima, K., & Villeneuve, A. M. (2014). DNA helicase HIM-6/BLM both promotes MutSgamma-dependent crossovers and antagonizes MutSgamma-independent interhomolog associations during caenorhabditis elegans meiosis. *Genetics, 198*(1), 193-207. doi:10.1534/genetics.114.161513

Severson, A. F., von Dassow, G., & Bowerman, B. (2016). Oocyte Meiotic Spindle Assembly and Function. *Curr Top Dev Biol, 116*, 65-98. doi:10.1016/bs.ctdb.2015.11.031

Shelton, C. A., Carter, J. C., Ellis, G. C., & Bowerman, B. (1999). The nonmuscle myosin regulatory light chain gene mlc-4 is required for cytokinesis, anterior-posterior polarity, and body morphology during Caenorhabditis elegans embryogenesis. *J Cell Biol, 146*(2), 439-451. doi:10.1083/jcb.146.2.439

Shirasu-Hiza, M., Coughlin, P., & Mitchison, T. (2003). Identification of XMAP215 as a microtubule-destabilizing factor in Xenopus egg extract by biochemical purification. *J Cell Biol, 161*(2), 349-358. doi:10.1083/jcb.200211095

Siomos, M. F., Badrinath, A., Pasierbek, P., Livingstone, D., White, J., Glotzer, M., & Nasmyth, K. (2001). Separase is required for chromosome segregation during meiosis I in Caenorhabditis elegans. *Current Biology, 11*(23), 1825-1835. doi:10.1016/s0960-9822(01)00588-7

Skold, H. N., Komma, D. J., & Endow, S. A. (2005). Assembly pathway of the anastral Drosophila oocyte meiosis I spindle. *J Cell Sci, 118*(Pt 8), 1745-1755. doi:10.1242/jcs.02304

Smith, G. R., & Nambiar, M. (2020). New Solutions to Old Problems: Molecular Mechanisms of Meiotic Crossover Control. *Trends Genet, 36*(5), 337-346. doi:10.1016/j.tig.2020.02.002

So, C., Seres, K. B., Steyer, A. M., Monnich, E., Clift, D., Pejkovska, A., Mobius, W., & Schuh, M. (2019). A liquid-like spindle domain promotes acentrosomal spindle assembly in mammalian oocytes. *Science, 364*(6447). doi:10.1126/science.aat9557

Srayko, M., Buster, D. W., Bazirgan, O. A., McNally, F. J., & Mains, P. E. (2000). MEI-1/MEI-2 katanin-like microtubule severing activity is required for Caenorhabditis elegans meiosis. *Genes Dev, 14*(9), 1072-1084.

Srayko, M., O'Toole E, T., Hyman, A. A., & Müller-Reichert, T. (2006). Katanin disrupts the microtubule lattice and increases polymer number in C. elegans meiosis. *Curr Biol, 16*(19), 1944-1949.

Sturgill, E. G., & Ohi, R. (2013). Kinesin-12 differentially affects spindle assembly depending on its microtubule substrate. *Curr Biol, 23*(14), 1280-1290. doi:10.1016/j.cub.2013.05.043

Sturtevant, A. H. (1913). The linear arrangement of six sex-linked factors in Drosophila, as shown by their mode of association. *Journal of Experimental Zoology, 14*(1), 43-59. doi:10.1002/jez.1400140104

Sugiyama, T., Pramanik, M. K., & Yumura, S. (2015). Microtubule-Mediated Inositol Lipid Signaling Plays Critical Roles in Regulation of Blebbing. *PLoS One, 10*(8), e0137032. doi:10.1371/journal.pone.0137032

Swan, K. A., Severson, A. F., Carter, J. C., Martin, P. R., Schnabel, H., Schnabel, R., & Bowerman, B. (1998). cyk-1: a C. elegans FH gene required for a late step in embryonic cytokinesis. *J Cell Sci, 111 ( Pt 14)*, 2017-2027.

Tanenbaum, M. E., Macůrek, L., Janssen, A., Geers, E. F., Alvarez-Fernández, M., & Medema, R. H. (2009). Kif15 cooperates with eg5 to promote bipolar spindle assembly. *Curr Biol, 19*(20), 1703-1711. doi:10.1016/j.cub.2009.08.027

Thawani, A., Kadzik, R. S., & Petry, S. (2018). XMAP215 is a microtubule nucleation factor that functions synergistically with the gamma-tubulin ring complex. *Nat Cell Biol, 20*(5), 575-585. doi:10.1038/s41556-018-0091-6

Timmons, L., & Fire, A. (1998). Specific interference by ingested dsRNA. *Nature, 395*(6705), 854.

Tinevez, J. Y., Schulze, U., Salbreux, G., Roensch, J., Joanny, J. F., & Paluch, E. (2009). Role of cortical tension in bleb growth. *Proc Natl Acad Sci U S A, 106*(44), 18581-18586. doi:10.1073/pnas.0903353106

Tovey, C. A., & Conduit, P. T. (2018). Microtubule nucleation by gamma-tubulin complexes and beyond. *Essays Biochem, 62*(6), 765-780. doi:10.1042/EBC20180028

Tsai, M. Y., Wang, S., Heidinger, J. M., Shumaker, D. K., Adam, S. A., Goldman, R. D., & Zheng, Y. (2006). A mitotic lamin B matrix induced by RanGTP required for spindle assembly. *Science, 311*(5769), 1887-1893. doi:10.1126/science.1122771

Tsvetkov, A. S., Samsonov, A., Akhmanova, A., Galjart, N., & Popov, S. V. (2007). Microtubule-binding proteins CLASP1 and CLASP2 interact with actin filaments. *Cell Motil Cytoskeleton, 64*(7), 519-530. doi:10.1002/cm.20201

Vanneste, D., Takagi, M., Imamoto, N., & Vernos, I. (2009). The role of Hklp2 in the stabilization and maintenance of spindle bipolarity. *Curr Biol, 19*(20), 1712-1717. doi:10.1016/j.cub.2009.09.019

Vargas, E., McNally, K., Friedman, J. A., Cortes, D. B., Wang, D. Y., Korf, I. F., & McNally, F. J. (2017). Autosomal Trisomy and Triploidy Are Corrected During Female Meiosis in Caenorhabditis elegans. *Genetics, 207*(3), 911-922. doi:10.1534/genetics.117.300259

Wang, S., Hassold, T., Hunt, P., White, M. A., Zickler, D., Kleckner, N., & Zhang, L. (2017). Inefficient Crossover Maturation Underlies Elevated Aneuploidy in Human Female Meiosis. *Cell, 168*(6), 977-989 e917. doi:10.1016/j.cell.2017.02.002

Wignall, S. M., & Villeneuve, A. M. (2009). Lateral microtubule bundles promote chromosome alignment during acentrosomal oocyte meiosis. *Nat Cell Biol, 11*(7), 839-844. doi:10.1038/ncb1891

Woglar, A., & Villeneuve, A. M. (2018). Dynamic Architecture of DNA Repair Complexes and the Synaptonemal Complex at Sites of Meiotic Recombination. *Cell, 173*(7), 1678-1691 e1616. doi:10.1016/j.cell.2018.03.066

Wolff, I. D., Tran, M. V., Mullen, T. J., Villeneuve, A. M., & Wignall, S. M. (2016). Assembly of Caenorhabditis elegans acentrosomal spindles occurs without evident microtubule-organizing centers and requires microtubule sorting by KLP-18/kinesin-12 and MESP-1. *Mol Biol Cell, 27*(20), 3122-3131. doi:10.1091/mbc.E16-05-0291

Woodruff, J. B., Ferreira Gomes, B., Widlund, P. O., Mahamid, J., Honigmann, A., & Hyman, A. A. (2017). The Centrosome Is a Selective Condensate that Nucleates Microtubules by Concentrating Tubulin. *Cell, 169*(6), 1066-1077 e1010. doi:10.1016/j.cell.2017.05.028

Yang, H. Y., McNally, K., & McNally, F. J. (2003). MEI-1/katanin is required for translocation of the meiosis I spindle to the oocyte cortex in C elegans. *Dev Biol, 260*(1), 245-259.

Yokoo, R., Zawadzki, K. A., Nabeshima, K., Drake, M., Arur, S., & Villeneuve, A. M. (2012). COSA-1 reveals robust homeostasis and separable licensing and reinforcement steps governing meiotic crossovers. *Cell, 149*(1), 75-87. doi:10.1016/j.cell.2012.01.052

Zhang, D., Tu, S., Stubna, M., Wu, W. S., Huang, W. C., Weng, Z., & Lee, H. C. (2018). The piRNA targeting rules and the resistance to piRNA silencing in endogenous genes. *Science, 359*(6375), 587-592. doi:10.1126/science.aao2840

Zhang, L., Ward, J. D., Cheng, Z., & Dernburg, A. F. (2015). The auxin-inducible degradation (AID) system enables versatile conditional protein depletion in C. elegans. *Development, 142*(24), 4374-4384. doi:10.1242/dev.129635